High-Spin γ-Ray Spectroscopy of ^{124}Ba, ^{124}Xe and ^{125}Xe

Dissertation
zur
Erlangung des Doktorgrades (Dr. rer. nat.)
der
Mathematisch-Naturwissenschaftlichen Fakultät
der
Rheinischen Friedrich-Wilhelms-Universität
Bonn

vorgelegt von

Ali Al-Khatib

aus
Al-Mabouja (Syrien)

Bonn 2009

Angefertigt mit Genehmigung der

Mathematisch–Naturwissenschaftlichen Fakultät der

Rheinischen Friedrich–Wilhelms–Universität Bonn

1. Referent: Professor Dr. H. Hübel
2. Referent: Professor Dr. K. T. Brinkmann

Tag der Promotion: 18.08.2009

Contents

List of Figures

List of Tables

Chapter 1

Introduction

Rotational spectra had been observed for the first time in excited atomic nuclei in 1938 [TW38]. This observation was attributed to the deviation from spherical shape [Boh51, BM53, BM75]. In quantum mechanics, when a perfectly spherical system rotates, it appears identical when it is viewed from any direction and no point of reference exists to which the change in position can be identified. Therefore, rotation cannot be defined for spherical nuclei. If the shape deviates from spherical symmetry, the nucleus can rotate and rotational spectra are observed.

Many nucleons contribute to the rotation which is referred to as collective excitation [BM69, BM75]. Depending on the mass region, nuclei have different deformations and, therefore, different shapes. Many nuclei show larger deformation with increasing excitation energy. The nuclear shape can be characterised by the deformation parameters β or ε and γ [RS80] (the Lund convention [ALL+79] is used for the definition of β and γ). The quadrupole deformation parameters β or ε represent the magnitude of the deformation and the triaxiality parameter γ describes the deviation from axial symmetry.

Transitional nuclei between spherical and strongly deformed regions of the nuclear chart are usually soft with respect to deformation changes. Shape change, including triaxiality, can be induced by the excitation of nucleons into specific deformation-driving orbitals. In the mass region around $A \approx 125$, which is the subject of this thesis, nuclei are predicted to be soft with respect to γ deformation already at low and medium spin [CFL83, CB85] and are susceptible to polarisation effects from excited nucleons [WGB+89, LDF+90, TJJ+94, GMB+96, WMW+01, SHD+04, AKSH+06, RHSH+07].

Rotational motion leads to Coriolis-induced alignments of high-j nucleons, which are in this mass region predominantly protons and neutrons from the $h_{11/2}$ unique-parity intruder subshells. The proton Fermi level lies in the lower part of the $h_{11/2}$ subshell which favours prolate shape whereas the neutron Fermi level lies in the upper part of the $h_{11/2}$ subshell which favours oblate shape. According to the opposite shape-driving forces of protons and neutrons, shape co-existence is expected and the interplay between the $h_{11/2}$ proton and neutron orbitals is of great interest for spectroscopic investigations [WGB+89, GMB+96]. Spectroscopic studies of the shape and collectivity changes as a function of proton and neutron number have been made previously in this mass region, e.g. for Xe, Cs, Ba, La and Ce nuclei [LDF+90, GLG+91, SLD+93, TJJ+94, TSR+94, TSP+95, WYN+95, SPV+97, SCW+99, WMW+01, WGB+89, PFM+90, WJA+91, GMB+96, VCD+99, PBB+01, SCF+00, MBES+88, PBB+03, SMCC+04, SHD+04, AKSH+06, RHSH+07, AKHB+08].

In addition, superdeformation has been established in this mass region [SZF02]. These extreme shapes are associated with the occupation of high-j intruder orbitals from higher-lying shells which approach the Fermi surface at high spin. Furthermore, high-deformation local minima appear in the Cranked Shell Model (CSM) calculations [Ben89, Ben90] which are responsible for the recently observed very long highly collective bands, extending to almost $I = 60$, in ^{126}Xe [RHSH+07].

An interesting observation in this mass region is that nuclei undergo a shape-change from collective prolate to non-collective oblate states at high spins [TSP+95, SHD+04]. In this spin range the transitions within the rotational bands loose collectivity and, finally, when all nucleons outside the core have their spins aligned, the bands terminate. For example, calculations for ^{124}Xe within the CSM [Ben89, Ben90] indicate that the deformation at low and medium spins is moderate, $\varepsilon \simeq 0.2$, in agreement with the deformation obtained from lifetime measurements [SDM+04]. Collective configurations with $\gamma \simeq 0^{\circ}$

and -50° are favoured for configurations with proton and neutron excitations, respectively. These are crossed by non-collective oblate states with $\gamma \simeq 60^{\circ}$ around spin $I \simeq 22$ where some rotational bands terminate. The non-collective states are favoured in the Xe isotopes because of a gap in the single-particle level spectrum at $Z = 54$ for $\varepsilon \simeq 0.2$ which leads to a lower energy of terminating states compared to, e.g., the $Z = 56$ Ba nuclei. Indeed, a transition to an irregular level pattern has been observed experimentally above spin $I \simeq 20$ in neighbouring ^{122}Xe [TSR+94] and ^{126}Xe [RHSH+07].

In the framework of this thesis, extensive spectroscopic investigations of three nuclei of the $A \approx 125$ region, ^{124}Ba, ^{124}Xe and ^{125}Xe, have been performed. These nuclei have been studied with the largest spectrometers available, Euroball and Gammasphere. The previously known level schemes of these nuclei [PFM+90, SCW+99, GLG+91] have been extended substantially, both in the low- and high-spin regions. Many new rotational bands could be established. Lifetimes have been measured for several of the long large-deformation bands. The rotational structures, shape co-existence and band termination at high spins have been investigated.

Nuclear models required to interpret the experimental results of this work are described briefly in chapter two. To study the nuclei at a very high angular momentum, proper experimental techniques are required to populate the high-spin states and to detect the emitted γ rays. An overview of these techniques are given in chapter three. Procedures of data processing that include pre-sorting (gain-matching, energy and efficiency calibration, Doppler-shift corrections, add-back and time gate) and data compression are reported in chapter four. Chapter five contains the description of the methods of data analysis, i.e. sorting of energy histograms, spin and parity assignments, determination of γ-ray intensities, linear polarisation measurements and lifetime measurements of excited nuclear states using the Doppler-Shift Attenuation Method (DSAM). The experiments performed to produce the data used in this thesis are explained in chapter six. The experimental results and configuration assignments for the ^{124}Ba, ^{124}Xe and ^{125}Xe nuclei are reported in chapters seven, eight and nine, respectively. The results are discussed in chapter ten and chapter eleven gives a short summary.

Most of the results obtained in this work have been published:

- A. Al-Khatib *et al.*, *High-Spin States in ^{124}Ba*, Acta Phys. Pol. B **36**, 1029 (2005).
- A. Al-Khatib *et al.*, *Competition between collective and noncollective excitation modes at high spin in ^{124}Ba*, Phys. Rev. C **74**, 014305 (2006).
- A. Al-Khatib *et al.*, *High-Spin Spectroscopy of ^{124,125,126}Xe*, Acta Phys. Pol. B **38**, 21 (2007).
- A. Al-Khatib *et al.*, *Transition to non-collective states at high spin in ^{124}Xe*, Eur. Phys. J. A **36**, 21 (2008).

Chapter 2

Rotation of Deformed Nuclei

Breaking of the spherical symmetry of a quantal system leads to an anisotropy that allows for the specification of an orientation. An attribute of the existence of such a deformation is the nuclear rotation [Boh51, BM53, BM75].

The deformed nuclear potential can be described by the Nilsson model [Nil55, NTS+69, NR95]. Within the framework of this model, the nucleons are assumed to move independently in an average anisotropic modified harmonic oscillator potential. This leads to the deformed shell model (independent-particle model) which describes the single-particle excitations as a function of deformation [Hey99, HGE97, Kra87, EV89, NR95, Cas00, BM69, BM75, Szy83, RS80].

On the other hand, in the collective model, protons and neutrons are assumed to be mutually coupled to each other in a way that reflects the short-ranged strong nuclear force between them [Hey99, HGE97, Kra87, EV89, NR95, Cas00, BM69, BM75, Szy83, RS80]. Rotational spectra result from collective motion that can be described within the framework of the collective model. The interplay between collective rotation and single-particle motion is addressed by the cranking model [BF79b, BF79a, BFM86, NR95, Szy83, RS80].

Nuclei have a limited number of nucleons. In some cases, the rotational angular momentum approaches the maximum spin that can be built from a specific configuration. This leads to a termination of the rotational motion and further angular momentum can only be generated by single-particle excitation [RXBR86, RB85, AR95, AFLR99].

2.1 Deformed Nuclear Shapes

A schematic drawing of a deformed nucleus is shown in Fig. 2.1. The relation between the semi-axes a,

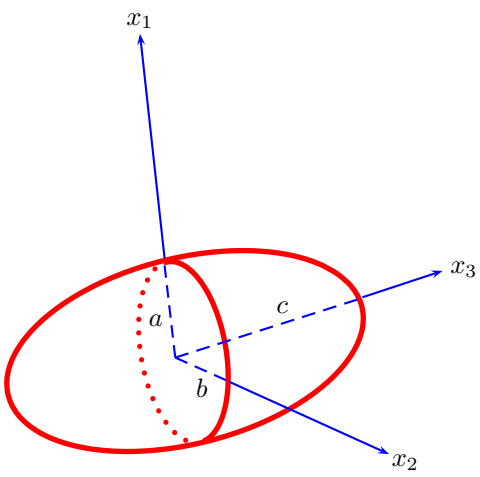

Figure 2.1: *Schematic illustration of a deformed nucleus with the body-fixed axes (intrinsic frame) $x_1x_2x_3$. The semi-axes are denoted by a, b and c.*

b and c determines the shape. The deformed nucleus takes an ellipsoidal shape when $a \neq b \neq c$. This corresponds to axially-asymmetric triaxial shapes, see Fig. 2.1. The case $a = b \neq c$ corresponds to an axially-symmetric shape, see Fig. 2.2(c). In the case of axial-symmetry we can define the deformation parameter δ [NR95]

$$\delta = 2\frac{c-b}{c+b}. \tag{2.1}$$

Prolate shape (cigar shape) corresponds to $\delta > 0$, see Fig. 2.2(a). Oblate shape (pan-cake shape) corresponds to $\delta < 0$, see Fig. 2.2(b). The axis ratio of an axially-symmetric nucleus ($c : a$) determines the strength of the deformation. Typically, normal deformation is defined by an axis ratio of $(c : a) \approx (1.2 : 1)$ and superdeformation by $(c : a) \approx (2 : 1)$. In general, the axis ratio depends on the mass region. The

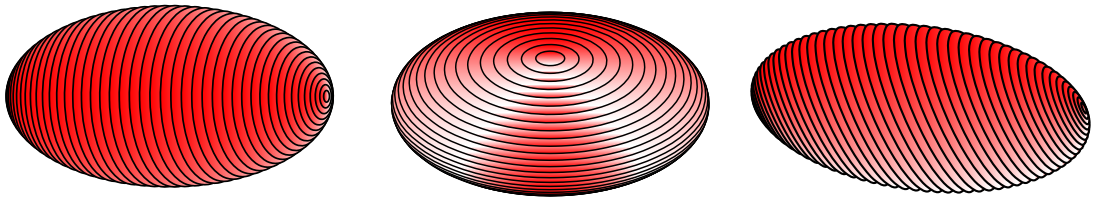

(a) *(b)* *(c)*

Figure 2.2: *Schematic presentation of nuclear shapes. Prolate shape (a), oblate shape (b) and triaxial shape (c).*

nuclear shape can be parametrised in terms of a spherical-harmonics $Y_{\lambda\mu}(\theta, \phi)$ expansion. The nuclear radius, $R(\theta, \phi)$, pointing form the origin to the surface of the nucleus is given by [RS80]

$$R(\theta, \phi) = R_0[1 + \sum_{\lambda=1}^{\infty} \sum_{\mu=-\lambda}^{\lambda} \alpha_{\lambda\mu} Y_{\lambda\mu}(\theta, \phi)]. \tag{2.2}$$

R_0 represents the radius at spherical equilibrium with the same volume and $\alpha_{\lambda\mu}$ are the shape parameters. In case of quadrupole deformation ($\lambda = 2$), the five shape parameters $\alpha_{2\mu}$ can be reduced to two [RS80], α_{20} and α_{22}, which are defined in terms of two new shape parameters (β_λ, γ) [RS80]

$$\alpha_{20} = \beta_2 \cos\gamma \tag{2.3}$$
$$\alpha_{22} = \tfrac{1}{\sqrt{2}}\beta_2 \sin\gamma. \tag{2.4}$$

The deformation parameter, β_2, represents the magnitude of the nuclear quadrupole deformation (elongation or flattening) and the nonaxiality, γ, represents the deviation of the nuclear shape from axial symmetry. Figure. 2.3 illustrates the possible nuclear shapes in the (β_2, γ) half-plane between $\gamma = -120^\circ$ and 60°. The nuclear shape can be fully described in the interval $0^\circ \leq \gamma \leq 60^\circ$. At $\gamma = 0^\circ$ and 120° the nuclear shape is prolate, whereas it is oblate at $\gamma = \pm 60^\circ$. Otherwise the shape is asymmetric or triaxial.

2.2 Nilsson Model

An axially-symmetric deformed nuclear potential is used within the framework of the Nilsson model [Nil55, NTS+69, NR95]. With the modified harmonic oscillator potential, the single-particle Hamiltonian reads

$$\hat{H} = -\frac{\hbar^2}{2M}(\partial_{x^2}^2 + \partial_{y^2}^2 + \partial_{z^2}^2) + \frac{M}{2}[\omega_\perp^2(x^2 + y^2) + \omega_z^2 z^2] - C\hat{L}\cdot\hat{S} - D(\hat{L}^2 - <\hat{L}^2>_N), \tag{2.5}$$

where $\omega_\perp = \omega_x = \omega_y \neq \omega_z$.

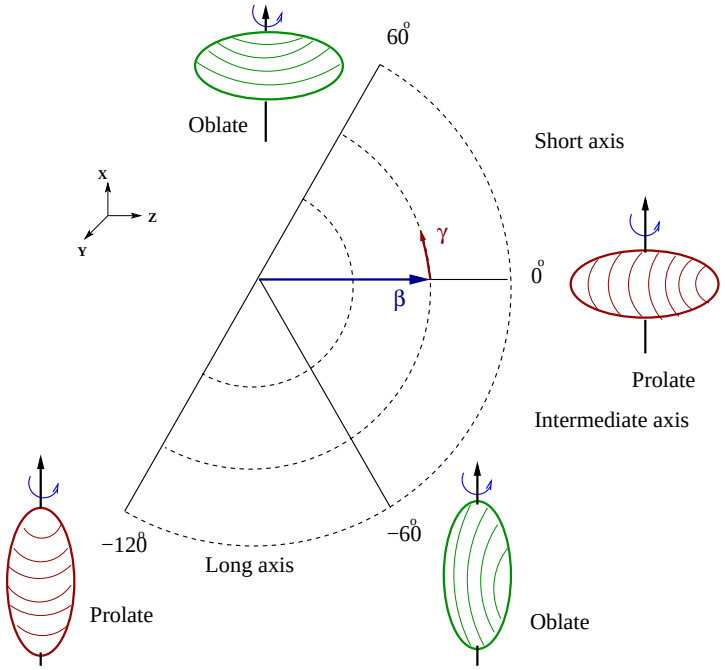

Figure 2.3: *Schematic drawing of the nuclear shape with respect to the deformation parameters (β_2, γ) (Lund convention [ALL+79]).*

It is convenient to introduce a new deformation parameter ε [NR95]

$$\omega_z = \omega_0(\varepsilon)(1 - \tfrac{2}{3}\varepsilon) \tag{2.6}$$

$$\omega_\perp = \omega_0(\varepsilon)(1 + \tfrac{1}{3}\varepsilon) \tag{2.7}$$

with ω_0 being weakly ε dependent. The distortion parameter ε is defined by [NR95]

$$\varepsilon = \frac{\omega_\perp - \omega_z}{\omega_0} \tag{2.8}$$

and $\varepsilon < 0$ corresponds to oblate deformation, $\varepsilon > 0$ to prolate deformation. In the limit of very large deformation, the states can be characterised by the so-called asymptotic quantum numbers (Nilsson quantum numbers) $[Nn_z\Lambda\Sigma]$ or $[Nn_z\Lambda]\Omega$ where $\Omega = \Lambda + \Sigma$. N is the principle quantum number and n_z its projection on the symmetry axis, $n_z = 0, 1, 2, 3, \ldots, N$. Λ, Σ and Ω are the projections of the orbital angular momentum L, the spin S and the total angular momentum J on the symmetry axis, respectively, see Fig. 2.4. The parity of the orbit is defined as $\pi = (-1)^l$. Each spherical (N, l, j) level is now split up into $j + \frac{1}{2}$ doubly-degenerate states, according to the $\pm\Omega$ degeneracy. Two examples of Nilsson energy-level diagrams are shown in Fig. 2.5. At moderate deformations $(\varepsilon \simeq 0.2 - 0.3)$, the asymptotic quantum numbers are only approximately valid.

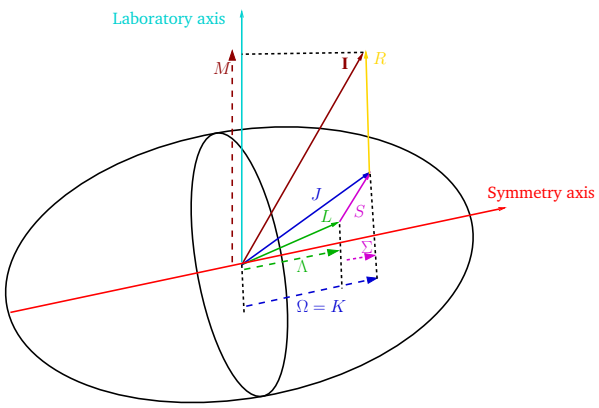

Figure 2.4: *Schematic drawing of an axially symmetric deformed nucleus indicating the different angular momentum quantum numbers. For large deformation $[Nn_z\Lambda\Sigma]$ or $[Nn_z\Lambda]\Omega$ are good quantum numbers[NR95].*

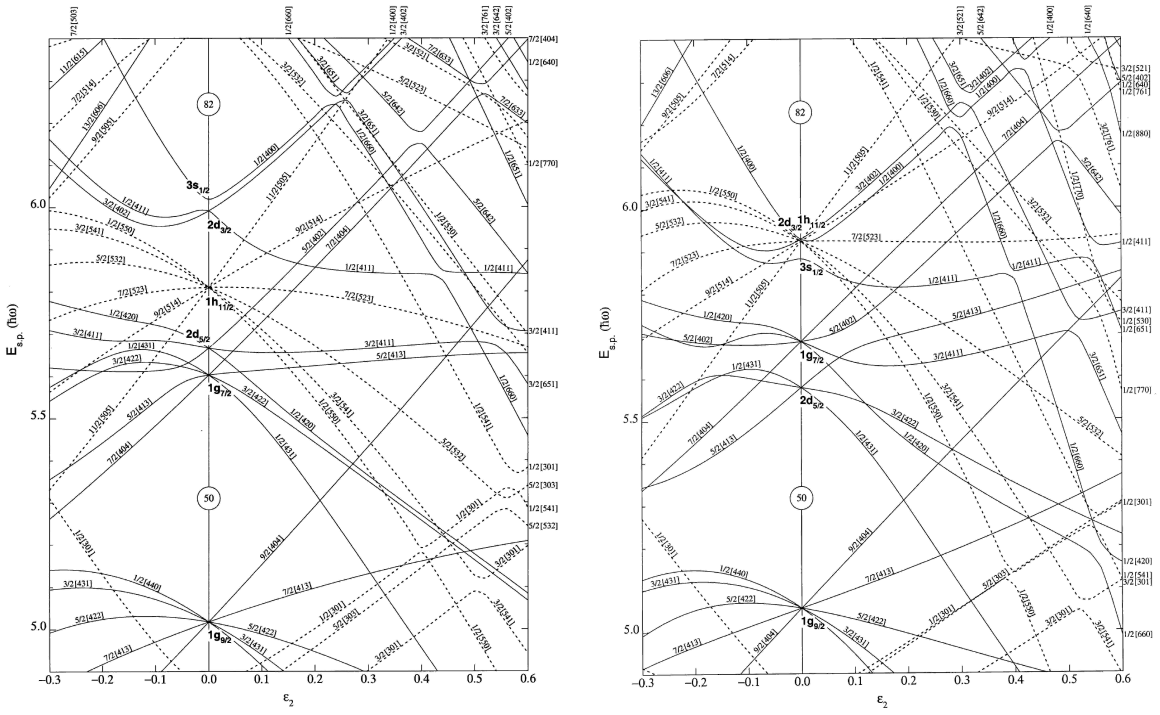

(a) *(b)*

Figure 2.5: *Nilsson diagram for the proton shell 50-82 (a) and for the neutron shell 50-82 (b), taken from [FBC99]. The single-particle energies, $E_{s.p.}$ are plotted as a function of the quadrupole deformation parameter ε_2.*

2.3 Cranking Model

Within the framework of the collective model the nucleons are assumed to move coherently. They are paired and form the *nuclear core*. Rotation is one degree of freedom of collective motion. The nucleus can be treated as a classical rigid body (rotor) [BM75]. The rotational spectrum of a pure collective rotation is given by [BM75]

$$\mathscr{E}_{rot}(I) = \frac{\hbar^2}{2\mathscr{I}} I(I+1), \tag{2.9}$$

where $\mathscr{I}$ is the moment of inertia and I is the total angular momentum. The effects of rotation on the single-particle states are described within the framework of the cranking model. The behaviour of nucleons is studied by rotating the nucleus with rotational frequency, ω, i.e. to crank the nucleus, hence the name cranking model. The first mathematical formulation of the model was made by Inglis [Ing54, Ing55] and has been further developed by Bengtsson and Frauendorf, see e.g. [BF79b, BF79a, BFM86]. The model provides a microscopic description of the influence of rotation on single-particle motion. The rotation is treated classically and the nucleons are considered as independent particles moving in an average rotating potential. To simplify the theoretical treatment, the intrinsic (body-fixed) coordinate system $(x_1x_2x_3)$ is used which has a fixed orientation at all times with respect to the nuclear potential. It rotates with rotational frequency, ω, relative to the laboratory coordinate system (xyz), see Fig. 2.6. If we assume that the intrinsic coordinates rotate around an axis perpendicular to the symmetry axis and the symmetry axis coincides with the intrinsic axis, x_3, and the intrinsic axis, x_1, coincides with the laboratory axis x, the total cranking Hamiltonian is given by

$$\mathscr{H}^{\omega} = \mathscr{H}^{0} - \omega J_x = \sum_{\mu} [\, h^0_{\mu} - \omega j_{x\mu}] \tag{2.10}$$

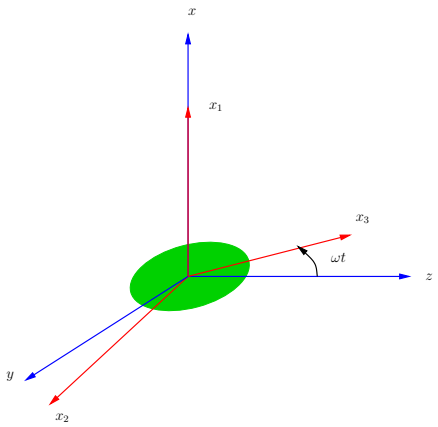

Figure 2.6: *The body-fixed (intrinsic) coordinates* $(x_1x_2x_3)$ *and the laboratory coordinates* (xyz).

where $\mathscr{H}^\omega$ and $h^\omega_\mu = h^0_\mu - \omega j_{x\mu}$ are the total and single particle Hamiltonians in the rotating frame, $\mathscr{H}^0$ and h^0_μ are the total and single-particle Hamiltonians in the laboratory system, and J_x and $j_{x\mu}$ are the total and single particle angular momentum projections onto the rotation axis. The $-\omega j_{x\mu}$ term contains the Coriolis and centrifugal forces [Szy83, VDS83, BG84]. The Coriolis force acts to align the angular momentum of the nucleons with the rotation axis [SS72, Ste75]. The eigenvalues of the Hamiltonian, $\mathscr{H}^\omega$, are known as Routhians. The total energy in the laboratory system is obtained as

$$\mathscr{E} = \sum_\mu e^\omega_\mu + \omega \sum_\mu \langle \mu^\omega | \, j_x \, | \mu^\omega \rangle \, , \tag{2.11}$$

where e^ω_μ denote the eigenvalues in the rotating frame. The projection of the total angular momentum onto the rotation axis can be determined by

$$I_x = \sum_\mu \langle \mu^\omega | \, j_x \, | \mu^\omega \rangle \, . \tag{2.12}$$

The slope of the Routhian is related to the alignment, i_x, that is the angular momentum gained by aligning a nucleon along the rotation axis. It is given by

$$i_x = -\frac{de^\omega_\mu}{d\omega}. \tag{2.13}$$

This relation makes it possible to compare the experimental aligned angular momenta with the theoretical Routhians. Because of the $-\omega j_x$ term, the time-reversal symmetry is broken. The Hamiltonian is only invariant under space reflection, parity π and under a rotation of 180° about the rotation axis, x. The rotation operator is given by

$$\mathscr{R}_x = e^{-i\pi j_x} \tag{2.14}$$

with the eigenvalues [BM75]

$$r = e^{-i\pi\alpha}, \tag{2.15}$$

where α is an additive quantum number known as signature [BM75]. It is related to the total angular momentum by

$$I = \alpha \bmod 2. \tag{2.16}$$

For a system with an even nucleon number

$$I = \begin{cases} 0, 2, 4, 6 \cdots & \text{if } r = +1 \;\; (\alpha = 0) \\ 1, 3, 5, 7 \cdots & \text{if } r = -1 \;\; (\alpha = 1) \end{cases} \tag{2.17}$$

while for a system with odd nucleon number

$$I = \begin{cases} 1/2, 5/2, 9/2 \cdots & \text{if } r = -i \;\; (\alpha = +1/2) \\ 3/2, 7/2, 11/2 \cdots & \text{if } r = +i \;\; (\alpha = -1/2) \end{cases} \tag{2.18}$$

The rotational states are characterised by the parity π and the signature α.

2.4 Cranked Nilsson-Strutinsky Formalism

The configuration-dependent Cranked Nilsson-Strutinsky (CNS) [BR85, NDB+85] formalism is a macroscopic-microscopic approach which uses the cranked Nilsson potential. The total energy of a rotating nucleus at a specific deformation $\bar{\varepsilon} \equiv (\varepsilon_2, \gamma, \varepsilon_4, \dots)$ and spin I_0 is calculated as

$$\mathscr{E}_{tot}(\bar{\varepsilon}, I_0) = \mathscr{E}_{RLD}(\bar{\varepsilon}, I = 0) + \delta E_{shell}(\bar{\varepsilon}, I_0), \tag{2.19}$$

where $\mathscr{E}_{RLD}$ is the energy of a rotating liquid drop given by [AFLR99]

$$\mathscr{E}_{RLD}(\bar{\varepsilon}, I = 0) = \mathscr{E}_{LD}(\bar{\varepsilon}, I = 0) + \mathscr{E}_{rot}(\bar{\varepsilon}, I_0). \tag{2.20}$$

$\mathscr{E}_{LD}$ is the energy within the framework of the liquid-drop model [AFLR99], and $\mathscr{E}_{rot}$ is the rotational energy of a rigid rotor [AFLR99]. The shell energy correction, δE_{shell}, is the difference between discrete, e_ν, and smoothed, $\tilde{e}_\nu$, single particle energy sums

$$\delta\mathscr{E}_{shell}(I_0) = \sum_\nu e_\nu(\omega, \bar{\varepsilon}) \mid_{I=I_0} - \sum_\nu \tilde{e}_\nu(\tilde{\omega}, \bar{\varepsilon}) \mid_{\tilde{I}=I_0} . \tag{2.21}$$

The smoothed sum is calculated using the Strutinsky procedure [Str67, ALL+79]. The total energy of a rotating nucleus can be calculated as a function of spin at any deformation. The particle configurations are specified by the total parity, π_{tot}, and total signature, α_{tot},

$$\pi_{tot} = \prod_{\nu\ occ} \pi_\nu \tag{2.22}$$

$$\alpha_{tot} = \sum_{\nu\ occ} \alpha_\nu \bmod 2. \tag{2.23}$$

2.5 Pairing Correlations

So far, the described nuclear models are based on the free motion of nucleons in an average potential which is just an approximation, since, there are also attractive short-range forces acting between nucleons in the same j-orbital. The existence of such pairing forces is justified by several experimental observations:

1. The ground states of all even-even nuclei have spin zero which suggests that nucleons are arranged in pairs so that their angular momenta are coupled to zero.

2. The even-even nuclei are lighter than odd-odd nuclei with the same atomic number A. This is known as *odd-even effect*. It is due to the fact that the total binding energy of an even-odd nucleus is smaller than the arithmetic mean of the binding energies of the two neighbouring even-even nuclei. Thus, we have the following relation for the masses of the neighbouring nuclei [RS80]

$$M_{Aodd} > \frac{M_{A-1} + M_{A+1}}{2}. \tag{2.24}$$

3. In even-even nuclei, the energy gap between the ground state and the first excited state is larger than that in even-odd, odd-even or odd-odd nuclei.

4. The level density of low lying states in even-odd or odd-odd nuclei is greater than those in even-even nuclei.

5. The agreement between the measured and calculated moments of inertia becomes much better if the paring force is included.

The starting point is to assume that the paring force only acts between nucleons with the same quantum numbers, but move in time reversed orbits. The paring interaction is a short-range interaction described by a δ function. If these nucleon pairs are close enough to the Fermi level, they may scatter from one pair of time reversed orbits to another unoccupied pair. In a classical approach, one could imagine that the nucleon pairs are orbiting around the nucleus in opposite directions and each time they collide, they scatter into another pair of orbits. Orbits close to Fermi surface can be partially occupied which smoothes out the Fermi surface [Cas00]. Including the pairing interaction leads to the concept of quasi-particles [BMP58] where particles and holes are substituted by quasi-particles and the particle-hole excitation by the creation of one quasi-particle and destruction of an other quasi-particle. Figure 2.7 illustrates particle and hole excitations (one-dimensional presentation) and quasi-particle excitations with and without pairing interaction (two-dimensional presentation). The independent single-

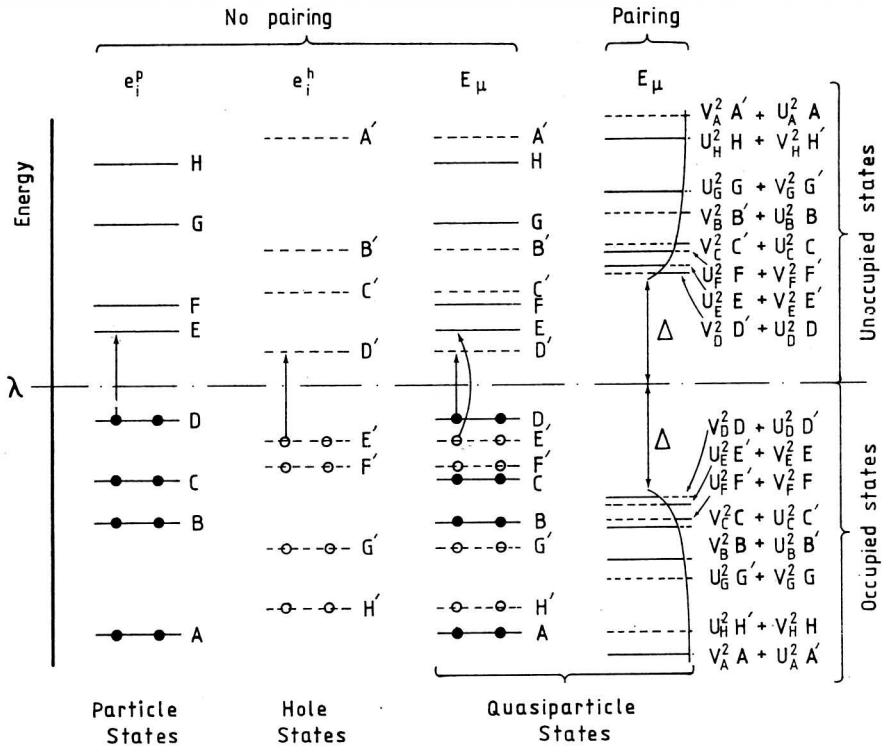

Figure 2.7: *Illustration of particle, hole and quasi-particle spectra. The first column (to the left) demonstrates the particle levels with energies relative to the Fermi energy, λ. The hole states are presented in the second column. It is constructed by reflecting the particle levels with respect to the Fermi level, as can be seen from the labelling of the levels. The third column shows the quasi-particle states. It is a two dimensional presentation constructed from particle and hole states. For example, the particle excitation from $D \rightarrow E$ and the hole excitation from $E' \rightarrow D'$ are equivalent to the two quasi-particle excitation in the quasi-particle presentation as indicated by the arrows. The pairing correlations modify the quasi-particle spectrum as shown in the fourth column. An energy gap of $\approx 2\Delta$ appears around the Fermi level where Δ is the gap parameter. Moreover the levels located immediately above and below the gap are strongly compressed. Each quasi-particle state consists of particle and hole amplitudes. The solid and open circles represent the particle and hole stats. Taken from [Gar83].*

particle approach can be transfered to the independent quasi-particle presentation using the Bogoliubov transformation [RS80]. The quasi-particle cranking Hamiltonian is given by [BG84]

$$\mathscr{H}^{\omega}_{qp} = \mathscr{H}^{0}_{sp} - \Delta(P^{+} + P) - \lambda N - \omega J_{x}. \tag{2.25}$$

$\mathscr{H}^{0}_{sp}$ is the single-particle Hamiltonian in the laboratory system. Δ is the gap parameter given by [Cas00] $\Delta = G\sum_{\mu\nu} U_{\mu}V_{\nu}$ with G being the strength of the pairing force, and U_{μ} and V_{ν} are the occupation and non-occupation probabilities of quasi-particle levels, respectively. P^{+} and P are the creation and

annihilation operators of quasi-particles, respectively. The $-\lambda N$ term is introduced to fix the particle number in the system. The chemical potential λ is chosen in such a way that the expectation value of the particle-number operator, N, is equal to the number of nucleons in the nucleus. The excitation energy of a quasi-particle at $\omega = 0$ is obtained from [BG84]

$$E_{\mu}^{qp} = \left[(e_{\mu} - \lambda)^2 + \Delta^2\right]^{1/2}, \tag{2.26}$$

where e_{μ} is the single-particle energy, λ is the Fermi level, and Δ is the gap parameter. The $(e_{\mu} - \lambda)$ term represents the excitation energy of the single-particle. Figure 2.8 demonstrates the effects of paring interaction and rotation on the independent single-particle motion in a deformed nuclear potential.

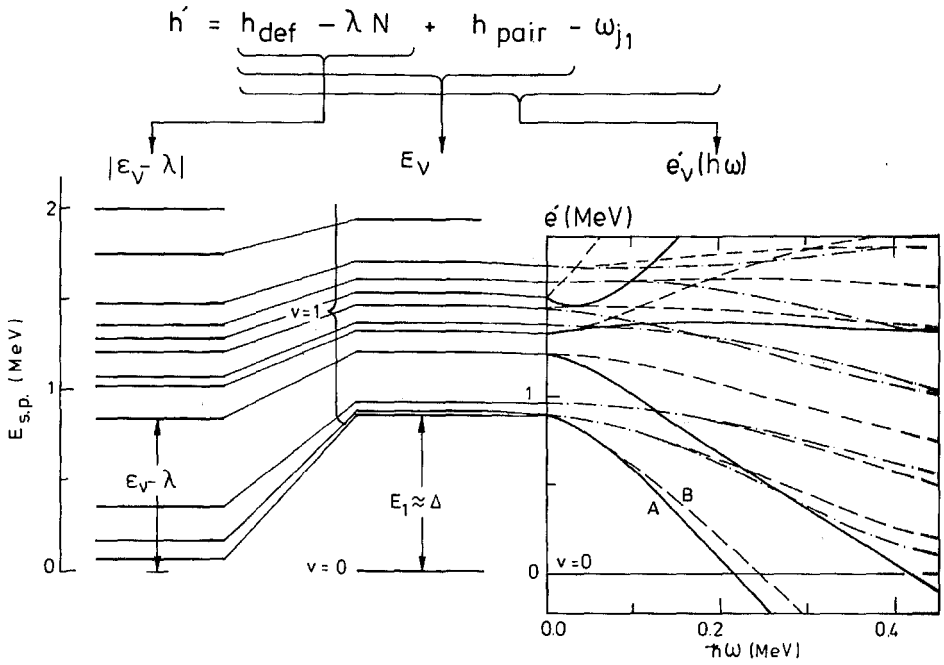

Figure 2.8: *Spectra of the cranking Hamiltonian with Nilsson potential (left column), with pairing interactions (middle column) and with rotation as a function of rotational frequency, ω. Taken from [Gar83].*

2.6 Comparison of Experimental Data with Theoretical Calculations

A rotational band is characterised experimentally by the transition energies, E_{γ}, and their intensities, I_{γ}, between the I and $I-2$ states and the angular correlation between these transitions. The measurement of the energies and multipolarities of the linking transitions from rotational bands to the known low-spin levels enables the determination of the excitation energies, E_{exc}, spins, I, and parities, π, of the levels within the rotational band. From lifetimes of the levels within the rotational band, the degree of collectivity is obtained.
To compare the experimental results with theoretical predictions, several experimental quantities are used:

1. Excitation energies with a rigid rotation reference subtracted, $E_{exc} - E_{RLD}$, as a function of spin, I, with the reference given by [RXBR86]

$$E_{RLD}(I) = \frac{1}{2\mathscr{I}_{rig}} I(I+1), \tag{2.27}$$

where $\frac{1}{2\mathscr{I}_{rig}} \approx 32.32A^{-5/3}\ \mathrm{Mev}/\hbar^2$.

2. Gamma-ray transitions, E_γ, as a function of spin.

3. Kinematic, $\mathscr{I}^{(1)}$, and dynamic, $\mathscr{I}^{(2)}$, moments of inertia as a function of spin, I, or rotational frequency, ω.

4. The transition quadruple moment, $Q_t(I)$, as a function of spin, I, when lifetime measurements are possible.

The transformation of the experimental excitation energies, E_{exc}, and the experimental angular momentum, I, to the intrinsic rotating frame of the nucleus, makes it possible to compare the experimental results to the theoretical calculations which are made in the rotating frame. For this purpose, we define the rotational frequency, ω, for a given state with angular momentum, I, as

$$\omega(I) = \hbar^{-1}\frac{dE(I)}{dI_x(I)}. \tag{2.28}$$

In practical calculations, the derivative is approximated by a quotient of finite differences. Therefore, 2.28 becomes

$$\omega(I) \approx \frac{\Delta E(I)}{\Delta I_x(I)} = \frac{E(I+1)-E(I-1)}{I_x(I+1)-I_x(I-1)}\hbar^{-1}, \tag{2.29}$$

where

$$I_x(I) = \sqrt{I(I+1)-K^2} \approx \sqrt{(I+\frac{1}{2})^2-K^2} \tag{2.30}$$

is the projection of the total angular momentum onto the rotation axis. K is the projection onto the symmetry axis. I is the average value of the angular momenta of the two values $I \pm 1$ relevant to the experimental energy levels $E(I \pm 1)$. The total experimental Routhian, E', is defined by

$$E'(I) = E(I) - \omega(I)I_x(I), \tag{2.31}$$

where

$$E(I) = \frac{1}{2}[E(I+1)+E(I-1)]. \tag{2.32}$$

$E'(I)$ contains both the collective and single-particle excitations. Also the projection of the total angular momentum onto the rotation axis, I_x, includes both, rotational and single-particle components. To extract information on the excited single particles, the collective part has to be subtracted from the total Routhian and the total angular momentum. This is achieved by subtracting a reference core. The experimental Routhian, e', and the aligned angular momentum, i_x, of the excited single particles are given by

$$e'(\omega) = E'(\omega) - E^{ref}(\omega) \tag{2.33}$$

and

$$i_x(\omega) = I_x(\omega) - I_x^{ref}(\omega) \tag{2.34}$$

where E^{ref} and I_x^{ref} are the total energy and angular momentum of the reference core. The ground-state band of an even-even nucleus is believed to be a proper reference that contains no particle excitations. In many cases, the yrast band above the first crossing with the ground-state bands is also used as a reference. More details can be found in [BFM86].

Because the moment of inertia is not constant, and the ground-state band can only be determined experimentally for a limited frequency range, the moment of inertia parametrisation,

$$\mathscr{I}_{ref} = \mathscr{I}_0 + \mathscr{I}_1\omega^2, \tag{2.35}$$

is used [Har65] where $\mathscr{I}_0$ and $\mathscr{I}_1$ are known as Harris parameters. The angular momentum of the reference system is obtained from

$$I_x^{ref} = \omega(\mathscr{I}_0 + \omega^2\mathscr{I}_1). \tag{2.36}$$

The Harris parameters, $\mathscr{I}_0$ and $\mathscr{I}_1$, are determined by fitting the experimental points in the I_x versus ω plot. The energy of the reference system is calculated from eq. 2.28

$$E^{ref}(\omega) = -\int I_x^{ref}(\omega)d\omega = -\frac{1}{2}\omega^2\mathscr{I}_0 - \frac{1}{4}\omega^4\mathscr{I}_1 + \frac{1}{8\mathscr{I}_0}. \tag{2.37}$$

In particularly, in case of rotational states connected with γ-ray transitions of energy E_γ and $E2$ multipolarity, where $\Delta I = 2$, the rotational frequency, ω, the kinematic, $\mathscr{I}^{(1)}$, and the dynamical, $\mathscr{I}^{(2)}$, moments of inertia can be calculated from experimental data using the following expressions [BFM86]

$$\omega \approx \frac{E_\gamma}{2} \quad [\mathrm{MeV}/\hbar] \tag{2.38}$$

$$\mathscr{I}^{(1)} \approx \frac{2}{E_\gamma} I \quad [\hbar/\mathrm{MeV}] \tag{2.39}$$

$$\mathscr{I}^{(2)} \approx \frac{4}{\Delta E_\gamma} \quad [\hbar^2/\mathrm{MeV}], \tag{2.40}$$

where ΔE_γ is the energy difference between two successive γ rays. The dynamic moment of inertia, $\mathscr{I}^{(2)}$, is independent of spin, I. This property is very useful in cases where spin and parity of a given rotational band are not known. A plot of $\mathscr{I}^{(2)}$ as a function of rotational frequency ω may help to draw conclusions about the configuration of the band by comparing it to similar known bands.

As an illustrative example, we consider the yrast band in ^{124}Ba [AKSH$^+$06]. Figures 2.9 and 2.10 show the experimental Routhian and alignment as a function of spin, respectively. The crossing frequencies, ω_c, and the aligned angular momentum gain, Δi_x, can be determined from the Routhian and alignment plots as demonstrated in Figs. 2.9 and 2.10, respectively. At a certain rotational frequency, the rotational frequency decreases while the angular momentum increases sharply. This is known as back-bending [BF79a] where the ground-state bands is crossed by a new configuration which means the nucleus changes its intrinsic structure. This frequency is called the crossing frequency, ω_c.

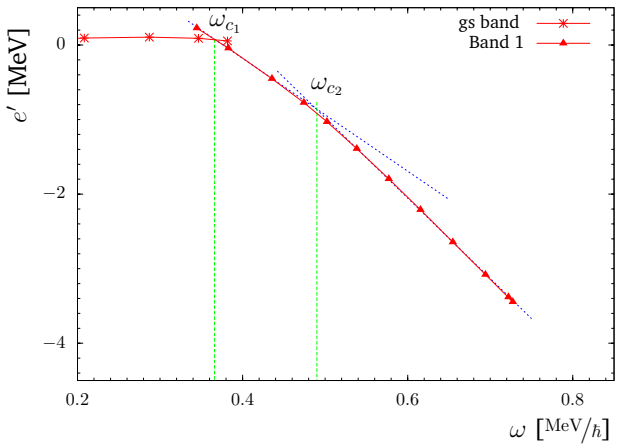

Figure 2.9: *Experimental Routhians, e' of the ground-state band and band 1 in ^{124}Ba as a function of rotational frequency, ω [AKSH$^+$06]. Band 1 crosses the ground-state band at a rotational frequency ω_{c_1}. Moreover, band 1 undergoes a second crossing at a rotational frequency ω_{c_2}.*

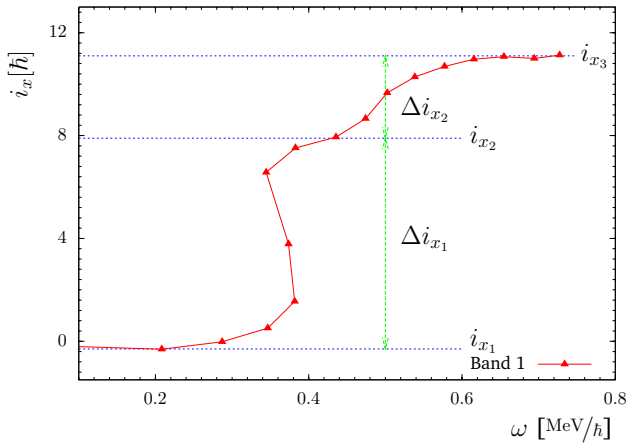

Figure 2.10: *Experimental aligned angular momentum, i_x, for band 1 (yrast band) in ^{124}Ba as a function of rotational frequency, ω [AKSH+06]. The two crossings seen in the Routhian 2.9, result in an alignment gain in two steps, Δi_{x_1} and Δi_{x_2}.*

2.7 Termination of Rotational Bands

Loss of collective rotation is one of the most interesting observations of rotating nuclei at high spins. That is, a rotational band with a specific quasi-particle configuration loses gradually or suddenly the collective behaviour and terminates in a non-collective aligned state with a configuration with the maximum spin that can be built within this configuration, see Fig. 2.11.

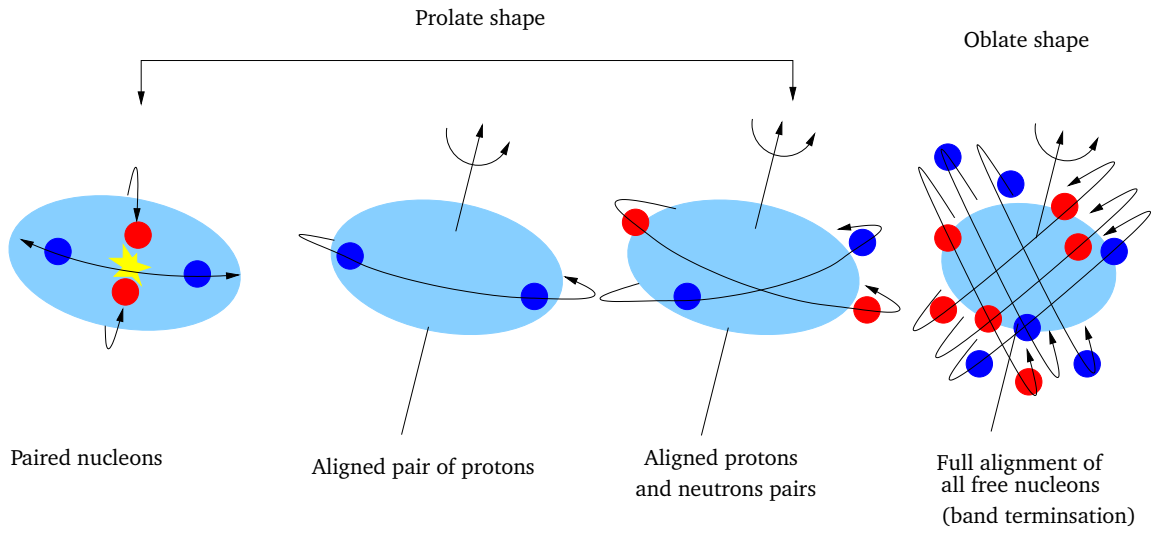

Figure 2.11: *Schematic illustration of generating angular momentum in a rotational band from a rotating nucleus (prolate shape) ending up in a fully aligned terminating state (oblate shape). The low-spin (lowest-energy) state involves time-reversed paired nucleons. By increasing the rotational frequency, the Coriolis force acts against the pairing force and nucleon pairs are broken and individual nucleons are getting aligned along the rotation axis. At higher rotational frequencies, more pairs are broken and at the end, all available valence nucleons outside the closed core are aligned along the rotation axis which gives the nucleus an oblate shape.*

The properties of terminating bands are investigated within the frame work of the configuration-dependent Cranked Nilsson-Strutinsky (CNS)approach [BR85, NDB+85] where a rotational band with a specific configuration can be traced to the terminating spin. The phenomenon of band termination has been reviewed in many articles, e.g. [NDB+85, RXBR86, BR85, AR95, AR96, AFLR99].

Types of band termination based on energy cost are favoured terminating bands, rigid rotation-like terminating bands and unfavoured terminating bands. Examples are shown in Fig. 2.12. An alternative way to study terminating bands is to consider their moments of inertia, $\mathscr{I}^{(1)}$, and, $\mathscr{I}^{(2)}$, as a function of rotational frequency, ω. Accordingly, the terminating bands can be divided into two types, smooth band termination where the dynamic moment of inertia, $\mathscr{I}^{(2)}$, varies smoothly with rotational frequency, ω,

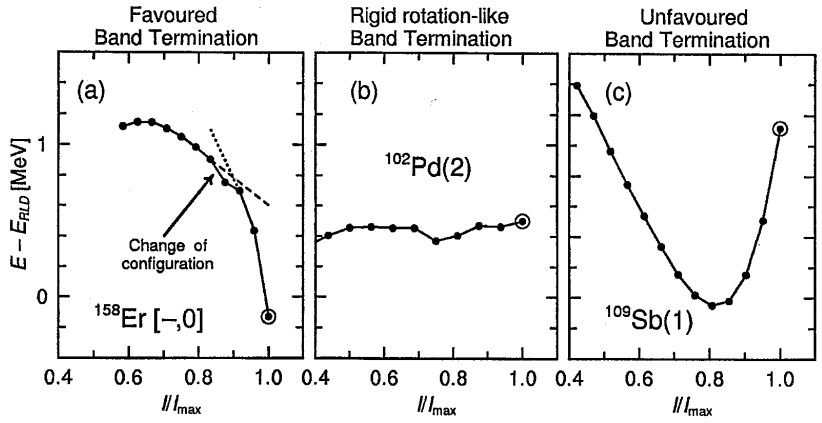

Figure 2.12: *Illustration of different types of terminating bands based on the energy cost taken from [AFLR99]. The excitation energy, E, of the experimental bands relative to a rigid rotor, E_{RLD}, are plotted as a function of the relative spin I/I_{max}. I_{max} is the maximum spin in the configuration assigned to the band.*

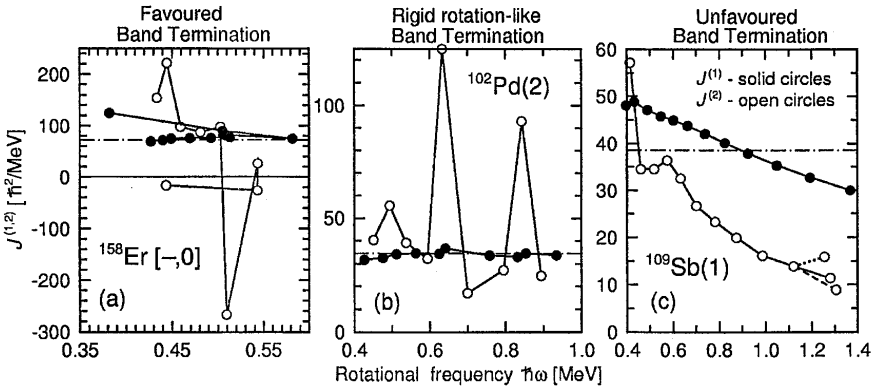

Figure 2.13: *Plots of kinematic, $\mathcal{J}^{(1)}$, (solid symbols) and dynamic, $\mathcal{J}^{(2)}$, (open symbols) moments of inertia of the bands presented in 2.12 to demonstrate different types of terminating bands based on the smoothness, taken from [AFLR99]. Panel c represents the smooth band termination while panels a and b present unsmooth terminating bands.*

as illustrated in Fig. 2.13, and unsmooth band termination when the dynamic moment of inertia, $\mathcal{J}^{(2)}$, changes drastically with ω and exhibits an irregular behaviour as demonstrated in Fig. 2.13.

Chapter 3

Generation and Detection of High-Spin States

In order to investigate the structure of the nuclei at very high angular momentum, special techniques are required. A proper nuclear reaction that transfers as much angular momentum as possible to the excited nuclei must be used. The hot nuclei de-excite via particle evaporation and γ-ray emission. The detection of the emitted γ rays provides information about the structure of the investigated nuclei. Therefore, an efficient detection system is required for the measurement of the emitted γ rays.

3.1 Excitation and De-excitation Mechanisms

The nuclei investigated in this work have been produced using heavy-ion fusion-evaporation reactions. with heavy-ion beams. Highly excited rapidly rotating compound nuclei were formed. If the compound nuclei survive fission, they cool down by particle evaporation and decay to the ground state by emitting γ rays.

3.1.1 Population of High-Spin States

Excited nuclei can be produced using several types of nuclear reactions. The best reaction is the one that can produce the nucleus with as much angular momentum, l, as possible and with the largest possible cross-section. It turned out that the heavy-ion induced fusion-evaporation reaction is the most efficient way to achieve the best balance between the highest angular momentum and a large cross-section [EV89]. When an accelerated heavy-ion projectile collides and fuses with a target nucleus, a compound nucleus may be formed. The compound nucleus is a very hot system and it cools down by emitting protons, neutrons or α particles. When the excitation energy of the nucleus becomes less than the particle binding energy, particle evaporation is no longer possible and the nucleus proceeds to cool down by emitting γ rays. This is the only way to lose energy and angular momentum until the nucleus reaches the ground state. In the classical approximation, the maximum value of angular momentum, l_{max}, transfered in the reaction is determined by the momentum of the projectile, $m_p v_p$, and by the impact parameter, b, according to the relation $l_{\text{max}} = m_p v_p b$. This simple relation demonstrates that high-energy heavy ions are the most capable projectiles to populate high-spin states. However, the impact parameter, b, plays an important role. Figure 3.1 illustrates the major reaction modes that depend on the impact parameter. When the impact parameter is large enough so that the nuclear density distributions of the projectile and the target nucleus do not overlap, Coulomb scattering occurs. In case of partial overlap of the nuclear matter of the projectile and the target, inelastic nuclear scattering may take place. When the density distributions overlap completely, they may fuse to form a compound nucleus. A fraction of the kinetic energy of the projectile is then transfered into excitation energy of the compound nucleus.

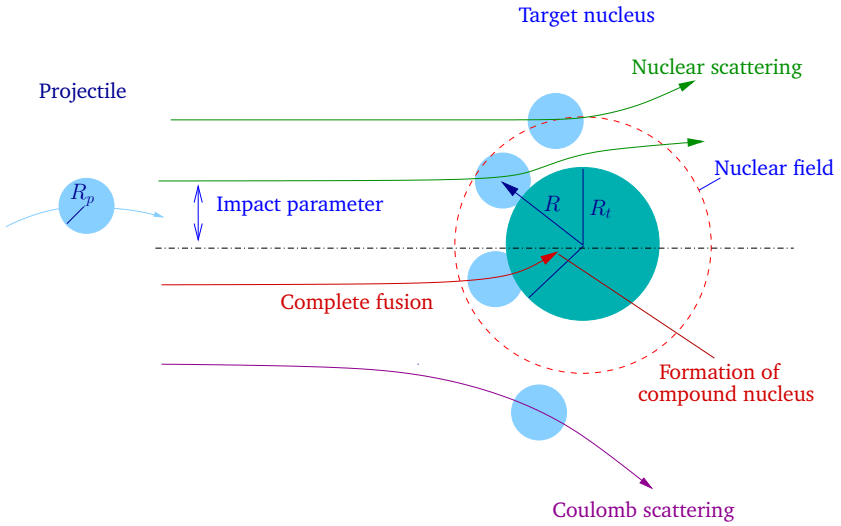

Figure 3.1: *Schematic illustration of heavy-ion collision types.*

The energy of the compound, E_{exc}, is given by

$$E_{\text{exc}} = E_{CM} + Q_{\text{fus}}, \tag{3.1}$$

where E_{CM} is the energy in the centre of mass system and is calculated from

$$E_{CM} = E_{\text{beam}} \frac{A_T}{A_T + A_P}, \tag{3.2}$$

where A_T and A_P are the mass numbers of the target nucleus and the projectile, respectively. Q_{fus} is the Q-value (the energy gained or lost when two ions fuse) and is given by

$$Q = E_B^P + E_B^T - E_B^{CN}, \tag{3.3}$$

where E_B^P, E_B^T and E_B^{CN} are the binding energy of the projectile, the target nucleus and the compound nucleus, respectively. The excitation energy of the compound nucleus is redistributed among its constituent nucleons. The excitation energy of the compound nucleus is typically 50 to 80 MeV and the transfered angular momentum is 50 to 80 $\hbar$.

3.1.2 Depopulation of High-Spin States

The fusion of the incident nucleus with the target nucleus occurs within 10^{-22} to 10^{-20} sec. The result is a highly excited compound nucleus that is spinning very rapidly. The hot compound nucleus can decay via several modes to the ground state. Figures 3.2 and 3.3 illustrate schematically the formation and the de-excitation of the compound nucleus. As the excitation energy of the compound nucleus is very high, at first it cools by particle emission (neutrons, protons or α particles) within $\approx 10^{-16}$ sec. The neutron evaporation in heavier nuclei is generally favoured since charged-particle emission is hindered by the Coulomb barrier. The nucleus loses an energy of about 8 MeV and about 1-2 $\hbar$ of angular momentum in each neutron evaporation. The particle evaporation occurs as long as the excitation energy is higher that the energy threshold for particle emission. When the excitation energy becomes less than the particle binding energy, it is no longer possible to evaporate particles and the compound nucleus enters the so-called entry-line for γ-ray emission, see Fig. 3.3, in $\approx 10^{-14}$ sec and it de-excites subsequently by emitting statistical γ rays (mainly $E1$-transitions). These are called quasi-continuum transitions, because the nuclear level density is very high and γ-ray lines are not resolvable. The yrast line represents the minimum excitation energy for a given spin. Close to the yrast line, discrete γ rays, $E2$ rotational cascades in case of deformed nuclei, are emitted in the decay to the ground state.

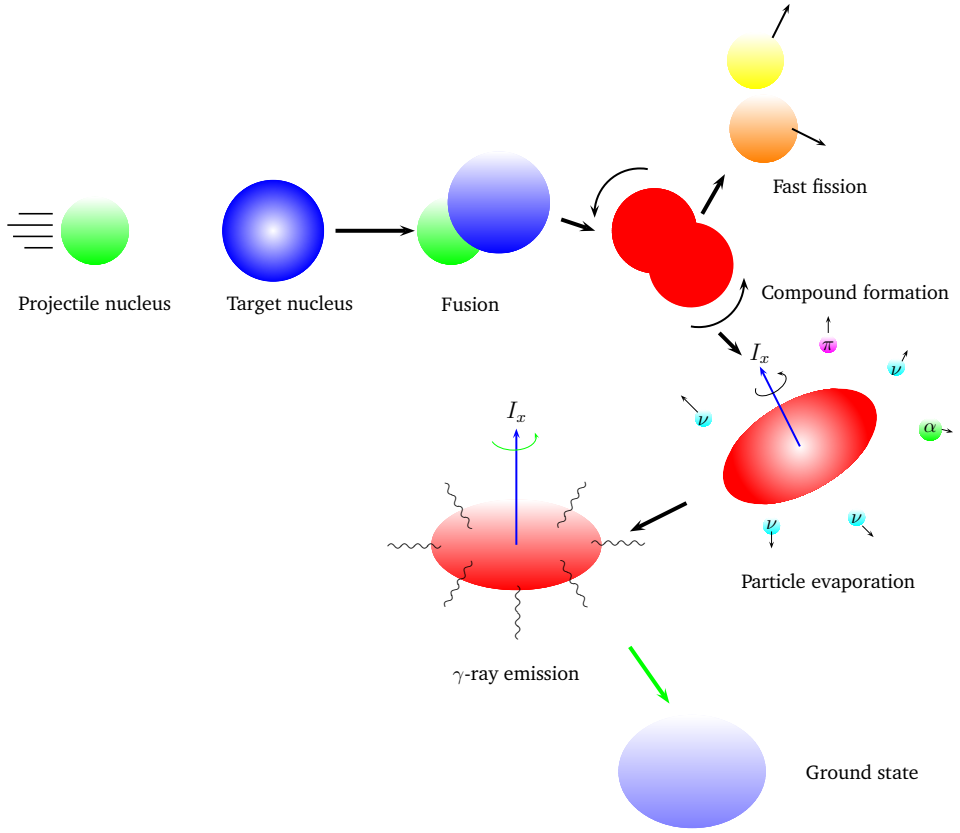

Figure 3.2: *Schematic illustration of the processes involved in the formation and the decay of a compound nucleus produced by a heavy-ion fusion-evaporation reaction.*

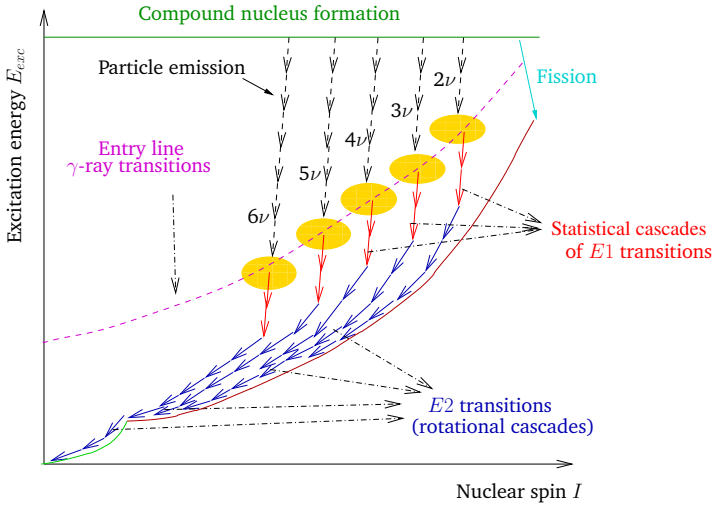

Figure 3.3: *Schematic plot of the excitation energy, E_{exc}, as a function of the nuclear spin I. The plot illustrates typical γ ray de-excitation paths, following the production of a very hot compound nucleus in a heavy-ion fusion-evaporation reaction. The yrast line represents the minimum excitation energy of a level at a given spin. The entry line (dashed curve) marks the start of γ-ray cascades following the particle evaporation.*

3.2 Detection of γ Radiation

Emission of γ rays occurs in nuclear radioactive decays or after nuclear reactions. The detection of the emitted γ-ray sequences provides essential information on the nuclear levels. The material used to detect γ rays must have a high efficiency to ensure high statistics and a high resolution to distinguish between γ rays that are closed in energy. Semi-conductor detectors made of High-Purity Germanium (HPGe)

crystals have excellent energy resolution but low detection efficiency. On the other hand, Scintillation detectors made of Sodium Iodide (NaI) or Bismuth Germanate ($Bi_4Ge_3O_{12}$) (BGO) have high efficiency but poor resolution.

3.2.1 Interaction of γ Radiation with Matter

There are mainly three types of interaction of γ quanta with matter: the photoelectric effect, Compton scattering and pair production.

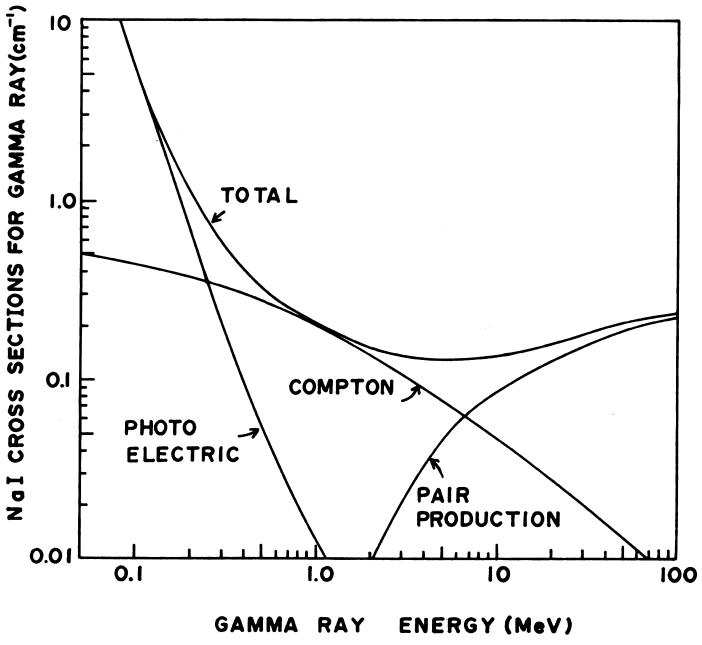

Figure 3.4: *Absorption cross section for γ rays in NaI(TI) as a function of energy. Taken from [EV89].*

The Photoelectric Effect

The energy of an incident γ ray is transfered completely to an atomic electron [Leo94]. This effect is dominant at low energies ($E_\gamma < 0.3$ MeV), see Fig. 3.4.

Compton Scattering

An incident γ ray with energy E_γ is scattered by an electron, and another γ ray with energy $E'_\gamma < E_\gamma$ is emitted at an angle θ with respect to the incident direction. The energy difference $E'_\gamma - E_\gamma$ is transfered to the electron. The energy of the scattered photon depends on the scattering angle and is given by [Leo94]

$$E'_\gamma = \frac{E_\gamma}{1 + (E_\gamma/m_0c^2)(1 - \cos\theta)}, \tag{3.4}$$

where m_0 is the rest mass of the electron (m_0c^2 = 0.511 MeV). Compton scattering is dominant in the energy range ($0.3 < E_\gamma < 5$ MeV), see Fig. 3.4.

Pair Production

This process dominates at higher energies ($E_\gamma > 5$ MeV) [Leo94], see Fig.3.4. It can only occur if the incident photon has an energy $E_\gamma \geq 2m_ec^2 = 1.022$ MeV where m_ec^2 is the electron mass. In this case, part of the energy of the incident photon goes into the creation of the electron-positron pair and the rest of the energy into kinetic energy of the pair.

3.2.2 Multi-Detector Arrays

The recent developments of Germanium (Ge) detectors and γ-ray spectrometers have enabled new and important observations in nuclear structure at very high spins. The development of the γ-ray spectrometers has been reviewed in several articles, e.g. [NBF94, BS96, LDV03].

A highly excited nucleus emits γ rays with an energy range of 0.1–20 MeV. Ge semi-conductor detectors are commonly used in this energy range since they have a very good energy resolution. On the other hand, Ge detectors have a low detection efficiency. Due to the large number of Compton-scattered γ rays which escape the crystal, a continuous background occurs in the energy spectrum and reduces the peak-to-background ratio. This effect has been significantly reduced by using the Compton-suppression technique. The Ge crystals are surrounded by BGO detectors, see Fig. 3.5. BGO detectors have high detection efficiency but low energy resolution. When a scattered γ ray from the Ge crystal hits the BGO shield, the event is rejected by the electronics of the detectors. This improves the peak-to-background ratio. The reduction of the background can be seen in Fig. 3.6.

Figure 3.5: *Schematic illustration of Ge detectors with Compton-suppression shields.*

Coincident γ rays can be recorded by using a detection system of at least two Ge detectors. A multi-detector array consists of many Ge crystals with anti-Compton shields. It is an excellent tool to record high-fold coincidence events with high statistics. High energy resolution is required to discriminate

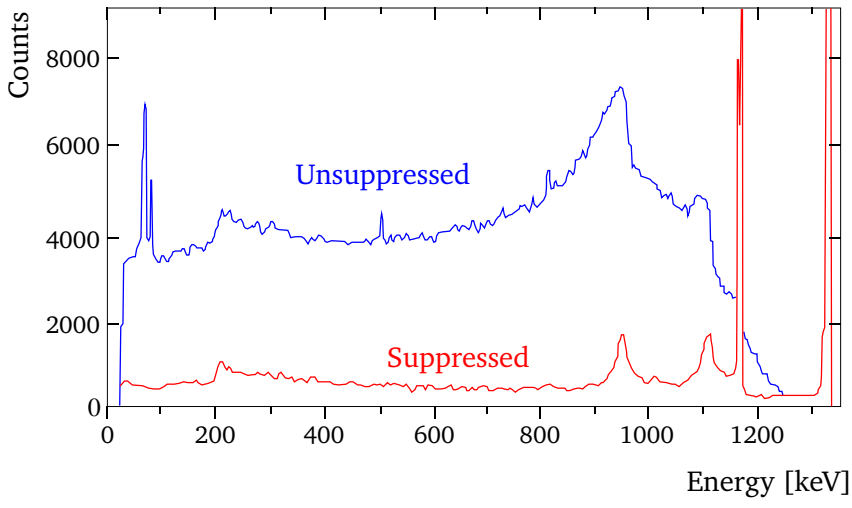

Figure 3.6: *Comparison of ^{60}Co spectra with and without Compton suppression [BS96].*

between γ rays that are closed in energy. The final resolution, $\Delta E_\gamma^{\text{final}}$, of an array depends on several factors:

1. $\Delta E_\gamma^{\text{int}}$ the intrinsic resolution of the detector system.

2. $\Delta E_\gamma^{\text{open}}$, $\Delta E_\gamma^{\text{angular}}$ and $\Delta E_\gamma^{\text{velocity}}$ the Doppler broadening induced by the opening angle of the detector, by the angular spread of the recoil nuclei in the target and by the velocity variation of the recoils, respectively.

   The total energy resolution, $\Delta E_\gamma^{\text{final}}$, is given by [BS96]

$$\Delta E_\gamma^{\text{final}} = [(\Delta E_\gamma^{\text{int}})^2 + (\Delta E_\gamma^{\text{open}})^2 + (\Delta E_\gamma^{\text{angular}})^2 + (\Delta E_\gamma^{\text{velocity}})^2]^{1/2}. \tag{3.5}$$

Euroball Detector Array

Euroball [Bec92, Sim97] was one of the largest γ-ray spectrometer arrays that had been built in the world for advanced studies in nuclear structure. It was the result of a collaboration of six European countries: United Kingdom, France, Italy, Germany, Sweden and Denmark. The Euroball IV spectrometer was the last phase in the development of the instrument, which was installed at IReS in Strasbourg, France. The spectrometer comprised 71 Compton-suppressed HPGe detectors which were arranged in a sphere-shaped array and 210 BGO detectors which were arranged in a sphere-shaped mini-array (the inner ball). Figure 3.7 shows an artist's impression of Euroball. A photograph of one half of the array is shown in Fig. 3.8(a). The closed array is visualised in Fig. 3.8(b).

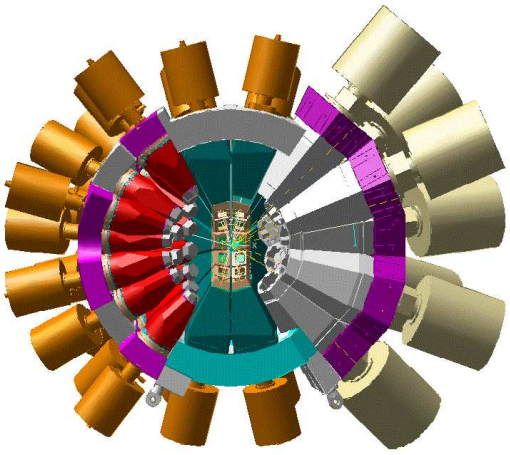

Figure 3.7: *Schematic cross section through the Euroball array showing the Cluster, Clover and large volume Tapered Ge detectors in their associated suppression shields.*

The detectors are of two different types: single-crystal and composite detectors:

Large Volume Single-Crystal Detectors (Tapered Detectors) Close packing design is used in the construction where each detector consists of a large single crystal housed in a cryostat. The crystal is surrounded by a Compton-suppression shield, see Fig. 3.5. These detectors are known also as Tapered detectors. Thirty Tapered detectors were mounted on the forward part of Euroball. They were placed 375 mm from the target in three rings at 15.45°, 34.60° and 52.30° to the beam direction. The total photo-peak efficiency of the Tapered detectors is limited due to the size of the crystals. It could be improved if the detector would be placed very close to the target, but this would increase the solid angle of the detectors and, hence, reduce the quality of the spectrum because of Doppler broadening.

Composite Detectors The total photo-peak efficiency that can be obtained using large single-crystal Ge detectors is limited by the size of the crystals and by the cost. To improve the photo-peak efficiency,

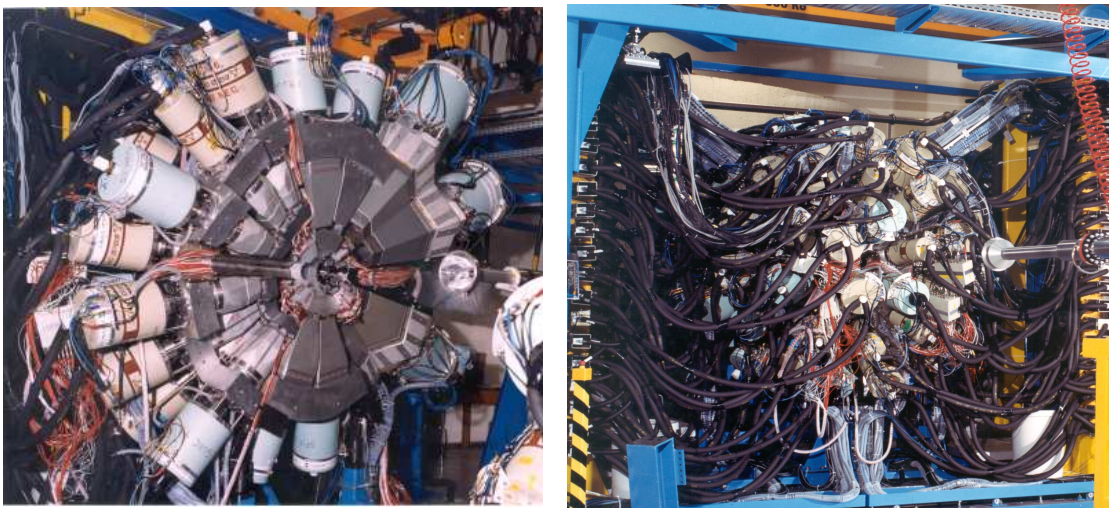

(a) *(b)*

Figure 3.8: *(a)One hemisphere of the Euroball spectrometer. In the centre, the beam pipe is visible. (b) Closed Euroball spectrometer. In the centre, of the sphere the hole for the beam pipe is visible. The dewar of each detector is connected to an automatic liquid nitrogen filling system through a black tube.*

composite detectors were developed. A composite detector is made up of several Ge crystals packed closely together and housed in the same cryostat.

The Clover Detectors The Clover detector consists of four HPGe n-type crystals arranged in the configuration of a "four-leaf Clover", see Fig. 3.9(a), and housed in the same cryostat.The Euroball array was equipped with 26 Clover detectors mounted in two rings near-perpendicular to the beam direction. The detector to target distance was not the same for all Clover detectors. The distance was 265 mm for all detectors in the forward ring, while it was 293 mm for the six Clover detectors in the ring at backward direction.

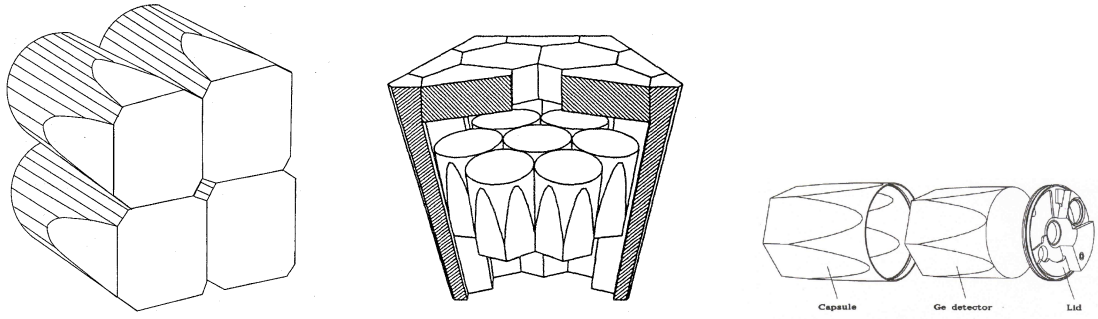

(a) *(b)* *(c)*

Figure 3.9: *(a) A schematic drawing of the four HPGe crystals packed inside a Clover detector. (b) A schematic view of the seven encapsulated HPGe crystals grouped inside a Cluster detector. (c) View of the encapsulated HPGe crystal.*

The Cluster Detectors The Cluster detector consists of seven tapered hexagonal HPGe crystals packed closely together and housed in the same cryostat, see Fig. 3.9(b). Each individual crystal is encapsulated in a 0.7 mm thick aluminium vacuum capsule to avoid surface contamination, see Fig. 3.9(c). The backward part of the Euroball spectrometer comprised 15 Cluster detectors located at a distance of 445 mm from the target.

The Euroball spectrometer consisted of 239 individual HPGe crystals. The full Euroball spectrometer has a total photo-peak efficiency of 9.4 % [Sim97] at a γ-ray energy of 1.3 MeV.

Gammasphere Detector Array

Gammasphere [Lee90] is the most powerful spectrometer to conduct research of nuclear structure, particularly at very high spins. At the moment it is installed at Argon National Laboratory (ANL), USA. The array comprises 110 tapered coaxial large-volume HPGe detectors with good energy resolution and high efficiency. Each cylindrical Ge detector is surrounded by a tapered hexagonal BGO anti-Compton shield for improving the peak-to-total (P/T) ratio. Detectors are grouped in rings, each consisting of 5 or 10 detectors, and are mounted symmetrically at 17 different angles with respect to the beam axis. At the time of our experiment, Gammasphere consisted of 100 Ge detectors. Figure 3.10 shows the half sphere and the closed sphere of the Gammasphere array. For γ rays with energy of $E_\gamma = 1.33$ MeV, the full Gammasphere spectrometer with 110 detectors has a total photo peak efficiency of 9.9 %, a P/T ratio of 0.6 and an energy resolution of 2.5 keV (FWHM) [Lee90].

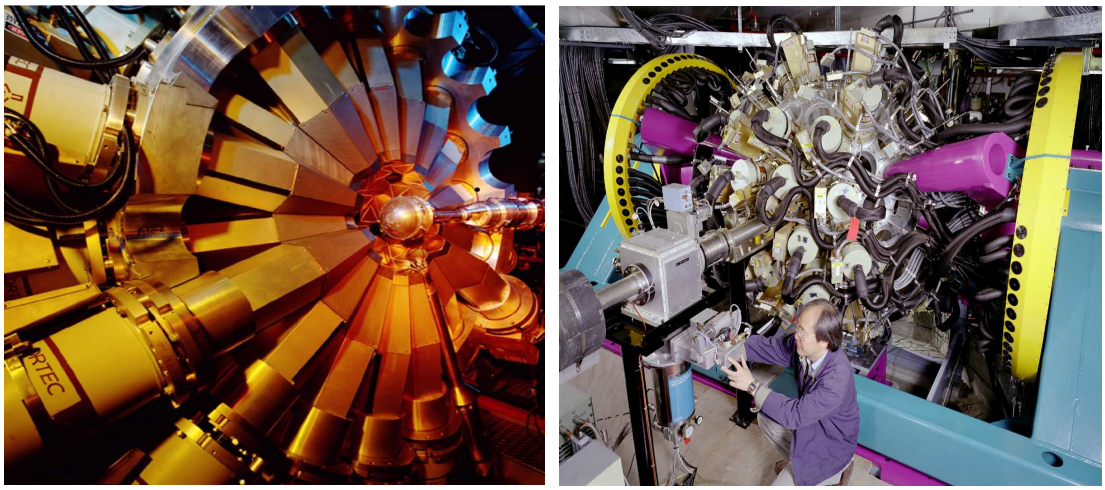

(a) *(b)*

Figure 3.10: *(a) One half-sphere of the Gammasphere spectrometer. The target chamber in the middle of the sphere is visible. (b) The closed Gammasphere spectrometer.*

Out of the 110 Ge detectors, 70 crystals are electronically divided into two segments (double-D shape), see Fig. 3.11. This reduces the opening angle to half and, therefore, reduces the Doppler broadening. The two D-shape crystals are housed inside a common cryostat. They have two separated contacts at the outer surface, see Fig. 3.11. This makes it possible to measure the energies deposited in each half of the crystal. The D-shape detectors are mounted around 90°, which significantly improves the resolution and also allows for linear polarisation measurements [SMA+98].

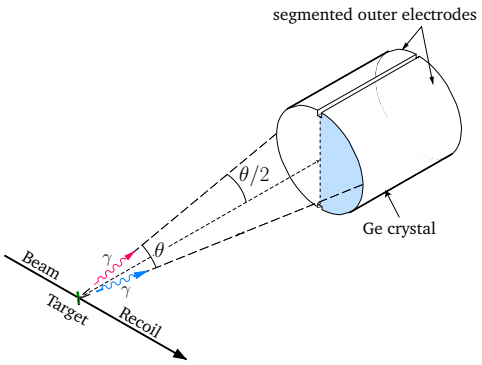

Figure 3.11: *Schematic illustration of a double-D segmented Ge detector.*

Chapter 4

Data Processing

In a high-spin-spectroscopy experiment, a huge amount of data is required to ensure good statistical accuracy for the results. As mentioned in the previous chapter, experiments that are performed with multi-detector arrays, e.g. with the Euroball and Gammasphere arrays, provide large data sets. In such experiments, the typical number of collected events is in the order of 10^9 which corresponds to several hundred Giga-Byte to be stored and processed. The volume of the data sets depends on the number of detectors, the number of detected γ rays, the data information written to tapes and the data format. Therefore, the organisation of the raw data is of great importance to permit fast access for further analysis. The treatment of the raw data can be divided into two main steps, *pre-sorting* and *compression*. *Pre-sorting* includes gain-matching, energy and efficiency calibration, Doppler-shift correction, setting of a time gate and add-back procedure. The data *compression* allows the choice of a more compact data format and the rejection of unusable events which reduces the size of the data set and speeds up the subsequent analysis.

4.1 Pre-sorting

4.1.1 Gain-Matching

The different detectors have different gains and for many detectors the gain is not stable and fluctuating during several days of measurements due to instability of the electronics time. The first step in data processing is to treat this problem. The data are split into sections with respect to time and spectra for each detector and section are generated. Spectra for each detector from all sections are shifted to fall on top of each other and the correction coefficients are extracted. This procedure is known as *gain-matching*. For each detector a set of correction coefficients is produced and used to describe its gain. This procedure is either made off-line as in the Euroball [Bec92, Sim97] array using the software package *gain-fit* [Ber] or online as in the Gammasphere [Lee90] array.

4.1.2 Energy and Efficiency Calibration

The energy of the incident γ rays are digitised in the Analog to Digital Converter (ADC) [Leo94] for each Ge detector, where the channel number is proportional (if there is no offset) to the energy of the incident γ ray. Usually, the gain of each detector is different. Therefore, the correlation between the channel and the energy has to be established using known radioactive sources. Generally, the detectors are calibrated before and after the experiment. For that purpose, standard sources such as ^{152}Eu, ^{133}Ba (for low energy) and ^{56}Co (for high energy) are used. The area and the peak positions (in channel numbers) are determined for each detector and compared to the known peaks in the calibration spectrum for each source. The energies are plotted against the channel numbers and fitted using a polynomial fit of the form

$$E = \sum_{n=1}^{k} (a + b_n x^n), \tag{4.1}$$

where E is the energy in keV and x is the channel number. Usually, a quadratic fit is sufficient.

To measure the relative intensities of the observed γ rays, it is necessary to determine the efficiency of the detectors as a function of energy. This can be achieved by using the radioactive sources where the relative intensities are well known and by fitting the data points using the following parametrisation [Rad95]

$$\ln(\epsilon) = [(A + Bx + Cx^2)^{-G} + (D + Ey + Fy^2)^{-G}]^{-1/G}, \tag{4.2}$$

where ϵ is the efficiency, $x = \ln(E_\gamma/100)$ and $y = \ln(E_\gamma/1000)$. The γ-ray energy E_γ is in keV. A, B and C are the fit parameters for the low-energy region and D, E and F are the fit parameters for the high-energy region. The G parameter determines the shape of the turn-over region between the high- and low-energy efficiency curves. To achieve a good efficiency calibration, the calibration source is mounted at the position of the target, and the same set-up configuration as during the experiment is used.

4.1.3 Doppler-Shift Correction

In a thin-target experiment, using a fusion-evaporation reaction, the γ rays are emitted in flight from the recoiling nuclei. Thus, the energies of the emitted γ rays are Doppler-shifted, and a correction is needed. If the recoil velocity is several percent of the speed of light, a relativistic correction has to be used

$$E_\gamma^D(\theta) = E_\gamma^0 \frac{\sqrt{(1 - \frac{v^2}{c^2})}}{1 - \frac{v}{c}\cos\theta}, \tag{4.3}$$

where $E_\gamma^D(\theta)$ is the energy of the γ ray emitted in flight, E_γ^0 is the γ-ray energy emitted at rest, $\frac{v}{c}$ is the ratio of the velocity of the recoiling nucleus to the speed of light and θ is the angle between the emitted γ ray and the beam direction. If the $\frac{v}{c} \ll 1$, the non-relativistic relation may be used

$$E_\gamma^D(\theta) = E_\gamma^0(1 + \frac{v}{c}\cos\theta). \tag{4.4}$$

The recoil velocity of the compound nucleus induces not only a Doppler-shift but also a Doppler-broadening. As can be seen from eq. 4.3, the Doppler-shift is minimal at $\theta = 90^\circ$, while the Doppler-broadening is maximal. Therefore, detectors with large opening angles situated at 90° will show large Doppler-broadening. To reduce this effect, several techniques have been developed. In the Gammasphere spectrometer [Lee90], the detectors around 90° are electronically segmented, see section 3.2.2, which reduces the detector opening angle and, hence, reduces the Doppler broadening. On the other hand, composite detectors, i.e. the Clover and Cluster detectors, have also been developed to improve the Doppler correction, see section 3.2.2. Each detector consists of several small crystals with a small opening angle.

4.1.4 Add-Back

A great advantage of the composite detectors is the enhancement of the peak-to-total ratio P/T by applying an add-back procedure. If a γ ray is scattered from one crystal into a neighbouring one, the two registered energies can be added to obtain the full energy. There is no definite rule for the add-back procedure, and several scenarios may be used based on probability concepts. The following criteria have been used in our Euroball experiments:

The Clover Detectors A schematic drawing of a Clover detector is shown in Fig. 4.1 in order to illustrate the add-back criteria:

- Signals from two neighbouring segments (horizontally or vertically) are added, e.g. AB or AC.
- Hits in two diagonal segments, e.g. AD, are discarded, because they probably do not originate from the same γ ray.
- Triple hits, e.g. ABD, are rejected, because it is difficult to decide if they were generated by one incident γ ray.

- The angle θ of the γ ray is assumed to be the average of the two angles of the two added γ rays.

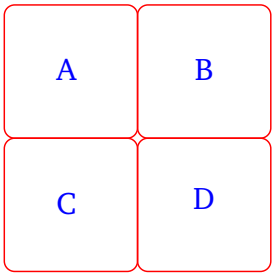

Figure 4.1: *Schematic drawing of a Clover detector. The four crystals are labelled A, B, C and D to explain the add-back procedure.*

The Cluster Detectors Figure 4.2 shows a schematic drawing of a Cluster detector to demonstrate the add-back criteria:

- Hits from two direct neighbouring segments are added, e.g. AB or CD.
- Signals from non-direct neighbouring segments (e.g. AE) are considered as two hits.
- Signals from three and more direct neighbouring segments (e.g. ABC, AGD and CGD) are rejected.
- In case of four signals, three direct neighbouring and a separated one (e.g. ABCE), the triple hit (ABC) is discarded and the single one (E) is treated as a single hit.

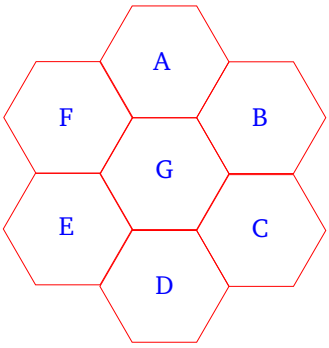

Figure 4.2: *Schematic drawing of a Cluster detector. The seven crystals are labelled A, B, C, D, E, F and G to explain the add-back procedure.*

4.1.5 Time Gate

When only the prompt γ-ray sequences are of interest in high-spin spectroscopy, a time gate is often set on the prompt coincidence peak to discard all the "slow" γ rays originating from radioactive decay, neutron-induced reactions in the Ge detector, or from levels under isomeric states. The prompt time gate also reduces the number of random coincidences. Before setting a time gate, the time peaks of all detectors have to be shifted to the same position to correct for samall differences in cable length and electronic timing.

4.1.6 Data Compression

To enable fast access to the data for the subsequent analysis, only the physical and interesting information is kept and redundant information is filtered out. A data format can be chosen which discards all the redundant information. Usually, the format of the compressed data includes detector identification numbers, γ-ray energies, time information and multiplicity. Another word for the sum-energy can be included, depending on the spectrometer. The compressed data can be written on magnetic tapes or hard disks.

Chapter 5

Data Analysis

5.1 Data Sorting: Energy Histograms and Nuclear Level Scheme

The purpose of this work was to construct complete and consistent level schemes of the investigated nuclei. After the data have been compressed, the coincidence relations between γ rays have to be analysed. The data initially can be visualised in a one dimensional histogram, a "spectrum", that contains the γ-ray energies on one axis and the number of counts on the other axis. This is referred to as a *total-projection* because no conditions are applied while sorting the γ-ray energies. To sort out coincidence spectra, one can specify a γ ray with energy E_{γ_1}, the so called *gate*, and inspect all the events which are in coincidence with E_{γ_1}. Only if an event contains E_{γ_1} the other γ-ray energies of this event are incremented. The result is a *one-dimensional single-gated spectrum*. If one would require two γ rays with energies of E_{γ_1} and E_{γ_2}, one would obtain a *one-dimensional double-gated spectrum* and so on.

The high-efficiency multi-detector arrays Euroball and Gammasphere provide high-fold coincidence data which permits sorting of higher-dimensional histograms. The coincidence information is necessary to construct the level schemes. The high-fold events can be decomposed into lower-fold sub-events [BPB+95] where the fold of the sub-event depends on the dimension of the considered histogram. A two-dimensional histogram is generated from two-fold-coincidence data, and is referred to as γ-γ matrix. To create a two-dimensional matrix, each event is unfolded into pairs of two energies $(E^{\gamma}_{x_i}, E^{\gamma}_{y_j})$ and the bins corresponding to $E^{\gamma}_{x_i}$ and $E^{\gamma}_{y_j}$ are incremented on the x- and y-axis, respectively. Such matrices can be sorted requiring a single gate or a list of gates. Using the matrix, only a single gate can be set on one of the energy axes, and the gated spectrum is projected on the other axis.

Higher-dimensional matrices can also be sorted from high-fold coincidence data, e.g. three- and four-dimensional histograms, so called *cubes* and *hypercubes* [Rad95]. This permits to inspect more accurately the data set by increasing the number of gating transitions. The three-dimensional histogram (*cube*) is produced form triple coincidences (γ^3). Four axes are required, x-, y- and z-axis for the γ-ray energies and the fourth axis for the related number of counts. The cell unit is a triplet of energies $(E^{\gamma}_{x_i}, E^{\gamma}_{y_j}, E^{\gamma}_{z_k})$. In this case one can apply single gates or double gates to obtain one-dimensional coincidence spectra. Quadruple-coincidence data (γ^4) can be used to create four-dimensional histograms (*hypercubes*). The cell unit is a quadruple of energies $(E^{\gamma}_{x_i}, E^{\gamma}_{y_j}, E^{\gamma}_{z_k}, E^{\gamma}_{w_l})$. In this case, single-, double- and triple-gated coincidence spectra can be produced. Compared to a two-dimensional matrix the statistics is reduced for the *cube* and *hypercube*, because of the rejection of the lower-fold events and the distribution of the events in the extra dimensions.

To clarify the essential idea of the coincidence method, a simple level scheme is drawn in Fig. 5.1. For example by setting a single gate on the γ_4 line, the transitions γ_5, γ_6, γ_7, γ_3 and γ_{10} appear in the coincidence spectrum. If a double gate is set on the γ_1 and γ_2 lines, only γ_3 is in coincidence, and if a double gate set on the γ_1 and γ_5 then the γ_9 and γ_6 transitions are in coincidence.

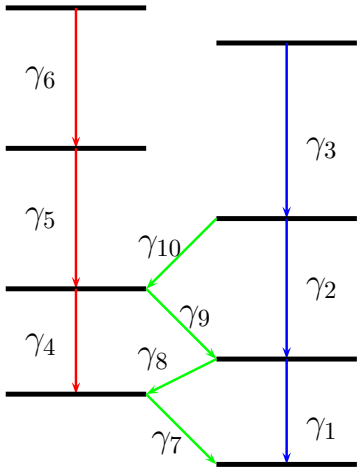

Figure 5.1: *Example of a level scheme to demonstrate the coincidence method.*

5.2 Spin and Parity Assignment

After the construction of the level scheme from the coincidence and intensity information, the next step is to determine the γ-ray multipolarities which are related to the spin values and parities of the relevant levels. This can be achieved by analysing the angular distributions, angular correlations and linear polarisations.

5.2.1 Angular Distribution

The theory of angular distributions has been discussed in detail in the literatures, see e.g. [GTH65, Fer65, Yam67]. The spins of an excited nuclear state produced by a heavy-ion fusion-evaporation reaction are aligned perpendicular to the beam axis [EIS+66, DMN+66, NSD+67]. Gamma rays emitted from aligned states show characteristic angular distributions depending on their multipolarities and the spins of the involved states. Assuming that the beam axis is the z axis, the population probability of nuclear sub-states, $P_m(I)$, can be expressed as a Gaussian distribution around $m = 0$ for a given spin I [Yam67]

$$P_m(I) = \frac{e^{-m^2/2\sigma^2}}{\sum_{m'=-I}^{I} e^{-m'^2/2\sigma^2}}, \tag{5.1}$$

where σ is the half-width. It is usually given as σ/I and can be determined experimentally. The case of $\sigma \to 0$ corresponds to complete alignment. The angular distribution probability, $W(\theta)$, of a γ ray emitted at angle θ is given by [FS65]

$$W(\theta) = 1 + \sum_k A_k P_k(\cos\theta). \tag{5.2}$$

The angular distribution coefficients, A_k, depend on the degree of alignment and on spins and multipole order of the involved states and transitions, respectively. $P(\theta)$ are Legendre polynomials. The high-spin states decay mostly via dipole and quadrupole transitions. Therefore, it is sufficient to consider $k = 2$ and 4 which results in

$$W(\theta) = 1 + A_2 P_2(\cos\theta) + A_4 P_4(\cos\theta). \tag{5.3}$$

If the high-spin states are partially aligned, eq. 5.3 becomes [Yam67]

$$W(\theta) = 1 + \alpha_2 A_2^{\max} P_2(\cos\theta) + \alpha_4 A_4^{\max} P_4(\cos\theta). \tag{5.4}$$

The index max refers to states with fully aligned angular momentum and α_2 and α_4 are the attenuation parameters. In the present work, we have not performed an angular distribution analysis.

5.2.2 Directional Correlation of γ Rays De-exciting Oriented States (DCO)

The multipolarity of γ rays emitted from aligned states can be also determined by measuring DCO ratios. The theory of the DCO has been extensively discussed, see e.g. [KSW73, SA75, BT87, KFML+89, EN92].

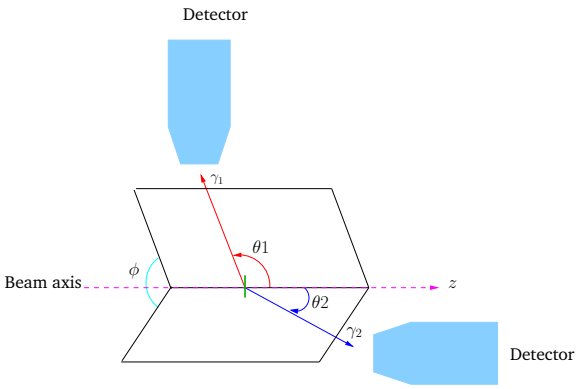

Figure 5.2: *Geometry of the detectors arrangement and the angles in a directional correlation of two successive γ rays γ_1 and γ_2 emitted from an oriented state.*

Assume two successive γ rays, γ_1 and γ_2 are emitted from an aligned state and observed at angles θ_1 and θ_2, respectively, with respect to the beam axis, z, with the angle ϕ, where ϕ is the angle between the two planes defined by the direction of the emitted γ rays and the z axis. Then the intensity $W(\theta_1, \theta_2, \phi)$ can be calculated from [EN92]

$$W(\theta_1, \theta_2, \phi) = N \sum_{\lambda\lambda_1\lambda_2} B_{\lambda_1}(I_1) A_{\lambda}^{\lambda_2\lambda_1}(\gamma_1) A_{\lambda_2}(\gamma_2) H_{\lambda\lambda_1\lambda_2} B_{\lambda_1}(\theta_1, \theta_2, \phi), \tag{5.5}$$

where N is a normalisation factor, B_{λ_1} describes the alignment of the state with respect to the z axis, the coefficients A contain the physical parameters, spins of the states involved and multipolarities and mixing ratios of the transitions and $H_{\lambda\lambda_1\lambda_2} B_{\lambda_1}(\theta_1, \theta_2, \phi)$ is the angular function. The indices λ are even integers [KSW73]. The DCO ratio is given by

$$R_{\mathrm{DCO}} = \frac{W(\theta_2, \theta_1, \phi)}{W(\theta_1, \theta_2, \phi)}. \tag{5.6}$$

In order to determine the DCO ratio from the experimental data, asymmetric γ-γ matrices are sorted with events recorded in the detectors at forward/backward (FB) angles with respect to the beam direction on one axis and those collected in the detectors near 90° on the other axis. The experimental DCO ratio can then be calculated from the observed γ-ray intensities I_γ as

$$R_{\mathrm{DCO}} = \frac{I_\gamma(\text{observed at FB, gate on} \sim 90^\circ)}{I_\gamma(\text{observed at} \sim 90^\circ, \text{gate on FB})}, \tag{5.7}$$

where gates are set on stretched $E2$ transitions. To enhance the statistics in the case of low-intensity transitions, two angular correlation γ-γ matrices can be sorted. The first one contains events registered at forward/backward angles on one axis and those detected in all detectors on the other axis. Similarly, the second matrix contains events recorded $\sim$90° on one axis and those detected in all detectors on the second axis. In these matrices, gates are set on the axis with events recorded in all detectors. Then the experimental ratio,

$$R_{\mathrm{A}} = \frac{I_\gamma(\text{observed at FB, gate on All})}{I_\gamma(\text{observed at} \sim 90^\circ, \text{gate on All})}, \tag{5.8}$$

is used to differentiate between stretched quadrupole and stretched dipole transitions. Values of the DCO and angular correlation ratios are around 0.6 and 1.0 for stretched dipole and stretched quadrapole transitions, respectively.

5.3 Determination of γ-Ray Intensities

Gamma-ray intensities can be used to support arguments, in addition to the coincidence analysis, for the arrangement and the ordering of γ rays in the level scheme. The number and type of detectors used in multi-detector arrays affect the intensity determination, because single and composite detectors (Clovers and Clusters) have different efficiencies.

To determine the intensity from a coincidence spectrum, a matrix gated on the lowest γ-ray transition is sorted. From the matrix a double-gated spectrum is produced. The relative intensities of the transitions above the gate are then determined. For example, in the ^{124}Ba experiment a matrix gated on the lowest transition $(2^+ \rightarrow 0^+)$ was sorted and then another gate on the $(4^+ \rightarrow 2^+)$ transition was set. The peak of the $(6^+ \rightarrow 4^+)$ has been fitted using the *gf3* program from the *RadWare* package [Rad95]. Then the number of counts obtained from the fit has been normalised to $N = 1000$. The intensities have to be corrected for detector efficiency so that the real intensity of a γray, γ_i, is given by $I_{\gamma_i}^{\text{real}} = \frac{I_{\gamma_i}^{\text{measured}}}{\epsilon_{\gamma_i}}$, where ϵ_{γ_i} is the efficiency calculated from eq. 4.2. The relative intensity $I_{\gamma_i}^{\text{relative}}$ of a γ-ray, γ_i, above the $(6^+ \rightarrow 4^+)$ transition is then calculated from $I_{\gamma_i}^{\text{relative}} = N \frac{I_{\gamma_i}^{\text{real}}}{I_{\gamma_{6^+ \rightarrow 4^+}}^{\text{real}}}$. The errors include the uncertainty of the fit and the background subtraction. It should be noted that intensities are only determined for transitions above the gate.

5.4 Linear-Polarisation Analysis

Linear-polarisation measurements of γ rays linking bands to levels of known spin and parity were made to determine the parity of the bands. The Clover detectors of the Euroball spectrometer were used for this purpose. The reference plane of each γ ray is spanned by the beam axis and by the emission direction of the γ ray. Compton-scattered events in neighbouring pairs of Ge crystals of the Clover detectors, scattered horizontally and vertically to the reference plane, were analysed separately. Two E_γ-E_γ matrices were created with either horizontally or vertically scattered γ rays incremented on one axis and γ rays from all the detectors on the other axis. Such pairs of matrices were sorted with gates on uncontaminated γ-ray transitions from different bands. The linear polarisation asymmetry ratio,

$$A(E_\gamma) = \frac{I_v(E_\gamma) - I_h(E_\gamma)}{I_v(E_\gamma) + I_h(E_\gamma)}, \tag{5.9}$$

is obtained by setting gates on γ-ray transitions in the two matrices. Here, I_v and I_h are the intensities of vertically and horizontally scattered γ rays of energy E_γ, respectively. The linear polarisation, P, can be calculated from this asymmetry ratio by $P = A(E_\gamma)\, Q(E_\gamma)$, where $Q(E_\gamma)$ is the polarisation sensitivity of the polarimeter, i.e. the Clover detectors in our experiments. For point-like detectors this quantity can be calculated using the Klein-Nishina formula [KN29]. For finite crystal-size detectors it is obtained by introducing a scaling factor to that for point-like detectors. The scaling factor has been measured for the Euroball array in different experiments. We have taken the polarisation sensitivity obtained in [RGH+01]. The polarisation asymmetry for unmixed stretched magnetic transitions is negative, whereas for electric transitions it is positive.

5.5 Lifetime Measurements of Excited States

5.5.1 Introduction

The nuclear deformation can be compared to theoretical model calculations to test the agreement between theory and experiment. Nuclear deformations cannot be measured directly but can be deduced from the quadrupole moment, which describes the nuclear charge distribution.

The nuclear moments are given by [NR96]

$$Q_{\lambda\mu} = \left(\frac{16\pi}{2\lambda+1}\right)^{1/2} < f|M(\lambda\mu)|i > . \tag{5.10}$$

It is called static moment when $i = f$ and transition moment if $i \neq f$. Example, Q_{22} is the static quadrupole moment, and Q_{20} is the transition quadrupole moment. $Q = 0$ in case of spherical shape, $Q > 0$ for a prolate shape (cigar-like shape) and $Q < 0$ for oblate shape (disc or pancake shape). By measuring the lifetime, τ, the transition quadrupole moment can be deduced which is related to the quadrupole deformation. The quadrupole deformation ε_2 can be obtained from [NR96]

$$Q_{20} = \frac{4}{5} Z r_0^2 A^{2/3} \left(\varepsilon_2 + 0.5\varepsilon_2^2\right), \tag{5.11}$$

where the higher-order terms are neglected. Several methods can be used to measure the nuclear lifetimes, see e.g. [SW68, NSS79, AF79]. The Doppler-Shift Attenuation Method (DSAM) is suited to measure lifetimes in time range of 10^{-11}–10^{-15} sec.

5.5.2 Doppler-Shift Attenuation Method (DSAM)

This method makes use of the fact that when an excited nucleus moves through material it is subject to the slowing-down process. Usually, the target thickness is around several hundred $\mu g/cm^2$ and the backing is several mg/cm^2, thick enough to ensure that the recoiling nuclei are stopped. Assume an excited nucleus recoiling inside the target with a recoil velocity, $v(t)$, then the energy of the γ ray emitted at angle θ with respect to the recoil direction is given by [AF79]

$$E_\gamma(\theta, t) = E_\gamma^0 \frac{\sqrt{1 - (\frac{v(t)}{c})^2}}{1 - \frac{v(t)}{c}\cos\theta}, \tag{5.12}$$

where $v(t)/c$ is the ratio of the recoil velocity, $v(t)$, of the recoiling nucleus to the speed of light and E_γ^0 is the γ-ray energy emitted from the nucleus at rest. If $\frac{v(t)}{c} \ll 1$, the formula is reduced to

$$E_\gamma(\theta, t) = E_\gamma^0[1 + \frac{v(t)}{c}\cos\theta]. \tag{5.13}$$

As we are investigating very high-spin states, the decay is very fast, i.e. the nuclei decay in flight inside the target and only centroid shifts are observed, but no line shapes. Therefore, line shapes are not considered in this work and only centroid shifts are determined.

The fractional shift, the so-called $F(\tau)$ ratio is defined as

$$F(\tau) = \frac{\langle E_\gamma(\theta)\rangle - E_\gamma^0}{E_\gamma^0 \frac{v_{\max}}{c}\cos\theta}, \tag{5.14}$$

where $\langle E_\gamma(\theta)\rangle$ is the average Doppler-shifted energy, E_γ^0 is the non-shifted energy and $\frac{v_{\max}}{c}$ is the velocity of the recoiling nucleus directly after the reaction. The theoretical $F(\tau)$ value can be expressed as [AF79]

$$F(\tau) = \frac{1}{v(0)\tau}\int_0^\infty v(t) e^{-t/\tau} dt. \tag{5.15}$$

The velocity function, $v(t)$, can be calculated from the stopping power [AF79]. Equation 5.14 can be re-written as

$$\langle E_\gamma(\theta)\rangle = E_\gamma^0 + F(\tau) E_\gamma^0 \frac{v_{\max}}{c}\cos\theta, \tag{5.16}$$

where $v_{\max}$ can be calculated from

$$v_{\max} = 1.389\sqrt{E_{\text{projectile}} \frac{m_{\text{projectile}}}{m^2_{\text{compound}}}} 10^9 \text{ cm/s} \tag{5.17}$$

with $E_{\text{projectile}}$ and $m_{\text{projectile}}$ being the energy and the mass, respectively, of the incident ion and m_{compound} is the mass of the compound nucleus formed in the reaction. If one plots the Doppler-shifted energy $\langle E_\gamma(\theta)\rangle$ of a transition as a function of $\cos\theta$, then the $F(\tau)$ values can be deduced from the slope of a linear fit according to 5.16. Then the experimental $F(\tau)$ values are compared with the calculated values.

For this purpose the simulation program *ft_fit_30* is used [Moo96]. The energy loss of the projectile and the compound nucleus in the target material is simulated using the *SRIM* program [SRI] which considers both, electronic and nuclear stopping power [ZBL85, LNST63, LNST68].

Also the energies, conversion coefficients and intensities of the γ-ray transitions of the investigated rotational band are used in the calculation of the $v(t)$ function. To account for non-observed transitions that populate the nuclear levels, the so-called side-feeding, a simple rotational side-feeding model is considered [AF79]. The program produces a matrix of Q_t versus Q_{sf}, which are the quadrupole moments of the rotational band and of side-feeding cascade, respectively, with the χ^2 values from the fit.

Chapter 6

Experiments

The present work is based on two experiments that have been performed to investigate ^{124}Ba and one experiment to study ^{124,125}Xe up to high angular momenta. The essential information about those experiments is summarised in table 6.1.

Table 6.1: *Information on the performed experiments. For more details see the text.*

Inspected nucleus	^{124}Ba		^{124,125}Xe
Reaction	^{64}Ni(^{64}Ni,4$n\gamma$)^{124}Ba	^{64}Ni(^{64}Ni,4$n\gamma$)^{124}Ba	^{82}Se(^{48}Ca,$xn\gamma$)$^{130-x}$Xe
Beam energy	265 MeV	255 and 261 MeV	205 MeV
Beam intensity	–	–	2.5–4.0 pnA
Accelerator	88-Inch cyclotron (LBLN)	Vivtron (IReS)	ATLAS (ANL)
Spectrometer	Gammasphere	Euroball + Diamant	Gammasphere
Target thickness	476 μg/cm^2	$\simeq$ 500 μg/cm^2	^{82}Se 500 μg/cm^2 on Au 500 μg/cm^2
Trigger condition	6 Ge's + 15 modules	3 Ge's + 11 BGO	6 Ge's + 15 modules
Collected events	1.2 $\cdot$ 10^9 (f$_\gamma \geq$ 4)	$\simeq$ 3 $\cdot$ 10^9 (f$_\gamma \geq$ 3)	$\simeq$ 3 $\cdot$ 10^9 (f$_\gamma \geq$ 4)

6.1 Ba Experiments

The heavy-ion fusion-evaporation reaction ^{64}Ni+^{64}Ni at beam energies of 255, 261 and 265 MeV has been used, in two experiments, to populate a wide range of nuclei in the neutron-deficient region with $A \simeq 125$. The initial aim of the experiments was to search for hyperdeformation in ^{126}Ba which was populated in the 2n exit channel. Reports on the search for hyperdeformation can be found in [Hüb05b, HHS+06, HHD+07]. The 4n exit channel leading to ^{124}Ba was the strongest channel observed in this experiment. It was employed to explore the structure of the ^{124}Ba nucleus at very high angular momentum.

6.1.1 Gammasphere Experiment

A ^{64}Ni beam with $E_{\text{beam}} = 265$ MeV was provided by the 88-Inch cyclotron at Lawrence Berkeley National Laboratory (LBNL). The target consisted of a ^{64}Ni foil of 476 μg/cm^2 thickness, enriched to 96.5 %. Gamma-ray coincidences were measured using the Gammasphere spectrometer (see section 3.2.2) with 100 Compton-suppressed Ge detectors at the time of the experiment. Events were written to Exabyte

magnetic tapes when a minimum of six Ge detectors after Compton suppression and 15 "*modules*" showed a signal. A *module* is defined as a Ge detector and the BGO scintillators of the suppression shields. Since the interest was very fast (prompt) emitted γ rays, a prompt time window was set. The data recorded included detector identification numbers, γ-ray energies and timing information. The detectors were calibrated using radioactive sources. After pre-sorting, a total of 1.2×10^9 events with γ-ray fold $f_\gamma \geq 4$ were obtained.

6.1.2 Euroball Experiment

The experiment was performed at the Institut de Recherches Subatomiques (IReS) in Strasbourg, France. The ^{64}Ni beams with energies of $E_{\text{beam}} = 255$ and 261 MeV were supplied by the Vivitron Tandem accelerator. The target consisted of a self-supporting foil of $\simeq 500$ $\mu g/cm^2$ thickness. The emitted γ rays were detected with the Euroball spectrometer, see section 3.2.2. At the time of the experiment, 230 individual Ge crystals out of the total of 239 of the full array could be used. To enhance the selection of the high-spin events, an "inner ball" of 210 BGO scintillation detectors was used as a multiplicity filter. In addition, the ancillary CsI(TI) detector array Diamant [SAA+97, GHM+04] was used. Diamant is a light-charged particle detector array consisting of 84 CsI scintillation detectors covering a geometrical solid angle of 95% of 4π. Each crystal has a thickness of 3 mm and a size of 14.5×14.5 mm^2. The CsI(TI) scintillators were wrapped in 1.5 μm thick aluminized Mylar foil for light reflection. To reduce the background caused by scatterd beam particles and δ electrons, Ta foils with thicknesses between 5 and 15 μm were mounted in front of the forward detectors (up to 67.5°). The Diamant array was placed inside the target chamber as illustrated in Fig. 6.1. Data were written to Digital Linear Tapes (DLT) when a minimum of three Ge crystals and 11 BGO detectors of the inner ball had fired. A time window was used in the analysis to select prompt γ rays. Radioactive sources were used to calibrate the detectors. The data recorded included detector identification numbers, γ-ray energies, timing information and information from the Diamant array. After pre-sorting, a total of $\simeq 3 \times 10^9$ events with $f_\gamma \geq 3$ were collected.

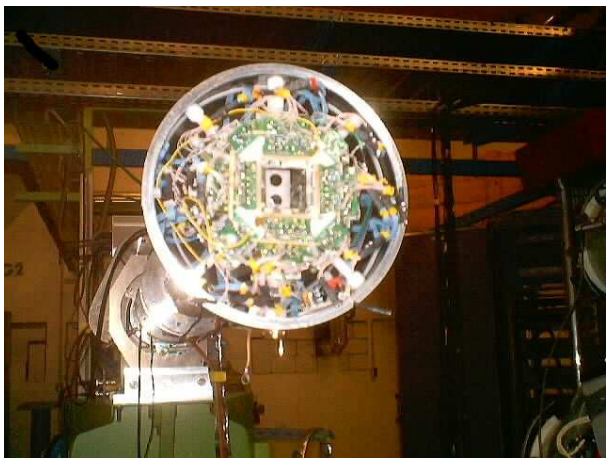

Figure 6.1: *Photograph showing the Diamant array mounted inside the target chamber.*

6.2 Xe Experiment

The experiment was performed at Argonne National Laboratory (ANL). The 205 MeV ^{48}Ca beam has been provided by the Argonne Tandem Linac Accelerator System (ATLAS). The primary goal of the experiment was to search for hyperdeformation predicted in ^{126}Xe and neighbouring nuclei. However, no discreet γ rays of the hyperdeformed states could be established. Accounts of the search for hyperdeformation can be found in [NN05, HHS+06].

In this work, we concentrate on the high-spin states in ^{124,125}Xe produced via the nuclear reactions ^{82}Se(^{48}Ca,$6n\gamma$)^{124}Xe and ^{82}Se(^{48}Ca,$5n\gamma$)^{125}Xe. The target was a 0.5 mg/cm^2 ^{82}Se foil evaporated on a 0.5 mg/cm^2 Au layer and the Se layer was protected by a thing Au film of 80 $\mu g/cm^2$ thickness. As the Au layer faced the, the beam energy at mid-target was reduced to about 199 MeV. To avoid target damage

and to enable the use of high beam intensities, the target was mounted on a four-sector rotating wheel, see Fig. 6.2. The beam was wobbled horizontally by about 5 mm [RHSH+07]. Under these conditions, the Se target sustained a beam current of about 4 pnA.

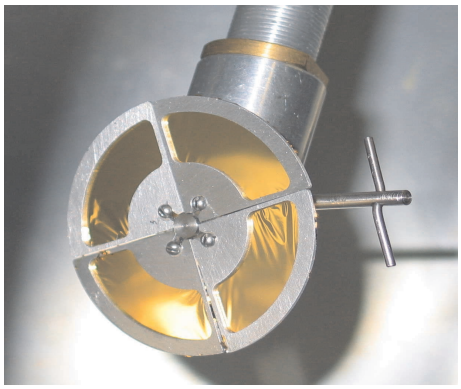

Figure 6.2: *The photograph shows the four-segmented target-wheel with the four targets are mounted.*

The emitted γ rays were detected with the Gammasphere spectrometer (see section 3.2.2) which consisted of 100 Compton-suppressed Ge detector at the time of the experiment. The data recorded included detector identification numbers, multiplicities, γ-ray energies and timing information. The detectors have been calibrated using radioactive sources. A total of 2.8×10^9 coincidence events with a Ge detector coincidence fold of $f_\gamma \geq 5$ have been collected.

Chapter 7

High-Spin Spectroscopy of ^{124}Ba

7.1 Introduction

The nucleus ^{124}Ba with N = 68 and Z = 56 lies in the transitional region between spherical and strongly deformed nuclei of the nuclear chart. It is believed to be soft with respect to γ deformation where the interplay between the deformation-driving forces of the $h_{11/2}$ protons and $h_{11/2}$ neutrons can be investigated. Thus, it has been subject to several studies [MBES+87, MBES+88, KHS+89, WJL+89, PFM+90]. These investigations show that the structure of ^{124}Ba at low and medium spins is dominated by collective excitations.

An additional interest arises because of the limited number of valance particles outside the closed core with Z = 50 and N = 64. When all valance nucleons are aligned along the rotation axis, they tend to polarise the nucleus towards an oblate shape. Eventually, the available spin is exhausted, in which case the total angular momentum is built entirely from particles with their spin vectors quantised along the rotation axis of the oblate nucleus. Experimentally, this effect is seen in γ-ray spectra as *band termination*, see section 2.7. Terminating states have been established at high spins, e.g., in ^{122}Xe [TSR+94] and ^{123}Cs [SHD+04], and it was pointed out [RXBR86] that terminating bands would also be expected in ^{124}Ba. Out of the aims of this work is to investigate this phenomenon.

7.2 Experimental Results

The previously known ^{124}Ba level scheme [PFM+90] has been significantly extended in this work. The previously known bands, labelled bands 1 to 8, are confirmed and extended to higher spins. In addition, six new bands, labelled bands 9 to 14 are observed for the first time in this work. Among the new bands, only band 11 is not firmly connected to the lower-spin part. Band 1 shows an irregular structure above spin $I^\pi = 34^+$ which is interpreted as band termination.

Level Scheme

The level scheme of ^{124}Ba constructed on the basis of the data from this work is presented in Fig. 7.1. The ordering of the γ rays has been determined from coincidence relationships and relative intensities. The lower-spin part was adopted from previous work [MBES+88, PFM+90, MBB+05]. The measured properties of γ-ray transitions are listed in table A.1.

Band 1

Band 1 was already established up to the $I^\pi = 34^+$ state [PFM+90]. Above this level several new transitions with energies of 1444.3, 1583.4, 1610.9, 1294.4 and 1368.4 keV have been observed in the present work. Figure 7.2(a) shows a γ-ray coincidence spectrum that demonstrates the forking of band 1 above the $I^\pi = 34^+$ level into the 1583.4 and 1610.9 keV sequence. The forking of band 1 above the $I^\pi = 36^+$ state into the 1294.4 and 1368.4 keV transitions is shown in Fig. 7.2(b). DCO ratio of the

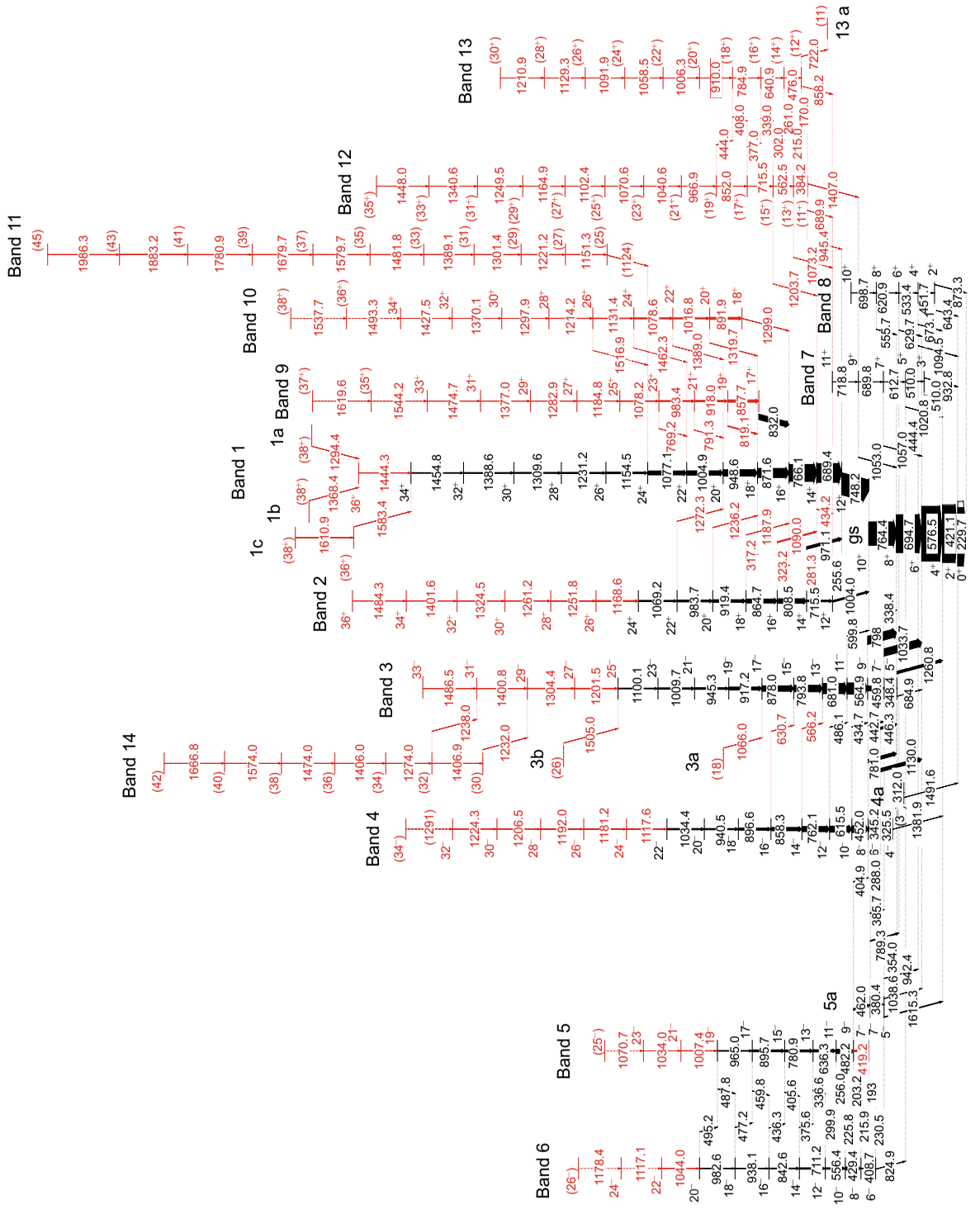

Figure 7.1: *Level scheme of ^{124}Ba constructed in this study [AKSH+06]. The low-spin states were adopted from previous work [MBES+88, PFM+90, MBB+05]. The measured properties of the γ-ray transitions are given in table A.1. Transition energies are given in keV and the widths of the arrows are proportional to relative γ-ray intensities. Parities and spins in parentheses are tentatively assigned, and dashed transitions are tentatively placed. The new structures are drawn with red colour.*

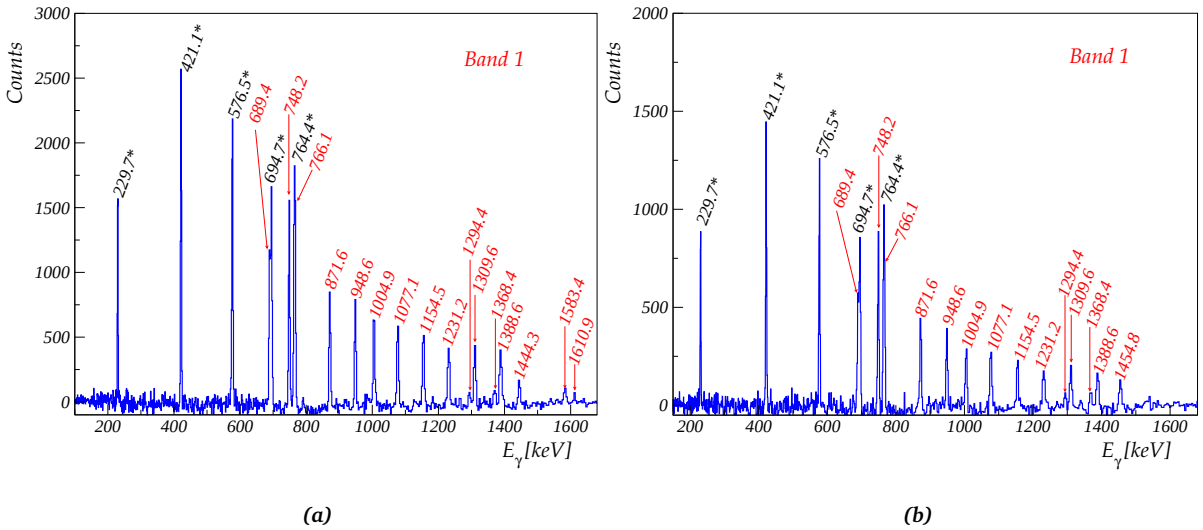

Figure 7.2: *Background-subtracted, summed triple-gated γ-ray coincidence spectrum of band 1. Spectrum (a) was produced by setting two gates from a list of transitions of 689.4, 766.1, 871.6, 948.6, 1004.9, 1077.1, 1154.5, 1231.2, 1309.6, 1388.6, 1454.8 and 1444.3 keV from band 1 and one gate on the 1454.8 keV γ ray. Spectrum (b) was produced by setting two gates on transitions of 689.4, 766.1, 871.6, 948.6, 1004.9, 1077.1, 1154.5, 1231.2, 1309.6, 1388.6 and 1454 keV of band 1 and one gate on the 1444.3 keV γ ray. The transitions belonging to the gs band are marked with single asterisks.*

1444.3 keV transition is compatible with a stretched quadrupole, probably $E2$, transition. For the other new transitions, the DCO ratios could not be determined. Hence, the high-spin levels are tentatively assigned and, therefore, given in parentheses in the level scheme, Fig. 7.1.

Band 2

Band 2 had already been observed in the previous work [PFM+90] up to the $I^\pi = 24^+$ state. In this work, six new transitions with energies of 1168.6, 1251.8, 1261.2, 1324.5, 1401.6 and 1484.3 keV have been detected and placed on top of the $I^\pi = 24^+$ level extending the band to a state at E_x = 16949 keV and $I^\pi = 36^+$. According to the DCO ratios, stretched quadrupole, probably $E2$, multipolarity was assigned to the 1168.6, 1251.8, and 1261.2 keV transitions. For the 1324.5, 1401.6 and 1484.3 keV transitions, no DCO ratios could be determined. However, due to the regularity of the band, $E2$ character may also be assumed. In addition, six new inter-band transitions with 1090.0, 323.2, 1187.9, 317.2, 1236.2 and 1272.3 keV have also been identified. A representative coincidence spectrum showing the transitions of band 2 is presented in Fig. 7.3.

Band 3

Band 3 was also initially identified up to $I^\pi = 25^-$ [PFM+90]. In our work, four new transitions with energies of 1201.5, 1304.4, 1400.8 and 1486.5 keV were added on top of the $I^\pi = 25^-$ level extending the band to a state at E_x = 15007 keV and $I^\pi = 33^-$. Furthermore, two side-transitions are observed, the 1066.0 keV transition feeds into the I^π=17$^-$ level and the 1505.0 keV line feeds into the $I^\pi = 25^-$ level, see Fig.7.1. Spin assignments were made up to the 1400.8 keV transition where the DCO ratios are compatible with stretched quadrupole, probably $E2$, multipolarity. For the 1486.5 keV no DCO ratios could be determined. However, $E2$ character is assumed. A γ-ray coincidence spectrum of band 3 is presented in Fig. 7.4.

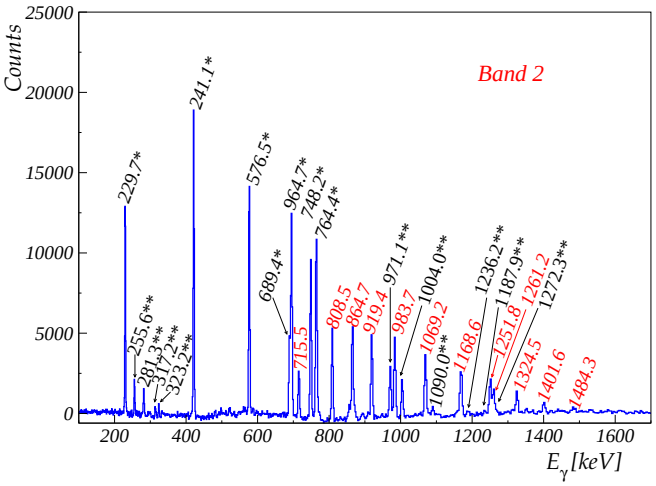

Figure 7.3: *Background-subtracted, summed triple-gated γ-ray coincidence spectrum from band 2. The spectrum was generated by setting one gate of a list of transitions from band 1 with energies of 229.7, 421.1, 576.5, 964.7 and 764.4 keV and two gates of a list of transitions from band 2 with energies of 715.5, 808.5, 864.7, 919.4, 983.7, 1069.2, 1168.6, 1251.8, 1261.2, 1324.5 and 1401.6 keV. The transitions belonging to the gs band are marked with single asterisks. Double asterisks mark the decay-out transitions from band 2 to band 1 as well as to the gs band.*

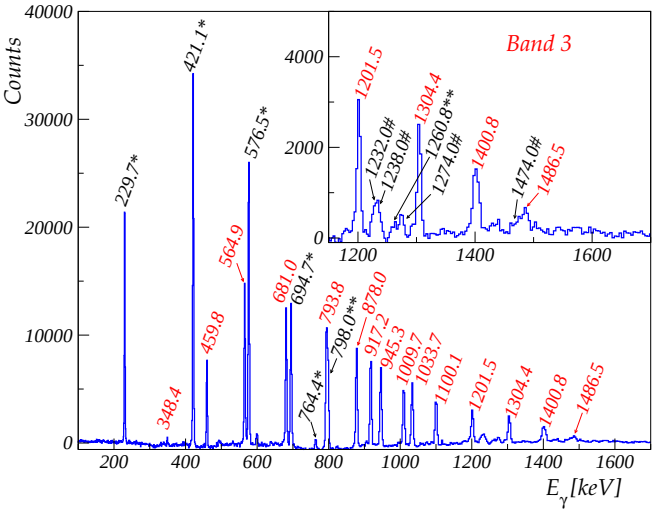

Figure 7.4: *Background-subtracted, summed triple-gated γ-ray coincidence spectrum of band 3. The spectrum was produced by summing all triple-gate combinations of transitions with energies of 459.8, 564.9, 681.0, 793.8, 878.0, 917.2, 945.3, 1009.7, 1100.1, 1201.5, 1304.4 and 1400.8 keV from band 3. The transitions belonging to the gs band are marked with single asterisks. Gamma rays marked by double asterisks are the linking transitions from band 3 to the gs band. Transitions marked with a hash mark belong to the new sequence labelled band 14, see the level scheme, Fig. 7.1.*

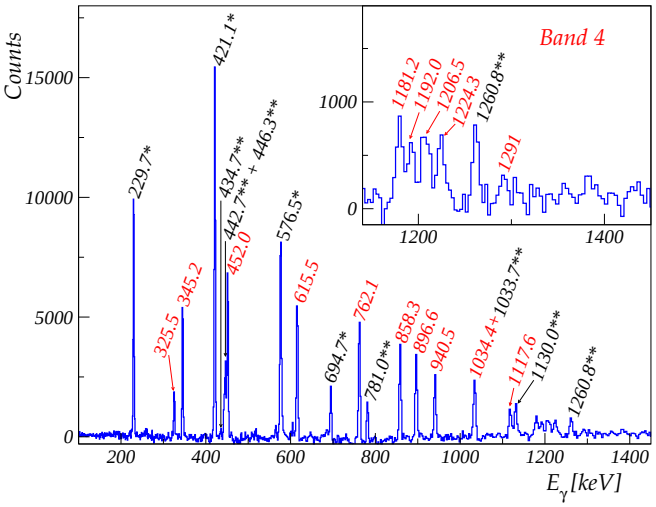

Figure 7.5: *Background-subtracted, summed triple-gated γ-ray coincidence spectrum of band 4. The spectrum was generated by summing all triple-gate combinations of transitions with 325.5, 345.2, 452.0, 615.5, 762.1, 858.3, 896.6, 940.5, 1034.4, 1117.6, 1181.2, 1192.0, 1206.5 and 1224.3 keV from band 4. Single and double asterisks denote transitions of the gs band and decay-out transitions to band 3 and to the gs band, respectively.*

Band 4

Band 4 was previously observed up to the $I^\pi = 20^-$ level [PFM+90]. In this study, the band was extended up to a state at E_x = 15476 kev and $I^\pi = 34^-$ by adding seven new transitions with energies of 1034.4, 1117.6, 1181.2, 1192.0, 1206.5, 1224.3 and 1291 keV on top of the $I^\pi = 20^-$ level. The DCO ratios were determined up to the 1117.6 keV transition and stretched quadrupole, presumably $E2$,

multipolarity was assigned. For the higher-lying transitions, because of the regularity of the band, $E2$ character may also be assumed. A representative gated γ-ray spectrum of band 4 is shown in Fig. 7.5.

Bands 5 and 6

The coupled bands 5 and 6 were known from previous work [MBES+88, PFM+90] up to spin $I^\pi = 19^-$ and $I^\pi = 20^-$, respectively. We have confirmed those sequences and added three transitions on top of the bands. Furthermore, the low-spin part has been rearranged. At 2647 and 2691 keV, two close-lying 7^- levels were previously known [PFM+90]. It has been proposed that the 2647 keV level belongs to band 5 but the 2691 keV state was not assigned as a member of the band [PFM+90]. Triple coincidence analysis has revealed a new 419.2 keV transition depopulating the 9^- band member to the 7^- level at 2691 keV which was earlier not observed, perhaps because it lies very close in energy to the strong 421.1 keV ($4^+ \rightarrow 2^+$) transition from the gs band. We reorded the 7^- states as illustrated in the level scheme of Fig. 7.1. The fairly strong 462.0 keV transition depopulating the 9^- level of band 5 to the 7^- level at 2647 keV probably can be explained by mixing of the 7^- states. Coincidence γ-ray spectra of bands 5 and 6 are presented in Figs. 7.6(a) and 7.6(b), respectively.

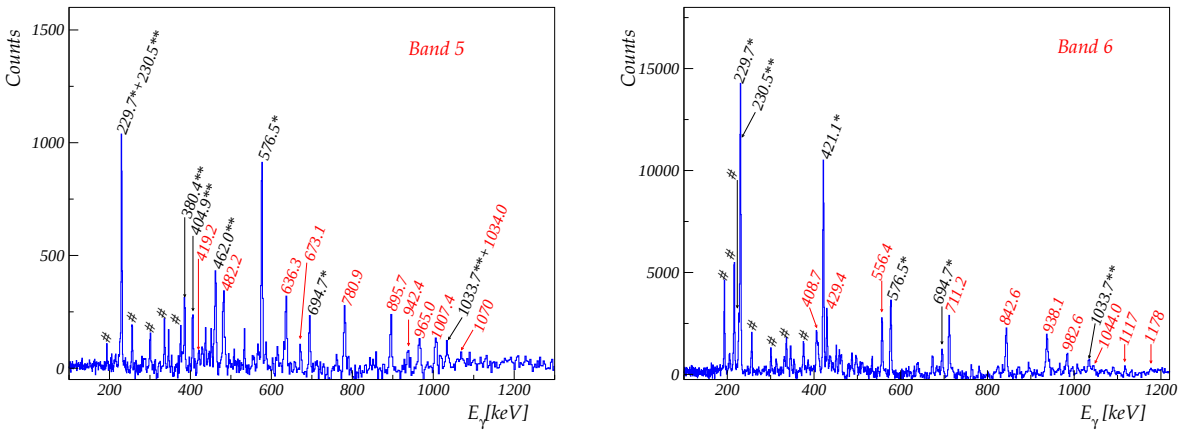

(a) *(b)*

Figure 7.6: *(a) Background-subtracted, summed triple-gated γ-ray coincidence spectrum from band 5 obtained by setting double gates on the transitions of 482.2, 636.3, 780.9, 895.7, 965.0, 1007.4 and 1034.0 keV of band 5 and a single gate on the 421.1 keV transition from the gs band. (b) Background-subtracted, summed double-gated γ-ray coincidence spectrum of band 6 generated by setting double gates of the form (A×B) where A is the list of transitions with energies of 429.4 and 556.4 kev and B is the list of transitions with energies of 711.2, 842.6, 938.1, 982.6, 1044.0 and 1178 keV. Single asterisks mark peaks of the gs band. Double asterisks mark the decay-out transitions. Inter-band transitions are marked with hash marks.*

Bands 7 and 8

Bands 7 and 8 are known from previous work [MBES+88, PFM+90]. In this experiment, they were weakly populated and could not be extended to higher spin.

Band 9

The new sequence of γ rays with energies of 857.7, 918.0, 983.4, 1078.2, 1184.8, 1282.9, 1377.0, 1474.7, 1544.2 and 1619.6 keV, labelled band 9, has been observed for the first time in this study. A gated γ-ray coincidence spectrum of band 9 is shown in Fig. 7.7. The band decays via several transitions with energies of 832.0, 819.1, 791.3 and 769.2 keV into band 1. The 832.0 keV transition from the state at $E_x = 5726$ keV, which feeds into the $I^\pi = 16^+$ level of band 1, was observed already by [PFM+90] where

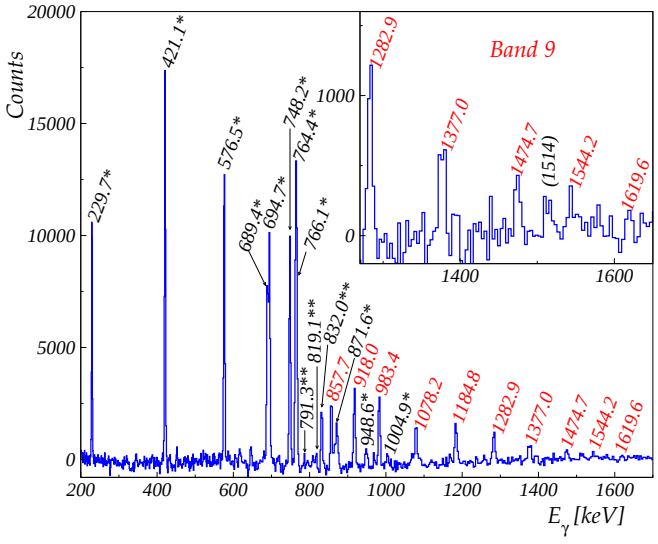

Figure 7.7: *Background-subtracted, summed triple-gated γ-ray coincidence spectrum of band 9. The spectrum was produced by setting one gate on the transitions of 229.7, 421.1, 576.5, 694.7, 764.4, 748,2, 689.4 and 766.1 keV of band 1 and two gates on the transitions of 832.0, 857.7, 918.0, 983.4, 1078.2, 1184.8, 1282.9, 1377.0, 1474.7, 1544.2 and 1619.6 keV of band 9. Single asterisks mark peaks of band 1. Gamma rays marked by double asterisks are the linking transitions from band 9 to band 1.*

mixed $M1/E2$ multipolarity was suggested. The DCO ratio of this transition is compatible with a dipole character. However, the linear polarisation asymmetry of this transition, measured with the Euroball Clover detectors, is small and negative, which confirms the earlier suggested mixed $M1/E2$ multipolarity. For an electric dipole, one would expect no mixing and, thus, a positive asymmetry [RGH+01]. Since the 832.0 keV transition feeds into the $I^\pi = 16^+$ level of band 1, this leads to $I^\pi = 17^+$ for the lowest level of band 9. No DCO ratio for the 819.1 keV linking transition could be established. The other linking transitions of 791.3 and 769.2 keV are tentatively placed in the level scheme, see Fig. 7.1. The transitions of 857.7, 918.0, 983.4 and 1078.2 keV are sufficiently strong for a determination of the DCO ratio. They are compatible with stretched quadrupole, presumably $E2$, character. Because of the regularity of the band we assign $E2$ multipolarity to the other in-band transitions. Hence, the band extends to a state at E_x = 10855 keV and $I^\pi = 37^+$.

Band 10

Also band 10 is observed for the first time in this study. It consists of ten transitions with energies of 891.9, 1016.8, 1078.6, 1131.4, 1214.2, 1297.9, 1370.1, 1427.5, 1493.3 and 1537.7 keV. A coincidence γ-ray spectrum of band 10 is presented in Fig. 7.8. The sequence decays into band 1 via several transitions with energies of 1299.0, 1319.7, 1389.0, 1462.3 and 1516.9 keV. Only the 1319.7 keV transition is clean and strong enough to allow a determination of the DCO ratio. This ratio is consistent with stretched quadrupole, probably $E2$, multipolarity. Since the 1319.7 keV line feeds into the $I^\pi = 18^+$ state of band 1, $I^\pi = 20^+$ is assigned to the 7084 keV level of band 10. DCO ratios could be determined only for the in-band transitions of 891.9, 1016.8, 1078.6, 1131.4 and 1214.2 keV. They are compatible with stretched quadrupole, probably $E2$ multipolarity. For the 1297.9, 1370.0, 1427.5, 1493.3 and 1537.7 keV transitions, $E2$ character has been assumed. Hence, the band extends to E_x = 18656 keV and $I^\pi = 38^+$.

Band 11

The new cascade labelled band 11 consists of eleven γ rays with energies of 1124.1, 1151.3, 1221.2, 1301.4, 1389.1, 1481.8, 1579.7, 1679.7, 1780.9, 1883.2 and 1986.3 keV. A representative coincidence γ-ray spectrum showing the transitions of band 11 is presented in Fig. 7.9. The sequence decays to band 1 where transitions up to the $I^\pi = 24^+$ level from band 1 are observed in coincidence with the new sequence.

The γ-ray transitions of band 11 show an energy difference that is smoothly increasing from 71 to 105 keV; only the energy difference between the 1124.1 and 1151.3 keV transitions is lower. Therefore, the 1124.1 keV γ-ray line may be a linking transition from band 11 to band 1. Moreover, several weak γ rays with energies of 1095, 1453, 1516, 1833 and 1914 keV are also observed in the coincidence spectrum, see Fig 7.9, but they could not be placed in the level scheme. They might be candidates

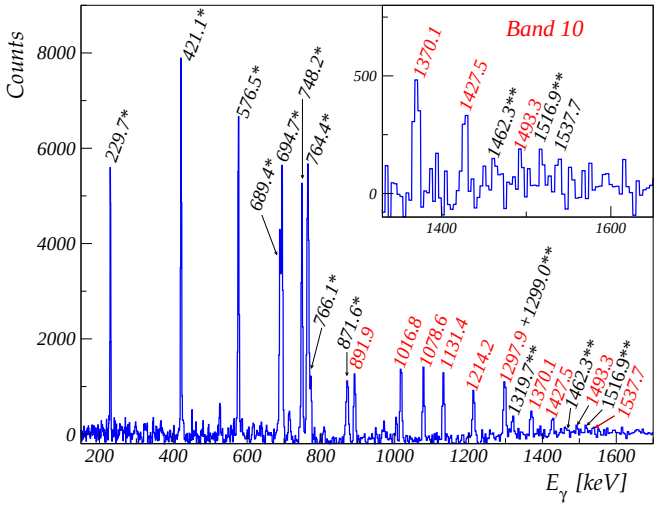

Figure 7.8: *Background-subtracted, summed triple-gated γ-ray coincidence spectrum of band 10. The spectrum was produced by setting one gate on the transitions of 229.7 421.1, 576.5, 694.7, 764.4, 748,2, 689.4 and 766.1 keV of band 1 and two gates on the transitions of 891.9, 1016.8, 1078.6, 1131.4, 1214.2, 1297.9, 1370.1, 1427.5, 1493.3 and 1537.7 keV of band 10. Single and double asterisks denote peaks of band 1 and linking transitions from band 10 to band 1, respectively.*

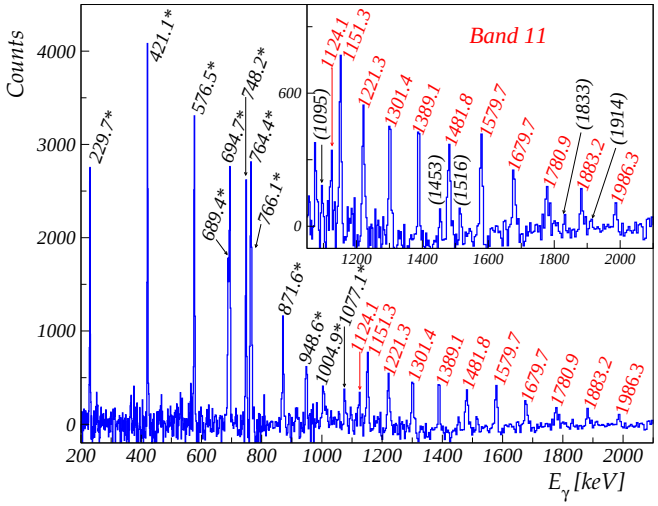

Figure 7.9: *Background-subtracted, summed triple-gated γ-ray coincidence spectrum of band 11, obtained by setting triple gates of the form (A×B×B) where A is the list of γ rays with energies of 229.7, 421.1, 576.5, 694.7, 764.4, 748,2, 689.4, 766.1, 871.6, 948.6, 1004.9 and 1077.1 keV of band 1 and list B contains the transitions with energies of 1124.1, 1151.3, 1221.2, 1301.4, 1389.1, 1481.8, 1579.7, 1679.7, 1780.9, 1883.2 and 1986.3 keV from band 11. Asterisks mark peaks of band 1. Energies in parentheses correspond to transitions observed in coincidence which are not placed in the level scheme.*

for decay-out transitions. Accordingly, band 11 is tentatively connected to band 1, see Fig. 7.1, and its excitation energy, parity and spin remain uncertain. No DCO ratios could be established. However, due to the regularity of the band, stretched $E2$ multipolarity has been assumed.

Bands 12 and 13

Also bands 12 and 13 are new γ-ray sequences observed in this work. Band 12 consists of twelve γ-ray transitions with energies of 384.2, 562.5, 715.5, 852.0, 966.9, 1040.6, 1070.6, 1102.4, 1164.9, 1249.5, 1340.6 and 1448.0 keV. The DCO ratios of the transitions with energies between 384.2 and 1102.4 keV are compatible with stretched quadrupole, presumably $E2$, multipolarity. For the other transitions, due to the regularity of the band, $E2$ charter was assumed.

Band 13 has nine transitions with energies of 476.0, 640.9, 784.9, 910.0, 1006.3, 1058.5, 1091.9, 1129.3 and 1210.9 keV. $E2$ multipolariy was assigned to the transitions of 476.0, 640.9, 784.9, 910.0, 1006.3, 1058.5, 1091.9 and 1129.3 keV where DCO ratios could be determined.

The lower parts of bands 12 and 13 are connected by several weak in-band $\Delta I = 1$ transitions with energies of 170.0, 215.0, 261.0, 302.0, 339.0, 377.0, 408.0 and 444.0 keV. Thus, they probably form a pair of signature-partner bands. No DCO ratios for those transitions could be determined. Bands 12 and 13 decay into bands 1, 2 and 7. Out of the decay-out transitions, only the 1407.0 keV line is firmly established. However, due to its low intensity, the DCO ratio has a large uncertainty and the multipolarity could not be determined reliably . The other linking transitions are not certain and, hence, they are shown as dashed lines in Fig. 7.1. Coincidence γ-ray spectra showing transitions in bands 12 and 13 are presented in Figs. 7.10(a) and 7.10(b), respectively.

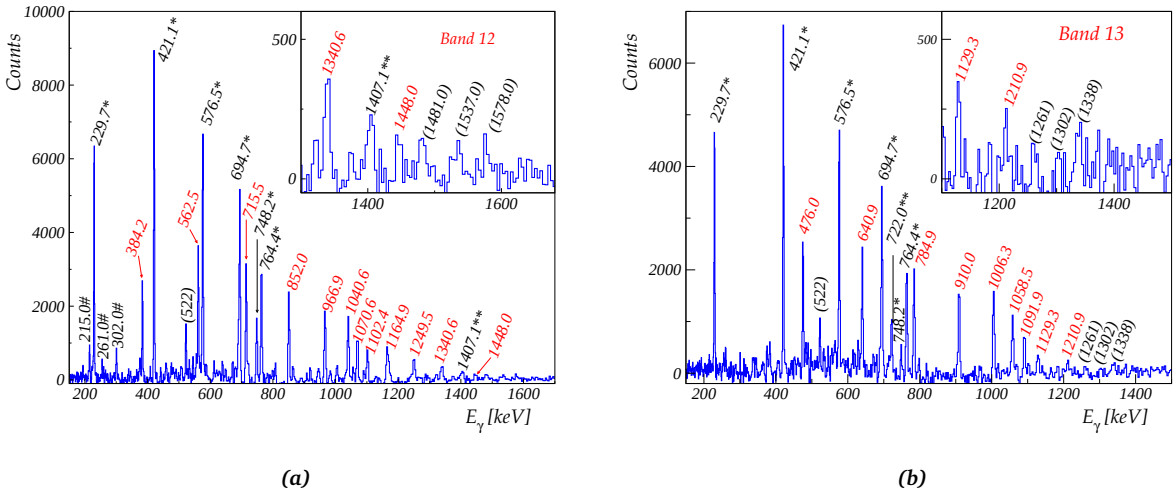

Figure 7.10: *Spectrum (a) shows a background-subtracted, triple-gated γ-ray coincidence spectrum of band 12 produced by setting one gate on the transitions of 229.7, 421.1, 576.5, 694.7 and 764.4 keV from band 1 and two gates on the transitions of 384.2, 562.5, 715.5, 852.0, 966.9, 1040.6, 1070.6, 1102.4, 1164.9, 1249.5, 1340.6 and 1448.0 keV from band 12. Spectrum (b) displays a background-subtracted, triple-gated spectrum from band 13 obtained by setting one gate on the transitions of 229.7, 421.1, 576.5, 694.7 and 764.4 keV from band 1 and two gates on the transitions of 476.0, 640.9, 784.9, 910.0, 1006.3, 1058.5, 1091.9, 1129.3 and 1210.9 keV from band 13. Single asterisks mark peaks of band 1. Double asterisks mark the decay-out transitions. The inter-band transitions are marked with hash marks. Energies in parentheses correspond to transitions observed in coincidence which could not be placed in the level scheme.*

Band 14

A new sequence of γ rays labelled band 14, with energies of 1406.9, 1274.0, 1406.0, 1474.0, 1574.0 and 1666.8 keV has been observed. It decays via the 1232.0 and 1238.0 keV γ rays into the $I^\pi = 29^-$ and $I^\pi = 31^-$ levels, respectively, of band 3. The DCO ratios of these linking transitions have large uncertainties due to low intensities. Thus, their multipolarities could not be reliably determined.

7.3 Band Structures in ^{124}Ba

The structure of the rotational bands in ^{124}Ba are interpreted within the framework of the Cranked Shell Modell (CSM) [BF79a, BF79b] and the configuration-dependent Cranked Nilsson-Strutinsky (CNS) [BR85, AFLR99] approach. Pairing interaction is very important at low and medium spins and has to be considered in the calculations whereas at higher spins pairing interactions are quenched due to Coriolis forces which become dominant at high rotational frequencies. Thus, the CSM with pairing can be used to explain the low- and medium-spin structures and the CNS model without pairing is adequate for the highest spin states.

To assign configurations to the bands, the observed excitation energies, band-crossing frequencies, alignment gains, parities and spins are commonly used. These quantities can be compared to those observed in neighbouring nuclei as well as to the CSM and CNS calculations. Furthermore, the signature splitting, $\Delta e'$, and the ratios of reduced magnetic dipole and electric quadrupole transition probabilities, $\frac{B(M1;I\rightarrow I-1)}{B(E2;I\rightarrow I-2)}$, can provide additional support for the configuration of the coupled bands.

In earlier work [MBES$^+$87, MBES$^+$88, KHS$^+$89, WJL$^+$89, PFM$^+$90, PL91, MBB$^+$05], configurations have been suggested for bands 1 to 8 in the low- and medium-spin regions. In this work, these assignments are confirmed and configurations for the new structures are suggested.

7.3.1 Cranked Shell Model (CSM) Calculations

Table 7.1 shows the shell model states, Nilsson orbitals and quasi-particle (qp) levels with (π, α) relevant in this mass region taken from [PFM+90]. In the rotating nuclei, the Coriolis interaction mixes the original states. Nonetheless, the shell model and Nilsson configurations are included for convenience.

Nucleon	Shell model states	Nilsson orbitals	(π, α)	qp Label
Protons	$(d_{5/2}, g_{7/2})$	$[422]^{3/2^+}$	$(+, +1/2)$	a
	$(d_{5/2}, g_{7/2})$	$[422]^{3/2^+}$	$(+, -1/2)$	b
	$(d_{5/2}, g_{7/2})$	$[420]^{1/2^+}$	$(+, +1/2)$	c
	$(d_{5/2}, g_{7/2})$	$[420]^{1/2^+}$	$(+, -1/2)$	d
	$g_{9/2}$	$[404]^{9/2^+}$	$(+, +1/2)$	a'
	$g_{9/2}$	$[404]^{9/2^+}$	$(+, -1/2)$	b'
	$h_{11/2}$	$[550]^{1/2^-}$	$(-, +1/2)$	f
	$h_{11/2}$	$[550]^{1/2^-}$	$(-, -1/2)$	e
	$h_{11/2}$	$[541]^{3/2^-}$	$(-, +1/2)$	h
	$h_{11/2}$	$[541]^{3/2^-}$	$(-, -1/2)$	g
Neutrons	$(s_{1/2}, d_{3/2})$	$[411]^{1/2^+}$	$(+, +1/2)$	A
	$(s_{1/2}, d_{3/2})$	$[411]^{1/2^+}$	$(+, -1/2)$	B
	$(d_{5/2}, g_{7/2})$	$[402]^{5/2^+}$	$(+, +1/2)$	C
	$(d_{5/2}, g_{7/2})$	$[402]^{5/2^+}$	$(+, -1/2)$	D
	$(d_{5/2}, g_{7/2})$	$[413]^{5/2^+}$	$(+, +1/2)$	A'
	$(d_{5/2}, g_{7/2})$	$[413]^{5/2^+}$	$(+, -1/2)$	B'
	$h_{11/2}$	$[523]^{7/2^-}$	$(-, +1/2)$	F
	$h_{11/2}$	$[523]^{7/2^-}$	$(-, -1/2)$	E
	$h_{11/2}$	$[532]^{5/2^-}$	$(-, +1/2)$	H
	$h_{11/2}$	$[532]^{5/2^-}$	$(-, -1/2)$	G

Table 7.1: *The labelling of quasi-particle (qp) orbitals in parity and signature (π, α) and the related shell model and Nilsson model states from which they originate at rotational frequency $\omega = 0.0$ $\mathrm{MeV}/\hbar$.*

The Potential-Energy Surfaces (PES) and the quasi-particle energies (Rauthians) for protons and neutrons are calculated using the Ultimate Cranker (UC) software package [Ben] for different configurations in ^{124}Ba. Examples of such calculations are shown in Figs. 7.11, 7.12 and 7.13. Figure 7.11 presents

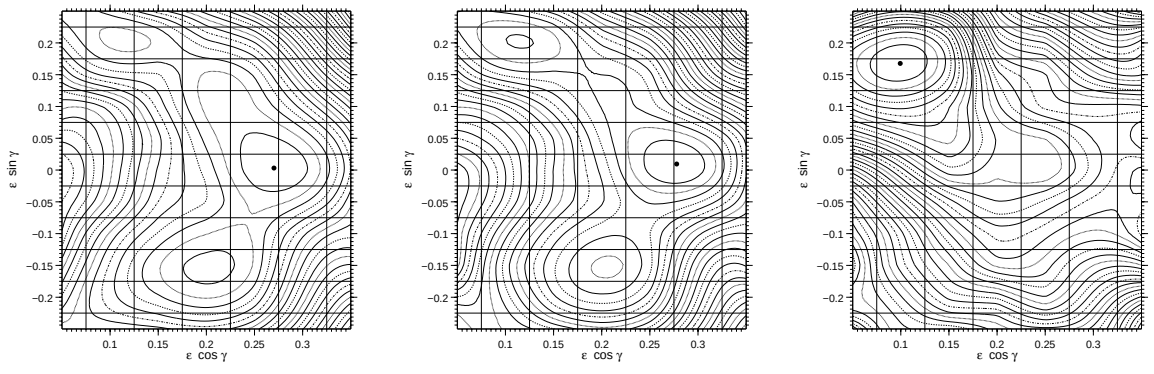

(a) *(b)* *(c)*

Figure 7.11: *Example of potential-energy surfaces (PES) calculated with the Ultimate Cranker code for ^{124}Ba. The calculation has been performed for the configurations (π, α) = (+,0) at spins I = 12 (a), 16 (b) and 36 (c).*

the PES calculated for the configuration $(\pi, \alpha) = (+, 0)$ at three different spin values I = 12, 16 and 36. For spin I = 12, three minima are observed. The lowest one at $(\varepsilon_2 \simeq 0.25, \gamma \simeq 0^\circ)$ corresponds to prolate shape, the second minimum at $(\varepsilon_2 \simeq 0.25, \gamma \simeq -38^\circ)$ is related to oblate shape and the third minimum at $(\varepsilon_2 \simeq 0.23, \gamma \simeq 60^\circ)$ corresponds to non-collective oblate shape (band termination). For spin I = 16, the lowest minimum lies at $(\varepsilon_2 \simeq 0.30, \gamma \simeq 0^\circ)$ which indicates that prolate-driving

high-j orbitals are getting aligned. At spin $I = 36$, the collective prolate and oblate shapes disappear and only the non-collective oblate minimum is well developed at $(\varepsilon_2 \simeq 0.18, \gamma \simeq 60^\circ)$. Figures. 7.12 and 7.13 show the Routhians for protons and neutrons corresponding to the minima $(\varepsilon_2 \simeq 0.25, \gamma \simeq 0^\circ)$ and $(\varepsilon_2 \simeq 0.25, \gamma \simeq -37^\circ)$, respectively. It can be seen that for the prolate shape with $\gamma \simeq 0^\circ$ the first $h_{11/2}$ proton crossing (Fig. 7.12(a)) takes place earlier than the $h_{11/2}$ neutron crossing (Fig. 7.12(b)) and this would drive the nucleus to prolate shape while for the $\gamma \simeq -37^\circ$ the $h_{11/2}$ neutron crossing occurs earlier (Fig. 7.13(b)) and this would polarise the nucleus shape towards oblate shape.

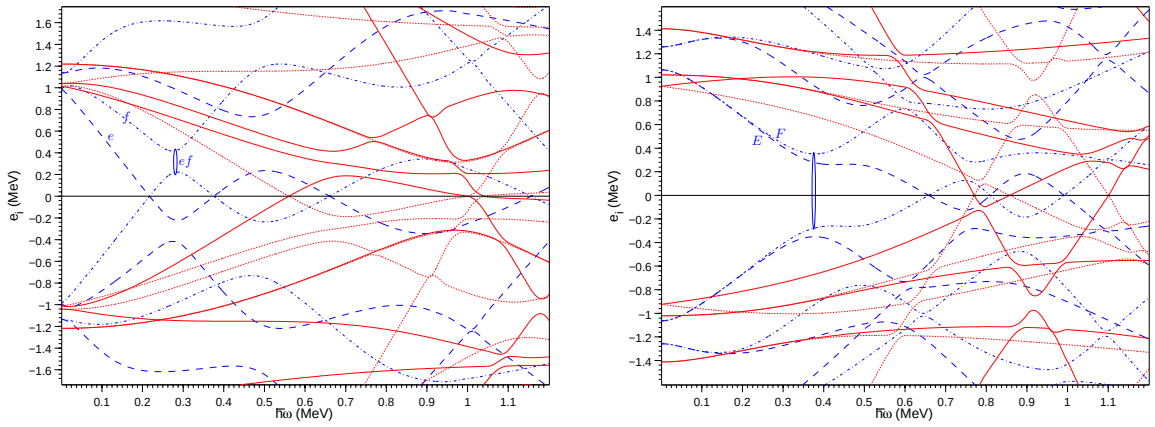

(a) *(b)*

Figure 7.12: *Quasi-particle energy levels (Routhinas) calculated as a function of rotational frequency for protons (a) and neutrons (b) at a deformation corresponding to the minimum ($\varepsilon = 0.25,\ \gamma = 0.0^\circ$). The parity and signature (π, α) of the levels are: $(+, +1/2)$–solid lines; $(+, -1/2)$–doted lines; $(-, -1/2)$–dashed lines; $(-, +1/2)$–dot-dashed lines.*

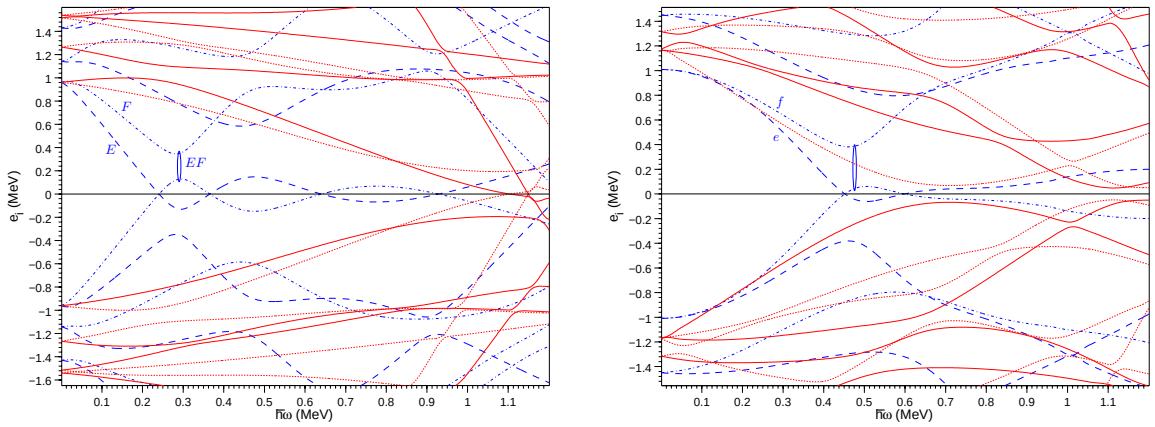

(a) *(b)*

Figure 7.13: *Quasi-particle energy levels (Routhians) calculated as a function of rotational frequency for protons (a) and neutrons (b) at a deformation corresponding to the minimum ($\varepsilon = 0.25,\ \gamma = -37^\circ$). The parity and signature (π, α) of the levels are: $(+, +1/2)$–solid lines; $(+, -1/2)$–dotted lines; $(-, -1/2)$–dashed lines; $(-, -1/2)$–dot-dashed lines.*

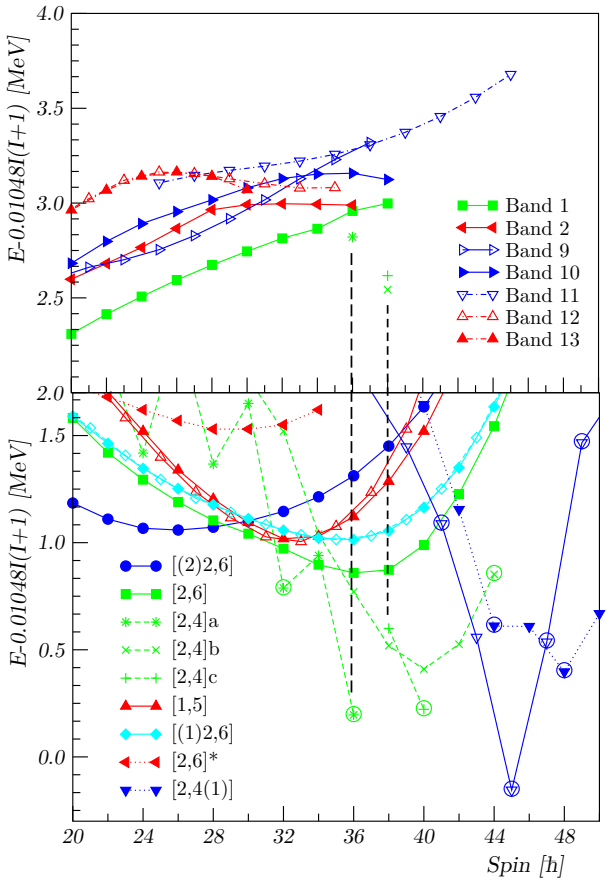

Figure 7.14: *Excitation energy, E, relative to a rigid-rotor reference, $E_{RLD} = \frac{1}{2\mathscr{I}_{rig}} I(I+1)$ where $\frac{1}{2\mathscr{I}_{rig}} \approx 32.32A^{-5/3}$ MeV/$\hbar^2$ [AFLR99], as a function of spin, I, for positive-parity bands in ^{124}Ba. The experimental bands are drawn in the upper panel and are compared with calculated bands in using the CNS formalism in the lower panel. Filled and open symbols correspond to signatures α=0 and 1, respectively. For band 11, spins and parity remain uncertain. Vertical dashed lines correspond to experimental and calculated favoured non-collective states as discussed in the text.*

7.3.2 Cranked Nilsson Strutinisky (CNS) Calculations

The configuration-dependent CNS formalism without pairing [BR85, AFLR99] can be used to interpret the behaviour of the rotational bands at high spins, typically for $I \geq 20$, where the pairing interaction is quenched by Coriolis forces and can be neglected. Figures. 7.14 and 7.15 present the results of the CNS calculation compared with the experimental excitation energies for the positive- and negative-parity bands in ^{124}Ba, respectively [AKSH$^+$06]. In the CNS calculations, the parameters given in [TAL$^+$84] for the A = 130 mass region were used.

As can be seen in Figs. 7.14 and 7.15, there is a difference between the absolute values of the experimental and calculated level energies. This is because the experimental level energies are given relative to the ground state, whereas the reference for the calculated levels is the liquid drop energy at $I = 0$. Therefore, the difference between the experimental and calculated energies depends essentially on the ground-state shell and pairing energy. Configurations in the CNS formalism are denoted by the number of particles in the different high-j intruder orbitals outside a closed core. Nevertheless, it must be mentioned that in the CNS formalism no separation into core and valance nucleons is made and all orbitals up to $N = 8$ are treated on an equal footing. In the case of ^{124}Ba, the nucleus ^{114}Sn with $Z = 50$ and $N = 64$ has been chosen as a core. Therefore, the configurations can be identified by the number of protons holes in the $g_{9/2}$ subshell, the number of protons in $h_{11/2}$ orbitals, and the number of neutrons in the $h_{11/2}$ and $i_{13/2}$ orbitals. The configurations are labelled using the shorthand notation $[(p_0)p_1, n_0(n_1)]$, where p_0 is the number of the proton holes in the $g_{9/2}$ subshell (left out when $p_0 = 0$), p_1 is the number of the $h_{11/2}$ protons, n_0 is the number of the neutrons in the $h_{11/2}$ orbitals, and n_1 is the number of $i_{13/2}$ neutrons (left out when $n_1 = 0$). The energy of each configuration is minimised at each spin in the deformation space $(\varepsilon_2, \varepsilon_4, \gamma)$, which enables the development of collectivity to be traced as a function of spin.

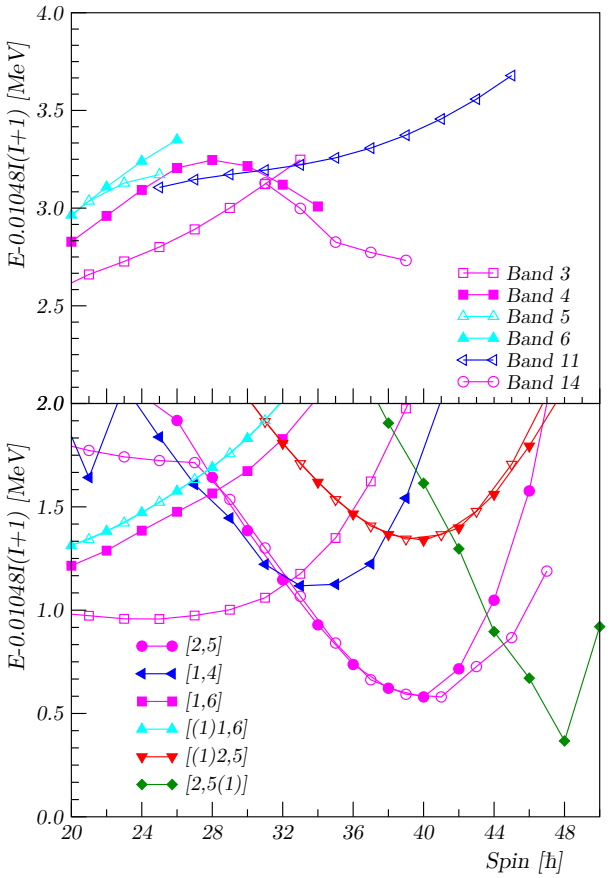

Figure 7.15: *Excitation energy, E, relative to a rigid-rotor reference, $E_{RLD} = \frac{1}{2\mathscr{I}_{rig}} I(I+1)$ where $\frac{1}{2\mathscr{I}_{rig}} \approx 32.32A^{-5/3}$ MeV/$\hbar^2$ [AFLR99], as a function of spin, I, for negative-parity bands in ^{124}Ba. The experimental bands are drawn in the upper panel and are compared with calculated bands using the CNS formalism in the lower panel. Filled and open symbols correspond to signatures α=0 and 1, respectively. For bands 11 and 14 , spins and parity are not firmly determined.*

7.3.3 Branching Ratios

The ratios of reduced magnetic dipole to electric quadrupole transition probabilities, $\frac{B(M1;I\rightarrow I-1)}{B(E2;I\rightarrow I-2)}$, can be used to extract information about the quasi-particle configurations of the coupled bands. The experimental ratios have been obtained from the γ-ray intensity ratios using

$$\frac{B(M1;I\rightarrow I-1)}{B(E2;I\rightarrow I-2)} = 0.697\frac{I_\gamma(M1;I\rightarrow I-1)}{I_\gamma(E2;I\rightarrow I-2)}\frac{E_\gamma^5(E2)}{E_\gamma^3(M1)}\frac{1}{1+\delta^2}\ [\mu_N/\mathrm{eb}]^2, \tag{7.1}$$

where E_γ and I_γ represent the energy in MeV and the intensity of the γ-ray transitions, respectively. The mixing ratio, δ, for the $\Delta I = 1$ transitions is small and δ^2 has been set to zero. The experimentally deduced $\frac{B(M1)}{B(E2)}$ ratios are compared with the theoretical values obtained using the following generalised expression for multi-quasi-particle configurations, formulated in [RAB+92, TJJ+94] and based on the geometrical model of Dönau and Frauendorf [DF82, Dön87]

$$\frac{B(M1;I\rightarrow I-1)}{B(E2;I\rightarrow I-2)} = \frac{12}{5Q_0^2\cos^2(\gamma+30^\circ)}\left[1-\frac{K_{tot}^2}{(I-\frac{1}{2})^2}\right]^{-2}\left\{(I-\frac{K_{tot}^2}{I^2})^{1/2}\left[K_1(g_1-g_R)(1\pm\frac{\Delta e'}{\hbar\omega})\right.\right.$$
$$\left.\left.+\sum_\lambda K_\lambda(g_\lambda-g_R)\right]-\frac{K_{tot}}{I}\left[(g_1-g_R)i_1+\sum_\lambda(g_\lambda-g_R)i_\lambda\right]\right\}^2. \tag{7.2}$$

K_λ, g_λ and i_λ stand for the K-value, gyromagnetic factor and aligned angular momentum, respectively, of the rotation- or Fermi-alinged quasiparticles involved in the configuration. K_1, g_1 and i_1 refer to the strongly coupled particle. The approximation $g_R = Z/A$ was used for the rotational g factor. $K_{tot} = K_1 + \sum_\lambda K_\lambda$ denotes the total K-value of the configuration. The values for the intrinsic g factors for the different orbitals, g_λ, as well as the quadrupole moment, $Q_0 = 3.9\ e.b.$, have been taken from [WJA+91].

The shape parameter γ was set to zero. The aligned angular momenta, i_λ, were determined from the alignment plots, see Fig. 7.16. The signature splitting, $\Delta e'$, was extracted from the experimental Routhians. The parameters used in the calculations are listed in table 7.2.

Bands	Subshell	Nilsson orbital	g-factor	K	$i[\hbar]$
3,4	$\pi h_{11/2}$	$[550]1/2^-$	1.17	0.5	5.0
	$\pi g_{7/2}$	$[422]3/2^+$	0.72	1.5	1.0
	$\pi d_{5/2}$	$[420]1/2^+$	1.38	0.5	1.0
5,6	$\pi h_{11/2}$	$[550]1/2^-$	1.17	0.5	5.0
	$\pi g_{9/2}$	$[404]9/2^+$	1.27	4.5	1.0
12,13	$\pi h_{11/2}$	$[550]1/2^-$	1.17	0.5	5.0
	$\pi d_{5/2}$	$[420]1/2^+$	1.38	0.5	1.0
	$\pi g_{9/2}$	$[404]9/2^+$	1.27	4.5	0.0
	$\nu h_{11/2}$	$[532]5/2^-$	-0.21	2.5	3.5
		$[541]3/2^-$	-0.21	1.5	3.5
	$\nu g_{7/2}$	$[402]5/2^+$	0.21	2.5	0.5
		$[404]7/2^+$	0.21	3.5	0.5
	$\nu d_{5/2}$	$[413]5/2^+$	-0.33	2.5	0.5

Table 7.2: *Parameters used in calculating the $\frac{B(M1)}{B(E2)}$ ratios. Furthermore, we assumed $g_R = Z/A$ and $Q_0 = 3.9$ e.b.*

7.3.4 Alignments, Routhians, Dynamic Moments of Inertia and Excitation Energies

Experimental aligned angular momenta, i_x, dynamic moments of inertia, $\mathcal{J}^{(2)}$, Routhians, e', and excitation energies, E_x, have been extracted from the present data for the observed bands in ^{124}Ba. Figure. 7.16 presents the alignment, i_x, as a function of rotational frequency, ω, for bands 1 to 10, 12 and 13 in ^{124}Ba. The dynamic moments of inertia, $\mathcal{J}^{(2)}$, as a function of rotational frequency, ω, are shown in Fig. 7.17 for all bands in ^{124}Ba. The energies of the aligned nucleon in the rotating frame for bands 1 to 10, 12 and 13 are plotted against rotational frequency, ω, in Fig. 7.18. The excitation energies, E_x, relative to a rigid-rotor reference, $E_{RLD} = \frac{1}{2\mathcal{J}_{rig}} I(I+1)$ where $\frac{1}{2\mathcal{J}_{rig}} \approx 32.32A^{-5/3}$ MeV/$\hbar^2$ [AFLR99], as a function of spin I are shown in Fig. 7.19. The experimental crossing frequencies, ω_c, alignments, i_x, alignment

Table 7.3: *Experimental crossing frequencies, ω_c, aligned angular momenta, i_x, alignment gains, Δi_x, and quasi-particle configurations for the observed bands in ^{124}Ba.*

Band	Config. before crossing	i_x [$\hbar$]	ω_c [MeV/$\hbar$]	Δi_x [$\hbar$]	Config. above 1^{st} crossing	ω_c [MeV/$\hbar$]	Δi_x [$\hbar$]	Config. above 2^{nd} crossing	ω_c [MeV/$\hbar$]	Δi_x [$\hbar$]
1	0-qp	0	0.37	8.2	ef	0.49	3.3	$efEF$	-	-
2	0-qp	0	0.41	6.2	EF	0.44	4.4	$EFef$	0.63	2.5
3	eb	≈ 5.1	0.46	6.0	$ebEF$	-	-	-	-	-
4	ea	5.4	0.44	4.0	$eaGH$	0.59	≈ 6.0	$eaGHEF$	-	-
5	eb'	5.8	0.44	> 6.1	$eb'EF$	-	-	-	-	-
6	ea'	5.8	0.44	> 5.8	$ea'EF$	-	-	-	-	-
7	γ-band	0	-	-	-	-	-	-	-	
8	γ-band	0	-	-	-	-	-	-	-	
9	$efGH$	11	-	-	-	-	-	-	-	-
10	$efFH$	9.5	-	-		-	-	-	-	-
12	$eb'EA'$	8.5	0.52	5.2	$eb'EA'GH$	-	-	-	-	-
13	$eb'FA'$	8.5	0.52	4.9	$eb'FA'GH$	-	-	-	-	-

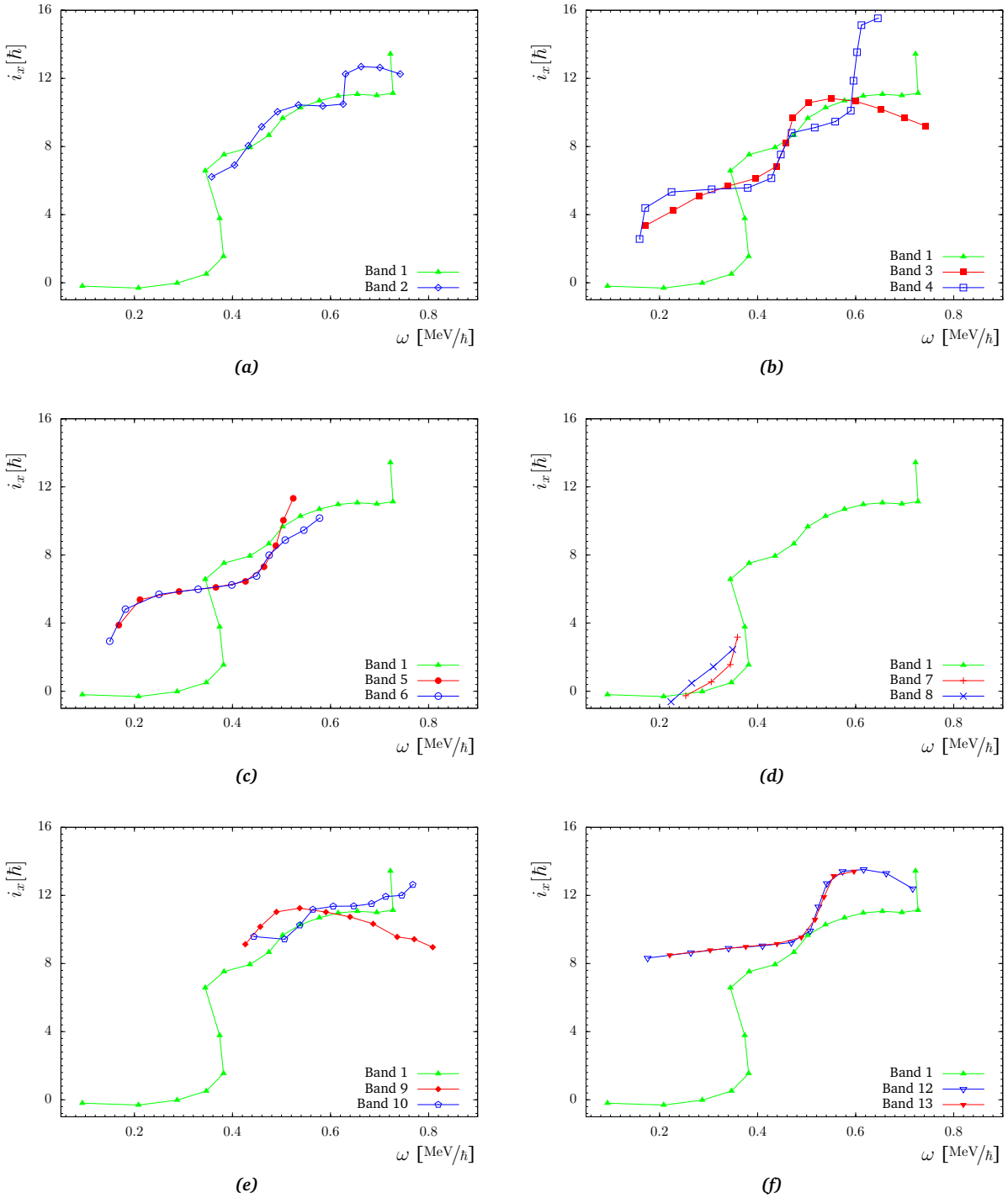

Figure 7.16: *Aligned angular momenta, i_x, as a function of rotational frequency ω for bands 1, 2, 3, 4, 5, 6, 7, 8, 9, 10, 12 and 13 in ^{124}Ba. A reference core with Harris parameters of $\mathscr{J}_0 = 17\ \hbar^2/\mathrm{MeV}$ and $\mathscr{J}_1 = 26\ \hbar^4/\mathrm{MeV}^3$ has been subtracted [AR96].*

gains, Δi_x and assigned quasiparticle configurations are listed in table 7.3.

As can be seen in Fig. 7.16, up to medium frequency, the alignment gain occurs roughly in two separate steps, one at low rotational frequency, around $\omega = 0.37$ MeV/$\hbar$ and another at higher rotational frequency, around $\omega = 0.45$ MeV/$\hbar$. The gain of angular momentum is caused by the decoupling and alignment either of $\pi h^2_{11/2}$ or $\nu h^2_{11/2}$ quasi-particles. The smaller differences in alignment at higher

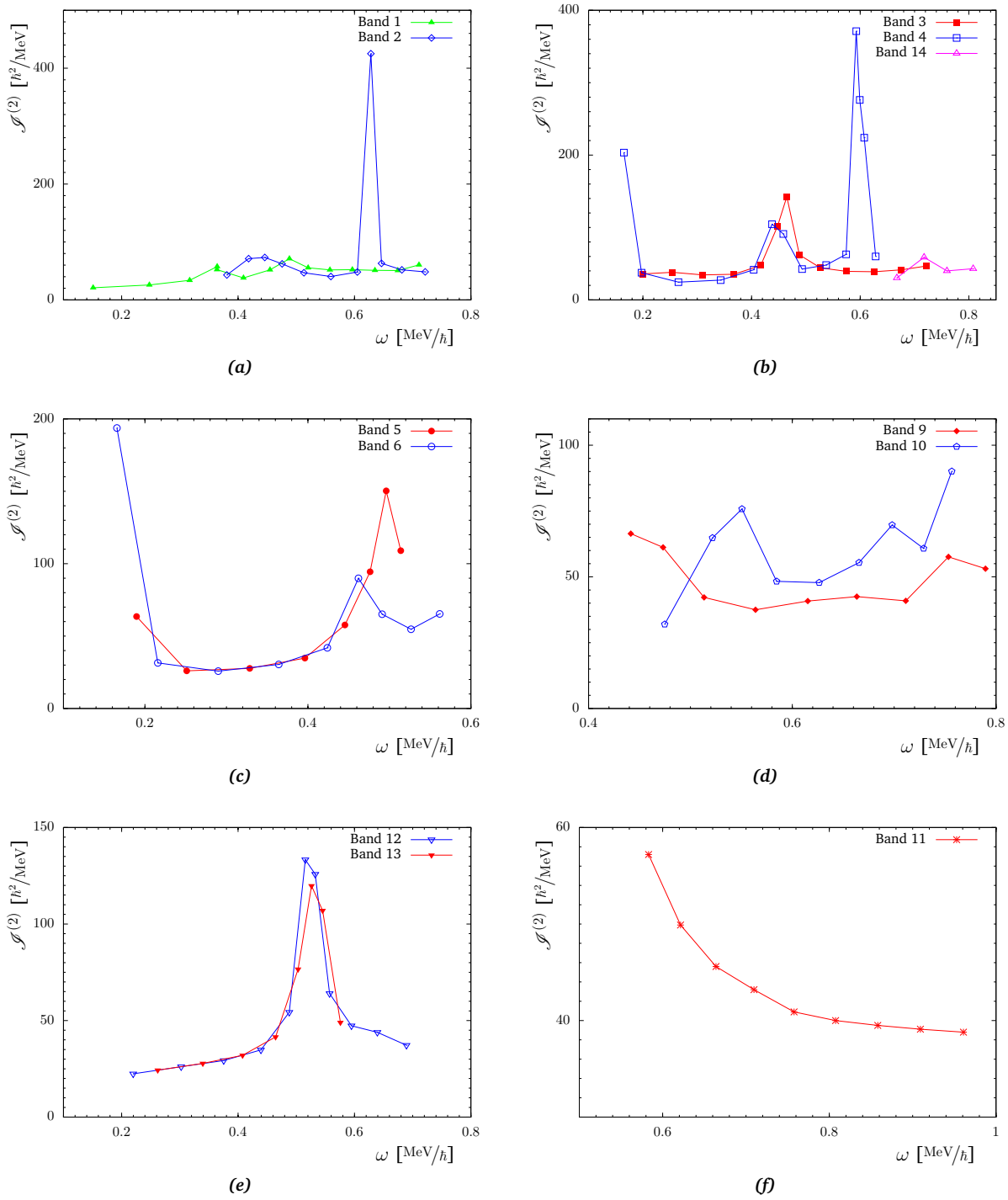

Figure 7.17: *Dynamic moments of inertia, $\mathcal{J}^{(2)}$, versus rotational frequency, ω, for bands in ^{124}Ba.*

frequencies are then caused by different quasi-particles with lower angular momentum j in the configurations. Deformation changes and differences in pairing could also affect the alignments. At the highest observed rotational frequencies, some of the bands exhibit an extra increase in alignment or other irregularities. The structural changes are also visible in the dynamic moments of inertia plots presented in Fig. 7.17.

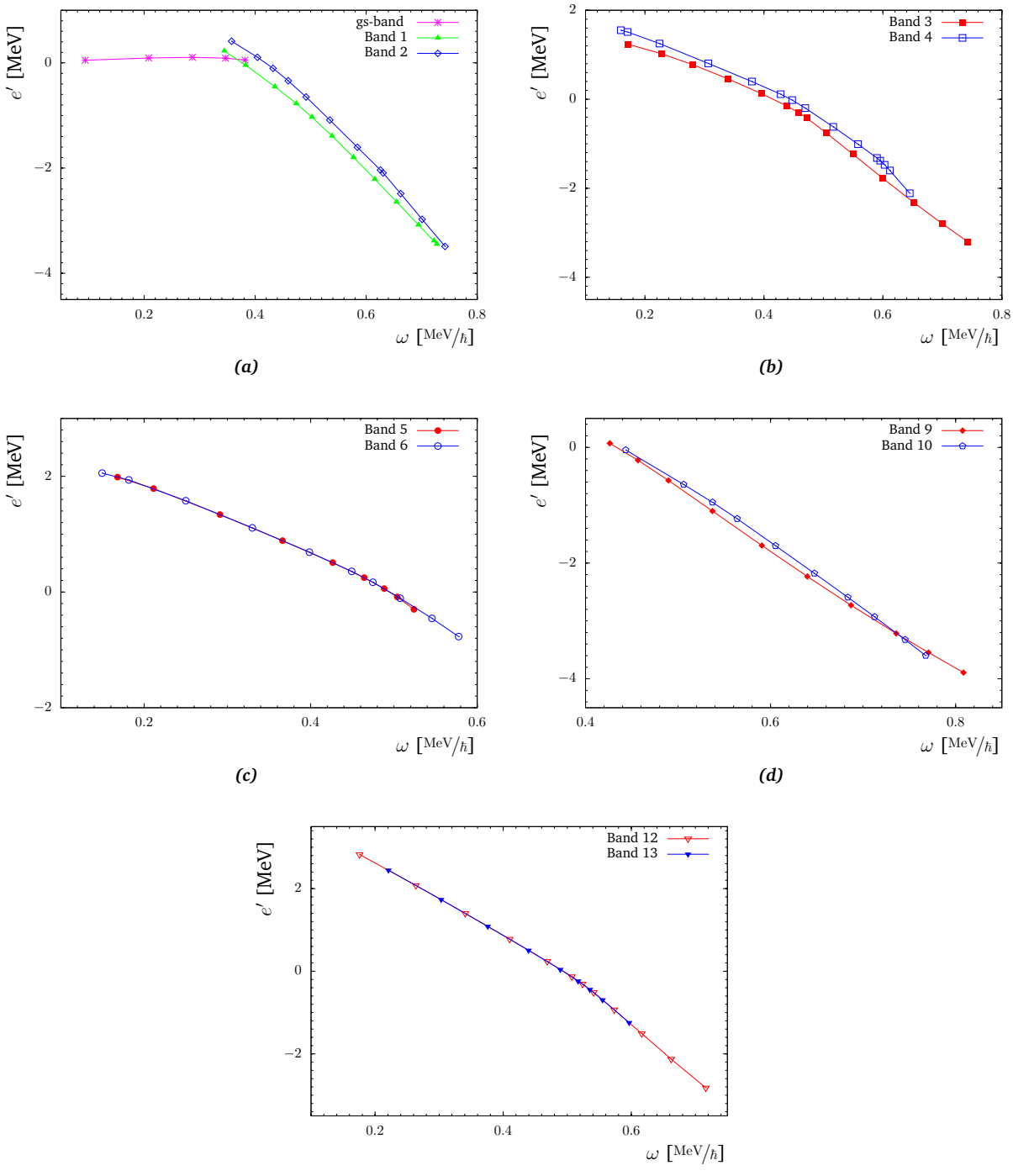

Figure 7.18: *Experimental Routhian, e', (single-particle energies in the rotating frame) versus rotational frequency, ω, for bands 1, 2, 3, 4, 5, 6, 9, 10, 12 and 13 in ^{124}Ba. A reference core with Harris parameters $\mathscr{I}_0 = 17\ \hbar^2/\mathrm{MeV}$ and $\mathscr{I}_1 = 26\ \hbar^4/\mathrm{MeV}^3$ has been subtracted [AR96].*

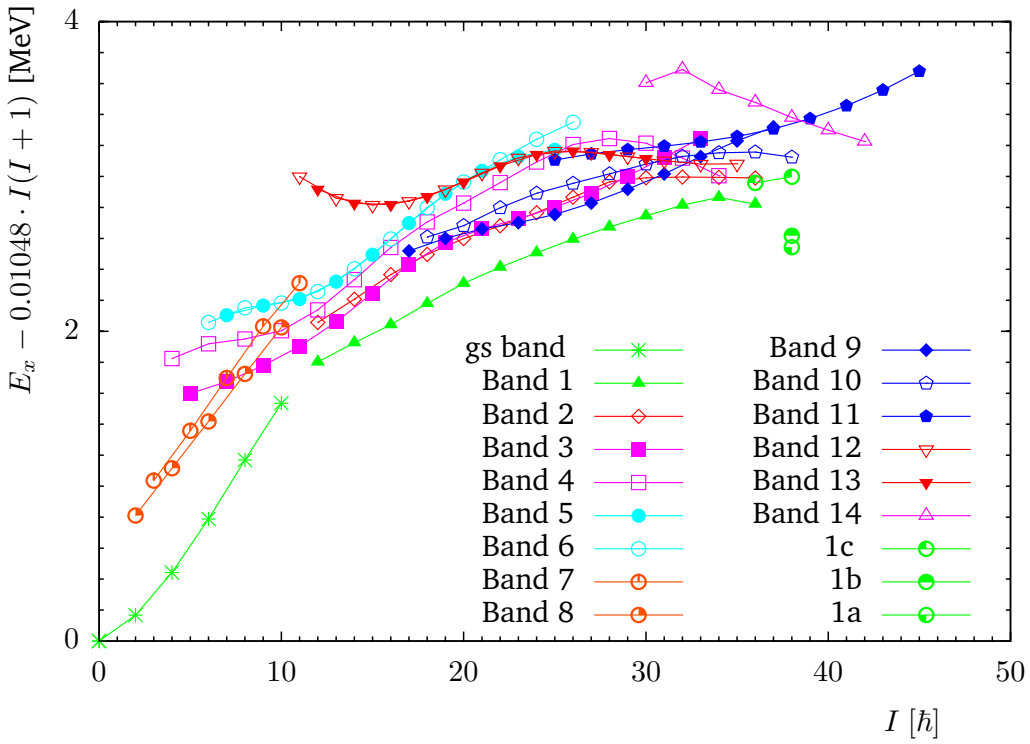

Figure 7.19: *Experimental excitation energies, E_x, relatvie to a rigid-rotor reference energy, $E_{RLD} = \frac{1}{2\mathscr{I}_{rig}} I(I+1)$ where $\frac{1}{2\mathscr{I}_{rig}} \approx 32.32 A^{-5/3}$ MeV/$\hbar^2$ [AFLR99], versus spin I for bands in ^{124}Ba. Spins and parities are uncertain for bands 11 and 14 and for 1a, 1b and 1c.*

7.4 Configuration Assignments

7.4.1 Uncoupled Bands

Band 1 (Yrast Sequence)

The yrast sequence exhibits a back-bend at a rotational frequency of $\omega_c = 0.37$ MeV/$\hbar$ where the ground-state (gs) band is crossed by band 1 (Fig. 7.18(a)) with a large gain in angular momentum, i_x, of $\Delta i_x = 8.2\ \hbar$ (Fig. 7.16(a)). Band 1 undergoes a second band crossing at a rotational frequency of $\omega_c = 0.49$ MeV/$\hbar$ (Fig. 7.18(a)) with a smaller alignment gain of $\Delta i_x = 3.3\ \hbar$ (Fig. 7.16(a)). This is in agreement with the observation by [PFM+90]. The first alignment has been explained as crossing of the gs band with the two-quasi-proton $h_{11/2}$, ef, band and the second alignment gain has been attributed to a pair of rotationally aligned $h_{11/2}$ quasi-neutrons , EF, [PFM+90]. Thus, the configuration of band 1 changes as 0-qp $\rightarrow \pi h^2_{11/2}(ef) \rightarrow \pi h^2_{11/2} \otimes \nu h^2_{11/2}(efEF)$.

As can be seen in Fig. 7.14, the CNS calculations predict the [2,6] $(\pi h^2_{11/2} \otimes \nu h^6_{11/2})$ configuration to be yrast above spin $I = 28$ until it is crossed by the steeply down-sloping [2,4] $(\pi h^2_{11/2} \otimes \nu h^4_{11/2})$ configuration. The [(2)2,6] $(\pi[(g^{-2}_{9/2})h^2_{11/2}] \otimes \nu h^6_{11/2})$ configuration is predicted to be lower than the [2,6] structure at lower spins, see Fig. 7.14. The difference between the [2,6] and [(2)2,6] configurations may be explained by two reasons. It is very likely that the calculated relative positions of the [2,6] and [(2)2,6] configurations depend on the Nilsson parameters where there is some uncertainty in their relative positions. Indeed, in the neighbouring ^{123}Cs nucleus, CNS calculations also predicted the [(2)2,6] below the [2,6] configuration in that spin region, while the observed alignment frequency favours the [2,6] assignment [SHD+04]. The discrepancy may also be due to remains of pairing at high spins. If pairing is not negligible, [2,6] is a four-quasi-particle configuration but [(2)2,6] is a six-quasi-particle configuration. The additional energy necessary to break a pair to form a six-quasi-particle excitation may lift the [(2)2,6] configuration in reality to higher energy than predicted by the CNS calculations which

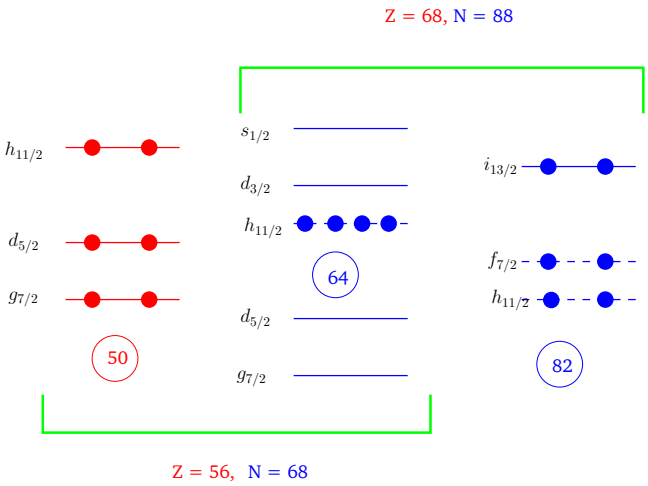

Figure 7.20: *Schematic demonstration of the analogy between the A=125 and 160 mass regions: filling of sub-shells in configurations with a few particles outside ^{114}Sn and ^{146}Gd cores. It was pointed out [RXBR86] that ^{124}Ba with 68 neutrons is analogous to ^{156}Er with 68 protons, and six valence protons in ^{124}Ba compared to six valence neutrons in ^{156}Er. A combination of the Z = 56 structure (left) with the N = 68 structure (middle) gives a configuration for ^{124}Ba with $I_{max} = 36^+$, while combining the Z = 68 proton structure (middle) with the N = 88 neutron structure (right) corresponds to the terminating state at $I = 42^+$ [RB85].*

neglect pairing. Therefore, band 1 very likely corresponds to the [2,6] $(\pi h_{11/2}^2 \otimes \nu h_{11/2}^6)$ configuration in the spin region of 22–34 $\hbar$, with shape parameters $\varepsilon_2 \simeq 0.24$ and $\gamma \simeq 0^\circ$, in agreement with the previous assignments [PFM+90].

Band 1 undergoes a structure change above the $I^\pi = 34$ level, see Fig. 7.1, where it forks into three branches. The appearance of irregular structures on top of a rotational band at high spins indicates that the rotational band loses collectivity, and single-particle alignments are favoured as an efficient way to generate angular momentum (band termination). Terminating bands have first been established in the the Dy-Er region [AR95]. However, it has been shown [RXBR86] that there are analogies between the A = 160 and 125 mass regions as illustrated in Fig. 7.20. The four protons in the $h_{11/2}$ sub-shell outside the Z = 64 core in ^{156}Er can be compared to four neutrons in the $h_{11/2}$ sub-shell in ^{124}Ba, which has N = 68 neutrons. Furthermore, six protons outside the Z = 50 closed core in ^{124}Ba is analogous to six neutrons above the N = 82 closed core in ^{156}Er. Therefore, the observed fully aligned configuration $\pi(h_{11/2})^4_{16} \otimes \nu[(h_{9/2})^2_8(f_{7/2})^2_6(i_{13/2})^2_{12}]$ of the $I^\pi = 42^+$ state in ^{156}Er is analogous to the configuration $\pi[(h_{11/2})^2_{10}(g_{7/2}d_{5/2})^4_{10}] \otimes \nu(h_{11/2})^4_{16}$ with $I = 36^+$ in ^{124}Ba. Indeed, the expectations based on this analogy are in a good agreement with the present CNS calculations.

As can be seen in Fig. 7.14, it can be distinguished between three types of states of [2,4] configuration defined above. The configuration [2,4]a indicates the states with only four valence neutrons, all located in the $h_{11/2}$ sub-shell relative to the N = 64 core, while [2,4]b and [2,4]c denote the states where one neutron and two neutrons, respectively, are excited from the $d_{5/2}g_{7/2}$ sub-shell to the $s_{1/2}d_{3/2}$ orbitals. The CNS calculation predicts the [2,4]a configuration to become yrast around $I^\pi = 34^+$ and to terminate at $I^\pi = 36^+$ in a strongly favoured state. Also, two favoured states at $I^\pi = 38^+$ and two favoured states at $I^\pi = 40^+$ are predicted corresponding to the [2,4]b and [2,4]c configurations. Two 36^+ states and three 38^+ states have been experimentally observed, see Fig. 7.1. However, in Fig. 7.14 a comparison of the relative positions of the calculated bands with different configurations with the relative positions of the experimental bands shows that the fully aligned calculated terminating configuration [2,4]a $(\pi[(h_{11/2})^2_{10}(g_{7/2}d_{5/2})^4_{10}] \otimes \nu(h_{11/2})^4_{16})$ can be considered as the most likely candidate for the $I^\pi = 36^+$ yrast state. This is a non-collective state characterised by the shape parameters $\varepsilon \approx 0.2$ and $\gamma = 60^\circ$. Its angular momentum is built entirely from the maximal aligned angular momenta of the valance nucleons of the [2,4]a configuration. In Fig. 7.14 two higher-energy nearly degenerate 36^+ states can be seen in the experimental data. According to their relative position, they possibly correspond to the [2,6] and [2,4]b configuration, respectively. Similarly, the [2,4]b and [2,4]c configurations may be assigned to the lowest strongly favoured 38^+ states and the [2,6] configuration to the highest-energy 38^+ state. The 38^+ states belonging to the the [2,4]b and [2,4]c configurations are partially aligned, and they are expected to terminate at spins 44 and 40, respectively, see Fig. 7.14.

An additional argument which supports our configuration assignment comes from the nucleus ^{123}Cs where a terminating state has been observed at $I^\pi = {}^{63}/_2{}^-$ associated with the [1,4] configuration [SHD+04]. The calculated [2,4] structure in ^{124}Ba is very similar to the calculated [1,4] structure in ^{123}Cs, but with an extra $h_{11/2}$ proton. Thus, the 36^+ state in ^{124}Ba is analogous to the $I^\pi = {}^{63}/_2{}^-$ terminating state in ^{123}Cs. As pointed out in [SHD+04], the states around this spin in ^{123}Cs are attributed

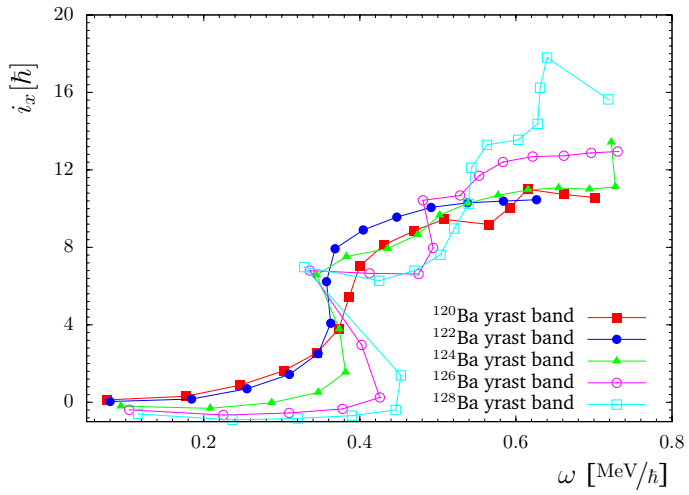

Figure 7.21: *Aligned spins, i_x, as a function of rotational frequency, ω, for the yrast bands in ^{120}Ba [SCF+00], ^{122}Ba [PBB+01], ^{124}Ba [AKSH+06], ^{126}Ba [WJA+91] and ^{128}Ba [VCD+99]. A reference core with Harris parameters $\mathcal{J}_0 = 17\ ^{\hbar^2}/_{\mathrm{MeV}}$ and $\mathcal{J}_1 = 26\ ^{\hbar^4}/_{\mathrm{MeV}^3}$ has been subtracted [AR96].*

to energy minima in the potential energy surface related to zero, one and two particle-hole excitations from neutron $(d_{5/2}g_{7/2})$ to $(s_{1/2}d_{3/2})$ orbitals. The calculations for ^{124}Ba also show the existence of these minima around spin $I = 36$.

The alignments of the yrast bands in ^{120,122,124,126,128}Ba are compared in Fig. 7.21. The rotational crossing frequencies, ω_c, and aligned quasi-particles are listed in table 7.4. It can be seen in Fig. 7.21 that the crossing frequency, ω_c, increases slightly with increasing neutron number and the back-bends become stronger. The first crossing has been attributed to rotationally aligned quasi-protons $h^2_{11/2}$. Except for the yrast band in ^{122}Ba, all bands undergo a second crossing which has been interpreted as an alignment of $h^2_{11/2}$ quasi-neutrons. The yrast bands in ^{126,128}Ba exhibit a third crossing which is not seen in the lighter isotopes. It has been interpreted as an alignment of a $g_{7/2}$ quasi-proton pair in ^{126}Ba [WJA+91] and to a $\nu h_{11/2}$ quasi-neutron pair in ^{128}Ba [VCD+99].

Table 7.4: *Experimental crossing frequencies, ω_c and aligned quasi-particles (qp) for the yrast bands in ^{120,122,124,126,128}Ba. $\omega_{c_1}, \omega_{c_2}$ and ω_{c_3} indicate the first, second and third crossing frequency, respectively.*

Isotope	ω_{c_1} [MeV/$\hbar$]	Aligned qp	ω_{c_2} [MeV/$\hbar$]	Aligned qp	ω_{c_3} [MeV/$\hbar$]	Aligned qp	Reference
^{120}Ba	0.38	$\pi h^2_{11/2}$	0.52	$\nu h^2_{11/2}$	-	-	[SCF+00]
^{122}Ba	0.36	$\pi h^2_{11/2}$	-	-	-	-	[PBB+01]
^{124}Ba	0.37	$\pi h^2_{11/2}$	0.49	$\nu h^2_{11/2}$	-	-	[AKSH+06]
^{126}Ba	0.39	$\pi h^2_{11/2}$	0.49	$\nu h^2_{11/2}$	0.56	$\pi g^2_{7/2}$	[WJA+91]
^{128}Ba	0.41	$\pi h^2_{11/2}$	0.54	$\nu h^2_{11/2}$	0.63	$\nu h^2_{11/2}$	[VCD+99]

Band 2

The gs band is crossed by band 2 at a rotational frequency of $\omega_c = 0.41$ MeV/$\hbar$, see Fig. 7.18(a), with an alignment gain of 6.2 $\hbar$, see Fig. 7.16(a). This has been interpreted as the alignment of a $\nu h_{11/2}$ quasi-neutron pair, EF, [PFM+90]. The band undergoes a second crossing at a rotational frequency of $\omega_c = 0.44$ MeV/$\hbar$ gaining 4.4 $\hbar$ of angular momentum, see Figs. 7.18(a) and 7.16(a). The second crossing at $\omega = 0.44$ MeV/$\hbar$ has been attributed to the decoupling of two-quasi-protons ef, of $\pi h^2_{11/2}$ origin where the configuration changes from a two-quasi-neutron $\nu h^2_{11/2}$ to the two-quasi-neutron-two-quasi-proton $(\nu h^2_{11/2} \otimes \pi h^2_{11/2})$ structure, $EFef$ [PFM+90]. In this frequency range, the configuration of band 2 is the same as in band 1. However, in band 1 the $\pi h^2_{11/2}$ quasi-protons are nearly fully aligned ($\Delta i_x = 8.2\ \hbar$) and the $\nu h^2_{11/2}$ quasi-neutrons exhibit a smaller alignment ($\Delta i_x = 3.3\ \hbar$), but in band 2 it is opposite: the

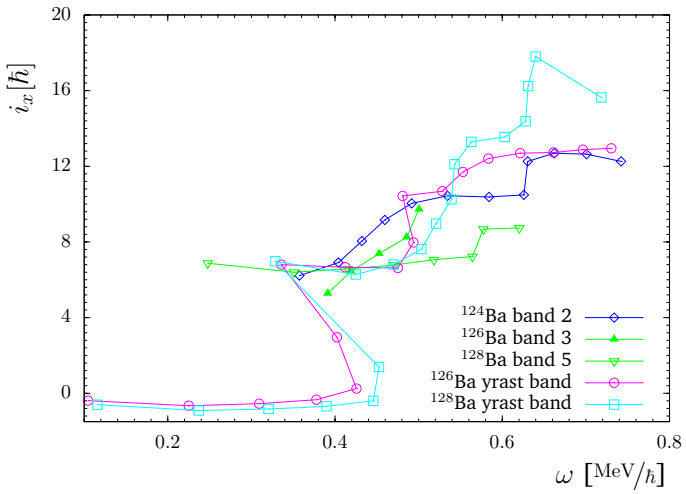

Figure 7.22: *Aligned spins, i_x, as a function of rotational frequency, ω, for band 2 in ^{124}Ba [AKSH+06], for band 3 and yrast band in ^{126}Ba [WJA+91] and for band 5 and yrast band ^{128}Ba [VCD+99]. A reference core with Harris parameters $\mathscr{I}_0 = 17\ \hbar^2/\mathrm{MeV}$ and $\mathscr{I}_1 = 26\ \hbar^4/\mathrm{MeV}^3$ has been subtracted [AR96].*

$\nu h^2_{11/2}$ quasi-neutrons are almost fully aligned ($\Delta i_x \approx 6.2\ \hbar$) and the $\pi h^2_{11/2}$ quasi-protons are partially aligned ($\Delta i_x = 4.4\ \hbar$).

Band 2 shows a third alignment gain of, $\Delta i_x = 2.5\ \hbar$, at $\omega_c = 0.63\ \mathrm{MeV}/\hbar$, see Figs. 7.18(a) and 7.16(a), which is not observed in band 1. A similar behaviour has been seen in the yrast bands of the neighbouring even-even nuclei ^{126}Ba [WJA+91] and ^{128}Ba [VCD+99] at a rotational frequency of $\omega_c = 0.56$ and 0.63 $\mathrm{MeV}/\hbar$ with angular momentum gains of ≈ 2 and $\approx 4\ \hbar$, respectively, as shown in Fig. 7.22. The crossing was attributed to the alignment of a $g_{7/2}$ quasi-proton pair in ^{126}Ba [WJA+91] and to a $\nu h_{11/2}$ quasi-neutron pair in ^{128}Ba [VCD+99]. These are alternative explanations for the behaviour of band 2 at high spins in ^{124}Ba.

Within the framework of CNS formalism, the calculated configurations above the first two band crossings in bands 1 and 2 are the same, i.e., both are represented by a pair of aligned $h_{11/2}$ neutrons and $h_{11/2}$ protons, though with a different distribution of the valence nucleons in the low-j orbitals. Indeed, a second minimum shows up in the calculations with deformation parameters $\varepsilon \approx 0.24$ and $\gamma \approx$ -30°. The related configuration is denoted [2,6]* in Fig. 7.14. With increasing spin, this minimum becomes more and more shallow and vanishes above spin 34. Moreover, the calculated relative energy difference between the first and second minimum does not agree well with that observed for bands 1 and 2. At spin $I = 22$, both the calculated and experimental energy differences are ≈ 250 keV. The calculation predicts the difference to increase with increasing spin up to ≈ 700 keV, while experimentally it is constant up to $I = 28$ and smoothly goes down above this spin to about 30 keV. This behaviour indicates a structure change around spin 28. Looking at Fig. 7.14, the [2,4]b structure can be a possible candidate for the configuration above spin 28 which is predicted to cross the [2,6] configuration at spin 36.

Bands 9 and 10

The new sequences 9 and 10 are built upon the $I^\pi = 17^+$ and $I^\pi = 18^+$, levels, respectively. Both bands decay into band 1 suggesting a similarity in structure. They start at high angular momentum with alignments of $i_x = 11$ and 9.5 $\hbar$, respectively (Fig. 7.16(e)). At higher spins, the bands show different alignment patterns. While the angular momentum of band 9 decreases, band 10 gradually gains angular momentum up to the highest-spin states observed. The quite large alignments suggest four-quasi-particle configurations for both bands. Thus, the $efGH$ and $efFH$ ($\pi h^2_{11/2} \otimes \nu h^2_{11/2}$) configurations were assigned tentatively to bands 9 and 10, respectively. The different alignments may be due to differences in the reference core. Band 9 shows a constant alignment when reducing the Harris parameters to $\mathscr{I}_0 = 13\ \hbar^2/\mathrm{MeV}$ and $\mathscr{I}_1 = 21\ \hbar^4/\mathrm{MeV}^3$.

The alignments and dynamic moments of inertia for bands 9 and 10 are compared to band 1 in ^{126}Ce [PBB+03], in Figs. 7.23 and 7.24, respectively. The upper part of band 1 in ^{126}Ce is similar to bands 9 and 10. Band 1 in ^{126}Ce is associated with the $efEF$ [PBB+03] configuration which supports our configuration assignment for bands 9 and 10.

In Fig. 7.14, it is shown that the calculated [1,5] CNS configuration could reproduce the observed properties reasonably well. However, it seems not likely that bands 9 and 10 are signature partners since

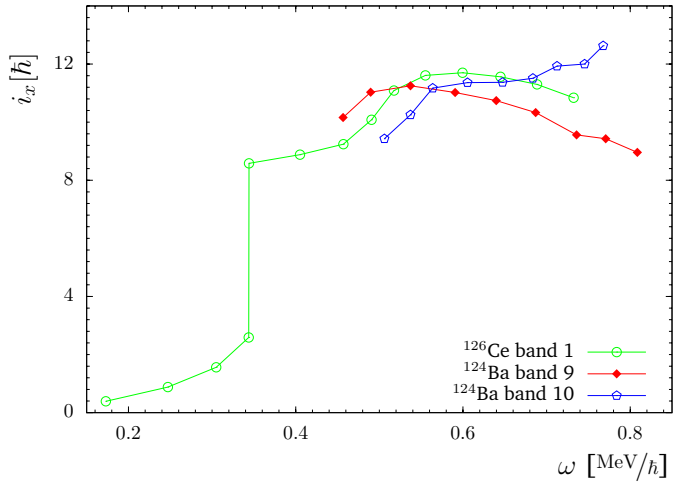

Figure 7.23: *Aligned angular momentum, i_x, as a function of rotational frequency, ω, for bands 9 and 10 in ^{124}Ba compared to band 1 in ^{126}Ce [PBB+03].*

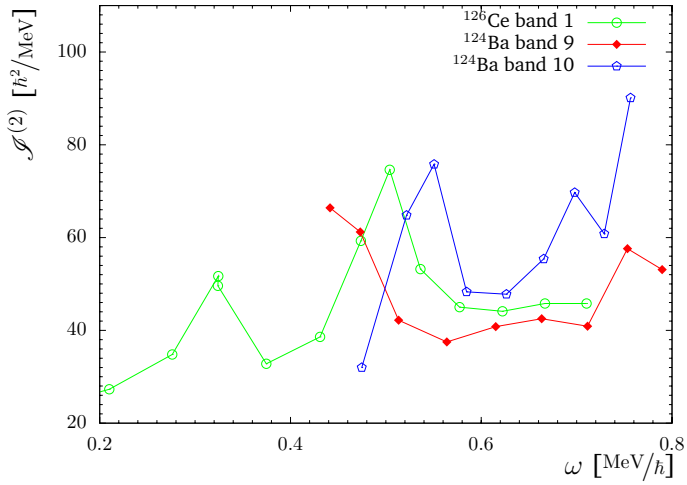

Figure 7.24: *Dynamic moment of inertia, $\mathcal{J}^{(2)}$, as a function of rotational frequency, ω, for bands 9 and 10 in ^{124}Ba compared to band 1 in ^{126}Ce [PBB+03].*

no inter-band transitions are observed. Moreover, the [1,5] configuration is assigned tentatively to bands 12 and 13, see section 7.4.2. Consequently, there are no good candidates predicted by the present CNS calculations for the configurations of these bands.

Band 11

Band 11 is the most interesting band observed in this data. It is not firmly connected to known levels in ^{124}Ba. Hence, its spin assignment is tentative. However, the systematics of excitation energies and spins of the bands observed in this nucleus permit an approximate placement in the level scheme and limit the spin range.

Band 11 decays into high-spin states in band 1 which means that their structures should have some similarities. According to our tentative spin assignment, it is observed only above spin 25 or 26 and extends up to spin 45 or 46 without showing any band crossing. The experimental dynamic moment of inertia, $\mathcal{J}^{(2)}$, of band 11 is decreasing gradually with increasing rotational frequency, see Fig. 7.17(f).

The behaviour of band 11 is similar to several high-spin bands seen in this mass region. Figure. 7.25 shows a comparison of the dynamic moment of inertia, $\mathcal{J}^{(2)}$, for band 11 in ^{124}Ba and for similar bands in ^{132}Ce [NKL+85, CLF+96, PCA+05] and ^{126}Xe [RHSH+07]. The ^{132}Ce SD1 band is highly deformed [PCA+05] with a transition quadrupole moment Q_t = 7.4(3) b [CLF+96]. For band a in ^{126}Xe the transition quadrupole moment has been estimated to be $Q_t \simeq$ 5.2 b [RHSH+07].

As can be seen in Fig. 7.25, the dynamic moment of inertia of band 11 lies between those of ^{126}Xe and ^{132}Ce. Therefore, it can be concluded that band 11 may have a larger deformation than the other bands in ^{124}Ba. The configuration $\pi(g_{7/2}^2 h_{11/2}^2) \otimes \nu(i_{13/2} h_{11/2})$ was proposed for band a in ^{126}Xe [RHSH+07]. The

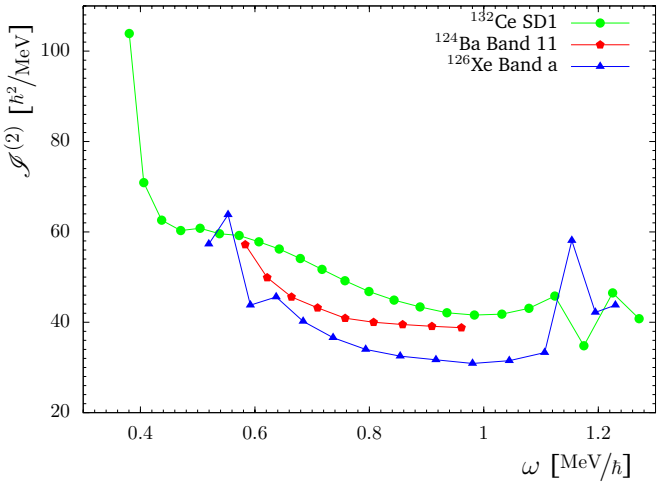

Figure 7.25: *Dynamic moments of inertia, $\mathscr{J}^{(2)}$, for band 11 in ^{124}Ba, the SD1 band in ^{132}Ce and band a in ^{126}Xe plotted as a function of rotational frequency, ω.*

excitation of an $i_{13/2}$ neutron may cause the larger deformation. However, a lifetime measurement is required for a final proof. The most likely candidate from the CNS calculations is the [2,5(1)] ($\pi h^2_{11/2} \otimes \nu h^5_{11/2} i_{13/2}$) configuration.

CSM calculations for ^{132}Ce show that the frequency dependence of the dynamic moment of inertia is a combined effect of gradual alignment of protons in $h_{11/2}$ and neutrons in $h_{9/2}$ and $h_{11/2}$ orbitals [WNJ+88]; a similar interpretation may apply also to band 11 in ^{124}Ba.

Band 14

Band 14 feeds band 3 around spin $I = 30$. Due to lack of statistics, its spin and parity are not firmly determined. If our tentative spin assignment is correct, band 14 has an alignment of $i_x \approx 5\ \hbar$ higher than that of band 3. This may be explained by a six-quasi-particle configuration.

7.4.2 Coupled Bands

Bands 3 and 4

The lowest-energy negative-parity sequences 3 and 4 form a pair of signature-partner bands with a large signature splitting, $\Delta\acute{e}$, see Fig. 7.18(b). Band 3 (the favoured signature), with $(\pi, \alpha) = (-, 1)$ may be associated with the eb ($\pi h_{11/2} g_{7/2}$) two-quasi-proton configuration while band 4 (the unfavoured signature), with $(\pi, \alpha) = (-, 1)$ may be associated with the ea or ec ($\pi h_{11/2}(g_{7/2}, d_{5/2})$) configurations [PFM+90]. Experimental $\frac{B(M1;I\rightarrow I-1)}{B(E2;I\rightarrow I-2)}$ ratios of reduced transition probabilities have been extracted for bands 3 and 4 from measured $\frac{I_\gamma(M1;I\rightarrow I-1)}{I_\gamma(E2;I\rightarrow I-2)}$ γ-ray intensity branching ratios and are plotted in Fig 7.26 together with the theoretical values for the $\pi h_{11/2} g_{7/2}$ and $\pi h_{11/2} d_{5/2}$ configurations. It is evident that the calculated ratios for the $\pi h_{11/2} d_{5/2}$ configuration agree better with the experimental points than those for the $\pi h_{11/2} g_{7/2}$ configuration. Thus, the $\pi h_{11/2} d_{5/2}$ configuration was assigned to bands 3 and 4 in the low-spin region. At higher spins, these configurations are expected to become more and more mixed. Bands 3 and 4 exhibit a band crossing at a rotational frequency of $\omega_c \approx 0.45$ MeV/$\hbar$ (Fig. 7.18(b)) with an alignment gain of $\Delta i_x = 4$ and 6 $\hbar$, respectively. The rather large gain in angular momentum indicates the involvement of $h_{11/2}$ neutrons or protons in the configurations above the crossing frequency. Accordingly, the $ebEF$ ($\pi h_{11/2}(d_{5/2}, g_{7/2}) \otimes \nu h^2_{11/2}$) and $eaGH$ ($\pi h_{11/2}(d_{5/2}, g_{7/2}) \otimes \nu h^2_{11/2}$) configurations were proposed for band 3 and 4, respectively, in the frequency range around 0.50 MeV/$\hbar$. Similar bands have previously been established in ^{126}Ba and ^{128}Ba associated with the configurations $\pi(h_{11/2} g_{7/2}) \otimes \nu h^2_{11/2}$ and $\pi(h_{11/2} g_{7/2}) \otimes \nu h^4_{11/2}$, respectively, [WJA+91, VCD+99]. It was proposed [WJL+89, PL91, MBB+05] that those bands built upon the two-quasi-proton structure are mixed with the octupole vibrational band which causes the large signature splitting at low spins.

Alignment plots for the yrast negative-parity bands in ^{124,126,128}Ba are presented in Fig. 7.27. It can bee seen that band 3 in ^{124}Ba and band 7 in ^{126}Ba are very similar. They exhibit a single crossing at

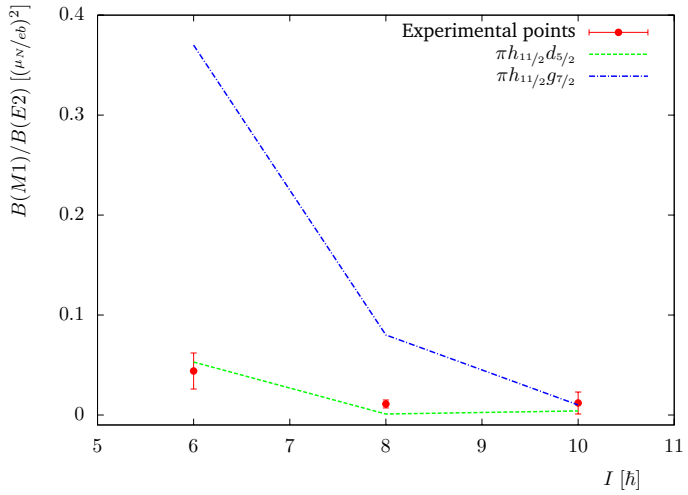

Figure 7.26: *Experimental $\frac{B(M1;I\rightarrow I-1)}{B(E2;I\rightarrow I-2)}$ ratios of reduced transition probabilities (solid points) for bands 3 and 4 and calculated values for the $\pi h_{11/2}d_{5/2}$ (dashed line) and $\pi h_{11/2}g_{7/2}$ (dot-dashed line) configurations.*

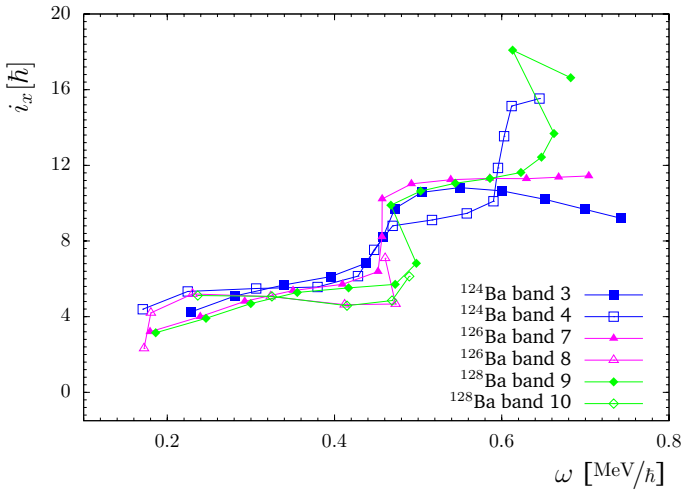

Figure 7.27: *Alignments, i_x, as a function of rotational frequency, ω, for bands 3 and 4 in ^{124}Ba, bands 7 and 8 in ^{126}Ba [WJA+91] and bands 9 and 10 in ^{128}Ba [VCD+99]. A reference core with Harris parameters $\mathcal{J}_0 = 17\ \hbar^2/\mathrm{MeV}$ and $\mathcal{J}_1 = 26\ \hbar^4/\mathrm{MeV}^3$ has been subtracted [AR96]. The filled symbols corresponds to signature $\alpha = 1$ and open symbols to $\alpha = 0$.*

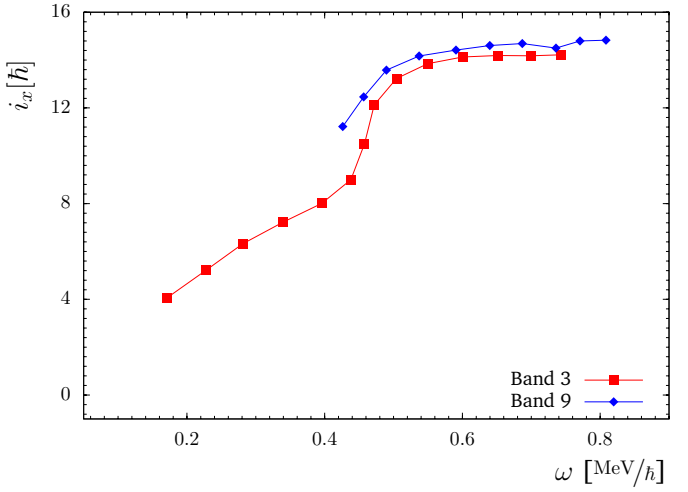

Figure 7.28: *Aligned angular momentum, i_x, as a function of rotational frequency,ω, for bands 3 and 9 in ^{124}Ba calculated with the Harris parameters $\mathcal{J}_0 = 13\ \hbar^2/\mathrm{MeV}$ and $\mathcal{J}_1 = 21\ \hbar^4/\mathrm{MeV}^3$*

the same rotational frequency of $\omega_c = 0.46\ ^{\mathrm{MeV}}/_{\hbar}$. Band 9 in ^{128}Ba shows the first crossing at a slightly higher frequency, $\omega_c = 0.48\ ^{\mathrm{MeV}}/_{\hbar}$ [VCD+99]. A second crossing takes place around $\omega_c = 0.63\ ^{\mathrm{MeV}}/_{\hbar}$ with a gain in alignment of about 4 $\hbar$ which has been attributed to an additional rotationally aligned quasi-neutron pair $\nu h^2_{11/2}$. At higher rotational frequencies ($> 0.6\ ^{\mathrm{MeV}}/_{\hbar}$), the angular momentum of band 3 is decreasing with increasing rotational frequency (Fig. 7.16(b)). A change to a reference core

with a smaller deformation may be responsible for that. A reduction of the Harris parameters to $\mathscr{I}_0 = 13\ \hbar^2/\mathrm{MeV}$ and $\mathscr{I}_1 = 21\ \hbar^4/\mathrm{MeV}^3$ results in a constant alignment for band 3, see Fig. 7.28.

A second alignment gain of $\Delta i_x \approx 6\ \hbar$ at a rotational frequency of $\omega_c = 0.59\ \mathrm{MeV}/\hbar$ is observed in band 4 (Fig. 7.16(b)). Such a large gain in angular momentum can only be achieved by a $h_{11/2}$ neutron or proton alignment. Band 3 does not show a similar increase at that frequency. Therefore, the corresponding alignment has to be blocked. It is most likely that it is caused by a pair of $h_{11/2}$ neutrons, e.g., EF, which are already aligned in band 3 at this frequency. Therefore, the $egGHEF$ $(\pi h_{11/2}(d_{5/2}, g_{7/2}) \otimes \nu h^4_{11/2})$ configuration is proposed for band 4 at the highest observed frequencies.

The CNS calculation suggest the [1,6] configuration at high spins. As shown in Fig 7.15, there is good agreement for the relative positions and slopes between the calculated [1,6] structures and the observed bands 3 and 4 up to spin 26.

Bands 5 and 6

The strongly coupled structures 5 and 6 form a pair of signature-partner bands with negligible signature splitting (Fig. 7.18(c)). Therefore, the eb' and $ea'(\pi g_{9/2} h_{11/2})$ proton configurations have been proposed for these bands [PFM+90]. The bands start with an alignment of $i_x = 5.8\ \hbar$ and they show an up-bending at a rotational frequency of $\omega_c = 0.44\ \mathrm{MeV}/\hbar$ with an alignment gain of $\Delta i_x > 6.1$ and $> 5.8\ \hbar$, for bands 5 and 6, respectively, (Fig. 7.16(c)). The up-bending is probably due to the engagement of a pair of rotationally aligned $\nu h^2_{11/2}(EF)$ quasi-neutrons. Therefore, the configurations $eb'EF$ and $ea'EF(\pi g_{9/2} h_{11/2} \otimes \nu h^2_{11/2})$ may be assigned to the high-spin part of bands 5 and 6.

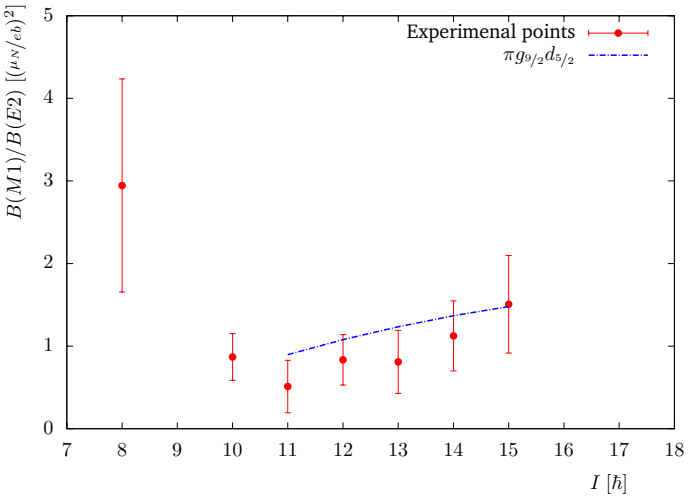

Figure 7.29: *Experimental $\frac{B(M1;I\to I-1)}{B(E2;I\to I-2)}$ ratios of reduced transition probabilities (solid points) for bands 5 and 6 and calculated values for the $\pi g_{9/2} h_{11/2}$ (dot-dashed line) configuration.*

Figure. 7.29 shows the experimental $\frac{B(M1;I\to I-1)}{B(E2;I\to I-2)}$ ratios obtained from this data and the calculated values for the $\pi g_{9/2} h_{11/2}$ configuration. At lower spin (8–10) rather large $\frac{B(M1)}{B(E2)}$ values have been determined. The experimental $\frac{B(M1)}{B(E2)}$ ratio for the $I^\pi = 9^-$ level could not be determined because of the strong 421.1 keV transition which comes in coincidence with the 419.2 keV γ ray. In this mass region, it has been observed, e.g. [WJA+91], that levels with the same spin and parity can mix. Such mixing may be responsible for the observed decay-out transitions in the lower part of band 5, see Fig 7.1. Moreover, large $\frac{B(M1)}{B(E2)}$ ratios are calculated for neutron configurations, e.g., for the $\nu h_{11/2} g_{7/2}$ or $\nu h_{11/2} s_{1/2}$ configurations. The increase of the $\frac{B(M1)}{B(E2)}$ ratios close to the bottom of bands 5 and 6 may be explained by mixing with these neutron configurations. The good agreement at medium spins corroborates the previous configuration assignment [PFM+90] which corresponds to the [(1)1,6] CNS configuration. As can be seen in Fig. 7.15, the theoretically predicted relative positions and slopes of the [(1)1,6] configuration agree with those of bands 5 and 6.

Bands 7 and 8

Bands 7 and 8 have been explained to be built on a γ-vibration [MBES+88, KHS+89]. No further information could be obtained from the present data.

Bands 12 and 13

The new coupled bands 12 and 13 exhibit no signature splitting (Fig. 7.18(e)). They start at rather high angular momentum with an alignment of $i_x = 8.5\ \hbar$ at low rotational frequency which indicates of possible multiquasiparticle configuration. Fig. 7.30 shows a comparison of the experimental $\frac{B(M1;I\rightarrow I-1)}{B(E2;I\rightarrow I-2)}$ ratios determined from our data with the theoretical values for three different configurations, $\pi(g_{9/2}h_{11/2})\otimes\nu(d_{5/2}h_{11/2})$, $\pi(g_{9/2}h_{11/2})\otimes\nu(g_{7/2}h_{11/2})$ and $\pi(d_{5/2}h_{11/2})\otimes\nu(g_{7/2}h_{11/2})$. As can be noticed, the calculated configurations $\pi(g_{9/2}h_{11/2})\otimes\nu(d_{5/2}h_{11/2})$ and $\pi(g_{9/2}h_{11/2})\otimes\nu(g_{7/2}h_{11/2})$ are close to the experimental data. These configuration are predicted to be mixed and it is not possible to differentiate between them. Therefore, we assign the configurations $eb'EA'$ and $eb'FA'(\pi(g_{9/2}h_{11/2})\otimes\nu((d_{5/2},g_{7/2})h_{11/2}))$ to bands 12 and 13, respectively. At a rotational frequency of $\omega = 0.52$ MeV/$\hbar$ bands 12 and 13 exhibit

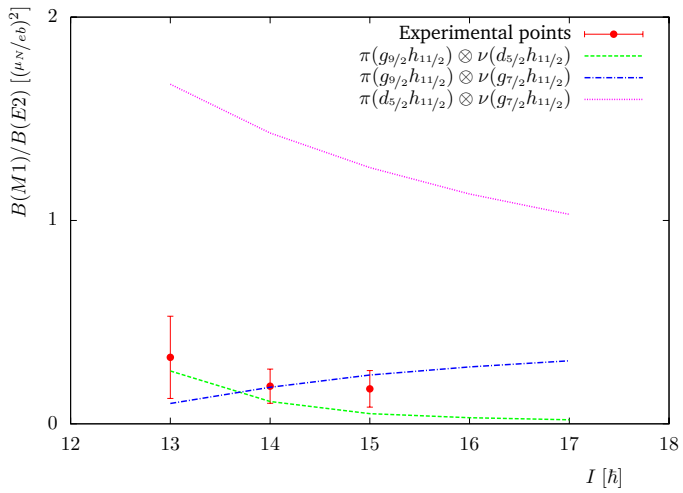

Figure 7.30: *Experimental $\frac{B(M1;I\rightarrow I-1)}{B(E2;I\rightarrow I-2)}$ ratios of reduced transition probabilities (solid points) for bands 12 and 13 compared to calculated values for the $\pi(g_{9/2}h_{11/2})\otimes\nu(d_{5/2}h_{11/2})$ (dashed-line), $\pi(g_{9/2}h_{11/2})\otimes\nu(g_{7/2}h_{11/2})$ (dot-dashed-line) and $\pi(d_{5/2}h_{11/2})\otimes\nu(g_{7/2}h_{11/2})$ (dot-line) configurations.*

a sudden increase in the alignment i_x (Fig. 7.16(f)), suggesting further quasi-particle excitations. The alignment gain of $\Delta i_x = 5.2$ and 4.9 $\hbar$, for bands 12 and 13, respectively, may be attributed to a pair of GH quasi-neutrons in $h_{11/2}$ orbitals. Indeed, bands 12 and 13 are very similar to band 2 in ^{125}La associated with $[422]3/2\otimes E_pF_p\otimes E_NF_N$ [HRJ+99]. As can be seen in Figs. 7.31 and 7.32, the band crossings take place at roughly the same frequency. The alignment gain in band 2 in ^{125}La has been interpreted

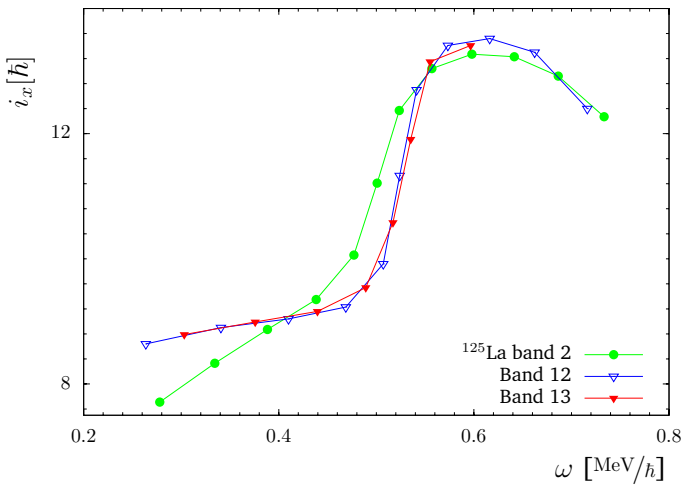

Figure 7.31: *Aligned angular momentum, i_x, as a function of rotational frequency, ω, for bands 12 and 13 in ^{124}Ba compared to band 2 in ^{125}La [HRJ+99].*

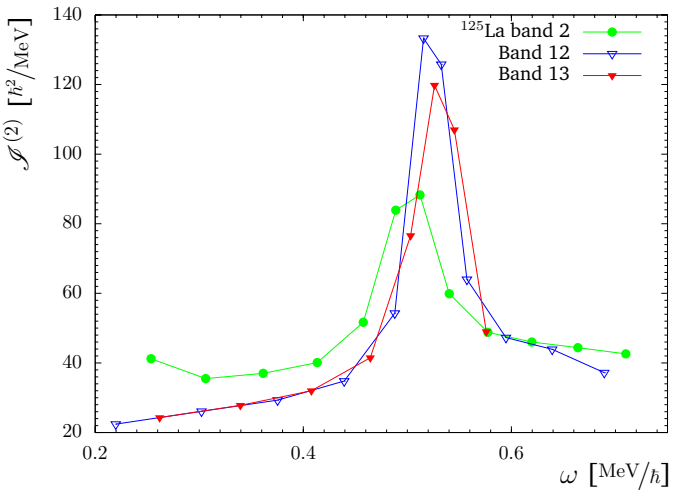

Figure 7.32: *Dynamic moments of inertia, $\mathscr{I}^{(2)}$, as a function of rotational frequency, ω, for bands 12 and 13 in ^{124}Ba compared to band 2 in ^{125}La [HRJ+99].*

as a consequence of rotationally aligned quasi-neutrons $h^2_{11/2}$, $E_N F_N$, which supports our suggestion for the configuration assignment above the crossing.

The present CNS calculation predicts two band structures with small signature splitting with the [1,5] and [(1)2,6] configurations (Fig. 7.14). Both configurations approach the yrast [2,6] configuration in the spin range 20–35. The [1,5] configuration is preferable to the [(1)2,6] configuration for two reasons. First, the experimental energy difference between the [1,5] and [2,6] configurations is predicted to decrease up to a spin of about 32 and then to increase at higher spins while this energy difference is expected to increase continuously in that spin region for the [(1)2,6] configuration, see Fig. 7.14. On the other hand, the energy difference between band 1 and bands 12 and 13 decreases above spin 24 and becomes small in the spin 30–35 region. Secondly, similar to the case of the [(1)2,6] configuration discussed above (7.4.1), the [(1)2,6] configuration probably in reality lies higher in energy than predicted due to the pairing interaction which is not considered in the CNS calculation.

Chapter 8

High-Spin Spectroscopy of ^{124}Xe

8.1 Introduction

Also the nucleus ^{124}Xe undergoes a shape-change from collective prolate to non-collective oblate states at high spins. The CSM [Ben89, Ben90] calculations for ^{124}Xe using the UC [Ben] code indicate that the deformation at low and medium spins is moderate, $\varepsilon \simeq 0.2$, in agreement with the deformation obtained from lifetime measurements [SDM+04]. Collective configurations with $\gamma \simeq 0^{\circ}$ and -50° are favoured for configurations with proton and neutron excitations, respectively. These are crossed by non-collective oblate states with $\gamma \simeq 60^{\circ}$ around spin $I \simeq 22$. The non-collective states are energetically favoured in the Xe isotopes because of a gap in the single-particle level spectrum at $Z = 54$ for $\varepsilon \simeq 0.2$, which leads to a lower energy of such states compared to, e.g., the $Z = 56$ Ba nuclei. Indeed, a transition to an irregular level pattern has been observed experimentally above spin $I \simeq 20$ in neighbouring ^{122}Xe [TSR+94] and ^{126}Xe [RHSH+07].

Previous investigations of ^{124}Xe have established band structures up to the spin $I = 20$ to 30 region in this nucleus [KYK+75, KYK+78, KKS+83, GKH+84, BPF+97, SCW+99, WMW+01, RBR+02, SDM+04]. In addition to several collective bands of $E2$ transitions, a sequence of enhanced $M1$ transitions with weak $E2$ crossovers was discovered, which was explained alternatively as a deformed high-K band or as a band of intermediate character with both, collective rotation and the shears mechanism[Hüb05a] contributing to the generation of angular momentum [BPF+97, SCW+99, RBR+02, SDM+04].
In this work, we investigate the predicted features mentioned above for ^{124}Xe at high angular momentum.

8.2 Experimental Results

In this section, the level scheme constructed for ^{124}Xe and γ-ray coincidence spectra will be presented. The previously known bands labelled 1–9 [GKH+84, BPF+97, SCW+99, SDM+04] are confirmed, some of them are extended to higher spins and new linking transitions and decay paths to the yrast band are observed. Two new side bands labelled A and B and two irregular structures labelled C and D are established. Bands 5, B and 8 show an irregular pattern at high spins. The irregular structures may be a fingerprint of the predicted transitions from collective to non-collective excitation.

Level Scheme

The level scheme of ^{124}Xe obtained in this work is shown in Fig. 8.1. It is based on previous work [GKH+84, BPF+97, SCW+99, SDM+04] and on γ-ray coincidence relationships, relative transition intensities and angular distributions determined from the present data.

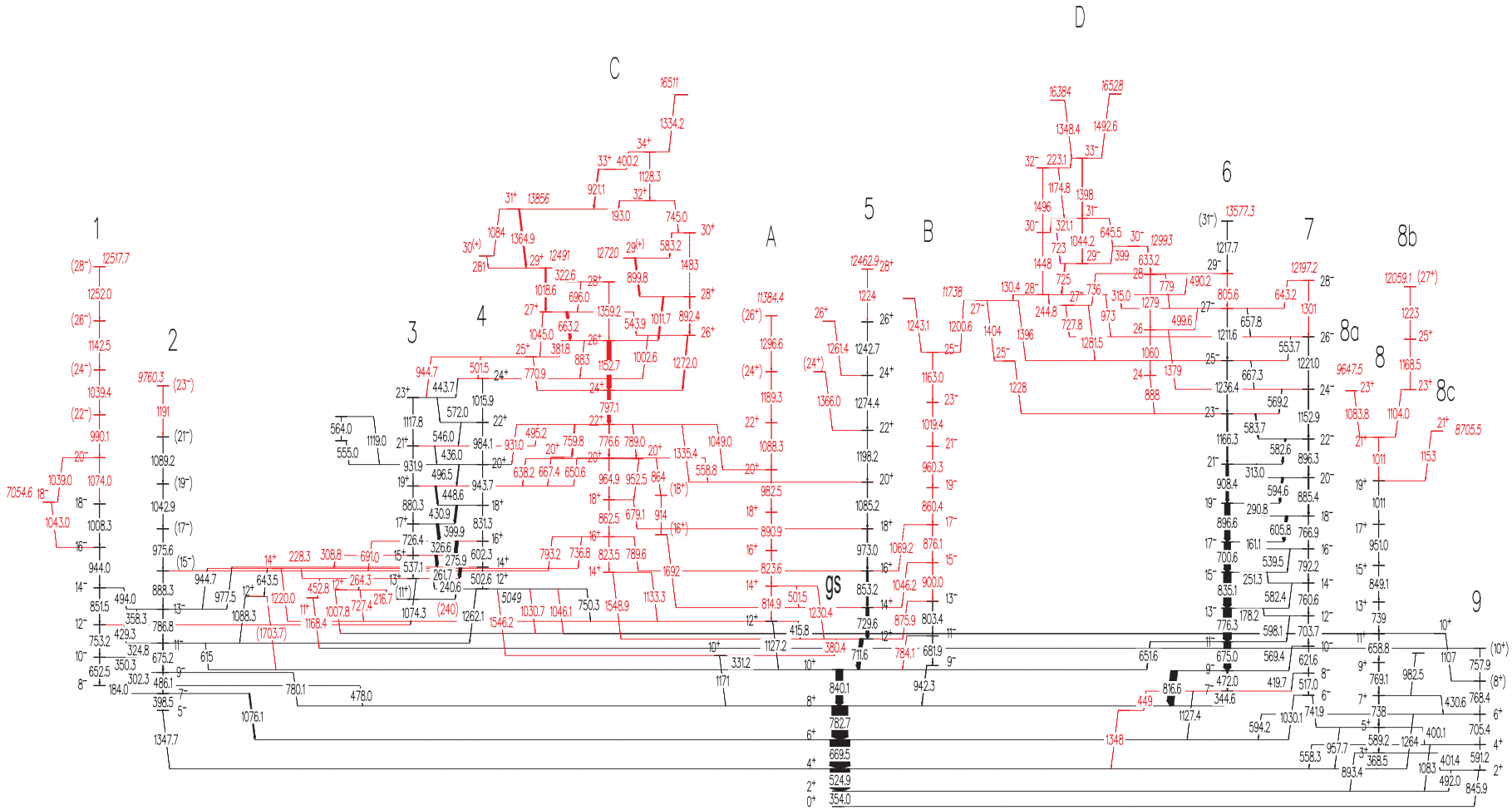

Figure 8.1: *Level scheme deduced for ^{124}Xe from this work. The transition energies are given in keV and their relative intensities are proportional to the widths of the arrows. Parities and spins in parentheses are tentatively assigned, and dashed transitions are tentatively placed. The new structures are drawn with red colour.*

The four new structures labelled A, B, C and D have been observed for the first time in this work. Furthermore, new transitions linking bands 3 and 4 to the low-spin part of the level scheme were discovered. As can be seen in Fig. 8.1, the level scheme consists of the ground-state (gs) band, band 5 (yrast band) with positive parity and ten excited side-bands with negative parity (bands 1, 2, 6, B and structure D) and positive parity (bands 3, 4, 7, 8, A and structure C).

Band 1

Band 1 was already known up to the $I^\pi = 18^-$ state [SCW+99]. In this work, five new γ-ray transitions with energies of 1074.0, 990.1, 1039.4, 1142.5 and 1252.0 keV have been added on top of the $I^\pi = 18^-$ state extending the band to $I^\pi = 28^-$ and an excitation energy of $E_x = 12517$ keV. Furthermore, a new level at $I^\pi = 18^-$ and E_x = 7050 very close to the band member with $I^\pi = 18^-$ and $E_x = 7020$ keV, was established. It is populated by the 1043.0 keV transition and depopulated via the 1039.0 keV transition which feeds into the $I^\pi = 16^-$ state of band 1. Gated γ-ray coincidence spectra of band 1 are presented in Fig. 8.2.

The DCO ratios of the 652.5, 753.2, 851.5, 944.0, 1008.3 and 1074.0 keV transitions are compatible with stretched quadrupole, probably $E2$, multipolarity. For the 990.1, 1039.4, 1142.5 and 1252.0 keV γ rays no DCO ratios could be determined. Therefore, the high-spin levels are tentatively assigned and their spin values are given in parentheses in Fig. 8.1.

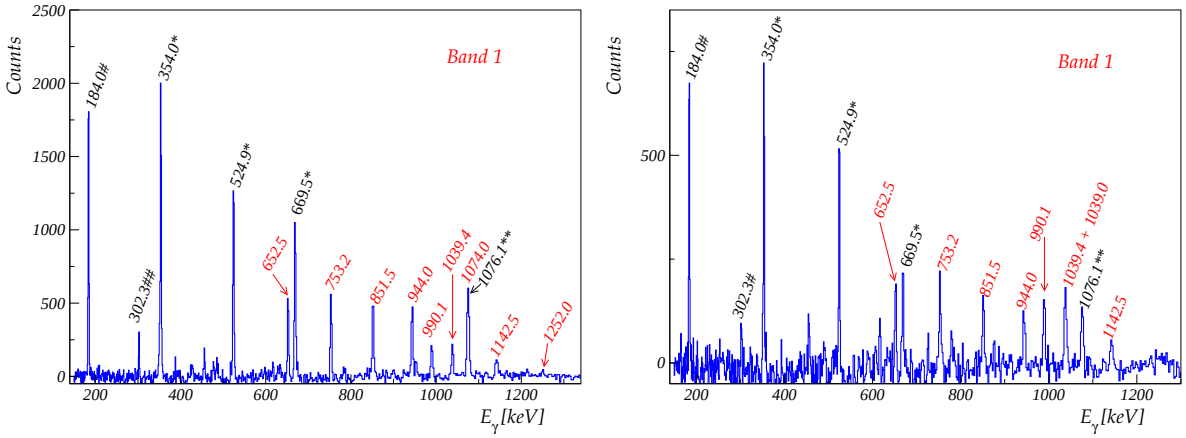

Figure 8.2: *Background-subtracted summed triple-gated γ-ray coincidence spectra of band 1. (a) The spectrum was produced by setting two gates on the transitions of 652.5, 753.2, 851.5, 944.0, 1074.0, 990.1, 1039.4, 1142.5 and 1252.0 keV and a third gate on the 1008.3 keV transition. (b) The spectrum was obtained by requiring two gates from a list of transitions of 652.5, 753.2, 851.5, 944.0, 1008.3, 1074.0, 990.1 and 1142.5 keV and one gate on the 1043.0 keV γ ray. Single asterisks mark transitions from the gs band. The decay-out transitions to the gs band are marked with double asterisks. Inter-band transitions are indicated with hash marks.*

Band 2

Band 2 was known up to the $I^\pi = 21^-$ state [SCW+99]. Only one transition with an energy of 1191 keV was added on top of the band extending the band to the $I^\pi = (23^-)$ state with E_x = 7959 keV. Figure 8.3 shows a γ-ray coincidence spectrum of band 2.

Bands 3 and 4

Bands 3 and 4 have been reported in [BPF+97, SCW+99]. In this work, the bands could not be extended to higher spin. But an additional 240 keV γ-ray transition was added at the bottom of band 4 which probably is of $M1$ character. Furthermore, new decay paths of γ rays with energies of 1546.2, 1262.1, 691.0, 264.3, 216.7, 727.4, 452.8, 1220.0 and 1703.7 keV have been identified which link bands 3 and

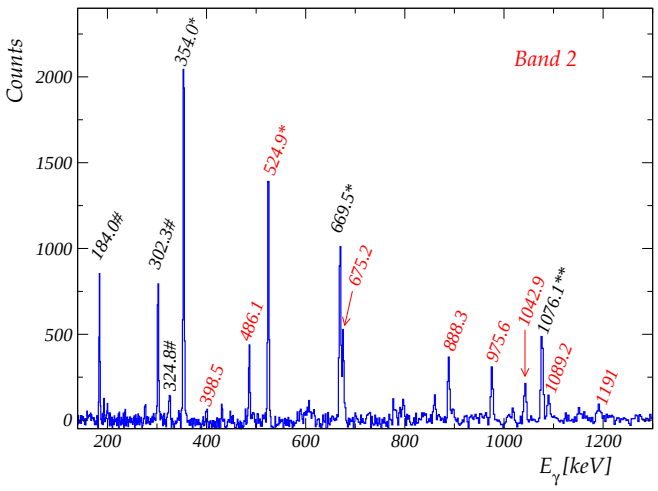

Figure 8.3: *Background-subtracted summed triple-gated γ-ray coincidence spectrum of band 2. It was produced by setting two gates on the transitions with 486.1, 675.2, 888.3, 975.6, 1042.9, 1089.2 and 1191 keV and one gate on the 786.8 keV transition. Single asterisks mark transitions from the gs band. The decay-out transitions to the gs band are marked with double asterisks. Inter-band transitions are indicated with hash marks.*

4 to bands 1 and 2 and to the gs band. Furthermore, we have established new decay transitions from the lower levels of band 4 to the $I^\pi = 11^+$ level in band 8 via the 1046.3 keV γ ray and to the $I^\pi = 8^+$ level in band 9 via the 1030.7 and 1107 keV transitions. A γ-ray coincidence spectrum is shown in Fig. 8.4.

In the previous work [SCW+99], the parity of bands 3 and 4 was not firmly assigned. A decay path of γ rays with energies of 1546.2 and 1171 keV of band 4 into the $I^\pi = 8^+$ level of the gs band has been observed. Together with the 331.2 keV transition, this suggests $I^\pi = 12^+$ for the head of band 4 with an excitation energy of $E_x = 5040$ keV. Moreover, the observed decay sequences into bands 2, 8 and 9 as well as to the gs band confirm the spins and positive parity of bands 3 and 4.

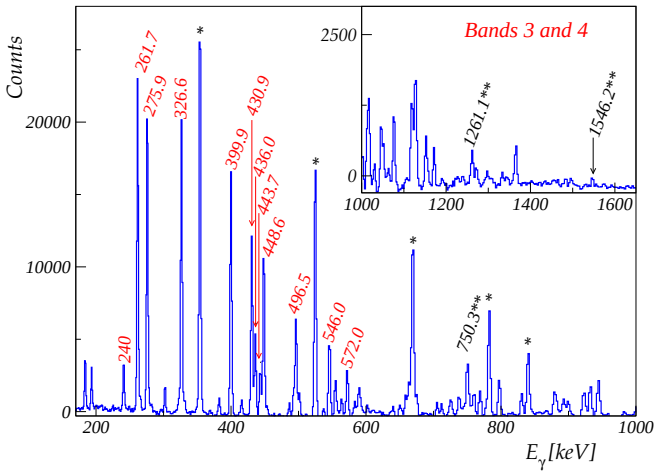

Figure 8.4: *Summed triple-gated coincidence γ-rays spectrum with background subtraction of bands 3 and 4. The spectrum was obtained by setting two gates on a list of the dipole transitions of 261.7, 279.9, 326.6, 399.9, 430.9, 448.6, 496.5, 436.0, 546.0, 572.0 and 443.7 keV of bands 3 and 4 and one gate on the 240 keV transitions. Single asterisks mark transitions belong to the gs band. The linking transitions are indicated by double asterisks.*

Band 5 (Yrast Sequence)

Band 5 had already been observed up to the $I^\pi = 26^+$ state [SCW+99]. One transition with energy of 1224 keV was added on top extending the band to the $I^\pi = 28^+$ state with an excitation energy of $E_x = 12462$ keV. Moreover, two new side-feeding transitions have been observed. The 1366 and 1261.4 keV transitions feed into the $I^\pi = 22^+$ and $I^\pi = 24^+$ levels, respectively. The DCO ratio of the 1261.4 keV γ ray is compatible with an $E2$ character. Representative coincidence γ-ray spectra showing the transitions in band 5 are displayed in Fig. 8.5. It is evident that the 1366.0 keV transition is parallel to the 1274.4 keV line and the 1261.4 keV transition is parallel to the 1242.7 keV γ ray. The spectra illustrate that the yrast band forks at $I^\pi = 22^+$ and $I^\pi = 24^+$ which could be due to single-particle excitation.

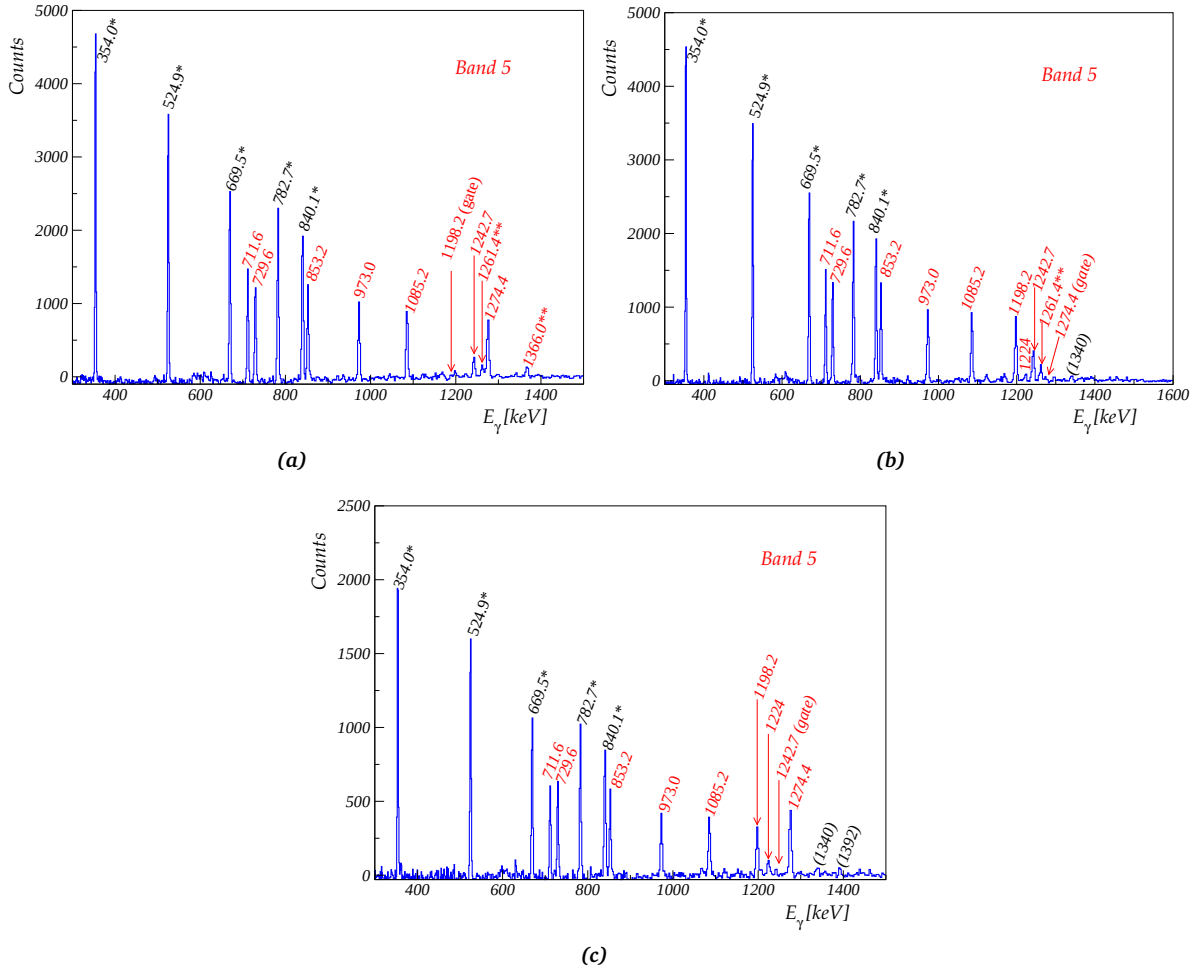

Figure 8.5: *Sum of triple-gated γ-ray coincidence spectra with background subtraction showing transitions from band 5. (a) Spectrum was obtained by setting two gates on a list of transitions of 711.6, 729.6, 853.2, 973.0, 1085.2, 1274.4, 1242.7 and 1224 keV from band 5 and one gate on the 1198.2 keV line of this band. (b) Spectrum was produced by setting two gates of a list of gates on transitions with 711.6, 729.6, 853.2, 973.0, 1085.2, 1198.2, 1242.7 and 1224 keV from band 5 and one gate on the 1274.4 keV γ ray. (c) Spectrum was produced by requiring two gates from a list of transitions of 711.6, 729.6, 853.2, 973.0, 1085.2, 1198.2, 1274.4 and 1224 keV of band 5 and one gate on the 1242.7 keV transition. Single asterisks mark the peaks of the gs band. Double asterisks denote transitions which feed into the high-spin states. Energies in parentheses correspond to transitions observed in coincidence but could not placed in the level scheme.*

Band 6

Band 6 was initially identified up to the $I^\pi = 29^-$ state with the 1217.7 keV γ ray being the top-most transition [SCW+99]. We have observed a new γ-ray line with energy of 805.6 keV. According to the DCO analysis, $E2$ multipolarity may be assigned to this transition. Based on their intensities, we have placed the 805.6 keV line on top of the $I^\pi = 27^-$ level and then placed the 1217.7 keV above it. A γ-ray coincidence spectrum of band 6 is presented in Fig. 8.6.

Band 7

Band 7 was already established up to the $I^\pi = 26^-$ state [SCW+99]. A new γ-ray transition with an energy of 1301 keV was placed on top of the band. Figure. 8.7 shows a γ-ray coincidence spectrum of band 7.

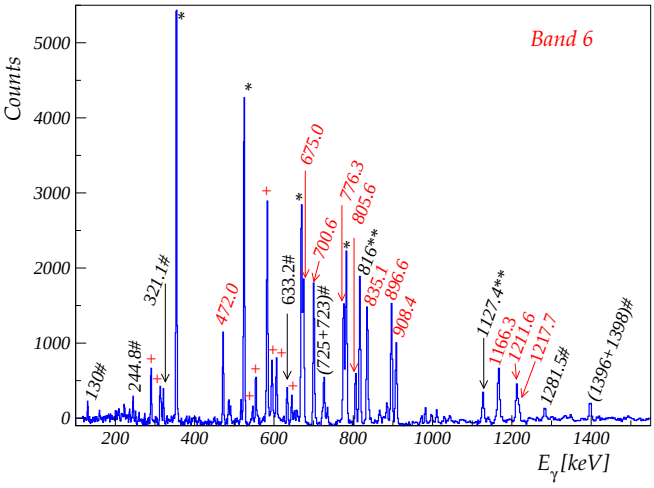

Figure 8.6: *Background-subtracted, summed triple-gated coincidence γ-ray spectrum of band 6. It was obtained by setting two gates from a list of transition with energies of 675.0, 776.3, 835.1, 700.6, 896.6, 908.4 and 1166.3 keV and one gate on the 1236.4 keV transition of band 6. Single asterisks mark transitions belonging to the gs band. Double asterisks mark linking transitions to the gs band. The inter-band $M1$ transitions are marked with plus signs. Transitions belonging to structure C are indicated with hash signs.*

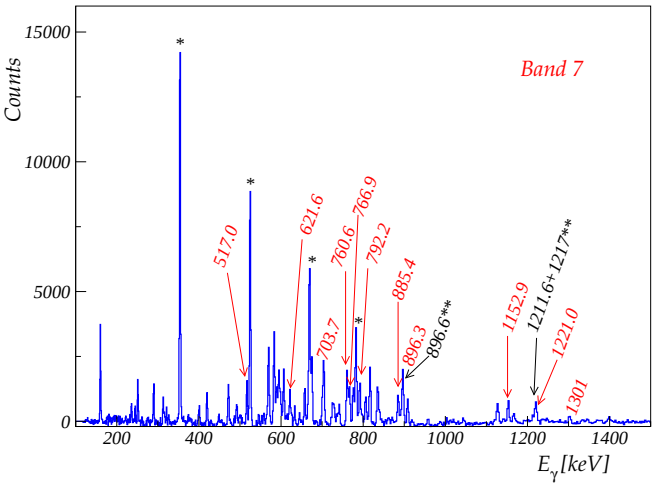

Figure 8.7: *Background-subtracted, summed triple-gated γ-ray coincidence spectrum of band 7. The spectrum was produced by setting three gates from a list of transitions from band 7 at 517.0, 621.6, 703.7, 760.6, 792.2, 766.9, 885.4, 896.3, 1152.9, 1221.0 and 1301 keV and summing over all possible combinations. Single asterisks mark peaks of the gs band. Unmarked peaks and peaks marked with double asterisks belong to band 6.*

Band 8

Band 8 had already been identified up to the $I^\pi = 19^+$ state [SCW+99]. Above this level several new γ rays with energies of 1011, 1153, 1083.8, 1104.0, 1168.5 and 1223 keV have been observed in the present study leading to an irregular level pattern, see Fig. 8.1. Figure. 8.8 shows four γ-ray coincidence spectra that illustrate the forking of band 8 above the $I^\pi = 19^+$ level into several branches. The DCO ratios of the new transitions are compatible with stretched quadrupole, presumably $E2$, transitions.

Band 9

Band 9 is known from previous work [GKH+84, SCW+99]. In this experiment it is weakly populated and could not be extended to higher spin.

Band A

The new sequence, labelled band A in the level scheme, Fig. 8.1, has been observed for the first time in this work. It consists of seven transitions with energies of 814.9, 823.6, 890.9, 982.5, 1088.3, 1189.3 and 1296.6 keV. A representative coincidence γ-ray spectrum is shown in Fig. 8.9. Band A is built on the previously known level at E_x = 4300 keV [SCW+99, SDM+04] to which $I^\pi = 12^+$ was tentatively assigned. The 1127.2 and 415.8 keV transitions depopulate this level into the 10^+ and 12^+ states of the gs band and band 5, respectively. We determined the DCO ratio of the 1127.2 keV γ ray which turned out to be compatible with a stretched quadrupole and probably has $E2$ character. Furthermore, we have observed two new decay-out transitions of 501.5 and 1230.4 keV. The DCO ratios of the in-band transitions with energies of 814.9, 823.6, 890.9, 962.5 and 1088.3 kev are compatible with a

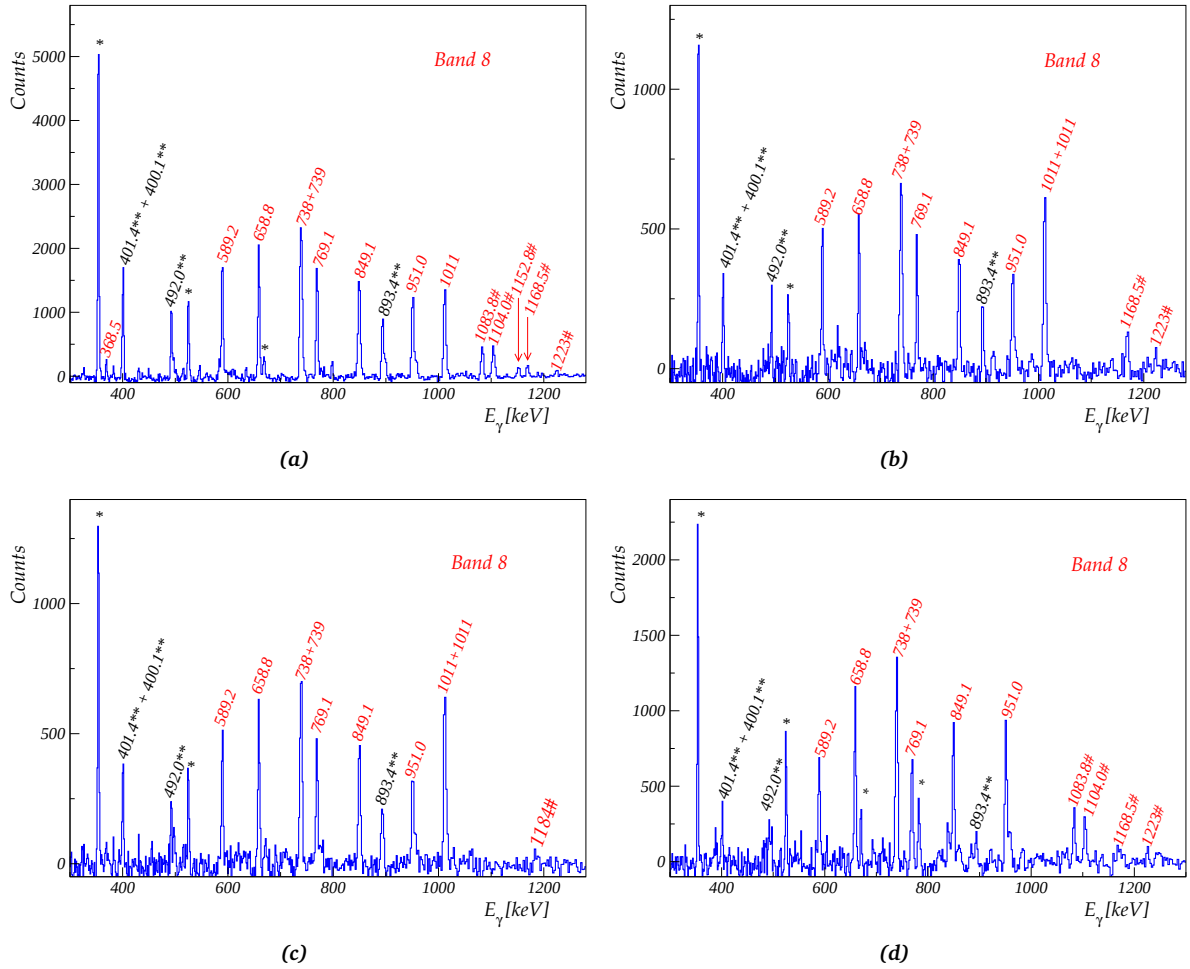

Figure 8.8: *Background-subtracted γ-ray coincidence spectra showing transitions of band 8. Single and double asterisks mark transitions of the gs band and the decay-out transitions, respectively. Transitions belonging to the new observed branches are indicated with hash marks. Spectra have been produced by setting triple gates of the form $(X \times X \times Y)$ where X is the list of γ rays with energies of of 589.2, 738, 769.1, 858.8, 739, 849.1 and 951.0 keV of band 8 and Y is equal to 1101 keV (a), 1104.0 keV (b) and 103.8 keV (c). Panel (d) shows a double-gated γ-ray spectrum of band 8 obtained by setting two gates on the 1011 keV doublet transition.*

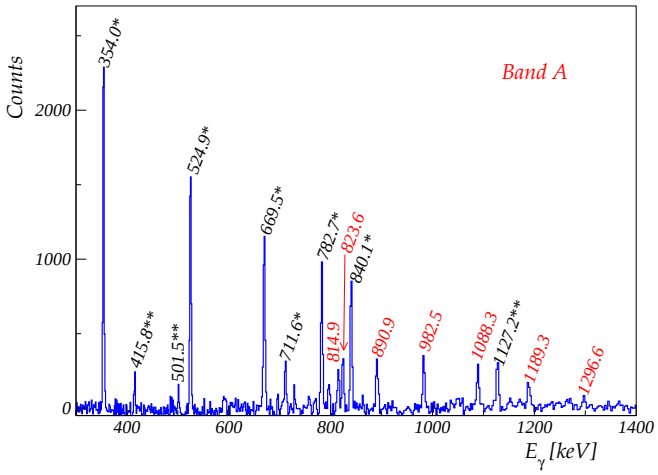

Figure 8.9: *Background-subtracted, summed triple-gated γ-ray coincidence spectrum of band A. The spectrum was produced by summing all triple-gate combinations of transitions with energies of 823.6, 890.9, 982.5, 1088.3, 1189.3 and 1296.6 keV of band A. The transitions of the gs band are marked with single asterisks. The decay-out transitions are indicated with double asterisks.*

stretched $E2$ character. The 1189.3 and 1296.6 keV transitions are tentatively assigned as being of $E2$ multipolarity.

Band B

Band B decays via the 942.3 keV transition into the $I^{\pi} = 8^{+}$ level of the gs band, see Fig.8.1. This transition and the two lowest members of this band, the 681.9 and 803.4 keV transitions, were known from previous work [GKH+84]. In this work, eight new transitions with energies of 900.0, 876.1, 860.4, 960.3, 1019.4, 1163.0, 1243.1 and 1200.6 keV have been observed and added on top of the 803.4 keV transition. In addition, several weak γ-ray lines of 784.1, 875.9, 1046.2 and 1069.2 keV linking band

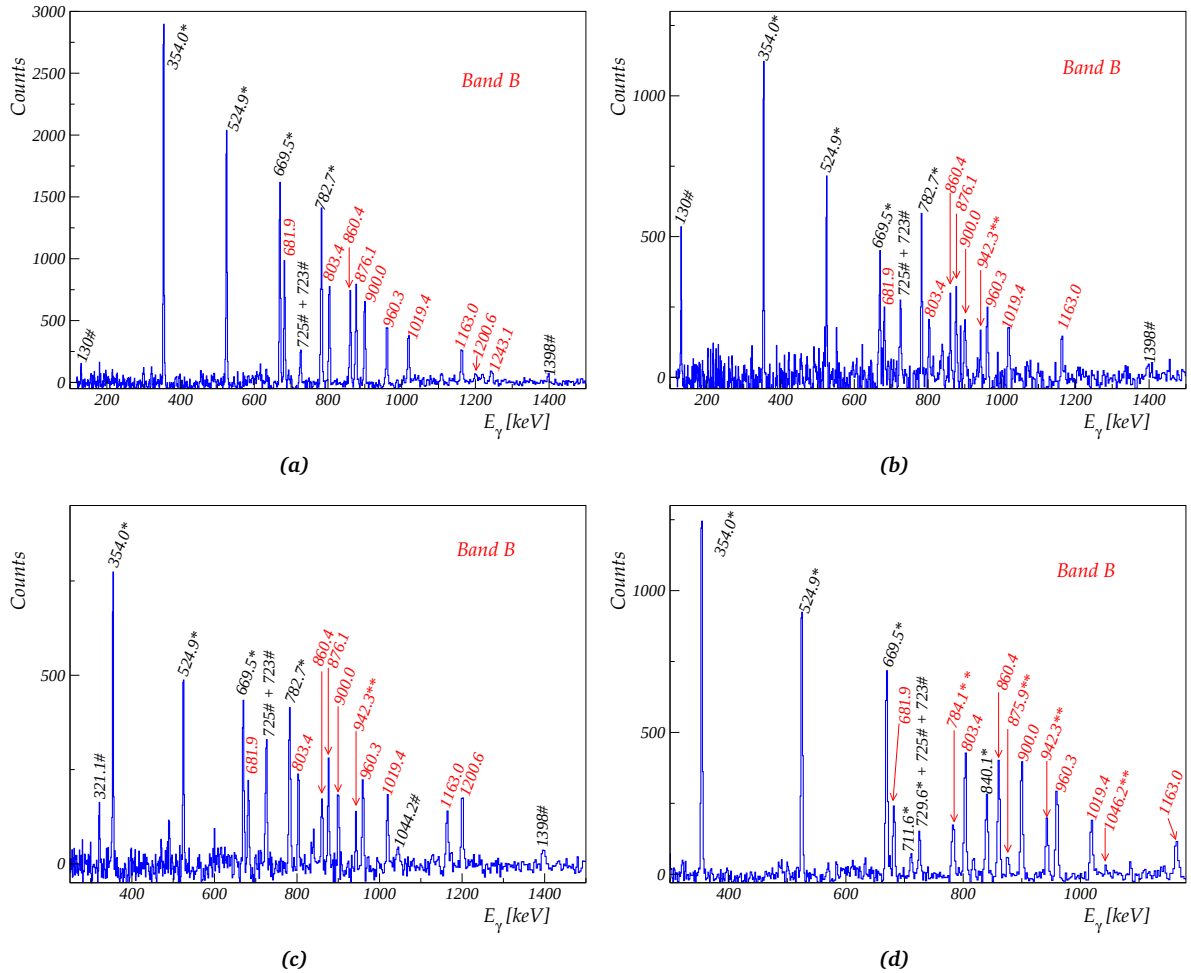

Figure 8.10: *Background-subtracted, triple-gated γ-ray coincidence spectra documenting the transitions of band B as well as the connections to the other structures. Spectrum (a) was produced by setting two gates from a list of transitions of 681.9, 803.4, 900.0, 876.1, 860.4, 960.3, 1019.4 and 1163.0 keV of band B and one gate on the 942.3 keV γ ray. Spectrum (b) was generated by setting two gates from a list of transitions with energies of 942.3, 681.9, 803.4, 900.0, 876.1, 860.4, 960.3, 1019.4 and 1163.0 keV and one gate on the 1200.6 keV γ ray. Spectrum (c) was obtained by requiring two gates from a list of transitions of 942.3 to 1163.0 keV and one gate on the 130 keV transition. Spectrum (d) was produced by requiring one gate from a list of transitions of 942.3, 681.9, 803.4, 900.0, 860.4, 960.3, 1019.4 and 1163.0 keV and one gate on the 782.7 keV transition from the gs band and one gate on the 876.1 keV transition from band B. Spectrum (d) demonstrates the linking transitions with energies of 784.1, 875.9 and 1046.2 keV. Single asterisks mark peaks of the gs band. Decay-out transitions from band B to the gs band and to band 5 are indicated with double asterisks. The hash mark is used to denote transitions belong to structure D.*

B to the gs band and to band 5 have been identified, as illustrated in Fig. 8.1. The 1069.2 keV γ ray is tentative, hence it is shown with a dashed line in Fig. 8.1. Gamma-ray coincidence spectra of band B are presented in Fig. 8.10. They illustrate the in-band transitions (Fig. 8.10(a)) and the forking above the 1163.0 keV transition into two branches with transition energies of 1200.6 and 1243.1 keV , see Fig. 8.10(b), where the third gate was set on the 1200.6 keV transition and the 1243.1 keV line does not show up. The top-feeding from structure D via the 130.4 keV line can be seen in Fig. 8.10(c) and the new observed decay-out transitions to the gs band and band 5 are visible in Fig. 8.10(d). The DCO values of the 681.9, 803.4, 900.0, 876.1, 860.4, 960.3 and 1019.4 keV γ rays are compatible with stretched quadrupole, probably $E2$, multipolarity. No DCO ratios could be extracted for the 1163.0, 1200.6 and 1243.1 keV lines. Hence, their multipolarity remains uncertain. However, $E2$ character is assumed for the 1163.0 keV γ ray.

A spin value of $I = 9$ was assigned to the band head. The assignment is based on the observed decay pattern of the band and on the measured DCO ratio, $R_{\mathrm{DCO}} = 0.72(9)$, of the 942.3 keV linking transition which is compatible with a stretched dipole, with $M1$ or $E1$ character. As can be seen in Fig. 8.1, band B is followed up to the $I = 25$ state which is fed by two transitions with energies of 1200.6 and 1243.1 keV, respectively. On the other hand, structure D decays into the 11738 keV level via the 130.4 keV stretched dipole transition and also this level is depopulated by the 1396 keV stretched quadrupole, $E2$ transition which is feeding into the $I^{\pi} = 25^{-}$ state of band 6, see Fig. 8.1. Thus, the $I^{\pi} = 27^{-}$ is adopted for the 11738 keV level and, hence, negative parity for band B.

Structure C

The complex group of levels, labelled C in Fig. 8.1, has been observed for the first time in this work. It consists of a band-like sequence of transitions with energies of 823.5, 862.5, 964.9, 776.6, 797.1 and 1152.7 keV between the states with $I^{\pi} = 14^{+}$ and 26^{+}, see Fig. 8.1. There are several close-lying levels with $I^{\pi} = 18^{+}, 20^{+}$ and 22^{+} and the many transitions between them are a sign of mixing. At higher spins, the structure becomes even more irregular. Spins and parities of the whole group of levels are firmly established by many connections to states with known properties and by the DCO ratios listed in table A.2. The spin-parity assignments are supported also by the decay into the coupled bands 3 and 4. Fig. 8.11 shows coincidence γ-ray spectra of structure C.

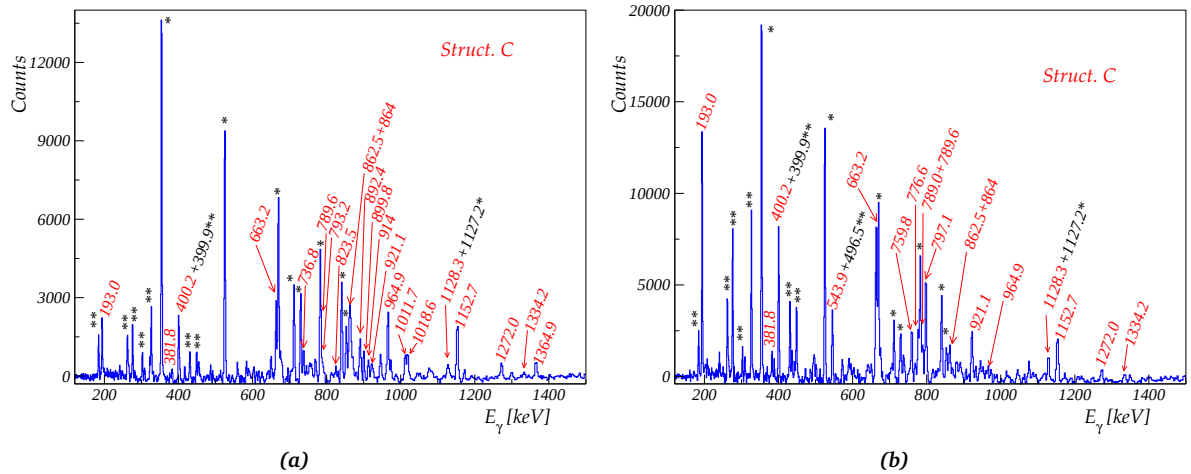

(a) ***(b)***

Figure 8.11: *Background-subtracted, double-gated γ-ray coincidence spectra showing transitions from structure C. Spectrum (a) was produced by gating on the 776.6 and 797.1 keV transitions. Spectrum (b) was obtained by setting a double gate on the 1018.6 and 1364.9 keV γ rays. Single asterisks mark peaks belonging to the gs band and double asterisks denote transitions from bands 1, 3 and 4.*

Structure D

Structure D was also observed for the first time in this study. It consists of many transitions with energies of 888, 1379, 1060, 499.6 1279, 779, 490.2, 633.2, 973, 315.0, 399, 1281.5, 727.8, 736, 1396, 1228, 1494, 224.8, 725, 723, 1448, 1496, 1044.2, 321.1, 1174.8, 1398, 1348.4 and 1492.6 keV. It decays into high-spin states of band B via the stretched dipole 130.4 keV transition and into the coupled negative-parity bands 6 and 7 via several decay paths, see Fig. 8.1. Stretched dipole and quadrupole transitions linking several of the levels to bands 6 and 7 establish their spins and negative parity, see Fig. 8.1 and table A.2. No DCO ratios could be extracted for the transitions of 1348.4 and 1492.6 keV depopulating high-energy levels at 16384 and 16528 keV, respectively. Thus, their spin and parity are not determined. Representative coincidence γ-ray spectra of structure D are presented in Fig. 8.12.

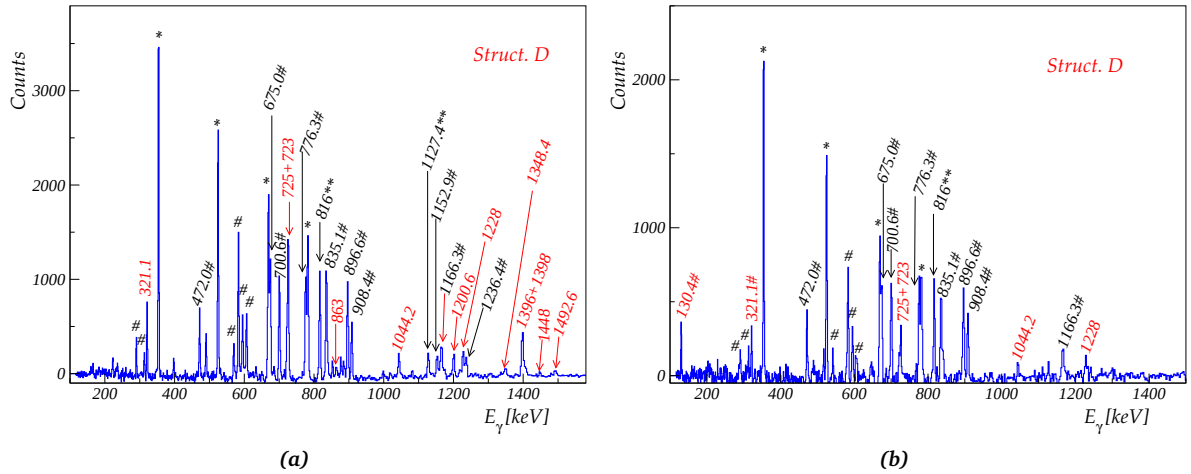

Figure 8.12: *Summed triple-gated γ-ray coincidence spectra demonstrating the coincidence between structure D and band 6. Spectrum (a) was produced by setting two gates of a list of transitions with energies of 472.0, 675.0, 776.3, 835.1, 700.6, 896.6, 908.4, 1166.3 and 1236.4 keV of band 6 and one gate on the 130.4 keV transition. Spectrum (b) was generated by requiring two gates of a list of transitions of 472.0, 675.0, 776.3, 835.1, 700.6, 896.6, 908.4, 1166.3 and 1236.4 keV of band 6 and one gate on the 1404 keV transition. Single and double asterisks denote transitions of the gs band and the decay-out γ rays, respectively. The inter-band and in-band transitions of band 6 are marked with hash signs.*

8.3 Band Structures in ^{124}Xe

Configuration assignments to the bands 1 to 8, A and B as well as to the irregular structures C and D are made on the basis of systematics of similar structures in neighbouring nuclei, and by comparison of aligned angular momenta, i_x, dynamic moments of inertia, $\mathscr{I}^{(2)}$, rotational crossing frequencies, ω_c, and relative excitation energies, E_x, with theoretical calculations.

8.3.1 Cranked Shell Model (CSM) Calculations

Using the UC software package [Ben], Potential-Energy Surfaces (PES) and quasi-particle energies in the rotating nuclei (Routhians) for neutrons and protons are calculated for different configurations in ^{124}Xe. Examples of such calculations are presented in Figs. 8.13 and 8.14. Figure 8.13 shows the PES calculated for the configuration $(\pi, \alpha) = (+,0)$ at three different spin values. Minima are evident for $\varepsilon \simeq 0.21$ with $\gamma \simeq -50^\circ$, $\varepsilon \simeq 0.28$ with $\gamma \simeq 3^\circ$ and for $\varepsilon \simeq 0.20$ with $\gamma \simeq 60^\circ$. This illustrates the co-existence of prolate and oblate shapes in ^{124}Xe. Figure 8.14 shows Routhians for neutrons and protons corresponding to the minima at $\varepsilon \simeq 0.21$ with $\gamma \simeq -45^\circ$ and $\varepsilon \simeq 0.30$ with $\gamma \simeq 0^\circ$. It can be seen that for oblate shape with $\gamma \simeq -45^\circ$ the neutron crossing occurs earlier than the proton crossing and this would drive the nucleus

to oblate shape while for the $\gamma \simeq 0^{\circ}$ the proton crossing takes place earlier and this would polarise the nuclear shape towards prolate shape. The relevant quasi-particle levels are listed in table 8.1.

qp Label	Shell model states	Nilsson orbitals	(π, α)
E_π	$(d_{5/2}, g_{7/2})$	$[420]1/2^+$	$(+, -1/2)$
	$(d_{5/2}, g_{7/2})$	$[422]3/2^+$	$(+, -1/2)$
F_π	$(d_{5/2}, g_{7/2})$	$[420]1/2^+$	$(+, +1/2)$
	$(d_{5/2}, g_{7/2})$	$[422]2/3^+$	$(+, +1/2)$
A_π	$h_{11/2}$	$[550]1/2^-$	$(-, -1/2)$
B_π	$h_{11/2}$	$[550]1/2^-$	$(-, +1/2)$
C_π	$h_{11/2}$	$[541]3/2^-$	$(-, -1/2)$
D_π	$h_{11/2}$	$[541]3/2^-$	$(-, +1/2)$
F_ν	$(s_{1/2}, d_{3/2})$	$[411]1/2^+$	$(+, +1/2)$
	$(d_{5/2}, g_{7/2})$	$[402]5/2^+$	$(+, +1/2)$
E_ν	$(s_{1/2}, d_{3/2})$	$[411]1/2^+$	$(+, -1/2)$
	$(d_{5/2}, g_{7/2})$	$[402]5/2^+$	$(+, -1/2)$
B_ν	$h_{11/2}$	$[523]7/2^-$	$(-, +1/2)$
A_ν	$h_{11/2}$	$[523]7/2^-$	$(-, -1/2)$
D_ν	$h_{11/2}$	$[532]5/2^-$	$(-, +1/2)$
C_ν	$h_{11/2}$	$[532]5/2^-$	$(-, -1/2)$

Table 8.1: *The labelling of quasi-particle (qp) orbitals in parity and signature (π, α) and the related shell and Nilsson model origin at rotational frequency $\omega = 0.0$ $^{\mathrm{MeV}}/_{\hbar}$ in ^{124}Xe.*

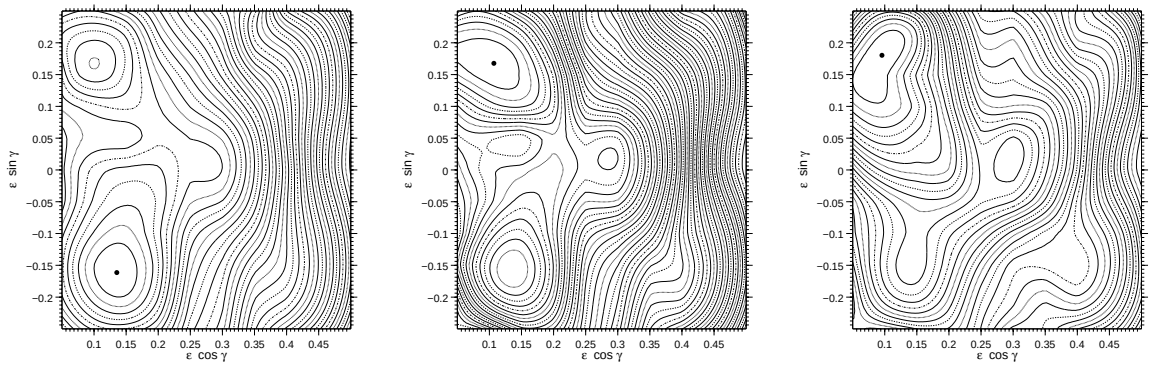

(a) *(b)* *(c)*

Figure 8.13: *Example of potential-energy surfaces (PES) calculated with the Ultimate Cranker code for ^{124}Xe. The calculation has been performed for configurations (π, α) = (+,0) at spins I = 12 (a), 16 (b) and 28 (c).*

8.3.2 Alignments, Routhians, Dynamic Moments of Inertia and Excitation Energies

Experimental aligned angular momenta, i_x, Routhians, e', dynamic moments of inertia, $\mathscr{J}^{(2)}$ and excitation energies, E_x, facilitate the interpretation of the observed structures. These quantities are shown in Figs. 8.15, 8.16, 8.17 and 8.18, respectively.

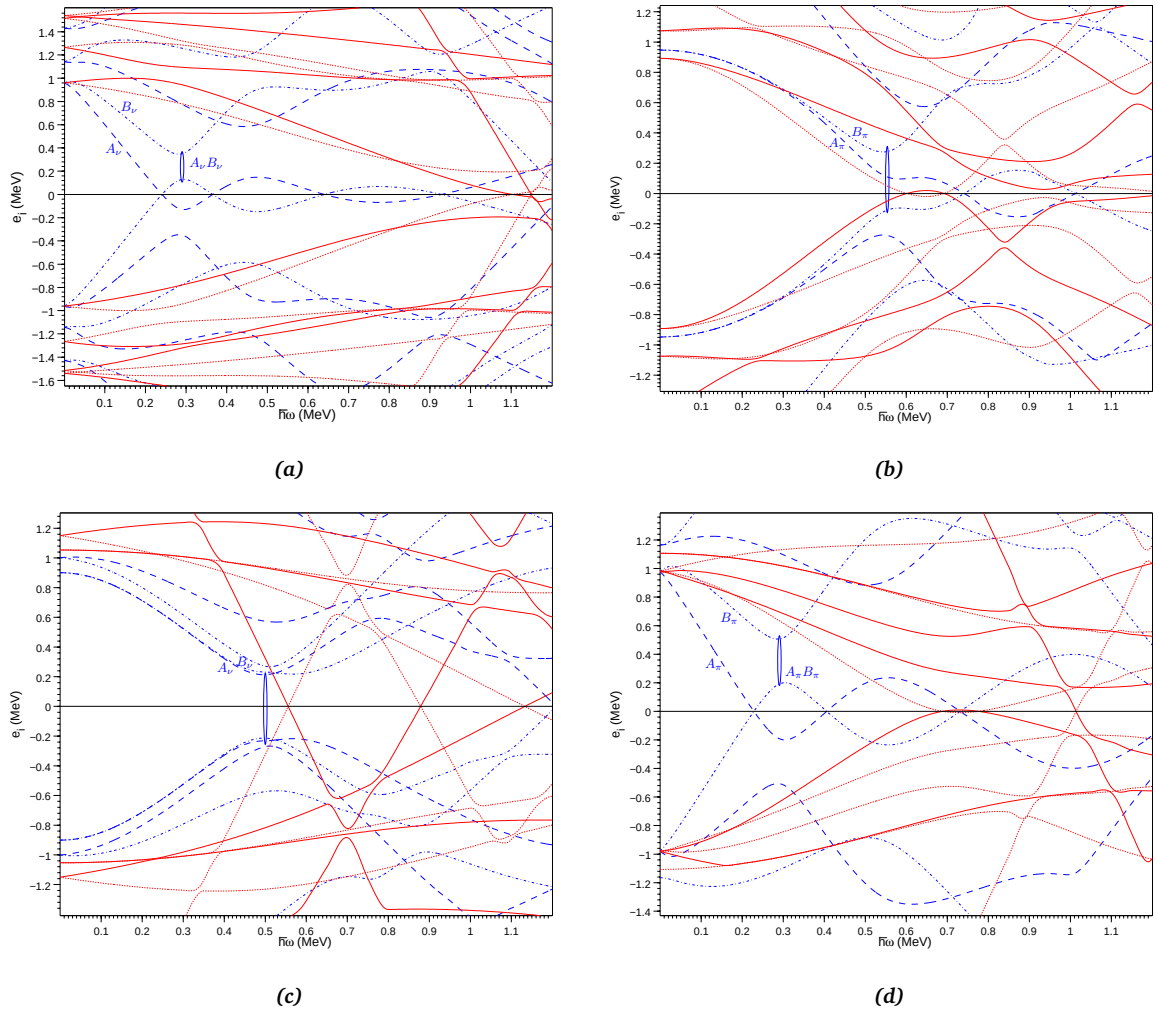

Figure 8.14: *Routhians calculated as a function of rotational frequency for neutrons (a) and protons (b) at a deformation corresponding to the minimum ($\varepsilon = 0.21,\ \gamma = -45^\circ$) and for neutrons (c) and protons (d) at a deformation corresponding to ($\varepsilon = 0.3,\ \gamma = 0^\circ$). The parity and signature (π, α) of the levels are: $(+, +1/2)$–solid lines; $(+, -1/2)$–dotted lines; $(-, -1/2)$–dashed lines; $(-, +1/2)$–dot-dashed lines.*

8.4 Configuration Assignments

8.4.1 Coupled bands

Bands 1 and 2

Bands 1 and 2 appear to be a pair of signature-partners with small signature splitting. It can be seen in Fig. 8.16(a) that their signature splitting increases gradually with rotational frequency. They start with aligned angular momentum of $i_x \approx 4\ \hbar$, see Fig. 8.15(a). Band 2 gains gradually angular momentum up to highest observed spins while band 1 exhibits a sudden back-bending at a rotational frequency of $\omega_c \approx 0.51\ ^{\mathrm{MeV}}/_{\hbar}$ with an alignment gain of $\Delta i_x \approx 6.7\ \hbar$. It has been suggested that bands 1 and 2 are built on the $\nu(h_{11/2}g_{7/2})$ (A_nE_n) configuration [SCW+99]. The rather large gain of angular momentum may be caused by an alignment of a pair of $\nu h^2_{11/2}$ quasi-neutrons. Thus, we assign the $\nu(h_{11/2}g_{7/2}) \otimes \nu h^2_{11/2}$ $(A_nE_nC_nD_n)$ configuration to band 1 above the crossing.

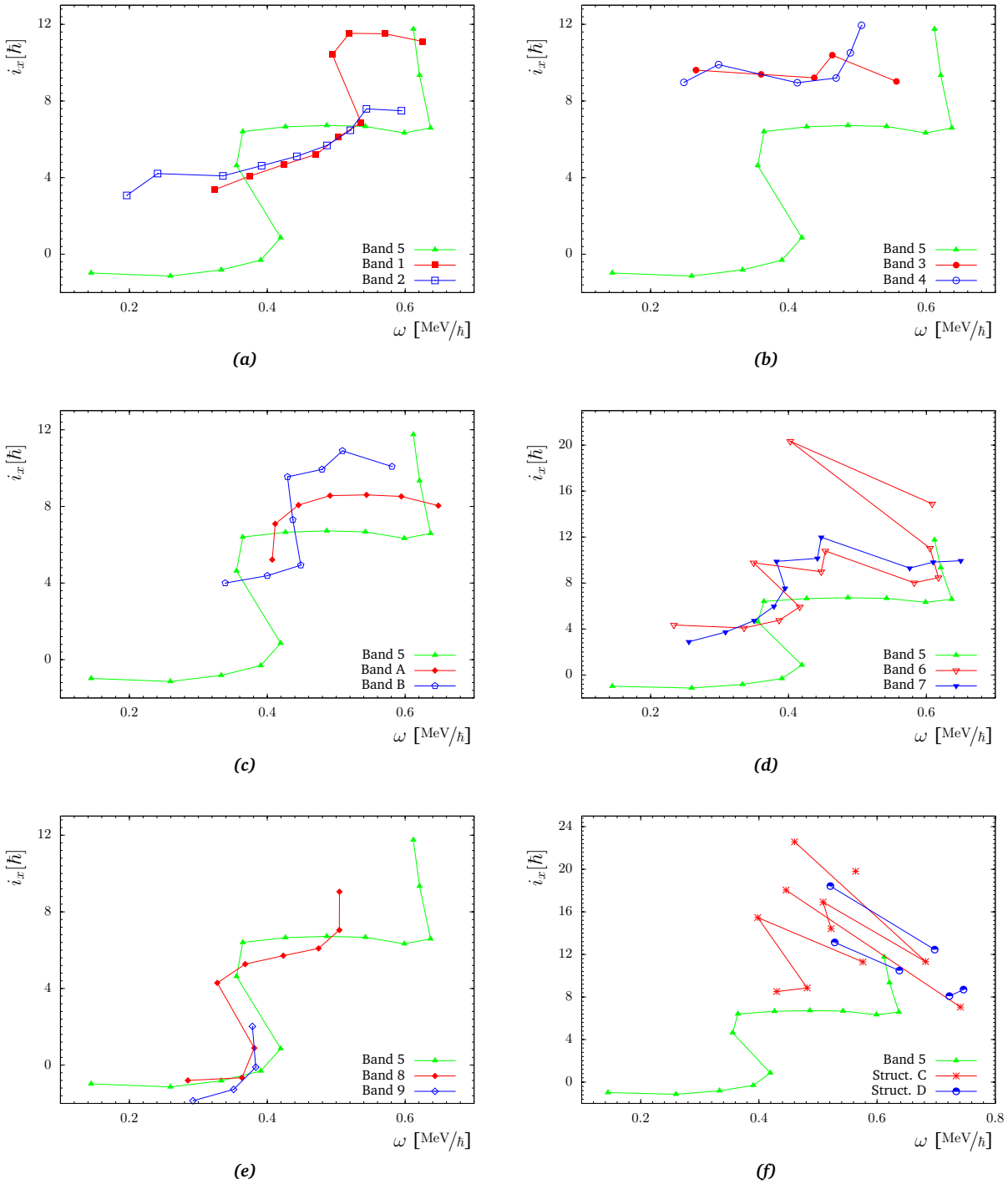

Figure 8.15: *Aligned angular momentum, i_x, as a function of rotational frequency, ω, for bands 1–8, A and B as well as for structures C and D in ^{124}Xe. A reference core with Harris parameters of $\mathscr{J}_0 = 16\ \hbar^2/\mathrm{MeV}$ and $\mathscr{J}_1 = 26\ \hbar^4/\mathrm{MeV}^3$ has been subtracted.*

Bands 3 and 4

The dipole bands 3 and 4 form a pair of signature partner bands with no signature splitting up to a rotational frequency $\omega \approx 0.42\ \mathrm{MeV}/\hbar$ (Fig. 8.16(b)). At higher rotational frequencies they exhibit a small signature splitting and inversion which may be attributed to a change in the quasi-particle configura-

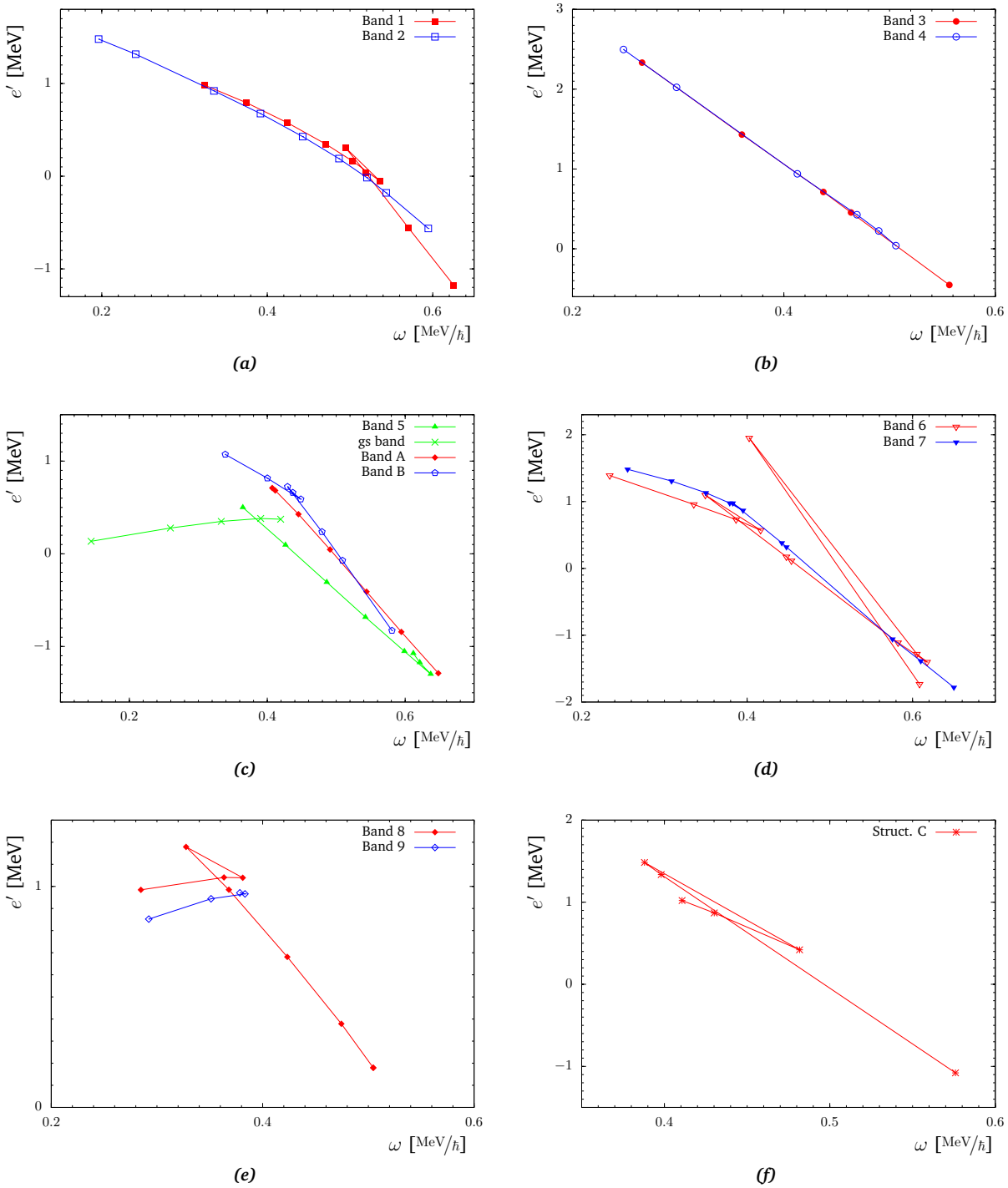

Figure 8.16: *Experimental Routhians, e', (single-particle energies in the rotating frame) versus rotational frequency, ω, for bands 1–8, A and B and for structure C in ^{124}Xe. A reference core with Harris parameters $\mathscr{I}_0 = 16\ \hbar^2/\mathrm{MeV}$ and $\mathscr{I}_1 = 26\ \hbar^4/\mathrm{MeV}^3$ has been subtracted.*

tion [SCW+99]. In addition, their initial aligned angular momentum is large, $i_x \approx 9\ \hbar$, see Fig. 8.15(b), suggesting a multi-quasi-particles configuration. They have been discussed extensively in [SCW+99] and a six-quasi-particle configuration has been suggested.

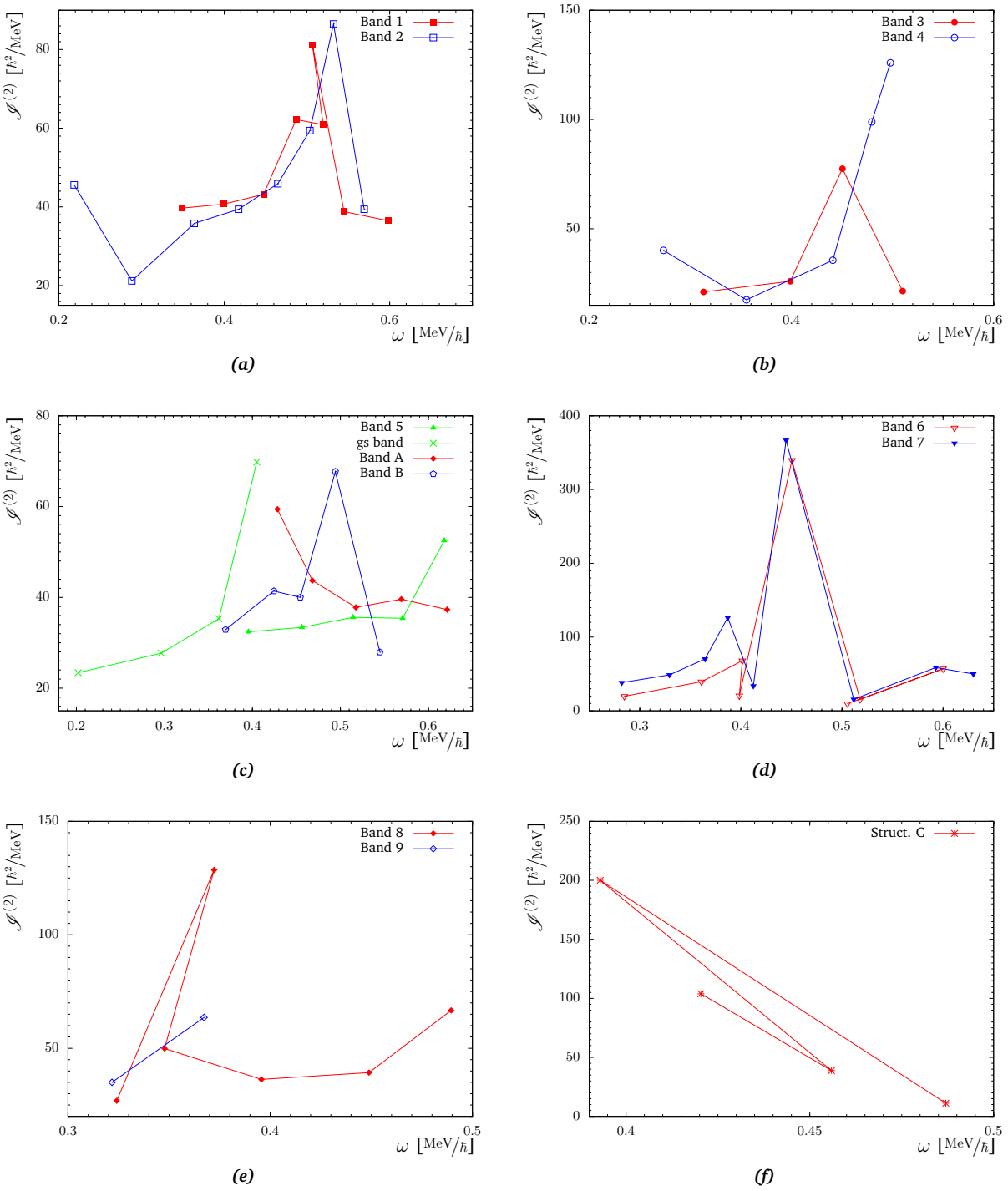

Figure 8.17: *Dynamic moments of inertia, $\mathscr{I}^{(2)}$, versus rotational frequency, ω, for bands 1–8, A and B and structure C.*

Bands 6 and 7

Band 6 is the negative-parity yrast band and forms with band 7 a pair of signature partners with large signature splitting, see Fig. 8.16(d). They start with an initial angular momentum of $i_x \approx 4.4\ \hbar$ and undergo a band crossing at a rotational frequency of $\omega_c \approx 0.38$ MeV/$\hbar$ with an alignment gain of $\Delta i_x \approx 6\ \hbar$, see Fig. 8.15(d). It was pointed out that bands 6 and 7 are based on the $A_\pi E_\pi$ and $A_\pi F_\pi$ of $\pi h_{11/2}(g_{7/2}d_{5/2})$

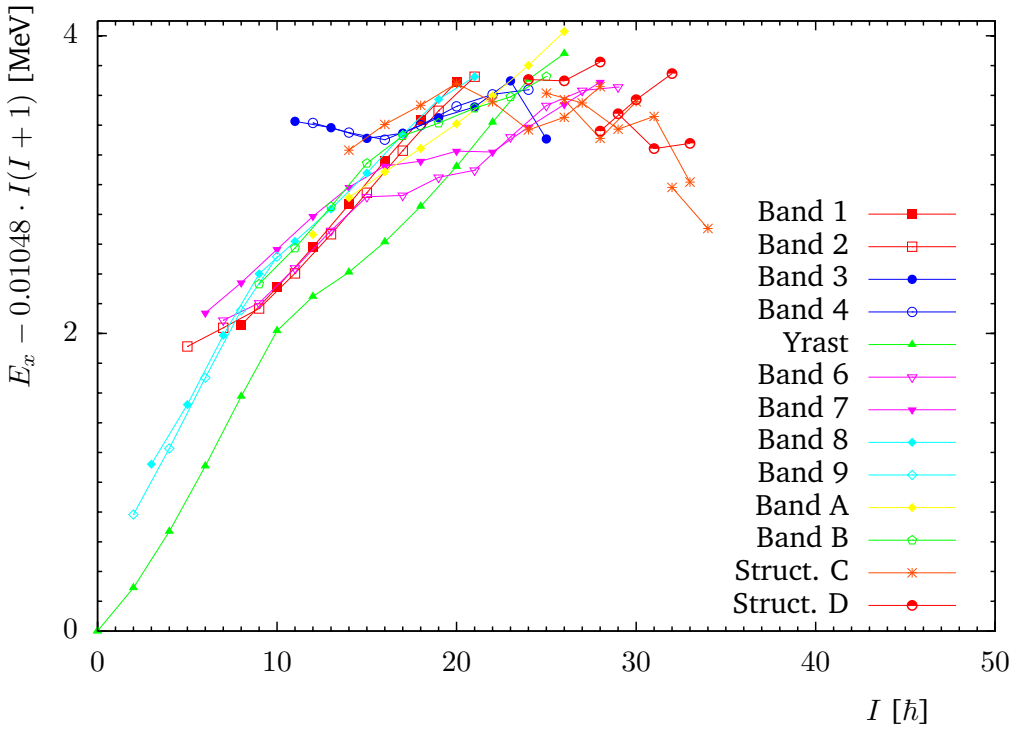

Figure 8.18: *Experimental excitation energies, E_x, relative to a rigid-rotor reference energy, $E_{RLD} = \frac{1}{2\mathscr{I}_{rig}} I(I+1)$, where, $\frac{1}{2\mathscr{I}_{rig}} \approx 32.32 A^{-5/3}$ MeV/$\hbar^2$ [AFLR99], as a function of spin I for all structures observed in ^{124}Xe.*

parentage, respectively. The crossing may be attributed to $\nu h^2_{11/2}$ alignment [GKH+84]. Therefore, the configurations $A_\pi E_\pi A_\nu B_\nu$ and $A_\pi F_\pi A_\nu B_\nu$ of $\pi h_{11/2}(g_{7/2}d_{5/2}) \otimes \nu h^2_{11/2}$ origin may be assigned to bands 6 and 7, respectively, after the crossing. In addition, band 6 shows a second sharp back-bending at a rotational frequency of $\omega \approx 0.60$ MeV/$\hbar$ with an average gain of angular momentum of $i_x \approx 7.5\ \hbar$. This could be understood by a second aligned pair of two-quasi-neutrons of $h^2_{11/2}$ parentage. Accordingly, band 6 probably has the $\pi h_{11/2}(g_{7/2}d_{5/2}) \otimes \nu h^4_{11/2}$ $(A_\pi E_\pi A_\nu B_\nu C_\nu D_\nu)$ configuration above the second crossing.

Bands 8 and 9

Bands 8 and 9 had been established to form a pair of quasi-γ bands [KYK+75]. Band 8 undergoes a band crossing at a rotational frequency of $\omega \approx 0.36$ MeV/$\hbar$ with an angular momentum gain of $\Delta i_x \approx 6\ \hbar$, see Fig. 8.15(e). The alignment pattern of band 8 is similar to that of band 5. Accordingly, the back-bending in band 8 may be attributed to an alignment of $\nu h^2_{11/2}$ neutrons. After the crossing, the band continues to gain angular momentum, with $\Delta i_x > 3.4\ \hbar$, up to the highest observed spin. The three branches observed above spin $I = 19$ may indicate terminating states.

8.4.2 Uncoupled Bands

Band 5 (Yrast Sequence)

The yrast sequence undergoes a sharp back-bending at a rotational frequency $\omega_c = 0.38$ MeV/$\hbar$ with an angular momentum gain of $i_x \approx 7.2\ \hbar$, see Figs. 8.16(c) and 8.15, respectively. This has been attributed to a rotationally aligned pair of two quasi-neutrons, $\nu h^2_{11/2}$ [KKS+83].

Fig. 8.19 presents the alignment plots of yrast bands in ^{120,122,124,126,128}Xe. The crossing-frequency, ω_c, decreases with increasing neutron number. Band 5 in ^{124}Xe exhibits a sudden up-bend above $\omega = 0.66$ MeV/$\hbar$. A similar behaviour has been observed in the yrast bands of ^{122}Xe and ^{126}Xe [TSR+94, WJA+91],

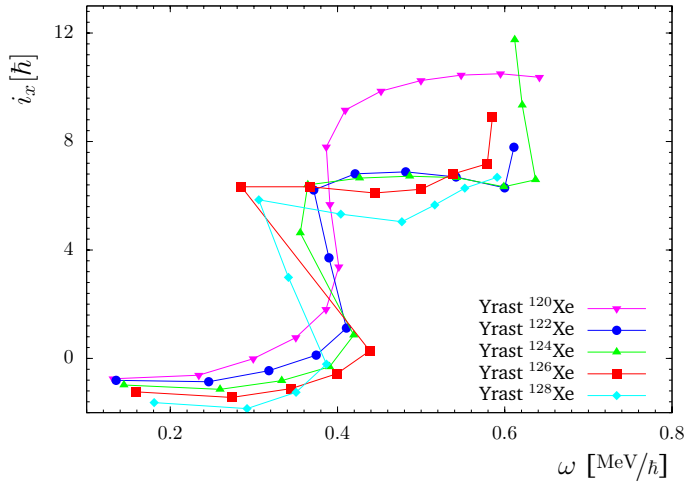

Figure 8.19: *Aligned angular momentum, i_x, as a function of rotational frequency ω for the yrast bands in ^{120}Xe [TJJ+94], ^{122}Xe [TSR+94], ^{124}Xe [AKHB+08], ^{126}Xe [WJA+91] and ^{128}Xe [OBE+06]. A reference core with Harris parameters $\mathcal{I} = 16$ $\hbar^2/MeV$ and $\mathcal{I} = 26$ $\hbar^4/MeV^3$ was subtracted.*

see Fig. 8.19. In addition, side-feeding transitions into the $I^\pi = 22^+$ and 24^+ levels are observed. Previous investigations on neighbouring nuclei have shown that above a spin value of $I \simeq 20$ the collective rotational character gives place to an irregular level pattern which indicates a competition between collective and single-particle configurations, see e.g., [SHD+04, TSR+94, GMB+96, AKSH+06]. Especially, in ^{122}Xe similar branchings and side-transitions have been observed [TSR+94] for which a number of configurations of the type $\pi[(h^2_{11/2})^2(g_{7/2}d_{5/2})^2] \otimes \nu[(h_{11/2})^4(g_{7/2}d_{5/2})^{-1}(s_{1/2})^1]$ have been suggested [TSR+94]. Single-particle configurations of this type probably explain the irregular states observed at the top of band 5 in ^{124}Xe.

Band A

The new sequence A has an initial alignment of about $i_x = 9.5\ \hbar$ (Fig. 8.15(c)) and crosses the ground-state band at a rotational frequency of $\omega_c = 0.41$ MeV/$\hbar$, see Fig. 8.16(c). The lowest levels of this band were known from previous work [SCW+99, SDM+04]. It has been suggested that it has the two quasi-proton configuration $A_\pi B_\pi$ of $\pi h^2_{11/2}$ parentage. Similar bands have been observed in ^{122,126,128}Xe [TSR+94, SLD+93, OBE+06]. Moreover, a comparison with UC calculations supports this assignment.

Band B

Band B starts with an initial alignment of $i_x \approx 5\ \hbar$ and undergoes a band crossing at a rotational frequency of $\omega_c \approx 0.44$ MeV/$\hbar$ with an alignment gain of $\Delta i_x \approx 5.6\ \hbar$, see Fig. 8.15(c).

As band B has negative parity, its configuration has to include an odd number of the unique-parity $h_{11/2}$ quasi-particles. One quasi-proton of $h_{11/2}$ parentage is already present in bands 6 and 7, which have the configurations $A_\pi E_\pi$ and $A_\pi F_\pi$ of $\pi h_{11/2}(g_{7/2}, d_{5/2})$ parentage, respectively, below the two-quasi-neutron crossing. Thus, we propose the configuration $\nu h_{11/2}(g_{7/2}, s_{1/2})$ $(A_\nu E_\nu)$ below and $\nu h_{11/2}(g_{7/2}, s_{1/2}) \otimes \nu h^2_{11/2}$ $(A_\nu E_\nu B_\nu C_\nu)$ above the band crossing.

The alignments of band B in ^{124}Xe and band N3 in ^{122}Xe are compared in Fig. 8.20. While band N3 shows a smooth up-bending around $\omega_c \approx 0.45$ MeV/$\hbar$, band B undergoes a back-bending around $\omega_c \approx 0.44$ MeV/$\hbar$. Band N3 was explained to be built on the $A_\nu E_\nu$ configuration and the alignment gain was attributed to an alignment of two quasi-protons $A_\pi B_\pi$ [TSR+94]. This would be an alternative explanation for band B in ^{124}Xe.

8.4.3 Non-Rotational Structures

The irregular structures C and D show large aligned angular momenta, i_x, see Fig. 8.15(f), which indicates multi-quasi-particle excitations. They are energetically favoured above spin $I = 27$, see Fig. 8.18, which may explain their relatively large intensities at high spins.

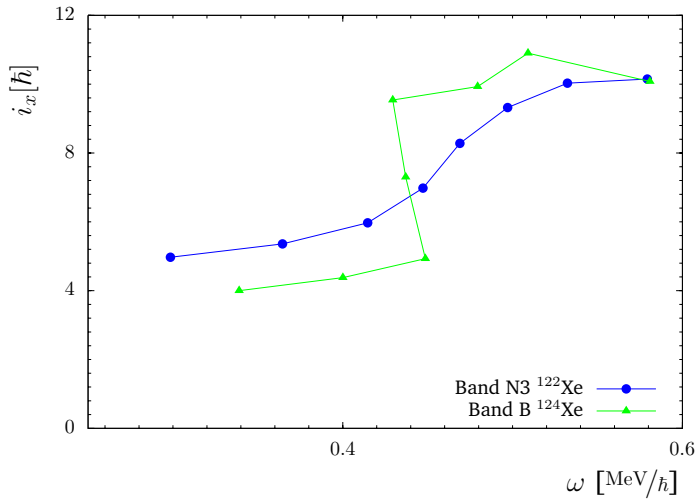

Figure 8.20: *Aligned angular momentum, i_x, as a function of rotational frequency, ω, for band A in ^{124}Xe compared to band N3 in ^{122}Xe [TSR+94].*

Structure C becomes irregular quickly with increasing spin. As can be seen in Fig. 8.1, levels from structure C mix with and decay into the positive-parity bands A, 3, 4 and 5, which contain an even number of proton or neutron quasi-particles of $h_{11/2}$ parentage. Accordingly, we may assume that structure C contains an even number of both, proton and neutron quasi-particles. Due to the opposite shape-driving effects of the $h_{11/2}$ protons and neutrons, it probably assumes a small triaxial or oblate shape.

Structure D decays through several decay-paths into the negative-parity bands 6, 7 and B, see Fig.8.1, where an odd number of quasi-particles is involved in the configuration. Negative parity could be assigned to most of the levels of group D. Thus, it is very likely that they also contain an odd number of $h_{11/2}$ quasi-particles.

Single-particle configurations with triaxial and oblate shapes contain five or six neutrons in the $h_{11/2}$, $d_{3/2}$ and $s_{1/2}$ orbitals and four protons in the $h_{11/2}$, $g_{7/2}$ and $d_{5/2}$ sub-shells. The transition from collective excitation to such non-collective excitations starts around spin $I = 22$ and reaches favourable terminating states when these particles are fully aligned. As can be seen in Fig. 8.18, an interesting feature is the observation of collective and single-particle excitations at similar energies over a rather wide spin range. Examples of configurations of terminating states are $\{\pi[(h_{11/2})^2(g_{7/2}d_{5/2})^2]_{16^+}\nu[(h_{11/2})^4(d_{3/2}s_{1/2})^2]_{18^+}\}_{34^+}$ and $\{\pi[(h_{11/2})^2(g_{7/2}d_{5/2})^2]_{16^+}\nu[(h_{11/2})^5(d_{3/2}s_{1/2})^1]_{19^-}\}_{35^-}$.

For high-spin states, typically above spin 20, CNS calculations without pairing provide configurations of terminating states in good agreement with experiment. In addition to the two configurations given above, favourable terminating states with $I^\pi = 32^-$ and 33^+ are found in such calculations. They contain one $h_{11/2}$ proton and four and five $h_{11/2}$ neutrons, respectively. States in sequences C and D may be associated with such configurations.

Chapter 9

High-Spectroscopy of ^{125}Xe

9.1 Introduction

Shape co-existence in ^{125}Xe has been established using in-beam γ-ray spectroscopy [HHL79, HJA+81, AGH+84, LGG+91, GLG+91, WUC+93, WYN+95, MLK+07]. Recently long high-spin bands extending into the spin 50 to 60 region have been identified in ^{125}Xe [AKHB+07] and ^{126}Xe [RHSH+07] . Four such bands in ^{126}Xe are connected to the low-spin structures and their spins and parities are firmly determined [RHSH+07]. They have been interpreted to be based on aligned $g_{7/2}$ and $h_{11/2}$ quasi-protons and $h_{11/2}$ and $i_{13/2}$ quasi-neutrons [RHSH+07]. Six similar bands exist in ^{125}Xe. Only two of them are connected to known levels. The $F(\tau)$ investigation indicates that their quadrupole deformation is higher than that of low spin bands. In the following, the new bands will be presented and the $F(\tau)$ analysis of the long bands will be explained.

9.2 Experimental Results

The level structures of the ^{125}Xe nucleus had been investigated previously up to a spin of about 20 $\hbar$ [HHL79, GLG+91, WUC+93, WYN+95]. In the present study, the level scheme has been significantly extended. The analysis has revealed six new long bands extending up to a spin of about $I \approx 60$. Two of the bands are linked to the low-spin states. Only the results for the high-spin states will be presented.

Level Scheme

The level scheme deduced for ^{125}Xe from this work is shown in Fig. 9.1. The low-spin structures have been adopted from previous work [GLG+91, WUC+93]. Some of them have been extended to higher spins. Six new long bands labelled L1, L2, L3, L4, L5 and L6 and the short side bands labelled L1a, L5a and L6a have been identified for the first time in this work. The angular correlation ratios of the γ-ray transitions of bands L3, L4, L5a and L5a are compatible with stretched quadrupole, probably $E2$, character [Eng04]. For bands L1, L2, L6 and L6a, $E2$ multipolarity may be assumed. Bands L1, L2, L3 and L6 could not be connected to known low-spin states. Thus, their spins, parities and excitation energies are not known. The decay paths from bands L4 and L5 to the low-spin states have been suggested as shown in Fig. 9.1. However, these decays could not be unambiguously determined.

9.2.1 Band L1

A new sequence of γ rays, labelled L1, with energies of 1071, 1117, 1201, 1301, 1412, 1524, 1636, 1731, 1812, 1922, 2035, 2149 and 2263 keV and a short side-branch, labelled L1a, with transitions of 1753, 1868, 1979 and 2087 keV have been observed. Band L1a is tentatively connected to L1 via the 1659 and 1681 keV γ rays. A coincidence spectrum is shown in Fig. 9.2. The band L1 could not be linked to the low-spin structures, thus, excitation energies, spins and parities remain undetermined. $E2$ multipolarity has been assumed for the γ-ray transitions.

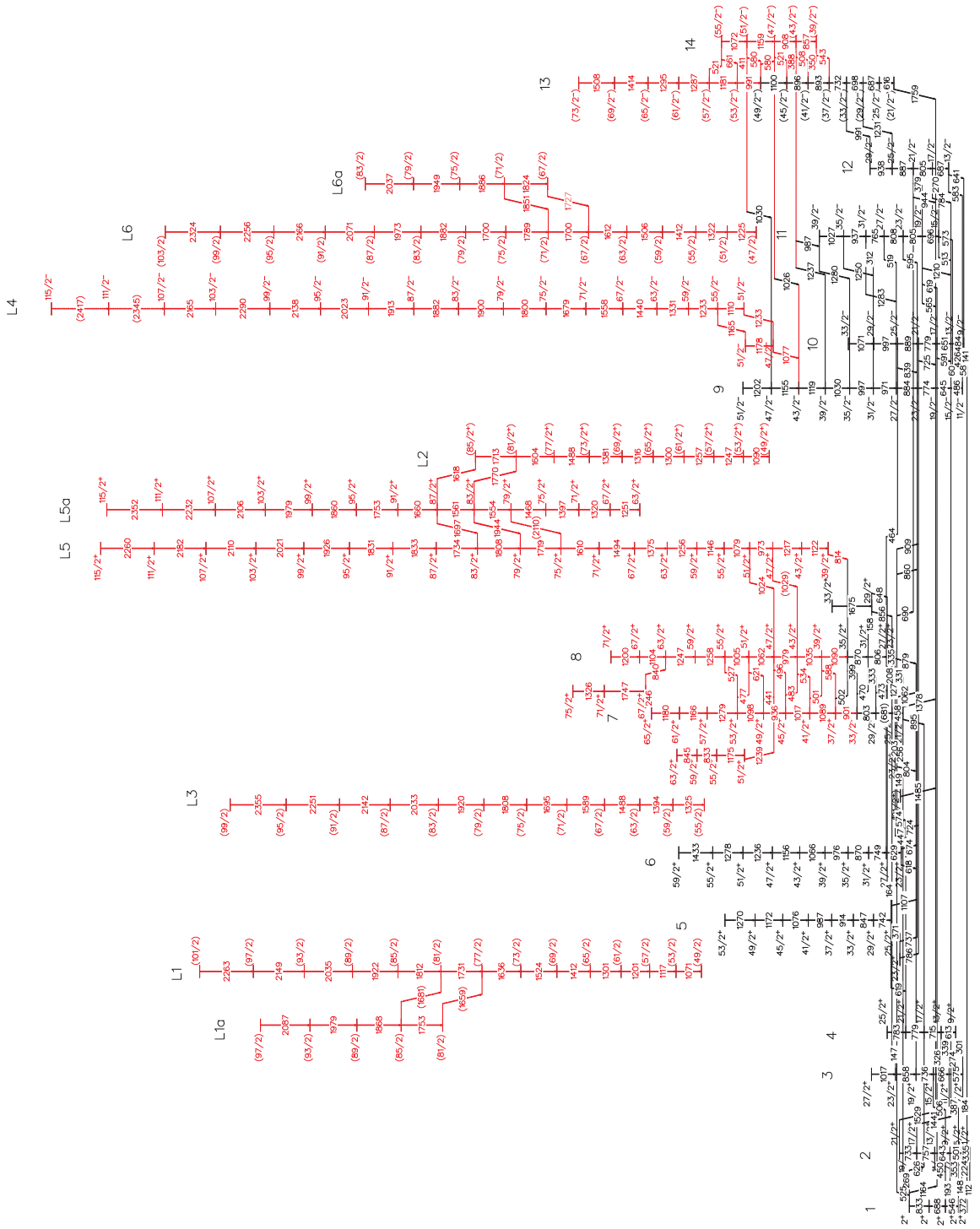

Figure 9.1: *Level scheme of ^{125}Xe deduced from this study. The low-spin structures were adopted from previous work [GLG+91, WUC+93]. Transition energies are given in keV. Parities and spins in parentheses are tentatively assigned, and dashed transitions are tentatively placed. The new structures are drawn with red colour.*

9.2.2 Band L2

The new cascade L2 with γ-ray transitions of 1090, 1247, 1257, 1300, 1316, 1381, 1488, 1604 and 1713 keV has also been observed for the first time in this work. $E2$ multipolarity has been assumed for the in-band transitions. No connections to low-spin structures could be established. Therefore, their

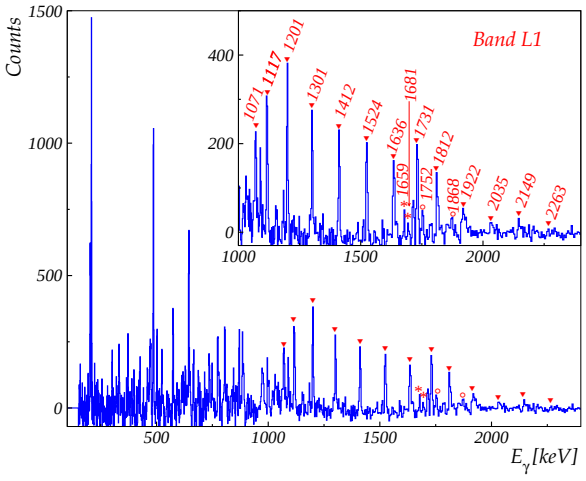

Figure 9.2: *Triple-gated, background-subtracted, γ-ray coincidence spectrum showing transitions of bands L1 and L1a in ^{125}Xe. The spectrum has been generated by summing all possible combinations of triple gates of the form $(A \times A \times A)$ where A is a gate list of transitions with energies of 1071, 1117, 1201, 1301, 1412, 1524, 1636, 1731, 1812, 1922, 2035, 2149 and 2263 keV. The filled triangles (▼) denote peaks of band L1. Transitions from the side-branch L1a are marked with open circle (○). Single asterisks (∗) indicate possible decay-out transitions from L1a to L1. The inset shows the transitions of bands L1 and L1a listed in keV. The unmarked transitions are low-lying γ rays in ^{125}Xe.*

excitation energies, spins and parities are not known. Figure 9.3 presents a γ-ray coincidence spectrum of band L2.

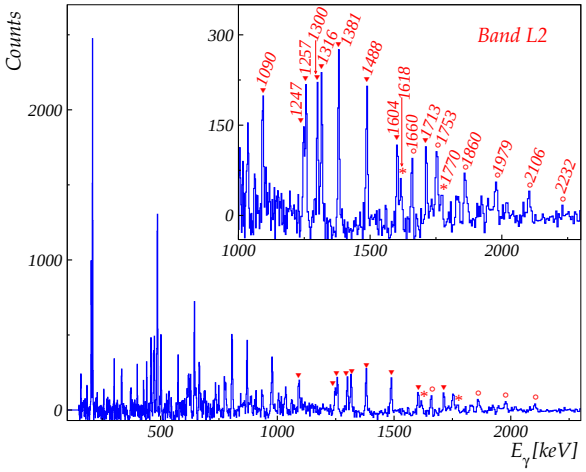

Figure 9.3: *Triple-gated, background-subtracted, γ-ray coincidence spectrum showing transitions of band L2 in ^{125}Xe. The spectrum has been generated by summing all possible combinations of triple gates of the form $(A \times A \times A)$ where A is a gate list of energies of 1090, 1247, 1257, 1300, 1316, 1381, 1488, 1604 and 1713 keV. The filled triangles (▼) mark peaks of band L2. Transitions of band L5a are denoted with open circles (○). Single asterisks (∗) indicate linking transitions from L5a to L2. The inset shows the transitions of bands L2 and L5a. The unmarked transitions are low-lying γ rays in ^{125}Xe.*

9.2.3 Band L3

Band L3 consists of eleven transitions with energies of 1325, 1394, 1488, 1589, 1695, 1808, 1920, 2033, 2142, 2251 and 2356 keV. As band L3 is not linked to the low-spin levels, its excitation energies, spins and parities remain undermined. The angular correlation ratios of the γ-ray transitions are compatible with stretched quadrupole, probably $E2$, multipolarity [Eng04]. A gated γ-ray spectrum of band L3 is shown in Fig. 9.4.

9.2.4 Band L4

The new sequence labelled L4 with γ rays of energies 1110, 1233, 1331, 1440, 1558, 1679, 1800, 1900, 1882, 1913, 2023, 2138, 2290, 2165, 2345 and 2417 keV has been identified. It decays to the $I^\pi = {}^{43}/_{2}^{-}$ level of band 11 via the transitions of 1233 and 1077 keV and the decay path with γ rays of 1166, 1178 and 1077 keV. A representative γ-ray spectrum of band L4 is shown in Fig. 9.5. The angular correlation ratios of the in-band and the decay-out transitions are compatible with a stretched $E2$ multipolarity [Eng04]. As the band decays into the $I^\pi = {}^{43}/_{2}^{-}$ level of band 11, spin and parity $I^\pi = {}^{51}/_{2}^{-}$ have been assigned to the lowest level of the band. Therefore, band L4 extends up to spin $I^\pi = {}^{115}/_{2}^{-}$ and an excitation energy of $E_x = 38.752$ MeV.

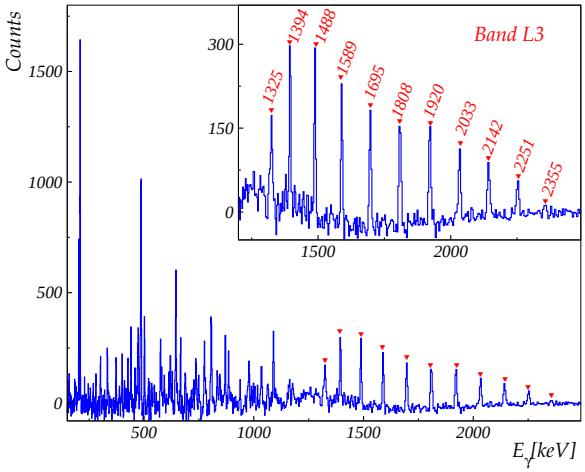

Figure 9.4: *Triple-gated, background-subtracted, γ-ray coincidence spectrum showing transitions from band L3 in ^{125}Xe. The spectrum has been obtained by summing all possible combinations of triple gates of the form ($A \times A \times A$) where A is a gate list of energies of 1325, 1394, 1488, 1589, 1695, 1808, 1920, 2033, 2142, 2251 and 2356 keV. The filled triangles (▼) indicate transitions of band L3. The inset shows the transitions listed in keV of band L3. The unmarked transitions are low-lying γ rays in ^{125}Xe.*

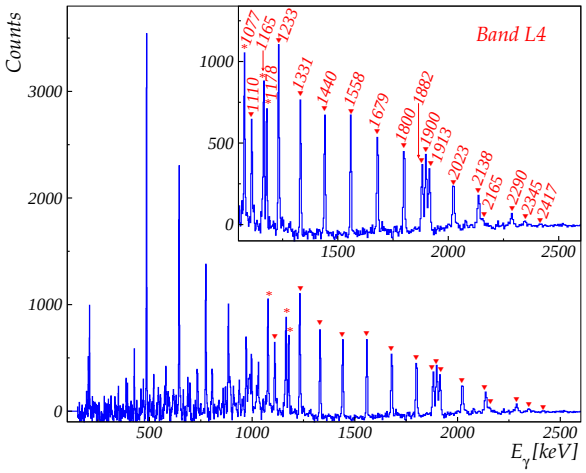

Figure 9.5: *Triple-gated, background-subtracted, γ-ray coincidence spectrum showing transitions from band L4 in ^{125}Xe. The spectrum has been produced by summing all possible combinations of triple gates of the form ($A \times A \times A$) where A is a gate list of energies of 1110, 1233, 1331, 1440, 1558, 1679, 1800, 1900, 1882, 1913, 2023, 2138, 2290, 2165, 2345 and 2417 keV. The filled triangles (▼) mark peaks of band L4. The decay-out transitions are denoted with single asterisks (∗). The inset shows the transitions listed in keV of bands L4. The unmarked transitions are low-lying γ rays in ^{125}Xe.*

9.2.5 Bands L5 and L5a

A new sequence of γ rays, labelled band L5, with energies of 1122, 1217, 973, 1079, 1146, 1256, 1375, 1494, 1610, 1719, 1808, 1734, 1833, 1831, 1926, 2021, 2110, 2182 and 2260 keV has been established. Band L5a forms a sequence of γ rays with energies of 1251, 1320, 1397, 1468, 1554, 1561, 1660, 1753, 1860, 1979, 2106, 2232 and 2352 keV. Band L5a decays into band L5 via the 1697 and 1944 keV transitions and the tentative 2110 keV line. Also decay paths via the 1770 and 1618 keV γ rays to the upper part of band L2 have been identified. Figure 9.6 shows coincidence spectra of bands L5 and L5a.

Band L5 decays via the 814 keV γ-ray transition to the $I^\pi = {}^{35}/_{2}^{+}$ level of band 8 and via the 1024 kev γ ray to the $I^\pi = {}^{47}/_{2}^{+}$ state. The angular correlation ratios of the in-band and the linking transitions suggest $E2$ character [Eng04]. Therefore, spin and parity $I^\pi = {}^{39}/_{2}^{+}$ have been given to the lowest level, extending the band to the $I^\pi = {}^{115}/_{2}^{+}$, E_x = 36.675 MeV level. The angular correlation ratios of the in-band transition of band L5a and the decay-out transitions to band L5 are also compatible with $E2$ character. Thus, spin and parity $I^\pi = {}^{63}/_{2}^{+}$ have been assigned to the band head.

9.2.6 Band L6

The new γ-ray cascade labelled L6 consists of fourteen transitions with energies of 1225, 1322, 1412, 1506, 1612, 1700, 1789, 1700, 1882, 1973, 2071, 2166, 2256 and 2324 keV. Furthermore, a side-branch, labelled L6a, with energies of 1824, 1886, 1949 and 2037 keV has been observed. It decays into band L6 via the 1727 and 1851 keV γ rays. Since the band is not connected to the levels with known spins and parities, spins, parities and excitation energies are unknown. A representative spectrum of band L6 is shown in Fig 9.7. $E2$ multipolarity may be assumed for the in-band transitions.

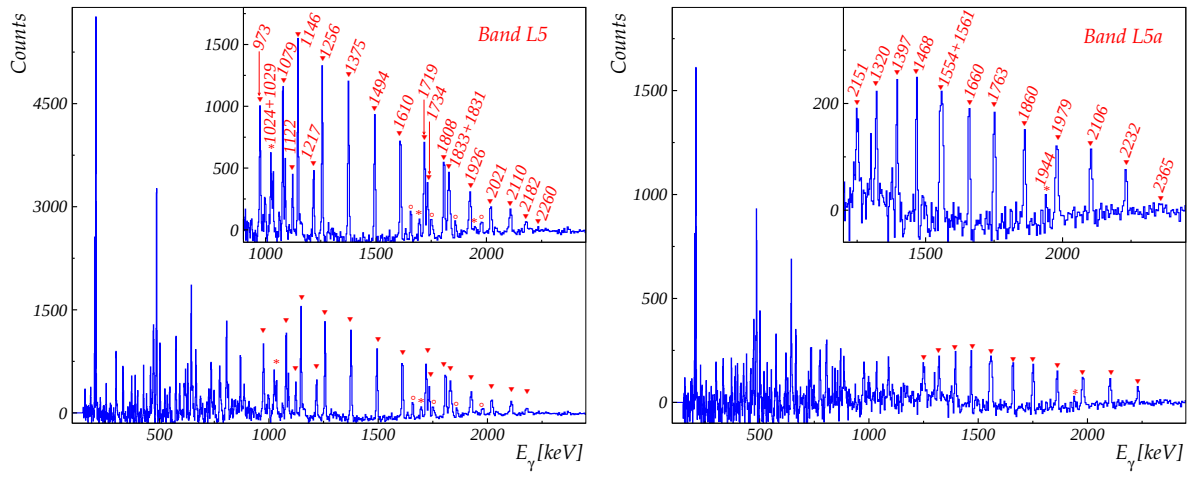

Figure 9.6: *Triple-gated, background-subtracted, γ-ray coincidence spectra for bands L5 ((a)) and L5a ((b))in ^{125}Xe. The spectrum of band L5 ((a)) has been generated by summing all possible combinations of triple gates of the form $(A \times A \times A)$ where A is a gate list of energies of 1079, 1146, 1256, 1375, 1494, 1610, 1719, 1808, 1734, 1833, 1831, 1926, 2021 and 2110 keV. The spectrum of band L5a ((b)) has been obtained by summing all possible combinations of triple gates of the form $(A \times A \times A)$ where A is a gate list of energies of 1251, 1320, 1397, 1468, 1554, 1561, 1660, 1753, 1860, 1979, 2106, 2232 and 2352 keV. The filled triangles (▼) denote peaks of bands L5 and L5a. Open circles (○) in the upper panel denote transitions of band L5a. Single asterisks (∗) indicate possible decay-out transitions from L5 to band 10 and from L5a to L5. The inset shows the transitions listed in keV of bands L5 and L5a. The unmarked transitions are low-lying γ rays in ^{125}Xe.*

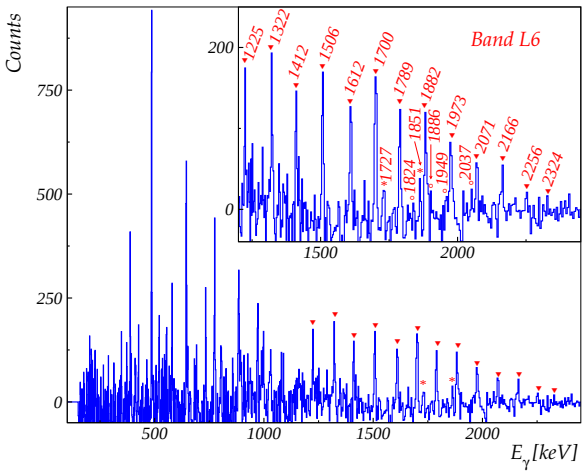

Figure 9.7: *Triple-gated, background-subtracted, γ-ray coincidence spectrum showing transitions of bands L6 (filled triangles (▼)) and L6a (open circles (○)) in ^{125}Xe. The spectrum has been obtained by summing all possible combinations of triple gates of the form $(A \times A \times A)$ where A is a gate list of energies of 1225, 1322, 1412, 1506, 1612, 1700, 1789, 1700, 1882, 1973, 2071, 2166, 2256 and 232 keV. Single asterisks (∗) indicate linking transitions from L6a to L6. The inset shows the transitions listed in keV of bands L6 and L6a. The unmarked transitions are low-lying γ rays in ^{125}Xe.*

9.2.7 $F(\tau)$-Analysis for the Long Bands

Usually, a thin target on a thick backing is used in DSAM experiments, where the recoil nuclei are stopped completely in the backing. In our experiment a thin target of 500 $\mu g/cm^2$ thickness was used, therefore, it was not possible to perform a proper Doppler-shift lifetime measurement to obtain the transition quadrupole moments from the transition probabilities. Nonetheless, due to the high γ-ray transition energies ($E_\gamma \approx 1.0-2.5$ MeV) of the long bands, and because of the E^5 dependence of the $E2$-transition probabilities, the lifetimes are expected to be very short so that a large portion of the γ rays are emitted from the recoiling nuclei along their travel through the target material. As the velocity distribution of the recoiling nuclei is changing as a function of time during their passage through the target, the emitted γ rays show different Doppler shifts. Indeed, $\frac{v(t)}{c}$ varies by about 6% from one end of the target to the other in our experiment. This effect can be used to measure the fractional Doppler shifts and to estimate

the lifetimes for the fastest γ-ray transitions as demonstrated in [CLA+95, NHAK+04, RHSH+07].

The fractional Doppler shifts, $F(\tau)$, have been determined for 10 transitions (1117, 1201, 1301, 1412, 1524, 1636, 1731, 1812, 1922 and 2035 keV) from band L1, eight transitions (1394, 1488, 1589, 1695, 1808, 1920, 2033 and 2142 keV) from band L3, nine transitions (1233, 1331, 1440, 1558, 1679, 1800, 1900, 1882 and 1913 keV) from band L4, ten transitions (1079, 1146, 1256, 1375, 1494, 1610, 1719, 1808, 1734 and 1833 keV) from band L5 and for ten transitions (1225, 1322, 1412, 1506, 1612,

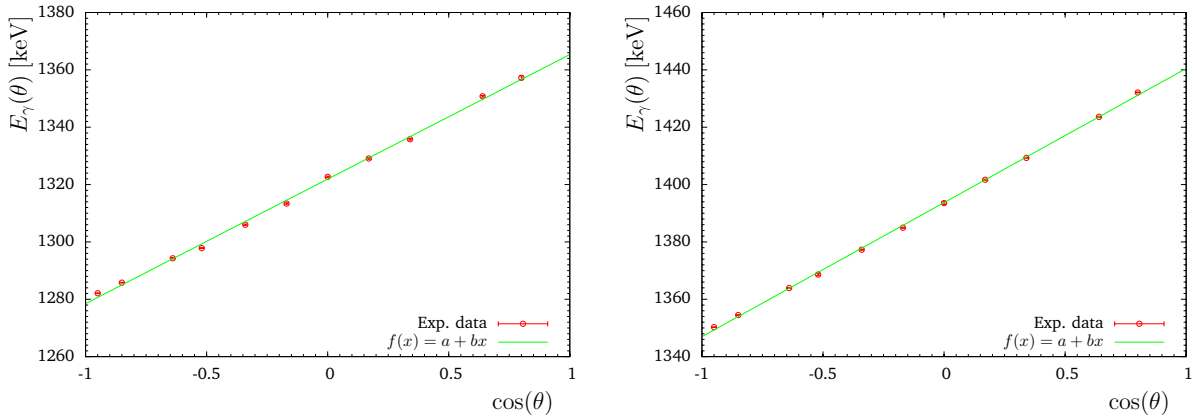

(a) $E_\gamma = 1325$ *keV* ***(b)*** $E_\gamma = 1394$ *keV*

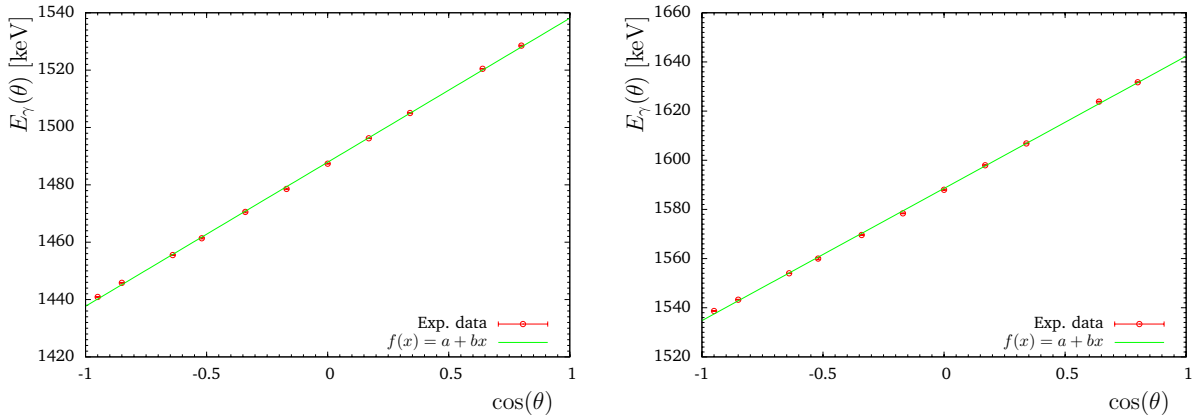

(c) $E_\gamma = 1488$ *keV* ***(d)*** $E_\gamma = 1589$ *keV*

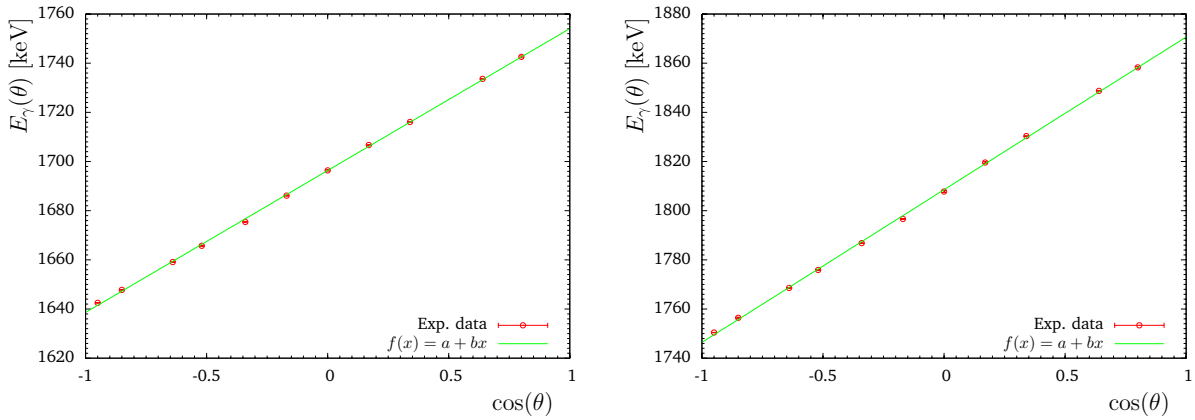

(e) $E_\gamma = 1695$ *keV* ***(f)*** $E_\gamma = 1808$ *keV*

Figure 9.8: *Plots of the γ-ray energies, $E_\gamma(\theta)$, as a function of detector angles, $\cos(\theta)$, for transitions in band L3.*

1700, 1789, 1882, 1973 and 2071 keV) from band L6.

To extract $F(\tau)$ from the experimental data, γ-ray-gated spectra have been sorted for different Ge-detector angle groups relative to the beam direction. The shifted γ-ray transitions, $\langle E_\gamma^D(\theta)\rangle$, have been measured at different angles, θ, relative to the beam direction. The fractional shifts can be calculated from eq. 5.14. The Doppler-shifted energies are plotted as a function of $\cos(\theta)$, and a linear fit to the data

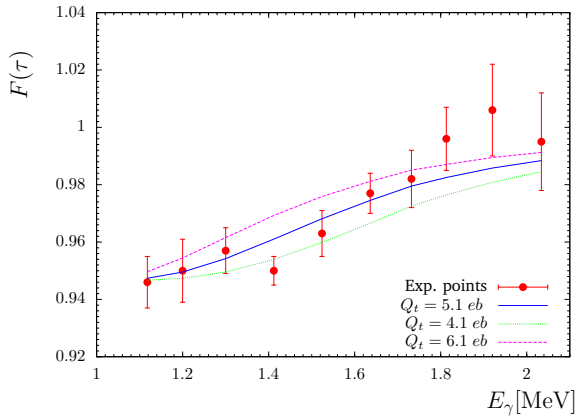

(a) *Band L1*

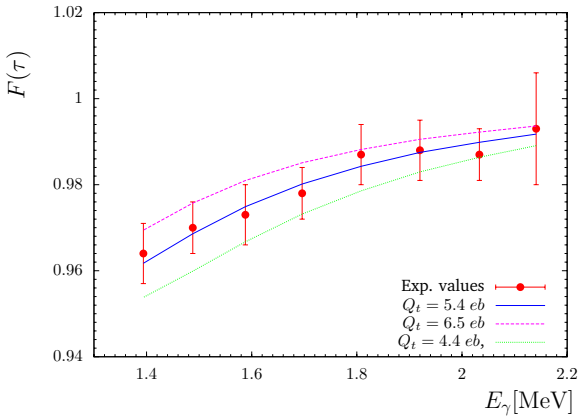

(b) *Band L3*

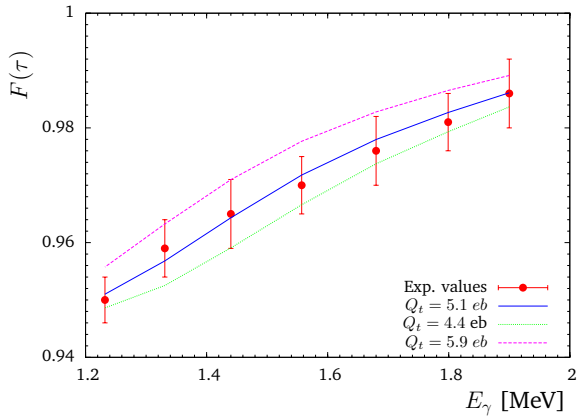

(c) *Band L4*

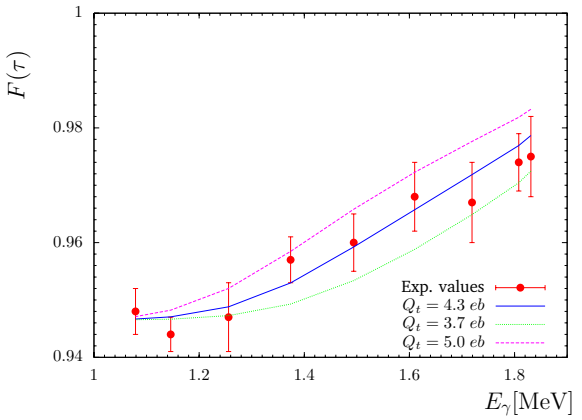

(d) *Band L5*

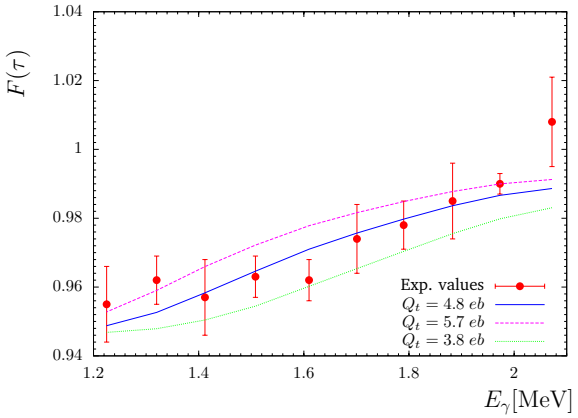

(e) *Band L6*

Figure 9.9: *Experimental (data points ●) and calculated (curves) fractional Doppler shifts, $F(\tau)$, for bands L1, L3, L4, L5 and L6 in ^{125}Xe. The curves for the upper (dashed line) and lower (dotted line) limits resulting from the uncertainty of the quadrupole moment are shown for comparison.*

provides the slope which is used to determine the $F(\tau)$ value for each transition. Figure 9.8 demonstrates this procedure for several transitions in band L3. In Fig. 9.9 the experimental $F(\tau)$ values are plotted versus γ-ray transition energy for bands L1, L3, L4, L5 and L6 and are compared to the calculated $F(\tau)$ values.

For the calculations the simulation program *Ft_Fit_30* [Moo96] was used, see section 5.5.2 for details. The program uses the least-squares method and produces a matrix of χ^2-values as a function of Q_t and Q_{sf}. We have considered the best fit to be with $Q_{sf} \approx 0.8\ Q_t$ and the smallest χ^2-value. The uncertainties of the quadrupole moments have been taken into account by including the upper and the lower limits of the calculations, see Fig. 9.9. The obtained Q_t and Q_{sf} values are listed in table 9.1.

Table 9.1: *Experimental transition and side-feeding quadrupole moments, Q_t and Q_{sf}, respectively, for bands L1, L3, L4, L5 and L6 in ^{125}Xe extracted form the present $F(\tau)$ analysis.*

Band	Q_t [b]	Q_{sf} [b]
L1	5.1 ± 1.0	$4.0\ ^{0.9}_{0.7}$
L3	$5.4\ ^{+1.1}_{-1.0}$	$4.2\ ^{1.0}_{0.7}$
L4	$5.1\ ^{+0.8}_{-0.7}$	$4.1\ ^{0.6}_{0.7}$
L5	$4.3\ ^{+0.7}_{-0.6}$	$3.4\ ^{0.6}_{0.5}$
L6	$4.8\ ^{+0.9}_{-1.0}$	$3.9\ ^{1.2}_{0.9}$

9.3 Band Structures in ^{125}Xe

The interpretation of the band structures is based on the observed aligned angular momenta, i_x, band-crossing frequencies, ω_c, dynamic moments of inertia, $\mathscr{J}^{(2)}$, quadrupole moments, Q, and excitation energies, E_x.

In the lower-spin region, where the deformation is small and the shape is fluctuating, the configurations are dominated by $h_{11/2}$ and $g_{7/2}$ neutrons and $h_{11/2}$ and $g_{7/2}$ protons [HHL79, GLG+91]. The following discussion is restricted to the long high-spin bands.

9.3.1 Dynamic Moments of Inertia

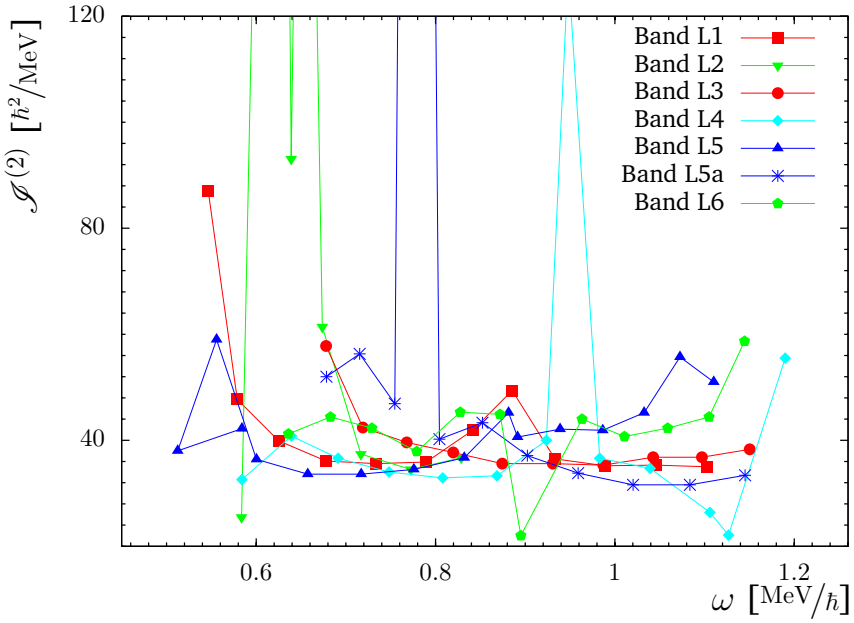

Figure 9.10: *Dynamic moments of inertia, $\mathscr{J}^{(2)}$, as a function of rotational frequency, ω, for high-spin bands in ^{125}Xe.*

The spin-independent quantity, the dynamic moment of inertia, $\mathscr{J}^{(2)}$, can be used to draw conclusions about the configurations of the bands for which spin, I, and parity, π, are not firmly determined.

The dynamic moments of inertia of bands L1, L2, L3, L4, L5, L5a and L6 are plotted in Fig 9.10 for comparison.

The dynamic moments of inertia exhibit a different behaviour as a function of rotational frequency. Bands L1, L2, L3 and L4 remain rather stable with an average value of $\mathcal{J}^{(2)} \approx 35\ \hbar^2/\mathrm{MeV}$ in the medium frequency range. The stable moments of inertia indicate constant deformation and the absence of band crossings. Large fluctuations are also observed at low rotational frequency for bands L2 and L5a which my be explained by interactions between nuclear levels of bands L2, L5 and L5a and configuration changes. At higher rotational frequencies, the dynamic moments of inertia of band L1 exhibit a small change at a rotational frequency of $\omega \approx 0.825\ ^{\mathrm{MeV}}/_{\hbar}$ while in band L4 it changes drastically at a rotational frequency of $\omega \approx 0.947$ which may be attributed to a crossing with another configuration. Moreover, the $\mathcal{J}^{(2)}$ of band L4 shows a minimum at a rotational frequency of $\omega \approx 1.126\ ^{\mathrm{MeV}}/_{\hbar}$ and then increases suddenly which may also be explained by interaction with other levels.

In contrast to the other high-spin bands, the dynamic moments of inertia of band L5 increase slightly with rotational frequency. At low frequency a small change in $\mathcal{J}^{(2)}$ is seen, probably due to interaction with band 8. In the frequency ranges of $\omega \approx 0.600$–$0.832\ ^{\mathrm{MeV}}/_{\hbar}$ and 0.981–$0.986\ ^{\mathrm{MeV}}/_{\hbar}$, the dynamic moments of inertia of band L5 show a stable behaviour with an average value of $\mathcal{J}^{(2)} \approx 35$ and $41\ \hbar^2/\mathrm{MeV}$, respectively. Small changes are observed at $\omega \approx 0.881$ and $1.070\ ^{\mathrm{MeV}}/_{\hbar}$, which may be caused by interaction with levels from band L5a and other configurations, respectively.

The dynamic moments of inertia of band L6 show two minima, a shallow one at $\omega \approx 0.779\ ^{\mathrm{MeV}}/_{\hbar}$ and a deeper one at $\omega \approx 0.985\ ^{\mathrm{MeV}}/_{\hbar}$. They may be attributed to configuration changes and interactions with levels from band L6a, respectively.

Similar long high-spin bands have been established in ^{126}Xe [RHSH+07]. They are connected to the low-spin states and hence, their spin and parities are known. Quasi-particle configurations of the type $\pi(g_{7/2}h_{11/2})\otimes\nu(h_{11/2}i_{13/2})$ have been assigned to those bands [RHSH+07]. The structure of the long bands in ^{125}Xe is expected to be similar to those in ^{126}Xe. However, due to the additional odd quasi-particle, differences are expected for ^{125}Xe. The dynamic moments of inertia, $\mathcal{J}^{(2)}$, are plotted as a function of rotational frequency, ω, for the high-spin bands in ^{125}Xe and ^{126}Xe for comparison in Fig. 9.11.

9.3.2 Quadrupole-Deformation

The transition quadrupole moments, Q_t, determined from the experimental data for bands L1, L3, L4, L5, L5a and L6 can be used to estimate the quadrupole deformation, ε_2, using the following relations [PFG+01]

$$Q_t = Q_{20}\frac{\cos(\gamma+30^\circ)}{\cos(30^\circ)} \quad \text{and} \quad Q_{20} = 0.0109ZA^{2/3}\beta_2(1+0.36\beta_2) \tag{9.1}$$

where Q_t is the transition quadrupole moment, Q_{20} is the quadrupole moment, γ is the triaxial deformation parameter, Z is the proton number, A is the mass number and β_2 is the quadrupole deformation. Here, we use the parameter $\varepsilon_2 \approx 0.95\beta_2$ instead of β_2. The quadrupole deformations, ε_2, for bands L1, L3, L4, L5, and L6 are listed in table 9.2.

Band	Quadrupole deformation ε_2	
	$\gamma = 0^\circ$	$\gamma = 5^\circ$
L1	0.29	0.31
L3	0.31	0.33
L4	0.29	0.31
L5	0.26	0.27
L6	0.28	0.29

Table 9.2: *Quadrupole deformation parameters, ε_2, calculated from the experimental transition quadrupole moments, Q_t, for two different values of the triaxiality parameter γ.*

9.3.3 Cranked-Shell Model (CSM) Calculations

The calculations have been performed utilising the UC software package [Ben]. Potential-Energy Surfaces (PES) and the quasi-particle energies, Routhians, for neutrons and protons are calculated for differ-

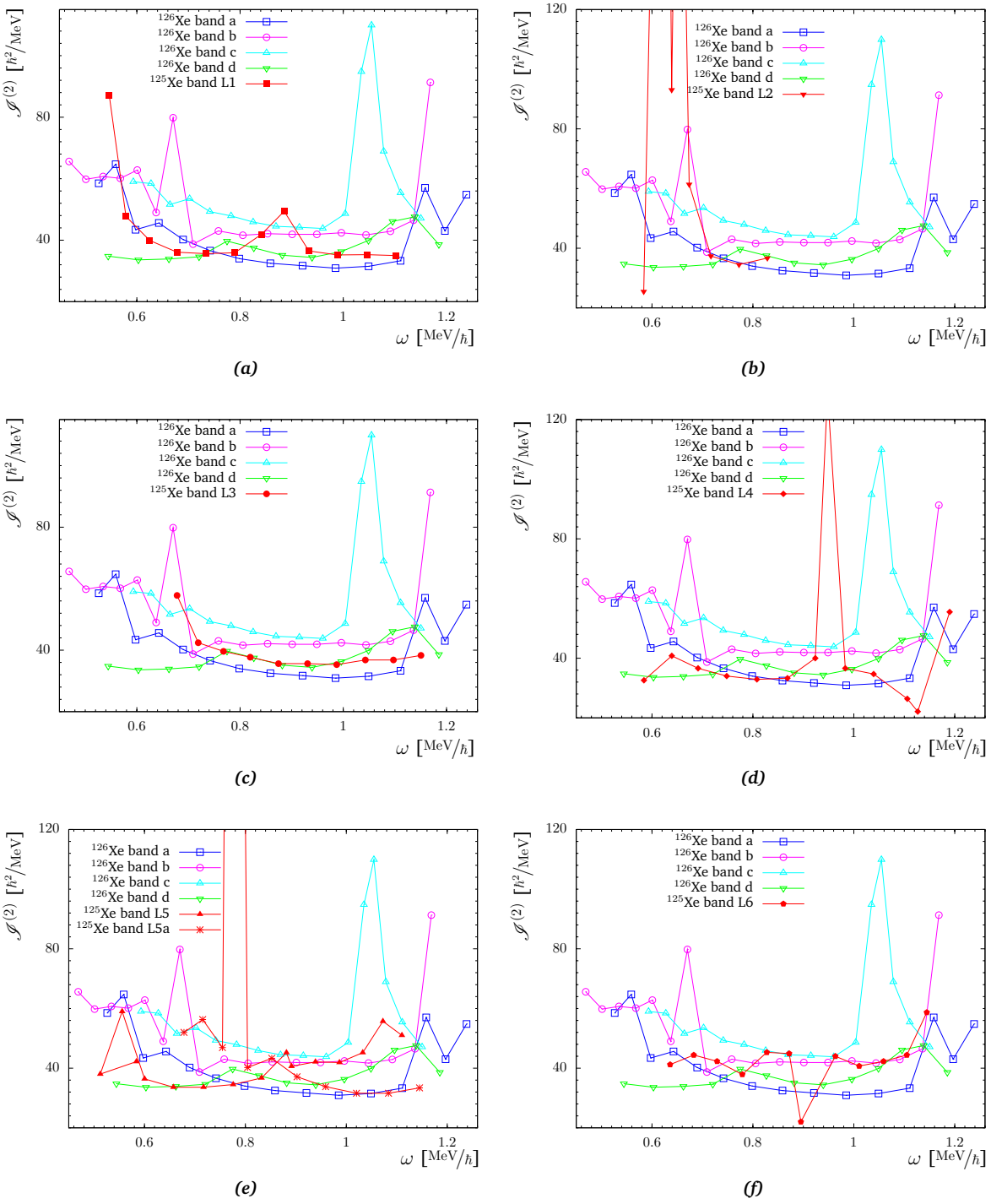

Figure 9.11: *Dynamic moments of inertia, $\mathscr{I}^{(2)}$, as a function of rotational frequency, ω, for bands L1 (a), L2 (b), L3 (c), L5 and L5a (e) and L6 (f) (filled symbols) in ^{125}Xe compared to $\mathscr{I}^{(2)}$ for similar long high-spin bands in ^{126}Xe [RHSH+07] (open symbols).*

ent configurations in ^{125}Xe. Figure 9.12 illustrates the PES calculated for the configuration $(\pi, \alpha) = (+, 1/2)$ at a spin value of $I = 61/2$. A minimum corresponding to ($\varepsilon \approx 0.34$, $\gamma \approx 5^\circ$) can be identified. It may correspond to one of the new observed long high-spin bands. Quasi-particle levels related to this minimum are shown in Fig. 9.13. It is observed, that $\nu i_{13/2}$ alignments occur at rotational frequencies of $\omega \approx 0.49$ and 0.91 MeV/$\hbar$ and $\nu h_{11/2}$ alignments take place at $\omega \approx 0.58$, 0.62 and 0.88 MeV/$\hbar$. Figure 9.14 presents PES calculation at higher spins for the configurations $(\pi, \alpha) = (+, 1/2), (+, -1/2), (-, 1/2)$ and $(-, -1/2)$.

Pronounced minima can be identified at ($\varepsilon_2 \approx 0.33,\ \gamma \approx 6^\circ$), ($\varepsilon_2 \approx 0.32,\ \gamma \approx 7^\circ$), ($\varepsilon_2 \approx 0.32,\ \gamma \approx 7^\circ$) and ($\varepsilon_2 \approx 0.30,\ \gamma \approx 7^\circ$) , see Figs. 9.14(a), 9.14(b), 9.14(c) and 9.14(d), respectively.

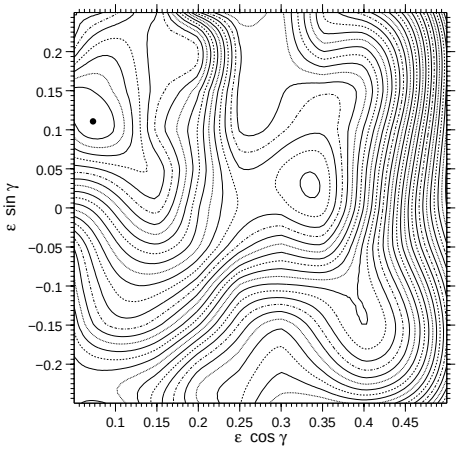

Figure 9.12: *Example of a potential-energy surface (PES) calculated with the Ultimate Cranker code for ^{125}Xe. The calculation has been performed for the configuration $(\pi, \alpha) = (+, 1/2)$ at spin $I = 61/2$. The minimum seen at ($\varepsilon_2 \approx 0.34,\ \gamma \approx 5^\circ$) may be responsible for the existence of one of the long high-spin bands.*

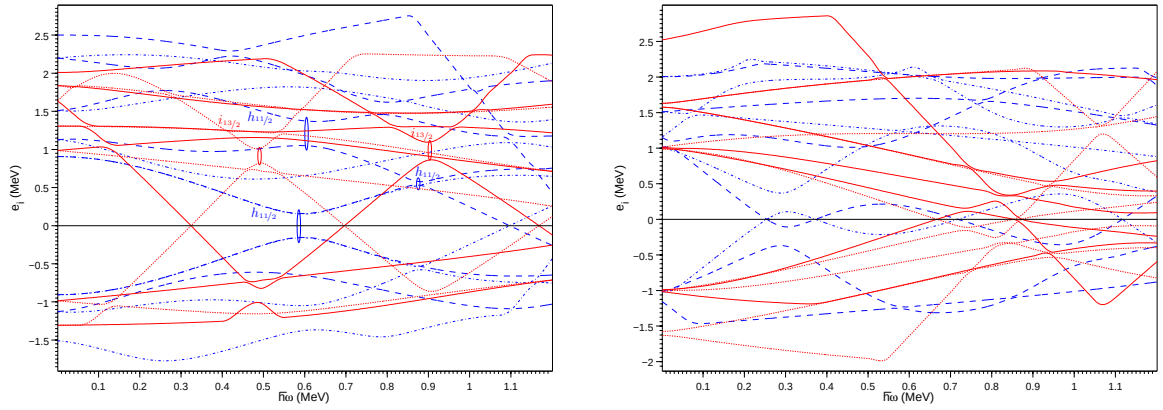

(a) ***(b)***

Figure 9.13: *Quasi-particle energies calculated as a function of rotational frequency for neutrons (a) and protons (b) at a deformation corresponding to the minimum ($\varepsilon \approx 0.34,\ \gamma \approx 5^\circ$). The parity and signature (π, α) of the levels are: $(+, +1/2)$–solid lines; $(+, -1/2)$–dotted lines; $(-, -1/2)$–dashed lines; $(-, +1/2)$–dot-dashed lines.*

9.4 Configuration Assignments

In the following, only the configuration of the new long high-spin bands will be discussed. According to the calculations, strongly prolate-driving intruder configurations are responsible for the observed properties of the bands. They are of neutron- $h_{11/2}$ and $i_{13/2}$ origin, but also further $h_{11/2}$ and $g_{7/2}$ proton orbitals play a role.

9.4.1 Band L1

Band L1 shows a constant dynamic moment of inertia, $\mathcal{J}^{(2)}$, in the frequency range ω = 0.6–1.1 $^{\mathrm{MeV}}/_{\hbar}$ and undergoes a band-crossing around a rotational frequency of $\omega \approx 0.68$ $^{\mathrm{MeV}}/_{\hbar}$, see Fig. 9.10. The trend of the $\mathcal{J}^{(2)}$ curve of this band is similar to that of band c in ^{126}Xe [RHSH+07] which suggest

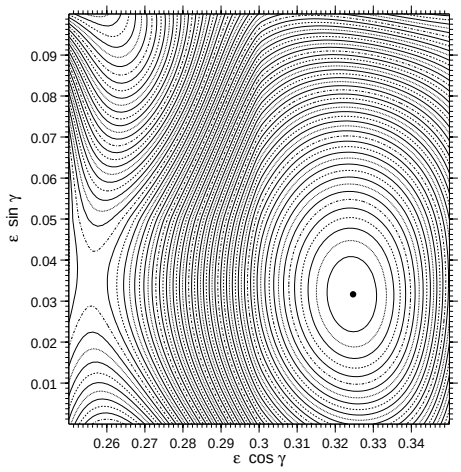

(a) *Pronounced minimum at* ($\varepsilon_2 \approx 0.33,\ \gamma \approx 6^\circ$)

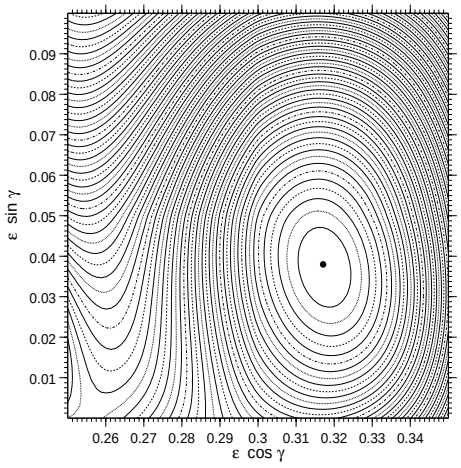

(b) *Pronounced minimum at* ($\varepsilon_2 \approx 0.32,\ \gamma \approx 7^\circ$)

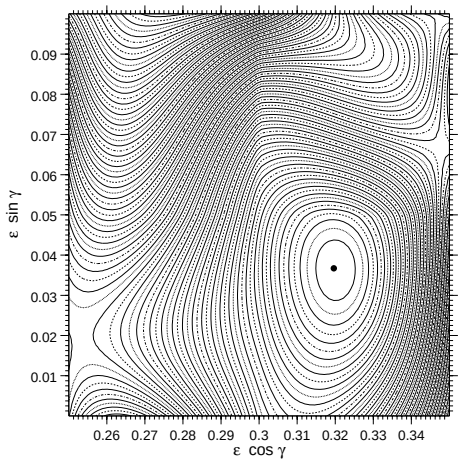

(c) *Pronounced minimum at* ($\varepsilon_2 \approx 0.32,\ \gamma \approx 7^\circ$)

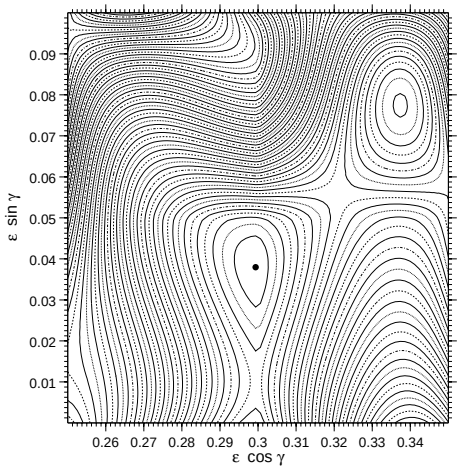

(d) *Pronounced minimum at* ($\varepsilon_2 \approx 0.30,\ \gamma \approx 7^\circ$)

Figure 9.14: *Examples of potential-energy surfaces (PES) calculated with the Ultimate Cranker code for ^{125}Xe around $\gamma \simeq 0^\circ$ and $\varepsilon_2 \simeq 0.25 - 0.35$. The calculation has been performed for the configurations $(\pi, \alpha) = (+, 1/2)$ at spin $I = 73/2$ (a), $(\pi, \alpha) = (+, -1/2)$ at spin $I = 67/2$ (b), $(\pi, \alpha) = (-, 1/2)$ at spin $I = 65/2$ (c) and $(\pi, \alpha) = (-, -1/2)$ at spin $I = 71/2$ (d).*

a similar configuration. The $\pi(g_{7/2}h_{11/2}) \otimes \nu(h_{11/2}i_{13/2})$ configuration has been assigned to band c in ^{126}Xe [RHSH+07], therefore, the configuration $\pi(g_{7/2}h_{11/2}) \otimes \nu(h_{11/2}i^2_{13/2})$ may be given to band L1.

9.4.2 Band L2

Band L2 shows large fluctuations in the frequency range 0.58–0.7 $^{\mathrm{MeV}}/_{\hbar}$ and then its $\mathcal{J}^{(2)}$ values become constant, see Fig. 9.10. Since spin and parity are not established, no configuration assignment can be made.

9.4.3 Band L3

Band L3 does not exhibit a structure change as can be seen in Fig. 9.10. The development of the $\mathcal{J}^{(2)}$ curve as a function of spin is similar to bands a, b and d in ^{126}Xe [RHSH+07]. Since spin and parity of band L3 are not determined, it is difficult to suggest a configuration. However, because of the similarity

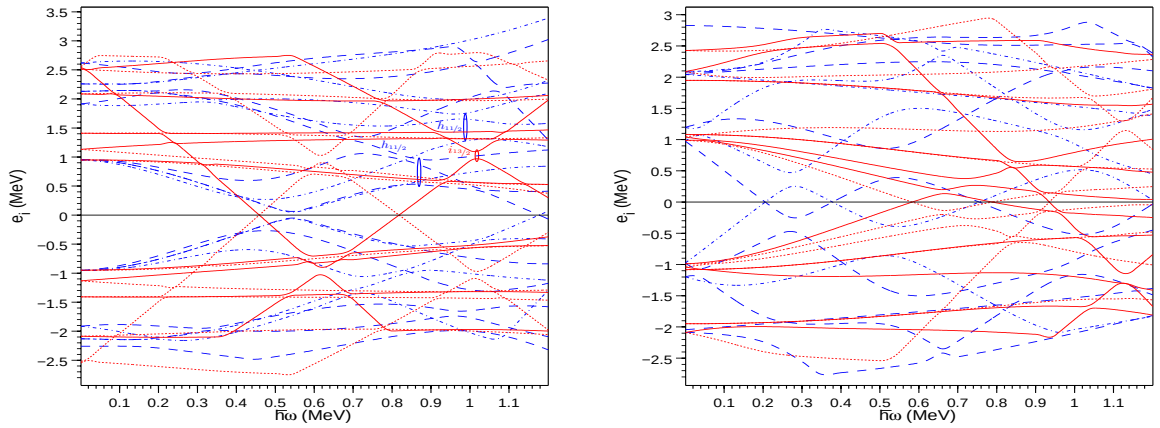

Figure 9.15: *Quasi-particle energy levels for $N = 71$ neutrons (a) and for $Z = 54$ protons (b) calculated for the $(\pi, \alpha) = (-, -1/2)$ configuration as a function of rotational frequency at a deformation corresponding to the minimum with $\varepsilon_2 \approx 0.30, \gamma \approx 7^\circ$. The parity and signature (π, α) of the levels are: $(+, +1/2)$–solid lines; $(+, -1/2)$–dotted lines; $(-, -1/2)$–dashed lines; $(-, +1/2)$–dot-dashed lines.*

to long bands in ^{126}Xe, most probably, the configuration of band L3 contains $h_{11/2}$ and $i_{13/2}$ neutron quasi-particles.

9.4.4 Band L4

As is evident in Fig. 9.10, band L4 undergoes a first crossing at a rotational frequency of $\omega \approx 0.94$ $^{\mathrm{MeV}}/_{\hbar}$ and perhaps a second crossing at $\omega \approx 1.2$ $^{\mathrm{MeV}}/_{\hbar}$. It has negative parity and signature $(\pi, \alpha) = (-, -1/2)$. As shown in Fig. 9.14, a pronounced minimum at $(\varepsilon_2 \approx 0.30,\ \gamma \approx 7^\circ)$ can be identified in good agreement with the experimental deformation, see table 9.2. The quasi-particle levels corresponding to this minimum for neutrons and protons are presented in Fig. 9.15. The $\nu h_{11/2}$ crossings occur at $\omega_c \approx 0.86$ and 0.98 $^{\mathrm{MeV}}/_{\hbar}$ and the $\nu i_{13/2}$ crossing at $\omega_c \approx 1.02^{\mathrm{MeV}}/_{\hbar}$. Therefore, the first crossing in band L4 may be attributed to the alignment of a pair of quasi-neutrons of $h_{11/2}$ origin and the second crossing to an alignment of a pair of $i_{13/2}$ neutrons. Thus, band L4 probably corresponds to the $\nu(h^3_{11/2} \otimes i^2_{13/2})$ configuration at high spins.

9.4.5 Bands L5

Band L5a decays to band L5 and to band L2 suggesting that they have similar structure. The dynamic moment of inertia of band L5 is roughly constant in the frequency range ω = 0.6–0.82 $^{\mathrm{MeV}}/_{\hbar}$. The first crossing can be identified around $\omega \approx 0.88$ $^{\mathrm{MeV}}/_{\hbar}$ and maybe a second crossing takes place around $\omega \approx 1.06$ $^{\mathrm{MeV}}/_{\hbar}$, see Fig. 9.10. Band L5 has positive parity and negative signature $(\pi, \alpha) = (+, -1/2)$. The behaviour of the $\mathscr{J}^{(2)}$ curve is similar to those in ^{126}Xe with the $\pi(g_{7/2}h_{11/2}) \otimes \nu(i_{13/2}h_{11/2})$ configuration. The $\pi(g_{7/2}h_{11/2}) \otimes \nu(h_{11/2}i^2_{13/2})$ may be a possible configuration for band L5.

9.4.6 Band L5a

Band L5a exhibits a band-crossing at a rotational frequency of $\omega \approx 0.78$ $^{\mathrm{MeV}}/_{\hbar}$ (Fig. 9.10). It decays into bands L5 and L2. If spin and parity assignments are correct, then band L5a has positive parity and negative signature. It may have a similar configuration as band L5.

9.4.7 Band L6

Band L6 shows a band crossing at a rotational frequency of $\omega \approx 0.88$ $^{\mathrm{MeV}}/_{\hbar}$. As parity and signature of the band are not known, it is difficult to suggest a configuration. But because of the similarity to

long bands in ^{126}Xe, the $\nu(h_{11/2} \otimes i^2_{13/2}$ or the $\nu(g_{7/2}h^2_{11/2})$ configurations may be suggested as possible candidates.

Chapter 10

Discussion

In the mass region around $A = 125$ the ground-state band in even-even nuclei is crossed around $I^\pi = 10^+$ at two different rotational frequencies by two-quasi-proton and two-quasi-neutron excitations of $h_{11/2}$ parentage, respectively. This results in a forking of the ground-state band into two branches with different deformation. Furthermore, strongly coupled negative-parity bands have been observed in this mass region, see e.g. [SLD+93, TJJ+94, TSR+94, TSP+95, WYN+95, SPV+97, SCW+99, WMW+01, WGB+89, PFM+90, WJA+91, GMB+96, VCD+99, PBB+01, SCF+00, MBES+88, PBB+03, SMCC+04].

An interesting feature is the transition from collective motion to single-particle excitation at high spins. The rotational bands terminate when a nucleus with a specific configuration reaches the maximum spin that can be built within this configuration. The only way to proceed generating angular momentum is to break the core and align single-particles. This phenomenon has been established previously in ^{123}Cs [SHD+04] and ^{122}Xe [TSP+95]. Evidence for terminating states in ^{124}Ba and ^{124}Xe is proposed in the present work.

The long bands discovered in ^{125}Xe are of special interest. Their deformation is higher than that of the low-spin structures. The presence of such bands may be attributed to the occupation of neutron $i_{13/2}$ and possibly $j_{15/2}$ orbitals.

10.1 Positive-Parity Bands in ^{124}Ba and ^{124}Xe

A common feature in the $A \approx 125$ mass region is the observation of two positive-parity two-quasi-particle bands based upon aligned $h^2_{11/2}$ quasi-neutrons and quasi-protons, respectively. This is evident in ^{124}Ba where the ground-state band is crossed by bands 1 and 2 and in ^{124}Xe where it is crossed by bands 5 and A. In ^{124}Ba, the ground-state band is crossed by bands 1 and 2 at rotational frequencies of $\omega^\pi_c = 0.37$ MeV/$\hbar$ and $\omega^\nu_c = 0.41$ MeV/$\hbar$, respectively. The first crossing is caused by the alignment of a pair of two quasi-protons of $\pi h_{11/2}$ origin, and the second crossing is due to the alignment of a pair of two quasi-neutrons of $\nu h_{11/2}$ parentage. In ^{124}Xe, the ground state-band is crossed by the two-quasi-neutron band (band 5) at a rotational frequency of $\omega^\nu_c = 0.38$ MeV/$\hbar$ and by the two-quasi-proton band (band A) at a frequency of $\omega^\pi_c = 0.41$ MeV/$\hbar$.

It is seen that the crossing frequency for the $\pi h^2_{11/2}$ configuration with the ground-state band is decreasing with increasing proton number and the crossing frequency for the $\nu h^2_{11/2}$ configuration is increasing with increasing proton number. This is in agreement with predictions in [WGB+89].

Band 1 in ^{124}Ba undergoes a second crossing at a rotational frequency of $\omega^\nu_c = 0.41$ MeV/$\hbar$ due to an alignment of an $h_{11/2}$ neutron pair, $\nu h^2_{11/2}$. Band 2 shows an alignment gain at a rotational frequency of $\omega^\pi_c = 0.44$ MeV/$\hbar$ due to the alignment of a $h_{11/2}$ proton pair, $\pi h^2_{11/2}$. At $\omega_c = 0.66$ MeV/$\hbar$ a further crossing occurs in this band which may be explained by the alignment of a pair of protons of $g_{7/2}$ origin or by a second pair of $h^2_{11/2}$ neutrons. However, bands 5 and A in ^{124}Xe do not show second band crossings. The configurations of bands 1 and 2 in ^{124}Ba as well as bands 5 and A in ^{124}Xe are summarised in table 10.1.

Table 10.1: *Configuration assignments of the two-lowest positive-parity bands in ^{124}Ba and ^{124}Xe.*

Band	Configuration assignment
Band 1 in ^{124}Ba (yrast)	$\pi h^2_{11/2} \otimes \nu h^2_{11/2}$
Band 2 in ^{124}Ba	$\nu h^2_{11/2} \otimes \pi h^2_{11/2} \otimes (\pi g^2_{7/2} or \nu h^2_{11/2})$
Band 5 in ^{124}Xe (yrast)	$\nu h^2_{11/2}$
Band A in ^{124}Xe	$\pi h^2_{11/2}$

Bands 7 and 8 in ^{124}Ba and bands 8 and 9 in ^{124}Xe are γ-vibrational bands. Band 8 in ^{124}Xe exhibits a back-bend at a rotational frequency of $\omega_c \approx 0.36$ $^{\mathrm{MeV}}/_{\hbar}$ which may be explained by the alignment of a pair of two quasi-neutrons, $\nu h^2_{11/2}$. Bands 7 and 8 in ^{124}Ba do not show any crossing.

Other uncoupled and coupled positive-parity bands, bands 9, 10, 12 and 13 are observed in ^{124}Ba, but no similar bands are seen in ^{124}Xe. The configurations assigned to the bands are shown in table 10.2. The configurations of bands 9 and 10 are based on four-quasi-particles and of bands 12 and 13 on six-quasi-particles.

Table 10.2: *Configuration assignments of the positive-parity side bands, bands 9, 10, 12 and 13 in ^{124}Ba.*

Band	Configuration assignment
band 9	$\pi h^2_{11/2} \otimes \nu h^2_{11/2}$
band 10	$\pi h^2_{11/2} \otimes \nu h^2_{11/2}$
band 12 and 13	$\pi(g_{9/2} h_{11/2}) \otimes \nu((d_{5/2}, g_{7/2}) h_{11/2}) \otimes \nu h^2_{11/2}$

10.2 Negative-Parity Bands in ^{124}Ba and ^{124}Xe

Negative-parity bands have been observed in ^{124}Ba and ^{124}Xe. Similar bands have been established in many neighbouring nuclei in this mass region, e.g. in ^{122}Xe [TSP+95], ^{126}Xe [RHSH+07], ^{128}Xe [OBE+06], ^{122}Ba [PBB+01], ^{126}Ba [WJA+91] and ^{128}Ba [VCD+99]. They are characterised by the observation of a very strong band (yrast band of negative parity) such as band 3 in ^{124}Ba and band 6 in ^{124}Xe and its signature partner, band 4 and band 7, respectively. As can be seen in the level schemes (Fig. 7.1 of ^{124}Ba and 8.1 of ^{124}Xe), the interaction between bands 6 and 7 in ^{124}Xe is much stronger than the interaction between bands 3 and 4 in ^{124}Ba. Table 10.3 shows their configuration assignments. The configuration of band 3 in ^{124}Ba is the same as the one of band 7 in ^{124}Xe and the configuration of band 4 in ^{124}Ba is the same as the one of band 7 in ^{124}Xe.

Table 10.3: *Configuration assignments of the two lowest negative-parity bands in ^{124}Ba and ^{124}Xe.*

Band	Configuration assignment
Band 3 in ^{124}Ba	$\pi(h_{11/2} d_{5/2}) \otimes \nu h^2_{11/2}$
Band 4 in ^{124}Ba	$\pi(h_{11/2} d_{5/2}) \otimes \nu h^4_{11/2}$
Band 6 in ^{124}Xe	$\pi[h_{11/2}(g_{7/2}, d_{5/2})] \otimes \nu h^4_{11/2}$
Band 7 in ^{124}Xe	$\pi[h_{11/2}(g_{7/2}, d_{5/2})] \otimes \nu h^2_{11/2}$

The coupled negative-parity bands 5 and 6 in ^{124}Ba and bands 1 and 2 in ^{124}Xe have also a similar structure. The bands in ^{124}Xe are built on $\nu(h_{11/2} g_{7/2})$ configuration and those in ^{124}Ba are built on $\pi(h_{11/2} g_{7/2})$ configuration.

10.3 High-Spin Bands in ^{125}Xe

Among the long high-spin bands observed in ^{125}Xe, only bands L4 and L5 are tentatively linked to known low-spin states. Bands L1, L2, L3 and L6 are not connected and their spins and parities are not determined experimentally. Configuration assignments are based on comparison to similar high-spin bands established in ^{126}Xe [RHSH+07]. The long bands in ^{126}Xe are linked to known states and, hence,

their spins and parities are well known. The configurations given to those bands in ^{126}Xe are listed in table 10.4.

Band	Configuration assignment	(π, α)
a	$\pi(g_{7/2}^2 h_{11/2}^2) \otimes \nu(h_{11/2} i_{13/2})$	$(-, 0)$
b	$\pi(g_{7/2} h_{11/2}) \otimes \nu(h_{11/2} i_{13/2})$	$(+, 0)$
c	$\pi(g_{7/2} h_{11/2}) \otimes \nu(h_{11/2} i_{13/2})$	$(+, 1)$
d	$\pi(g_{7/2}^2 h_{11/2}^2) \otimes \nu(h_{11/2} i_{13/2})$	$(-, 1)$

Table 10.4: *Configuration assignments of the long high-spin bands a, b, c and d in ^{126}Xe [RHSH+07].*

Configurations can only be suggested for bands L4 and L5. However, the trend of the dynamic moments of inertia of high-spin bands in ^{125}Xe is similar to those in ^{126}Xe which suggests similar configurations. The configuration of bands L1, L2, L3 and L6 may include the $h_{11/2}$ and $i_{13/2}$ quasi-neutrons, and this would explain their relatively high deformation, see 9.2. If the spin and parity assignments are correct, band L4 has negative parity and negative signature, $(\pi, \alpha) = (-, -1/2)$, and band L5 has positive parity and negative signature, $(\pi, \alpha) = (+, -1/2)$. Possible configurations for bands L4 and L5 are shown in table 10.5.

Band	Configuration assignment	(π, α)
L4	$\nu(h_{11/2}^3 \otimes i_{13/2}^2)$	$(-, -1/2)$
L5	$\pi(g_{7/2} h_{11/2}) \otimes \nu(h_{11/2} i_{13/2}^2)$	$(+, -1/2)$

Table 10.5: *Configuration assignments suggested for the long high-spin bands L4 and L5 in ^{125}Xe.*

10.4 Band Termination

Terminating states have been established previously in ^{122}Xe [TSP+95] and ^{123}Cs [SHD+04]. The terminating states established in ^{124}Ba and ^{124}Xe extend this feature to these heavier nuclei. The yrast band (band 1) in ^{124}Ba shows irregular patterns above spin $I^\pi = 36^+$ where several branches were observed. The $I^\pi = 36^+$ state has been identified as a terminating state with the configuration $\pi[(h_{11/2})^2_{10}(g_{7/2}d_{5/2})^4_{10}] \otimes \nu(h_{11/2})^4_{16}$. Furthermore, the irregular structures C and D observed in ^{124}Xe provide evidence of the transition from collective to non-collective states. Possible configurations of terminating states are $\{\pi[(h_{11/2})^2(g_{7/2}d_{5/2})^2]_{16^+}\nu[(h_{11/2})^4(d_{3/2}s_{1/2})^2]_{18^+}\}_{34^+}$ and $\{\pi[(h_{11/2})^2(g_{7/2}d_{5/2})^2]_{16^+}\nu[(h_{11/2})^5(d_{3/2}s_{1/2})^1]_{19^-}\}_{35^-}$.

Chapter 11

Summary

Within the framework of this thesis, high-spin states in ^{124}Ba, ^{124}Xe and ^{125}Xe nuclei have been investigated. The data used in this work were acquired in three experiments. Excited states in ^{124}Ba, ^{124}Xe and ^{125}Xe were populated using the heavy-ion fusion-evaporation reactions ^{64}Ni(^{64}Ni,$4n$)^{124}Ba at beam energies of 255, 261 and 265 MeV and ^{82}Se(^{48}Ca,$6n, 5n$)^{124,125}Xe at a beam energy of 205 MeV, respectively. Gamma-ray coincidences were measured using the Euroball and Gammasphere spectrometers, respectively.

The energy-level scheme of ^{124}Ba has been significantly extended. Previously known bands (1–8) have been extended to higher spins and six new bands (9–14) have been established. DCO ratios and relative intensities have been determined for transitions with sufficient intensities. Bands 9, 10 and 14 are firmly connected to known states and bands 11, 12 and 13 are only tentatively connected to the lower-lying levels.

Configurations have been assigned to the band structures based on the comparison with predictions of the CSM in the lower-spin region and with the CNS model at high spins. The positive-parity yrast band, band 1, shows the typical behaviour of band termination at the highest spins. Configurations for the terminating states are suggested on the basis of the CNS calculations. One of the new bands, band 11, extends to spins around 46 without band crossing. Its dynamic moment of inertia decreases steadily, similar to those of large-deformation bands in this mass region. Bands 12 and 13 are suggested to be built on four-quasi-particle configurations and band 14 on a six-quasi-particle configuration.

The level scheme of ^{124}Xe has been extended compared to previous work. Two new side bands (A and B) were observed and several of the previously known bands were extended in the high- as well as in the low-spin region. Two irregular high-spin structures (C and D) have also been established. DCO ratios and relative intensities have been determined for transitions with sufficient intensities.

Configuration assignments to the new structures are proposed on the basis of systematics and by comparing experimental properties with calculations within the framework of the CSM. The irregularities of the highest observed spins are a fingerprint of a transition from collective to non-collective behaviour.

The level scheme of the ^{125}Xe has been significantly extended. The most fascinating feature is the observation of the long bands (L1, L2, L3, L4, L5, L5a and L6) extending to the spin $I \approx {}^{115}/_{2}$ region. Bands L1, L2, L3 and L6 could not be connected to the known low-spin states. Bands L4 and L5 were tentatively linked to known states.

The lifetimes of states within these long bands are extremely short. They decay while the nucleus recoils inside the target. Therefore, it was possible to apply a DSAM analysis to estimate the transition quadrupole moments of the long bands and, hence, the corresponding deformations.

Configuration assignments for the long band are suggested on the basis of the CSM. They are proposed to be built on quasi-protons of $h_{11/2}$ origin and quasi-neutrons of $h_{11/2}$ and $i_{13/2}$ parentage. The occupation of the $i_{13/2}$ orbitals drives the nucleus to large deformation which explains the higher deformation of the long bands compared to the low-spin bands.

Appendix A

Tables

Table A.1: Energies, relative intensities, DCO ratios, multipolarity and spin assignments of γ-ray transitions of ^{124}Ba

Excitation E_x(keV)	Energy[a] E_γ(keV)	Intensity[b] I_γ	R^c_{DCO} ratio	Band$_i$ → Band$_f$	Assignment $I^\pi_i \rightarrow I^\pi_f$	Multipolarity
230	229.7	536(31)	-	$gs \rightarrow gs$	$2^+ \rightarrow 0^+$	$E2$
652	421.1	524(28)	-	$gs \rightarrow gs$	$4^+ \rightarrow 2^+$	$E2$
873	643.4	-	-	$8 \rightarrow gs$	$2^+ \rightarrow 2^+$	$M1$
873	873.3	-	-	$8 \rightarrow gs$	$2^+ \rightarrow 0^+$	$E2$
1162	510.0	-	-	$7 \rightarrow gs$	$3^+ \rightarrow 4^+$	$M1$
1162	932.8	-	-	$7 \rightarrow gs$	$3^+ \rightarrow 2^+$	$M1$
1228	576.5	500	0.90	$gs \rightarrow gs$	$6^+ \rightarrow 4^+$	$E2$
1325	451.7	-	-	$8 \rightarrow 8$	$4^+ \rightarrow 2^+$	$E2$
1325	673.1	-	-	$8 \rightarrow gs$	$4^+ \rightarrow 4^+$	$M1$
1325	1094.5	-	-	$8 \rightarrow gs$	$4^+ \rightarrow 2^+$	$E2$
1672	444.4	-	-	$7 \rightarrow gs$	$5^+ \rightarrow 6^+$	$M1$
1672	510.0	-	-	$7 \rightarrow 7$	$5^+ \rightarrow 3^+$	$E2$
1672	1020.8	-	-	$7 \rightarrow gs$	$5^+ \rightarrow 4^+$	$M1$
1722	1491.6	-	-	$4a \rightarrow gs$	$(3^-) \rightarrow 2^+$	$E1$
1858	533.4	-	-	$8 \rightarrow 8$	$6^+ \rightarrow 4^+$	$E2$
1858	629.7	-	-	$8 \rightarrow gs$	$6^+ \rightarrow 6^+$	$M1$
1913	684.9	-	-	$3 \rightarrow gs$	$5^- \rightarrow 6^+$	$E1$
1913	1260.8	23(5)	0.74	$3 \rightarrow gs$	$5^- \rightarrow 4^+$	$E1$
1923	694.7	348(22)	1.00	$gs \rightarrow gs$	$8^+ \rightarrow 6^+$	$E2$
2034	312.0	-	0.45	$4 \rightarrow 4a$	$4^- \rightarrow (3^-)$	$M1$
2034	1381.9	-	1.11	$4 \rightarrow gs$	$4^- \rightarrow 4^+$	$E1$
2262	338.4	2(1)	-	$3 \rightarrow gs$	$7^- \rightarrow 8^+$	$E1$
2262	348.4	6(1)	-	$3 \rightarrow 3$	$7^- \rightarrow 5^-$	$E2$
2262	1033.7	67(16)	0.66	$3 \rightarrow gs$	$7^- \rightarrow 6^+$	$E1$
2267	354.0	-	-	$5a \rightarrow 3$	$5^- \rightarrow 5^-$	$M1$
2267	942.4	-	-	$5a \rightarrow 8$	$5^- \rightarrow 4^+$	$E1$
2267	1038.6	-	-	$5a \rightarrow gs$	$5^- \rightarrow 6^+$	$E1$
2267	1615.3	6(2)	-	$5a \rightarrow gs$	$5^- \rightarrow 4^+$	$E1$
2285	612.7	-	-	$7 \rightarrow 7$	$7^+ \rightarrow 5^+$	$E2$
2285	1057.0	-	-	$7 \rightarrow gs$	$7^+ \rightarrow 6^+$	$M1$
2359	325.5	13(2)	1.32	$4 \rightarrow 4$	$6^- \rightarrow 4^-$	$E2$
2359	446.3	22(4)	0.35	$4 \rightarrow 3$	$6^- \rightarrow 5^-$	$M1$
2359	1130.0	31(7)	0.99	$4 \rightarrow gs$	$6^- \rightarrow 6^+$	$E1$
2479	555.7	-	-	$8 \rightarrow gs$	$8^+ \rightarrow 8^+$	$M1$

Table A.1: (Continued.)

2479	620.9	-	-	$8 \rightarrow 8$	$8^+ \rightarrow 6^+$	$E2$
2498	230.5	64(12)	0.58	$6 \rightarrow 5a$	$6^- \rightarrow 5^-$	$M1$
2498	824.9	-	-	$6 \rightarrow 7$	$6^- \rightarrow 5^+$	$E1$
2647	288.0	2(1)	-	$5a \rightarrow 4$	$7^- \rightarrow 6^-$	$M1$
2647	380.4	5(2)	1.05	$5a \rightarrow 5a$	$7^- \rightarrow 5^-$	$E2$
2647	385.7	7(2)	0.67	$5a \rightarrow 3$	$7^- \rightarrow 7^-$	$M1$
2647	789.3	8(3)	-	$5a \rightarrow 8$	$7^- \rightarrow 6^+$	$E1$
2688	764.4	213(32)	0.97	$gs \rightarrow gs$	$10^+ \rightarrow 8^+$	$E2$
2691	193.0	39(14)	0.41	$5 \rightarrow 6$	$7^- \rightarrow 6^-$	$M1$
2705	345.2	46(8)	0.99	$4 \rightarrow 4$	$8^- \rightarrow 6^-$	$E2$
2705	442.7	6(3)	0.48	$4 \rightarrow 3$	$8^- \rightarrow 7^-$	$M1$
2705	781.0	29(6)	0.75	$4 \rightarrow gs$	$8^- \rightarrow 8^+$	$E1$
2722	459.8	43(9)	1.13	$3 \rightarrow 3$	$9^- \rightarrow 7^-$	$E2$
2722	798.0	75(8)	0.50	$3 \rightarrow gs$	$9^- \rightarrow 8^+$	$E1$
2906	215.9	23(11)	0.35	$6 \rightarrow 5$	$8^- \rightarrow 7^-$	$M1$
2906	408.7	6(4)	-	$6 \rightarrow 6$	$8^- \rightarrow 6^-$	$E2$
2975	689.8	-	-	$7 \rightarrow 7$	$9^+ \rightarrow 7^+$	$E2$
2975	1053.0	-	-	$7 \rightarrow gs$	$9^+ \rightarrow 8^+$	$M1$
3110	203.2	-	-	$5 \rightarrow 6$	$9^- \rightarrow 8^-$	$M1$
3110	404.9	6(2)	0.77	$5 \rightarrow 4$	$9^- \rightarrow 8^-$	$M1$
3110	419.2	15(3)	-	$5 \rightarrow 5$	$9^- \rightarrow 7^-$	$E2$
3110	462.0	14(5)	0.90	$5 \rightarrow 5a$	$9^- \rightarrow 7^-$	$E2$
3157	434.7	3(1)	-	$4 \rightarrow 3$	$10^- \rightarrow 9^-$	$M1$
3157	452.0	61(17)	1.02	$4 \rightarrow 4$	$10^- \rightarrow 8^-$	$E2$
3178	698.7	-	-	$8 \rightarrow 8$	$10^+ \rightarrow 8^+$	$E2$
3287	564.9	101(22)	1.09	$3 \rightarrow 3$	$11^- \rightarrow 9^-$	$E2$
3287	599.8	-	-	$3 \rightarrow gs$	$11^- \rightarrow 10^+$	$E1$
3335	225.8	13(3)	-	$6 \rightarrow 5$	$10^- \rightarrow 9^-$	$M1$
3335	429.4	28(6)	1.01	$6 \rightarrow 6$	$10^- \rightarrow 8^-$	$E2$
3437	748.3	196(13)	0.97	$1 \rightarrow gs$	$12^+ \rightarrow 10^+$	$E2$
3591	256.0	13(5)	-	$5 \rightarrow 6$	$11^- \rightarrow 10^-$	$M1$
3591	482.2	39(8)	0.95	$5 \rightarrow 5$	$11^- \rightarrow 9^-$	$E2$
3692	255.6	6(3)	0.74	$2 \rightarrow 1$	$12^+ \rightarrow 12^+$	$M1$
3692	1004.0	16(5)	1.17	$2 \rightarrow gs$	$12^+ \rightarrow 10^+$	$E2$
3694	718.8	-	-	$7 \rightarrow 7$	$11^+ \rightarrow 9^+$	$E2$
3772	486.1	-	-	$4 \rightarrow 3$	$12^- \rightarrow 11^-$	$M1$
3772	615.5	56(16)	1.03	$4 \rightarrow 4$	$12^- \rightarrow 10^-$	$E2$
3891	299.9	16(4)	-	$6 \rightarrow 5$	$12^- \rightarrow 11^-$	$M1$
3891	556.4	13(5)	0.97	$6 \rightarrow 6$	$12^- \rightarrow 10^-$	$E2$
3968	681.0	94(25)	1.15	$3 \rightarrow 3$	$13^- \rightarrow 11^-$	$E2$
4127	434.2	-	-	$1 \rightarrow 2$	$14^+ \rightarrow 12^+$	$E2$
4127	689.4	173(13)	1.03	$1 \rightarrow 1$	$14^+ \rightarrow 12^+$	$E2$
4228	336.6	7(2)	-	$5 \rightarrow 6$	$13^- \rightarrow 12^-$	$M1$
4228	636.3	20(4)	1.15	$5 \rightarrow 5$	$13^- \rightarrow 11^-$	$E2$
4382	689.9	-	-	$12 \rightarrow 2$	$(11^+) \rightarrow 12^+$	$M1$
4382	945.4	-	-	$12 \rightarrow 1$	$(11^+) \rightarrow 12^+$	$M1$
4382	1407.0	-	-	$12 \rightarrow 7$	$(11^+) \rightarrow 9^+$	$E2$
4408	281.3	3(1)	0.53	$2 \rightarrow 1$	$14^+ \rightarrow 14^+$	$M1$
4408	715.5	14(4)	1.22	$2 \rightarrow 2$	$14^+ \rightarrow 12^+$	$E2$
4408	971.1	24(6)	1.38	$2 \rightarrow 1$	$14^+ \rightarrow 12^+$	$E2$
4534	566.2	-	-	$4 \rightarrow 3$	$14^- \rightarrow 13^-$	$M1$
4534	762.1	48(16)	1.03	$4 \rightarrow 4$	$14^- \rightarrow 12^-$	$E2$
4552	170.0	-	-	$13 \rightarrow 12$	$(12^+) \rightarrow (11^+)$	$M1$
4552	722.0	-	0.74	$13 \rightarrow 13a$	$(12^+) \rightarrow (11)$	-

Table A.1: (Continued.)

4552	858.2	-	-	$13 \rightarrow 7$	$(12^+) \rightarrow 11^+$	$M1$
4604	375.6	5(2)	-	$6 \rightarrow 5$	$14^- \rightarrow 13^-$	$M1$
4604	711.2	13(6)	1.00	$6 \rightarrow 6$	$14^- \rightarrow 12^-$	$E2$
4762	793.8	61(9)	1.03	$3 \rightarrow 3$	$15^- \rightarrow 13^-$	$E2$
4767	215.0	-	-	$12 \rightarrow 13$	$(13^+) \rightarrow (12^+)$	$M1$
4767	384.2	-	1.14	$12 \rightarrow 12$	$(13^+) \rightarrow (11^+)$	$E2$
4767	1073.2	-	-	$12 \rightarrow 7$	$(13^+) \rightarrow 11^+$	$E2$
4893	766.1	156(13)	1.05	$1 \rightarrow 1$	$16^+ \rightarrow 14^+$	$E2$
5010	405.6	3(1)	-	$5 \rightarrow 6$	$15^- \rightarrow 14^-$	$M1$
5010	780.9	20(3)	0.92	$5 \rightarrow 5$	$15^- \rightarrow 13^-$	$E2$
5028	261.0	-	-	$13 \rightarrow 12$	$(14^+) \rightarrow (13^+)$	$M1$
5028	476.0	-	1.05	$13 \rightarrow 13$	$(14^+) \rightarrow (12^+)$	$E2$
5216	323.2	3(2)	0.78	$2 \rightarrow 1$	$16^+ \rightarrow 16^+$	$M1$
5216	808.5	42(8)	1.35	$2 \rightarrow 2$	$16^+ \rightarrow 14^+$	$E2$
5216	1090.0	11(5)	-	$2 \rightarrow 1$	$16^+ \rightarrow 14^+$	$E2$
5330	302.0	-	-	$12 \rightarrow 13$	$(15^+) \rightarrow (14^+)$	$M1$
5330	562.5	-	1.03	$12 \rightarrow 12$	$(15^+) \rightarrow (13^+)$	$E2$
5330	1203.7	-	-	$12 \rightarrow 1$	$(15^+) \rightarrow 14^+$	$M1$
5392	630.7	-	-	$4 \rightarrow 3$	$16^- \rightarrow 15^-$	$M1$
5392	858.3	31(11)	0.94	$4 \rightarrow 4$	$16^- \rightarrow 14^-$	$E2$
5446	436.3	2(1)	-	$6 \rightarrow 5$	$16^- \rightarrow 15^-$	$M1$
5446	842.6	9(2)	0.85	$6 \rightarrow 6$	$16^- \rightarrow 14^-$	$E2$
5639	878.0	51(12)	1.00	$3 \rightarrow 3$	$17^- \rightarrow 15^-$	$E2$
5669	339.0	-	-	$13 \rightarrow 12$	$(16^+) \rightarrow (15^+)$	$M1$
5669	640.9	-	1.00	$13 \rightarrow 13$	$(16^+) \rightarrow (14^+)$	$E2$
5726	832.0	48(9)	0.27	$9 \rightarrow 1$	$17^+ \rightarrow 16^+$	$M1$
5764	871.6	84(15)	1.10	$1 \rightarrow 1$	$18^+ \rightarrow 16^+$	$E2$
5906	459.8	-	-	$5 \rightarrow 6$	$17^- \rightarrow 16^-$	$M1$
5906	895.7	18(3)	1.12	$5 \rightarrow 5$	$17^- \rightarrow 15^-$	$E2$
6046	377.0	-	-	$12 \rightarrow 13$	$(17^+) \rightarrow (16^+)$	$M1$
6046	715.5	-	1.01	$12 \rightarrow 12$	$(17^+) \rightarrow (15^+)$	$E2$
6081	317.2	-	-	$2 \rightarrow 1$	$18^+ \rightarrow 18^+$	$M1$
6081	864.7	37(9)	0.93	$2 \rightarrow 2$	$18^+ \rightarrow 16^+$	$E2$
6081	1187.9	-	-	$2 \rightarrow 1$	$18^+ \rightarrow 16^+$	$E2$
6192	1299.0	-	-	$10 \rightarrow 1$	$18^+ \rightarrow 16^+$	$E2$
6290	896.6	20(8)	1.21	$4 \rightarrow 4$	$18^- \rightarrow 16^-$	$E2$
6383	477.2	-	-	$6 \rightarrow 5$	$18^- \rightarrow 17^-$	$M1$
6383	938.1	9(2)	-	$6 \rightarrow 6$	$18^- \rightarrow 16^-$	$E2$
6454	408.0	-	-	$13 \rightarrow 12$	$(18^+) \rightarrow (17^+)$	$M1$
6454	784.9	-	1.04	$13 \rightarrow 13$	$(18^+) \rightarrow (16^+)$	$E2$
6556	917.3	29(6)	1.15	$3 \rightarrow 3$	$19^- \rightarrow 17^-$	$E2$
6583	819.1	7(2)	-	$9 \rightarrow 1$	$19^+ \rightarrow 18^+$	$M1$
6583	857.7	22(9)	0.95	$9 \rightarrow 9$	$19^+ \rightarrow 17^+$	$E2$
6705	1066.0	-	-	$3a \rightarrow 3$	$(18) \rightarrow 17^-$	-
6712	948.6	59(13)	1.06	$1 \rightarrow 1$	$20^+ \rightarrow 18^+$	$E2$
6871	487.8	-	-	$5 \rightarrow 6$	$19^- \rightarrow 18^-$	$M1$
6871	965.0	7(2)	0.96	$5 \rightarrow 5$	$19^- \rightarrow 17^-$	$E2$
6898	444.0	-	-	$12 \rightarrow 13$	$(19^+) \rightarrow (18^+)$	$M1$
6898	852.0	-	1.06	$12 \rightarrow 12$	$(19^+) \rightarrow (17^+)$	$E2$
7000	919.4	25(6)	1.08	$2 \rightarrow 2$	$20^+ \rightarrow 18^+$	$E2$
7000	1236.2	-	-	$2 \rightarrow 1$	$20^+ \rightarrow 18^+$	$E2$
7084	891.9	20(10)	0.91	$10 \rightarrow 10$	$20^+ \rightarrow 18^+$	$E2$
7084	1319.7	-	0.92	$10 \rightarrow 1$	$20^+ \rightarrow 18^+$	$E2$
7230	940.5	13(6)	0.90	$4 \rightarrow 4$	$20^- \rightarrow 18^-$	$E2$

Table A.1: (Continued.)

7365	910.0	-	1.08	$13 \rightarrow 13$	$(20^+) \rightarrow (18^+)$	$E2$
7366	495.2	-	-	$6 \rightarrow 5$	$20^- \rightarrow 19^-$	$M1$
7366	982.6	4(2)	-	$6 \rightarrow 6$	$20^- \rightarrow 18^-$	$E2$
7502	945.3	16(4)	1.26	$3 \rightarrow 3$	$21^- \rightarrow 19^-$	$E2$
7503	791.3	-	-	$9 \rightarrow 1$	$21^+ \rightarrow 20^+$	$M1$
7503	918.0	12(4)	0.87	$9 \rightarrow 9$	$21^+ \rightarrow 19^+$	$E2$
7717	1004.9	41(10)	1.08	$1 \rightarrow 1$	$22^+ \rightarrow 20^+$	$E2$
7865	966.9	-	1.16	$12 \rightarrow 12$	$(21^+) \rightarrow (19^+)$	$E2$
7878	1007.4	-	-	$5 \rightarrow 5$	$21^- \rightarrow 19^-$	$E2$
7984	983.7	18(4)	1.09	$2 \rightarrow 2$	$22^+ \rightarrow 20^+$	$E2$
7984	1272.3	-	-	$2 \rightarrow 1$	$22^+ \rightarrow 20^+$	$E2$
8101	1016.8	11(5)	1.08	$10 \rightarrow 10$	$22^+ \rightarrow 20^+$	$E2$
8101	1389.0	-	-	$10 \rightarrow 1$	$22^+ \rightarrow 20^+$	$E2$
8263	1034.4	11(5)	0.91	$4 \rightarrow 4$	$22^- \rightarrow 20^-$	$E2$
8371	1006.3	-	1.06	$13 \rightarrow 13$	$(22^+) \rightarrow (20^+)$	$E2$
8411	1044.0	-	-	$6 \rightarrow 6$	$22^- \rightarrow 20^-$	$E2$
8486	769.2	-	-	$9 \rightarrow 1$	$23^+ \rightarrow 22^+$	$M1$
8486	983.4	10(4)	1.11	$9 \rightarrow 9$	$23^+ \rightarrow 21^+$	$E2$
8512	1009.7	14(4)	0.95	$3 \rightarrow 3$	$23^- \rightarrow 21^-$	$E2$
8795	1077.1	37(9)	1.22	$1 \rightarrow 1$	$24^+ \rightarrow 22^+$	$E2$
8905	1040.6	-	1.22	$12 \rightarrow 12$	$(23^+) \rightarrow (21^+)$	$E2$
8913	1034.0	-	-	$5 \rightarrow 5$	$23^- \rightarrow 21^-)$	$E2$
9054	1069.2	12(3)	0.90	$2 \rightarrow 2$	$24^+ \rightarrow 22^+$	$E2$
9179	1078.6	10(5)	0.84	$10 \rightarrow 10$	$24^+ \rightarrow 22^+$	$E2$
9179	1462.3	-	-	$10 \rightarrow 1$	$24^+ \rightarrow 22^+$	$E2$
9381	1117.6	5(1)	0.89	$4 \rightarrow 4$	$24^- \rightarrow 22^-$	$E2$
9430	1058.5	-	1.25	$13 \rightarrow 13$	$(24^+) \rightarrow (22^+)$	$E2$
9528	1117.1	-	-	$6 \rightarrow 6$	$(24^-) \rightarrow (22^-)$	$E2$
9566	1078.2	6(2)	1.25	$9 \rightarrow 9$	$25^+ \rightarrow 23^+$	$E2$
9613	1100.1	8(2)	1.37	$3 \rightarrow 3$	$25^- \rightarrow 23^-$	$E2$
9918	1124.1	-	-	$11 \rightarrow 1$	$(25) \rightarrow 24^+$	-
9951	1154.5	15(6)	1.11	$1 \rightarrow 1$	$26^+ \rightarrow 24^+$	$E2$
9976	1070.6	-	1.07	$12 \rightarrow 12$	$(25^+) \rightarrow (23^+)$	$E2$
9984	1070.7	-	-	$5 \rightarrow 5$	$(25^-) \rightarrow (23^-)$	$E2$
10223	1168.6	10(3)	0.97	$2 \rightarrow 2$	$26^+ \rightarrow 24^+$	$E2$
10312	1131.4	5(2)	1.16	$10 \rightarrow 10$	$26^+ \rightarrow 24^+$	$E2$
10312	1516.9	-	-	$10 \rightarrow 1$	$26^+ \rightarrow 24^+$	$E2$
10521	1091.9	-	1.12	$13 \rightarrow 13$	$(26^+) \rightarrow (24^+)$	$E2$
10563	1181.2	4(1)	-	$4 \rightarrow 4$	$26^- \rightarrow 24^-$	$E2$
10707	1178.4	-	-	$6 \rightarrow 6$	$(26^-) \rightarrow (24^-)$	$E2$
10751	1184.8	2(2)	-	$9 \rightarrow 9$	$27^+ \rightarrow 25^+$	$E2$
10814	1201.5	6(2)	1.29	$3 \rightarrow 3$	$27^- \rightarrow 25^-$	$E2$
11029	1151.3	-	-	$11 \rightarrow 11$	$(27) \rightarrow (25)$	$E2$
11079	1102.4	-	1.13	$12 \rightarrow 12$	$(27^+) \rightarrow (25^+)$	$E2$
11118	1505.0	-	-	$3b \rightarrow 3$	$(26) \rightarrow 25^-$	-
11183	1231.2	11(4)	0.86	$1 \rightarrow 1$	$28^+ \rightarrow 26^+$	$E2$
11475	1251.8	6.3(3.8)	0.97	$2 \rightarrow 2$	$28^+ \rightarrow 26^+$	$E2$
11526	1214.2	3(2)	0.91	$10 \rightarrow 10$	$28^+ \rightarrow 26^+$	$E2$
11651	1129.3	-	1.21	$13 \rightarrow 13$	$(28^+) \rightarrow (26^+)$	$E2$
11755	1192.0	2(1)	-	$4 \rightarrow 4$	$28^- \rightarrow 26^-$	$E2$
12035	1282.9	-	-	$9 \rightarrow 9$	$29^+ \rightarrow 27^+$	$E2$
12118	1304.4	5(1)	1.02	$3 \rightarrow 3$	$29^- \rightarrow 27^-$	$E2$
12246	1164.9	-	-	$12 \rightarrow 12$	$(29^+) \rightarrow (27^+)$	$E2$
12290	1221.2	-	-	$11 \rightarrow 11$	$(29) \rightarrow (27)$	$E2$

Table A.1: (Continued.)

12492	1309.6	10(3)	1.27	$1 \rightarrow 1$	$30^+ \rightarrow 28^+$	$E2$
12738	1261.2	4(1)	0.93	$2 \rightarrow 2$	$30^+ \rightarrow 28^+$	$E2$
12826	1297.9	-	-	$10 \rightarrow 10$	$30^+ \rightarrow 28^+$	$E2$
12862	1210.9	-	-	$13 \rightarrow 13$	$(30^+) \rightarrow (28^+)$	$E2$
12961	1206.5	-	-	$4 \rightarrow 4$	$(30^-) \rightarrow (28^-)$	$E2$
13350	1232.0	-	0.8[e]	$14 \rightarrow 3$	$(30) \rightarrow 29^-$	-
13413	1377.0	-	-	$9 \rightarrow 9$	$31^+ \rightarrow 29^+$	$E2$
13498	1249.5	-	-	$12 \rightarrow 12$	$(31^+) \rightarrow (29^+)$	$E2$
13519	1400.8	4(2)	1.18	$3 \rightarrow 3$	$31^- \rightarrow 29^-$	$E2$
13592	1301.4	-	-	$11 \rightarrow 11$	$(31) \rightarrow (29)$	$E2$
13881	1388.6	9(3)	1.22	$1 \rightarrow 1$	$32^+ \rightarrow 30^+$	$E2$
14063	1324.5	3.6(2.9)	-	$2 \rightarrow 2$	$32^+ \rightarrow 30^+$	$E2$
14185	1224.3	-	-	$4 \rightarrow 4$	$32^- \rightarrow 30^-$	$E2$
14196	1370.1	-	-	$10 \rightarrow 10$	$32^+ \rightarrow 30^+$	$E2$
14757	1238.0	-	0.94[e]	$14 \rightarrow 3$	$(32) \rightarrow 31^-$	-
14757	1406.9	-	-	$14 \rightarrow 14$	$(32) \rightarrow (30)$	$E2$
14838	1340.6	-	-	$12 \rightarrow 12$	$(33^+) \rightarrow (31^+)$	$E2$
14887	1474.7	-	-	$9 \rightarrow 9$	$33^+ \rightarrow 31^+$	$E2$
14981	1389.1	-	-	$11 \rightarrow 11$	$(33) \rightarrow (31)$	$E2$
15007	1486.5	-	-	$3 \rightarrow 3$	$33^- \rightarrow 31^-$	$E2$
15336	1454.8	6(2)	1.38[d]	$1 \rightarrow 1$	$34^+ \rightarrow 32^+$	$E2$
15465	1401.6	-	-	$2 \rightarrow 2$	$34^+ \rightarrow 32^+$	$E2$
15476	1290.9	-	-	$4 \rightarrow 4$	$(34^-) \rightarrow 32^-$	$E2$
15624	1427.5	-	-	$10 \rightarrow 10$	$34^+ \rightarrow 32^+$	$E2$
16031	1274.0	-	1.42[e]	$14 \rightarrow 14$	$(34) \rightarrow (32)$	$E2$
16286	1448.0	-	-	$12 \rightarrow 12$	$(35^+) \rightarrow (33^+)$	$E2$
16434	1544.2	-	-	$9 \rightarrow 9$	$(35^+) \rightarrow 33^+$	$E2$
16463	1481.8	-	-	$11 \rightarrow 11$	$(35) \rightarrow (33)$	$E2$
16780	1444.3	5(2)	1.41[d]	$1 \rightarrow 1$	$36^+ \rightarrow 34^+$	$E2$
16918	1583.4	-	-	$1c \rightarrow 1$	$(36^+) \rightarrow 34^+$	$E2$
16949	1484.3	-	-	$2 \rightarrow 2$	$36^+ \rightarrow 34^+$	$E2$
17117	1493.3	-	-	$10 \rightarrow 10$	$(36^+) \rightarrow 34^+$	$E2$
17437	1406.0	-	-	$14 \rightarrow 14$	$(36) \rightarrow (34)$	$E2$
18042	1579.7	-	-	$11 \rightarrow 11$	$(37) \rightarrow (35)$	$E2$
18055	1619.6	-	-	$9 \rightarrow 9$	$(37^+) \rightarrow (35^+)$	$E2$
18075	1294.4	-	-	$1a \rightarrow 1$	$(38^+) \rightarrow 36^+$	$E2$
18149	1368.4	-	-	$1b \rightarrow 1$	$(38^+) \rightarrow 36^+$	$E2$
18529	1610.9	-	-	$1c \rightarrow 1c$	$(38^+) \rightarrow (36^+)$	$E2$
18656	1537.7	-	-	$10 \rightarrow 10$	$(38^+) \rightarrow (36^+)$	$E2$
18911	1474.0	-	-	$14 \rightarrow 14$	$(38) \rightarrow (36)$	$E2$
19722	1679.7	-	-	$11 \rightarrow 11$	$(39) \rightarrow (37)$	$E2$
20485	1574.0	-	-	$14 \rightarrow 14$	$(40) \rightarrow (38)$	$E2$
21503	1780.9	-	-	$11 \rightarrow 11$	$(41) \rightarrow (39)$	$E2$
22152	1666.8	-	-	$14 \rightarrow 14$	$(42) \rightarrow (40)$	$E2$
23386	1883.2	-	-	$11 \rightarrow 11$	$(43) \rightarrow (41)$	$E2$
25372	1986.3	-	-	$11 \rightarrow 11$	$(45) \rightarrow (43)$	$E2$

[a] Uncertainties of γ-ray energies are between 0.1 and 0.6 keV depending on their intensity.

[b] Intensities are normalized to the 576.5 keV transition with $I_\gamma = 500$.

[c] Uncertainties in the DCO rations are between 0.03 and 0.2.

[d] Ratio obtained from angular distribution matrices.

[e] Uncertainty > 50 % due to low statistics.

Table A.2: Energies, relative intensities, DCO ratios, multipolarity and spin assignments of γ-ray transitions of ^{124}Xe

Excitation E_x [keV]	Assignment $I_i^\pi \rightarrow I_f^\pi$	Energy[a] E_γ [keV]	Intensity[b] I_γ	Multipolarity	R_{DCO} ratio
2809	$8^- \rightarrow 7^-$	184.0	66	$M1$	0.59±0.04
2809	$8^- \rightarrow 8^+$	478.0	-	$E1$	-
3462	$10^- \rightarrow 9^-$	350.3	6	$M1$	-
3462	$10^- \rightarrow 8^-$	652.5	36	$E2$	-
4216	$12^- \rightarrow 11^-$	429.4	-	$M1$	-
4216	$12^- \rightarrow 10^-$	753.2	35	$E2$	1.0±0.1
5068	$14^- \rightarrow 13^-$	494.0	-	$M1$	0.55±0.22
5068	$14^- \rightarrow 12^-$	851.5	30	$E2$	1.01±0.10
6012	$16^- \rightarrow 14^-$	944.0	25	$E2$	1.02±0.11
7020	$18^- \rightarrow 16^-$	1008.3	15	$E2$	1.08±0.19
8094	$20^- \rightarrow 18^-$	1039.0	11	$E2$	-
8094	$20^- \rightarrow 18^-$	1074.0	-	$E2$	-
9084	$(22^-) \rightarrow 20^-$	990.1	-	$E2$	-
10123	$(24^-) \rightarrow (22^-)$	1039.4	-	$E2$	-
11266	$(26^-) \rightarrow (24^-)$	1142.5	-	$E2$	-
12518	$(28^-) \rightarrow (26^-)$	1252.0	-	$E2$	-
2227	$5^- \rightarrow 4^+$	1347.8	6	$E1$	-
2625	$7^- \rightarrow 5^-$	398.5	8	$E2$	-
2625	$7^- \rightarrow 6^+$	1076.1	70	$E1$	-
3111	$9^- \rightarrow 8^-$	302.3	48	$M1$	-
3111	$9^- \rightarrow 7^-$	486.1	20	$E2$	-
3111	$9^- \rightarrow 8^+$	780.1	-	$E1$	-
3787	$11^- \rightarrow 10^-$	324.8	12	$M1$	-
3787	$11^- \rightarrow 10^+$	615.4	-	$E1$	-
3787	$11^- \rightarrow 9^-$	675.2	60	$E2$	-
4574	$13^- \rightarrow 12^-$	358.3	3	$M1$	0.53±0.14
4574	$13^- \rightarrow 11^-$	786.8	30	$E2$	-
5462	$(15^-) \rightarrow 13^-$	888.3	20	$E2$	-
6438	$(17^-) \rightarrow (15^-)$	975.6	15	$E2$	-
7480	$(19^-) \rightarrow (17^-)$	1042.9		$E2$	-
8570	$(21^-) \rightarrow (19^-)$	1089.2	-	$E2$	-
9760	$(23^-) \rightarrow (21^-)$	1190.7	-	$E2$	-
5049	$12^+ \rightarrow (11^+)$	240	-	$M1$	-
5049	$12^+ \rightarrow 12^+$	750.3	15	$M1$	-
5049	$12^+ \rightarrow 10^+$	1030.7	-	$E2$	-
5049	$12^+ \rightarrow 11^+$	1046.1	-	$M1$	-
5049	$12^+ \rightarrow 11^-$	1262.1	23	$E1$	-
5049	$12^+ \rightarrow 10^+$	1546.2	-	$E2$	-
5551	$14^+ \rightarrow 13^+$	261.7	150	$M1$	0.63±0.09
5551	$14^+ \rightarrow 12^+$	502.6	-	$E2$	-
5551	$14^+ \rightarrow 13^-$	977.5	-	$E1$	-
6153	$16^+ \rightarrow 15^+$	326.1	160	$M1$	0.62±0.09
6153	$16^+ \rightarrow 14^+$	602.3	-	$E2$	-
6153	$16^+ \rightarrow (15^-)$	691.0	-	$E1$	-
6984	$18^+ \rightarrow 17^+$	430.9	110	$M1$	0.60±0.11
6984	$18^+ \rightarrow 16^+$	831.3	-	$E2$	-
7928	$20^+ \rightarrow 19^+$	496.5	50	$M1$	0.64±0.20
7928	$20^+ \rightarrow 18^+$	943.7	-	$E2$	-
8910	$22^+ \rightarrow 21^+$	546.0	20	$M1$	-
8910	$22^+ \rightarrow 20^+$	984.1	-	$E2$	-

Table A.2: (Continued.)

9926	$24^+ \rightarrow 23^+$	443.7	25	$M1$	-
9926	$24^+ \rightarrow 22^+$	1015.9	-	$E2$	-
5290	$13^+ \rightarrow 12^+$	240.6	-	$M1$	-
5290	$13^+ \rightarrow 12^+$	264.3	25	$M1$	-
5290	$13^+ \rightarrow 11^+$	452.8	15	$E2$	-
5290	$13^+ \rightarrow 12^-$	1074.3	-	$E1$	-
5827	$15^+ \rightarrow 14^+$	275.9	145	$M1$	0.65±0.08
5827	$15^+ \rightarrow 14^+$	308.8	27	$M1$	-
5827	$15^+ \rightarrow 13^+$	537.1	-	$M1$	-
6553	$17^+ \rightarrow 16^+$	399.9	144	$M1$	0.83±0.15
6553	$17^+ \rightarrow 15^+$	726.4	-	$E2$	-
7432	$19^+ \rightarrow 18^+$	448.6	82	$M1$	0.69±0.12
7432	$19^+ \rightarrow 17^+$	880.3	-	$E2$	-
8364	$21^+ \rightarrow 20^+$	436.0	22	$M1$	0.62±0.15
8364	$21^+ \rightarrow 19^+$	931.9	-	$E2$	-
9482	$23^+ \rightarrow 22^+$	572.0	15	$M1$	-
9482	$23^+ \rightarrow 21^+$	1117.8	-	$E2$	-
354	$2^+ \rightarrow 0^+$	354.0	700	$E2$	-
879	$4^+ \rightarrow 2^+$	524.9	1000	$E2$	-
1548	$6^+ \rightarrow 4^+$	669.5	1031	$E2$	1.09±0.04
2331	$8^+ \rightarrow 6^+$	782.7	814	$E2$	1.13±0.16
3171	$10^+ \rightarrow 8^+$	840.1	361	$E2$	0.99±0.04
3883	$12^+ \rightarrow 10^+$	380.4	-	$E2$	-
3883	$12^+ \rightarrow 10^+$	711.6	200	$E2$	1.06±0.07
4612	$14^+ \rightarrow 12^+$	729.6	155	$E2$	1.12±0.05
5466	$16^+ \rightarrow 14^+$	853.2	110	$E2$	1.02±0.06
6439	$18^+ \rightarrow 16^+$	973.0	54	$E2$	1.06±0.05
7524	$20^+ \rightarrow 18^+$	1085.2	33	$E2$	0.98±0.06
8722	$22^+ \rightarrow 20^+$	1198.2	23	$E2$	-
9996	$24^+ \rightarrow 22^+$	1274.4	22	$E2$	1.06±0.08
11239	$26^+ \rightarrow 24^+$	1242.7	8	$E2$	1.01±0.19
12463	$28^+ \rightarrow 26^+$	1224.0	-	$E2$	-
4298	$12^+ \rightarrow 12^+$	415.8	11	$M1$	1.06±0.21
4298	$12^+ \rightarrow 10^+$	1127.2	-	$E2$	-
5113	$14^+ \rightarrow 14^+$	501.5	7	$M1$	-
5113	$14^+ \rightarrow 12^+$	814.9	20	$E2$	-
5113	$14^+ \rightarrow 12^+$	1230.4	-	$E2$	-
5937	$16^+ \rightarrow 14^+$	823.6	27	$E2$	-
6828	$18^+ \rightarrow 16^+$	890.9	25	$E2$	-
7810	$20^+ \rightarrow 18^+$	982.5	12	$E2$	-
8898	$22^+ \rightarrow 20^+$	1088.3	7	$E2$	-
10088	$(24^+) \rightarrow 22^+$	1189.3	4	$E2$	-
11384	$(26^+) \rightarrow (24^+)$	1296.6	-	$E2$	-
5518	$14^+ \rightarrow 13^+$	228.3	-	$M1$	-
5518	$14^+ \rightarrow 12^+$	643.5	-	$E2$	-
5518	$14^+ \rightarrow 13^-$	944.7	-	$M1$	-
5518	$14^+ \rightarrow 12^+$	1220.0	-	$E2$	-
5026	$12^+ \rightarrow (11^+)$	216.7	-	$M1$	-
5026	$12^+ \rightarrow 12^+$	727.4	-	$M1$	-
5026	$12^+ \rightarrow 10^+$	1007.8	-	$E2$	-
8483	$- \rightarrow 20^+$	555.0	-	-	-
9047	$- \rightarrow$	564.0	-	-	-
9047	$- \rightarrow 20^+$	1119.0	-	-	-
11258	$26^+ \rightarrow 24^+$	1261.4	3	$E2$	1.09±0.24

Table A.2: (Continued.)

10088	$(24^+) \rightarrow 22^+$	1366.0	-	$E2$	-
3502	$10^+ \rightarrow 10^+$	331.2	9	$M1$	-
3502	$10^+ \rightarrow 8^+$	1171.3	-	$E2$	-
6305	$(16^+) \rightarrow 14^+$	1692.3	-	$E2$	-
7218	$(18^+) \rightarrow (16^+)$	914.0	-	$E2$	-
4875	$12^+ \rightarrow 11^-$	1088.3	-	$E1$	-
4875	$12^+ \rightarrow 10^+$	1703.7	-	$E2$	-
5432	$14^+ \rightarrow 12^+$	1133.3	-	$E2$	-
5432	$14^+ \rightarrow 12^+$	1548.9	-	$E2$	-
6255	$16^+ \rightarrow 14^+$	736.8	18	$E2$	1.16±0.14
6255	$16^+ \rightarrow 16^+$	789.6	} 37	$M1$	} 1.13±0.10
8859	$22^+ \rightarrow 20^+$	789.0		$E2$	
6255	$16^+ \rightarrow (15^-)$	793.2	12	$E1$	-
6255	$16^+ \rightarrow 14^+$	823.5	14	$E2$	1.28±0.25
7118	$18^+ \rightarrow 18^+$	679.1	-	$M1$	-
7118	$18^+ \rightarrow 16^+$	862.5	25	$E2$	1.09±0.09
8083	$20^+ \rightarrow 20^+$	558.8	-	$M1$	-
8083	$20^+ \rightarrow 19^+$	650.6	-	$M1$	-
8083	$20^+ \rightarrow (18^+)$	864.1	12	$E2$	-
8083	$20^+ \rightarrow 18^+$	964.9	32	$E2$	1.18±0.08
8859	$22^+ \rightarrow 21^+$	495.2	-	$M1$	-
8859	$22^+ \rightarrow 20^+$	759.8	60	$E2$	1.01±0.10
8859	$22^+ \rightarrow 20^+$	776.6	52	$E2$	1.07±0.08
8859	$22^+ \rightarrow 20^+$	931.0	-	$E2$	-
8859	$22^+ \rightarrow 20^+$	1049.0	-	$E2$	-
8859	$22^+ \rightarrow 20^+$	1335.4	-	$E2$	-
9656	$24^+ \rightarrow 22^+$	797.1	181	$E2$	1.14±0.10
10809	$26^+ \rightarrow 25^+$	381.8	18	$M1$	0.50±0.17
10809	$26^+ \rightarrow 24^+$	883	-	$E2$	-
10809	$26^+ \rightarrow 24^+$	1152.7	220	$E2$	1.16±0.06
12168	$28^+ \rightarrow 27^+$	696.0	-	$M1$	-
12168	$28^+ \rightarrow 26^+$	1359.2	-	$E2$	-
8099	$20^+ \rightarrow 19^+$	667.4	15	$M1$	-
10928	$26^+ \rightarrow 24^+$	1002.6	-	$E2$	-
10928	$26^+ \rightarrow 24^+$	1272.0	60	$E2$	1.03±0.20
11821	$28^+ \rightarrow 26^+$	892.4	50	$E2$	1.22±0.26
11821	$28^+ \rightarrow 26^+$	1011.7	81	$E2$	0.89±0.08
13304	$30^+ \rightarrow 29^{(+)}$	583.2	39	$M1$	0.71±0.09
13304	$30^+ \rightarrow 28^+$	1483.0	-	$E2$	-
8070	$20^+ \rightarrow 19^+$	638.2	22	$M1$	-
8070	$20^+ \rightarrow 18^+$	952.5	23	$E2$	1.03±0.07
11472	$27^+ \rightarrow 26^+$	543.9	-	$M1$	-
11472	$27^+ \rightarrow 26^+$	663.2	129	$M1$	0.53±0.04
11472	$27^+ \rightarrow 25^+$	1045.0	-	$E2$	-
12491	$29^+ \rightarrow 28^+$	322.6	16	$M1$	0.66±0.12
12491	$29^+ \rightarrow 27^+$	1018.6	80	$E2$	1.07±0.11
12720	$29^{(+)} \rightarrow 28^+$	899.8	82	$M1$	0.63±0.11
4837	$11^+ \rightarrow (10^+)$	1168.4	-	$M1$	-
7055	$18^- \rightarrow 16^-$	1043.0	-	$E2$	-
10427	$25^+ \rightarrow 24^+$	501.5	-	$M1$	-
10427	$25^+ \rightarrow 24^+$	770.9	-	$M1$	-
10427	$25^+ \rightarrow 23^+$	944.7	-	$E2$	-
13856	$31^+ \rightarrow 30^{(+)}$	1083.5	-	$M1$	-
13856	$31^+ \rightarrow 29^+$	1364.9	79	$E2$	1.00±0.16

Table A.2: (Continued.)

14777	$33^+ \rightarrow 31^+$	921.1	54	$E2$	1.17±0.21
12772	$30^{(+)} \rightarrow 29^+$	281.4	-	$M1$	-
14049	$32^+ \rightarrow 31^+$	193.0	21	$M1$	0.57±0.05
14049	$32^+ \rightarrow 30^+$	745.0	15	$E2$	-
15177	$34^+ \rightarrow 33^+$	400.2	15	$M1$	-
15177	$34^+ \rightarrow 32^+$	1128.3	20	$E2$	1.13±0.27
16511	$- \rightarrow 34^+$	1334.2	16	$M1$	-
2676	$7^- \rightarrow 8^+$	344.6	-	$E1$	-
2676	$7^- \rightarrow$	448.6	-	$E1$	-
2676	$7^- \rightarrow 6^+$	1127.4	-	$E1$	-
3148	$9^- \rightarrow 7^-$	472.0	63	$E2$	1.02±0.07
3148	$9^- \rightarrow 8^+$	816.6	356	$E1$	0.7±0.03
3823	$11^- \rightarrow 10^+$	651.6	37	$E1$	0.72±0.12
3823	$11^- \rightarrow 9^-$	675.0	365	$E2$	1.0±0.07
4599	$13^- \rightarrow 12^-$	178.2	3	$M1$	-
4599	$13^- \rightarrow 11^-$	776.3	417	$E2$	-
5434	$15^- \rightarrow 14^-$	251.3	14	$M1$	-
5434	$15^- \rightarrow 13^-$	835.1	389	$E2$	1.01±0.04
6135	$17^- \rightarrow 16^-$	161.1	36	$M1$	-
6135	$17^- \rightarrow 15^-$	700.6	336	$E2$	1.01±0.05
7031	$19^- \rightarrow 18^-$	290.8	45	$M1$	-
7031	$19^- \rightarrow 17^-$	896.6	286	$E2$	1.02±0.05
7940	$21^- \rightarrow 20^-$	313.0	42	$M1$	0.42±0.07
7940	$21^- \rightarrow 19^-$	908.4	142	$E2$	1.08±0.08
9106	$23^- \rightarrow 22^-$	583.7	60	$M1$	-
9106	$23^- \rightarrow 21^-$	1166.3	69	$E2$	1.03±0.08
10342	$25^- \rightarrow 24^-$	667.3	-	$M1$	-
10342	$25^- \rightarrow 23^-$	1236.4	41	$E2$	1.04±0.09
11554	$27^- \rightarrow 26$	499.6	-	$M1$	-
11554	$27^- \rightarrow 26^-$	657.8	18	$M1$	-
11554	$27^- \rightarrow 25^-$	1211.9	34.	$E2$	-
12360	$29^- \rightarrow 28^-$	490.2	-	$M1$	-
12360	$29^- \rightarrow 27^-$	735.7	-	$E2$	-
12360	$29^- \rightarrow 27^-$	805.6	33	$E2$	1.13±0.21
13577	$(31^-) \rightarrow 29^-$	1217.7	25	$E2$	-
2578	$6^- \rightarrow 5^+$	741.9	-	$E1$	-
2578	$6^- \rightarrow 6^+$	1030.1	-	$E1$	-
3095	$8^- \rightarrow 7^-$	419.7	4	$M1$	-
3095	$8^- \rightarrow 6^-$	517.0	11	$E2$	-
3717	$10^- \rightarrow 9^-$	569.4	12	$M1$	0.48±0.11
3717	$10^- \rightarrow 8^-$	621.6	15	$E2$	-
4421	$12^- \rightarrow 11^-$	598.0	19	$M1$	-
4421	$12^- \rightarrow 10^-$	703.7	40	$E2$	-
5181	$14^- \rightarrow 13^-$	582.4	14	$M1$	-
5181	$14^- \rightarrow 12^-$	760.6	38	$E2$	-
5974	$16^- \rightarrow 15^-$	539.5	30	$M1$	-
5974	$16^- \rightarrow 14^-$	792.2	45	$E2$	-
6741	$18^- \rightarrow 17^-$	605.9	138	$M1$	0.48±0.05
6741	$18^- \rightarrow 16^-$	766.9	28	$E2$	-
7626	$20^- \rightarrow 19^-$	594.7	106	$M1$	0.53±0.19
7626	$20^- \rightarrow 18^-$	885.4	70	$E2$	-
8522	$22^- \rightarrow 21^-$	582.6	80	$M1$	0.61±0.14
8522	$22^- \rightarrow 20^-$	896.3	65	$E2$	-
9675	$24^- \rightarrow 23^-$	569.2	31	$M1$	-

Table A.2: (Continued.)

9675	$24^- \rightarrow 22^-$	1152.9	60	$E2$	-
10896	$26^- \rightarrow 25^-$	553.7	-	$M1$	-
10896	$26^- \rightarrow 24^-$	1221.0	25	$E2$	1.04±0.32
12197	$28^- \rightarrow 27^-$	643.2	-	$M1$	-
12197	$28^- \rightarrow 26^-$	1301.1	15	$E2$	-
1247	$3^+ \rightarrow 4^+$	368.5	15	$M1$	-
1247	$3^+ \rightarrow 2^+$	401.4	-	$M1$	-
1247	$3^+ \rightarrow 2^+$	893.4	-	$M1$	-
1837	$5^+ \rightarrow 4^+$	400.1	-	$M1$	-
1837	$5^+ \rightarrow 3^+$	589.2	-	$E2$	1.06±0.09
1837	$5^+ \rightarrow 4^+$	957.7	-	$M1$	-
2575	$7^+ \rightarrow 6^+$	430.6	-	$M1$	-
2575	$7^+ \rightarrow 5^+$	738	53	$E2$	1.01±0.04
3344	$9^+ \rightarrow 7^+$	769.1	22	$E2$	1.09±0.07
4003	$11^+ \rightarrow 9^+$	658.8	21	$E2$	1.03±0.06
4742	$13^+ \rightarrow 11^+$	739	15	$E2$	1.01±0.04
5591	$15^+ \rightarrow 13^+$	849.1	21	$E2$	1.02±0.05
6542	$17^+ \rightarrow 15^+$	951.0	18	$E2$	1.06±0.05
7553	$19^+ \rightarrow 17^+$	1011.0	} 9	$E2$	} 1.07±0.66
8564	$21^+ \rightarrow 19^+$	1011.0		$E2$	
846	$2^+ \rightarrow 2^+$	492.0	-	$M1$	-
846	$2^+ \rightarrow 0^+$	845.9	-	$E2$	-
1437	$4^+ \rightarrow 4^+$	558.3	-	$M1$	-
1437	$4^+ \rightarrow 2^+$	591.2	-	$E2$	-
1437	$4^+ \rightarrow 2^+$	1083.2	-	$E2$	-
2143	$6^+ \rightarrow 6^+$	594.2	-	$M1$	-
2143	$6^+ \rightarrow 4^+$	705.4	-	$E2$	-
2143	$6^+ \rightarrow 4^+$	1263.7	-	$E2$	-
2911	$(8^+) \rightarrow 6^+$	768.4	-	$E2$	-
3669	$(10^+) \rightarrow (8^+)$	757.9	-	$E2$	-
9647	$23^+ \rightarrow 21^+$	1083.8	2	$E2$	1.02±0.1
9668	$23^+ \rightarrow 21^+$	1104.0	2	$E2$	1.48±0.42
10836	$25^+ \rightarrow 23^+$	1168.5	2	$E2$	1.64±0.4
12059	$(27^+) \rightarrow 25^+$	1222.9	-	$E2$	-
3273	$9^- \rightarrow 8^+$	942.3	28	$E1$	0.72±0.09
3955	$11^- \rightarrow 9^-$	681.9	28	$E2$	1.12±0.17
3955	$11^- \rightarrow 10^+$	784.1	5	$E1$	-
4759	$13^- \rightarrow 11^-$	803.4	23	$E2$	1.0±0.1
4759	$13^- \rightarrow 12^+$	875.9	2	$E1$	-
5659	$15^- \rightarrow 13^-$	900.0	23	$E2$	1.04±0.11
5659	$15^- \rightarrow 14^+$	1046.2	-	$E1$	-
6535	$17^- \rightarrow 15^-$	876.1	16	$E2$	1.1±0.2
6535	$17^- \rightarrow 16^+$	1069.2	-	$E1$	-
7395	$19^- \rightarrow 17^-$	860.4	15	$E2$	1.01±0.12
8355	$21^- \rightarrow 19^-$	960.3	13	$E2$	1.05±0.19
9375	$23^- \rightarrow 21^-$	1019.4	-	$E2$	1.11±0.18
10538	$25^- \rightarrow 23^-$	1163.0	6	$E2$	-
3557	$- \rightarrow 7^+$	982.5	-	$M1$	-
11738	$27^- \rightarrow 25^-$	1200.6	-	$E2$	-
11738	$27^- \rightarrow 25^-$	1395.9	} 60	$E2$	} 1.25±0.30
15036	$33^- \rightarrow 31^-$	1397.9		$E2$	
11738	$27^- \rightarrow 25^-$	1404.4	-	$E2$	-
11781	$- \rightarrow 25^-$	1243.1	-	$E1$	-
11869	$28^- \rightarrow 27^-$	130.4	12	$M1$	0.61±0.17

Table A.2: (Continued.)

11869	$28^- \rightarrow 27^-$	244.8	10	$M1$	0.62±0.14
11869	$28^- \rightarrow 27^-$	315.0	14	$M1$	0.42±0.10
11869	$28^- \rightarrow 26^-$	972.6	-	$E2$	-
13317	$30^- \rightarrow 29^-$	723	} 77	$M1$	} 0.41±0.10
12594	$29^- \rightarrow 28^-$	725		$M1$	
13317	$30^- \rightarrow 28^-$	1448.1	-	$E2$	-
14813	$32^- \rightarrow 31^-$	1174.8	-	$M1$	-
14813	$32^- \rightarrow 30^-$	1496	-	$E2$	-
2227	$- \rightarrow 4^+$	1348.2	-	$E2$	-
9994	$24 \rightarrow 23^-$	888.4	-	$M1$	-
11054	$26 \rightarrow 24$	1060.0	-	$E2$	-
11054	$26 \rightarrow 24^-$	1379.2	-	$E2$	-
12333	$28 \rightarrow 27^-$	779.0	-	$M1$	-
12333	$28 \rightarrow 26$	1279.0	-	$E2$	-
13638	$31^- \rightarrow 30^-$	321.1	30	$M1$	0.41±0.08
13638	$31^- \rightarrow 30^-$	645.5	9	$M1$	-
13638	$31^- \rightarrow 29^-$	1044.2	31	$E2$	-
15036	$33^- \rightarrow 32^-$	223.1	6	$M1$	0.76±0.29
11624	$27^- \rightarrow 26^-$	727.8	-	$M1$	-
11624	$27^- \rightarrow 25^-$	1281.5	11	$E2$	-
16528	$- \rightarrow 33^-$	1492.6	-	$E1$	-
16384	$- \rightarrow 33^-$	1348.4	-	$E1$	-
12993	$30^- \rightarrow 29^-$	399.0	-	$M1$	-
12993	$30^- \rightarrow 29^-$	633.2	42	$M1$	0.77±0.11
4018	$10^+ \rightarrow (8^+)$	1107.0	-	$E2$	-
8706	$21^+ \rightarrow 19^+$	1152.8	4	$E2$	1.0±0.1
10334	$25^- \rightarrow 23^-$	1228.0	-	$E2$	-

[a] Uncertainties of γ-ray energies are between 0.1 and 0.6 keV depending on their intensity.

[b] Intensities are normalized to the 524.9 keV transition with I_γ = 1000.

[b] Uncertainties are between 10 and 30% depending on intensities.

Bibliography

[AF79] T. K. Alexander and J. Foster: *Advances in Nuclear Physics: chapter3*, vol. 10 (Plenum Press, New York, 1979)

[AFLR99] A. V. Afanasjev, D. B. Fossan, G. J. Lane, and I. Ragnarsson: «Termination of rotational bands: Disappearance of quantum many-body collectivity». Phys. Rep. **322**, 1 (1999)

[AGH+84] D. Alber, H. Grawe, H. Haas, H. E. Mahnke, W. Semmler, and W. D. Zeitz: «Recoil Distance Lifetime Measurements in ^{125}Xe». Nucl. Phys. A **413**, 353 (1984). URL http://dx.doi.org/10.1016/0375-9474(84)90379-8

[AKHB+07] A. Al-Khatib, H. Hübel, P. Bringel, C. Engelhardt, A. Neußer-Neffgen, G. B. Hagemann, C. Hansen, B. Berskind, G. Sletten, A. Bracco, F. Camera, G. Benzoni, P. Fallon, R. Clark, M. Carpenter, R. Janssen, T. Khoo, P. Chowdhury, and H. Amro: «High-Spin Spectroscopy of ^{124,125,126}Xe». Acta Phys. Pol. A **38**, 1431 (2007). URL http://th-www.if.uj.edu.pl/acta/vol38/pdf/v38p1431.pdf

[AKHB+08] A. Al-Khatib, H. Hübel, P. Bringel, C. Engelhardt, A. Neusser-Neffgen, G. B. Hagemann, C. Hansen, B. Berskind, G. Sletten, A. Bracco, F. Camera, G. Benzoni, P. Fallon, R. Clark, M. Carpenter, R. Janssen, T. Khoo, P. Chowdhury, and H. Amro: «Transition to non-collective states at high spin in ^{124}Xe». Eur. Phys. J. A **36**, 21 (2008). doi:10.1140/epja/i2008-10570-1. URL http://publish.edpsciences.com/abstract/epjA/v36/p21

[AKSH+06] A. Al-Khatib, A. Singh, H. Hübel, P. Bringel, A. Bürger, J. Domscheit, A. Neußer-Neffgen, G. Schönwaßer, G. Hagemann, C. R. Hansen, B. Herskind, G. Sletten, J. Wilson, J. Timár, A. Algora, Z. Dombrádi, J. Gál, G. Kalinka, J. Molnár, B. Nyakó, D. Sohler, L. Zolnai, R. Clark, M. Cromaz, P. Fallon, I. Lee, A. Macchiavelli, D. Ward, H. Amr, W. Ma, M. Kmiecik, A. Maj, J. Styczen, K. Zuber, K. Hauschild, A. Korichi, A. Lopez-Martens, J. Roccaz, S. Siem, F. Hannachi, J. Scheurer, P. Bednarczyk, T. Byrski, D. Curien, O. Dorvaux, G. Duchêne, B. Gall, F. Khalfallah, I. Piqueras, J. Robin, A. Görgen, K. Juhász, S. Patel, A. Evans, G. Rainovski, G. Benzoni, A. Bracco, F. Camera, S. Leoni, P. Mason, B. Million, A. P. R. Sacchi, O. Wieland, C. Petrache, D. Petrache, G. L. Rana, R. Moro, G. D. Angelis, J. Lisle, B. Cederwall, K. Lagergen, R. Lieder, E. Podsvirova, W. Gast, H. Jäger, and N. R. and: «Competition between collective and noncollective excitation modes at high spin in ^{124}Ba». Phys. Rev. C **74**, 014 305 (2006). doi:10.1103/PhysRevC.74.014305. URL http://link.aps.org/abstract/PRC/v74/e014305

[ALL+79] G. Andersson, S. E. Larsson, G. Leander, P. M. ller, S. G. Nilsson, I. Ragnarsson, S. A. berg, R. Bengtsson, J. Dudek, B. Nerlo-Pomorska, K. Pomorski, and Z. Szymański: «Nuclear shell structure at very high angular momentum». Nucl. Phys. A **268**, 205 (1979). URL http://dx.doi.org/10.1016/0375-9474(76)90461-9

[AR95] A. V. Afanasjev and I. Ragnarsson: «Gradual Loss of Collectivity in Rotational Bands in the A $\approx$ 110 (Z $\geq$ 50, N $\approx$ 60) Mass Region». Nucl. Phys. A **591**, 387 (1995). URL http://dx.doi.org/10.1016/0375-9474(95)00196-8

[AR96] A. V. Afanasjev and I. Ragnarsson: «The coexistence of the intruder $\nu i_{13/2}$, superdeformed and terminating bands in the $A \sim 135$ mass region». Nucl. Phys. A **608**, 176 (1996). URL http://dx.doi.org/10.1016/0375-9474(96)00257-6

[Bec92] F. A. Beck: «EUROBALL: Large gamma ray spectrometers through european collaborations». Prog.Part.Nucl.Phys. **28**, 443 (1992). URL http://dx.doi.org/10.1016/0146-6410(92)90047-6

[Ben] R. Bengtsson: «Ultimate Cranking Package» URL http://www.matfys.lth.se/~ragnar/ultimate.html,http://www.matfys.lth.se/~ragnar/nusma.html

[Ben89] T. Bengtsson: «A method to remove virtual interactions with applications to nuclear spectroscopy». Nucl. Phys. A **496**, 56 (1989). URL http://dx.doi.org/10.1016/0375-9474(89)90216-9

[Ben90] T. Bengtsson: «The high-spin structure of ^{158}Er». Nucl. Phys. A **512**, 124 (1990). URL http://dx.doi.org/10.1016/0375-9474(90)90007-9

[Ber] M. Bergström: «Programe package Tennis-1.0.0 and Euroball Gain-1.03.»

[BF79a] R. Bengtsson and S. Frauendorf: «An interpretation of backbending in terms of crossing of the ground state band with an aligned two-quasiparticle band». Nucl. Phys. A **314**, 27 (1979). URL http://dx.doi.org/10.1016/0375-9474(79)90552-9

[BF79b] R. Bengtsson and S. Fraunendorf: «Quasiparticle spectra near the yrast line». Nucl. Phys. A **327**, 139 (1979). URL http://dx.doi.org/10.1016/0375-9474(79)90322-1

[BFM86] R. Bengtsson, S. Frauendorf, and R. R. May: «Quasiparticle levels in rotating rare earth nuclei: A cranked shell-model dictionary». At. Data Nucl. Data Tables **35**, 15 (1986). URL http://dx.doi.org/10.1016/0092-640X(86)90028-8

[BG84] R. Bengtsson and J. G. Garrett: «The cranking model - theoretical and experimental bases». In T. Engeland, J. Rekstand, and J. S. Vaagen (Eds.), *Collective phenomena in Atomic Nuclei*, page 193 (World Scientific, Singapore, 1984)

[BM53] A. Bohr and B. R. Mottelson: «Rotational States in Even-Even Nuclei». Phys. Rev. **90**, 717 (1953). doi:10.1103/PhysRev.90.717.2. URL http://link.aps.org/doi/10.1103/PhysRev.90.717.2

[BM69] A. Bohr and B. R. Mottelson: *Nuclear Structure*, vol. I (W. A. Benjamin, Inc., New York, 1969)

[BM75] A. Bohr and B. R. Mottelson: *Nuclear Structure*, vol. II (W. A. Benjamin, Inc., New York, 1975)

[BMP58] A. Bohr, B. R. Mottelson, and D. Pines: «Possible Analogy between the Excitation Spectra of Nuclei and Those of the Superconducting Metallic State». Phys. Rev. **110**, 936 (1958). doi:10.1103/PhysRev.110.936. URL URL:http://link.aps.org/doi/10.1103/PhysRev.110.936

[Boh51] A. Bohr: «On the Quantization of Angular Momenta in Heavy Nuclei». Phys. Rev. **81**, 134 (1951). doi:10.1103/PhysRev.81.134. URL http://link.aps.org/doi/10.1103/PhysRev.81.134

[BPB+95] C. W. Beausang, D. Prevost, M. H. Bergstrom, G. deFrance, B. Haas, J. C. Lisle, C. Theisen, J. Timár, P. J. Twin, and J. N. Wilson: «Using high-fold data from the new generation of γ-ray detector arrays». Nucl. Instr. Meth. A **364**, 560 (1995). URL http://dx.doi.org/10.1016/0168-9002(95)00438-6

[BPF+97] G. L. Bianco, C. Protochristov, G. Falconi, N. Blasi, D. Bazzacco, G. de Angelis, D. Napoli, M. Cardona, A. Kreiner, and H. Somacal: «A dipole band in ^{124}Xe». Z. Phys. A **359** (1997)

[BR85] T. Bengtsson and I. Ragnarsson: «Rotational bands and particle-hole excitations at very high spin». Nucl. Phys. A **436**, 14 (1985). URL http://dx.doi.org/10.1016/0375-9474(85)90541-X

[BS96] C. W. Beausang and J. Simpson: «Large arrays of escape suppressed spectrometers for nuclear structure experiments». J. Phys. G: Nucl. Part. Phys. A **22**, 527 (1996). URL http://www.iop.org/EJ/article/0954-3899/22/5/003/g605r1.pdf

[BT87] C. Bargholtz and P. E. Tegneér: «Gamma-gamma directional correlations: Simplifications at high spin». Nucl. Instr. Meth. A **256**, 513 (1987). URL http://dx.doi.org/10.1016/0168-9002(87)90295-6

[Cas00] R. F. Casten: *Nuclear Structures from a Single Perspective* (Oxford University Press, Oxford, 2000)

[CB85] R. F. Casten and P. von Brentano: «An extensive region of O(6) like nuclei near A = 130». Phys. Lett. B **152**, 22 (1985). URL http://dx.doi.org/10.1016/0370-2693(85)91131-1

[CFL83] Y. S. Chen, S. Frauendorf, and G. A. Leander: «Shape of rotating quasiparticle orbits and signature splitting in La, Ce, and Pr nuclei». Phys. Rev. C **28**, 2437 (1983). doi:10.1103/PhysRevC.28.2437. URL http://link.aps.org/doi/10.1103/PhysRevC.28.2437

[CLA+95] B. Cederwall, I. Y. Lee, S. Asztalos, M. J. Brinkman, J. A. Becker, R. M. Clark, M. A. Deleplanque, R. M. Diamond, P. Fallon, L. P. Farris, E. A. Henry, J. R. Hughes, A. O. Macchiavelli, and F. S. Stephens: «Measurement of ultra-fast γ-ray transitions from heavy-ion compound-nucleus reactions». Nucl. Instr. Meth. A **354**, 591 (1995). doi:10.1016/0168-9002(94)01468-X. URL http://dx.doi.org/10.1016/0168-9002(94)01468-X

[CLF+96] R. M. Clark, I. Y. Lee, P. Fallon, D. T. Joss, S. J. Asztalos, J. A. Becker, L. Bernstein, B. Cederwall, M. A. Deleplanque, R. M. Diamond, L. P. Farris, K. Hauschild, W. H. Kelly, A. O. Macchiavelli, P. J. Nolan, N. O'Brien, A. T. Semple, F. S. Stephens, and R. Wadsworth: «Relative Deformations of Superdeformed Bands in ^{131,132}Ce». Phys. Rev. Lett. **76**, 3510–3513 (1996). doi:10.1103/PhysRevLett.76.3510. URL http://link.aps.org/doi/10.1103/PhysRevLett.76.3510

[DF82] F. Dönau and S. Frauendorf: «Branching ratio». In N. R. Johnson (Ed.), *High Angular Momentum Properties of Nuclei*, page 143 (Hardwood Academic, New York, 1982)

[DMN+66] R. M. Diamond, E. Matthias, J. O. Newton, , and F. S. Stephens: «Nuclear Alignment in Heavy-Ion Reactions». Phys. Rev. Lett. **16**, 1205 (1966). doi:10.1103/PhysRevLett.16.1205. URL http://link.aps.org/doi/10.1103/PhysRevLett.16.1205

[Dön87] F. Dönau: «Electromagnetic radiation of rotating nuclei». Nucl. Phys. A **471**, 469 (1987). URL http://dx.doi.org/10.1016/0375-9474(87)90094-7

[EIS+66] H. Ejiri, M. Ishihara, M. Sakai, K. Katori, and T. Inamura: «Anisotropy of conversion electrons from vibrational levels and rotational levels excited by $(\pi, 2n)$ reactions». Nucl. Phys. A **89**, 641 (1966)

[EN92] L. P. Ekström and A. Nordlund: «Gamma-Gamma correlations with detector arrays». Nucl. Instr. Meth. A **313**, 421 (1992). URL http://dx.doi.org/10.1016/0168-9002(92)90820-T

[Eng04] C. Engelhardt: *Bestimmung der Multipolordnung von γ-Übergängen zwischen Hochspinzuständen in ^{125}Xe und ^{126}Xe*. Master's thesis, Helmholtz Institut für Strahlen- und Kernphysik, Bonn (2004)

[EV89] E. Ejiri and M. J. A. de Voigt: *Gamma-Ray and Electron Spectroscopy in Nuclear Physics* (Clarendon Press, Oxford, 1989)

[FBC99] B. R. Firestone, C. Baglin, and S. Y. F. Chu: «Table of Isotopes». John Wiley & Sons, Inc., New York (1999)

[Fer65] A. J. Ferguson: *Nuclear Correlation Methods in Gamma-Ray Spectroscopy* (North-Holand Publishing Company-Amesterdam, 1965)

[FS65] H. Frauenfelder and R. M. Steffen: *Angular Correlations ,Alpha- Beta- and Gamma-Ray Spectroscopy*, vol. 2 (North-Holand Publishing Co., Amsterdam, 1965)

[Gar83] D. D. Garrett: «Spectroscopy in a rotating deformed nucleus». Nucl. Phys. A **409**, 259c (1983). URL http://dx.doi.org/10.1016/0375-9474(83)90689-9

[GHM+04] J. Gál, G. Hegyesi, J. Molnár, B. M. Nyakó, G. Kalinka, J. N. Scheurer, M. M. Aléonard, J. F. Chemin, J. L. Pedroza, K. Juhász, and V. F. E. Pucknell: «The VXI electronics of the DIAMANT particle detector array». Nucl. Instr. Meth. A **516**, 502 (2004). URL http://dx.doi.org/10.1016/j.nima.2003.08.158

[GKH+84] W. Gast, U. Kaup, H. Hanewinkel, R. Reinhardt, K. Schiffer, K. Schmittgen, K. Zell, J. Wrzesinski, A. Gelberg, and P. von Brentano: «Excited States in ^{124}Xe». Z. Phys. A **318**, 123 (1984)

[GLG+91] A. Granderath, D. Lieberz, A. Gelberg, W. Lieberz, R. Wirowski, P. von Brentano, and R. Wyss: «Excited states in ^{125}Xe». Nucl. Phys. A **524**, 153 (1991). URL http://dx.doi.org/10.1016/0375-9474(91)90021-W

[GMB+96] A. Granderath, P. F. Mantica, R. Bengtsson, R. Wyss, P. von Brentano, A. Gelberg, and F. Seiffert: «Shapes and rotational structures of neutron $h_{11/2}$ configurations in the Xe–Ba–Ce region». Nucl. Phys. A **597**, 427 (1996). URL http://dx.doi.org/10.1016/0375-9474(95)00484-X

[GTH65] S. R. D. Groot, H. A. Tolhoek, and W. J. Huiskamp: *Orintation of Nuclei at low Temperatures; Alpha- Beta- and Gamma-Ray Spectroscopy*, vol. 2 (North-Holand Publishing Co., Amsterdam, 1965)

[Har65] S. M. Harris: «Higher order corrections to the cranking model». Phys. Rev. **138**, B509 (1965). doi:10.1103/PhysRev.138.B509. URL http://link.aps.org/doi/10.1103/PhysRev.138.B509

[Hey99] K. Heyde: *Basic Ideas and Concepts in Nuclear Physics* (IOP Publishing Ltd, London, UK, 1999)

[HGE97] P. E. Hodgson, E. Gadioli, and E. G. Erba: *Introductory Nuclear Physics* (Clarendon Press, Oxford, 1997)

[HHD+07] B. Herskind, G. Hagemann, T. Dossing, C. Hansen, N. Schunck, G. Sletten, S. O. degård, H.Hübel, P. Bringel, A. Bürger, A. Neußer, A. Singh, A. Al-Khatib, S. Patel, B. M.Nyako, A. Algora, Z. Dombradi, J. Gal, G. Kalinka, D. Sohler, J. Molnar, J. Timar, L. Zolnai, K. Juhasz, A. Bracco, S. Leoni, F. Camera, G. Benzoni, P. Mason, A. Paleni, B. Million, O. Wieland, P. Bednarczyk, F. Azaiez, T. Byrski, D. Curien, O. Dakov, G. Duchene, F. Khalfallah, B. Gall, L. Piqeras, J. Robin, J. Dudek, N. Rowley, N. Redon, F. Hannachi, J. Scheurer, J. Wilson, A. Lopez-Martens, A. Korichi, K. Hauschild, J. Roccaz, S. Siem, P. Fallon, I. Lee, A. Gorgen, A. Maj, M. Kmiecik, M. Brekiesz, J. Styczen, K. Zuber, J. Lisle, B. Cederwall, K. Lagergren, A. Evans, G. Rainovski, G. D. Angelis, G. L. Rana, R. Moro, R. Lieder, E. Lieder, W. Gast, H. Jager, A. Pasternak, C. Petrache, and D. Petrache: «Light Charged Particles as Gateway to Hyperdeformation». Acta Phys. Pol. A **38**, 1421 (2007)

[HHL79] H. Helppi, J. Hattula, and A. Luukko: «Even- and odd-parity band structures in ^{125}Xe». Nucl. Phys. A **332**, 183 (1979). URL http://dx.doi.org/10.1016/0375-9474(79)90103-9

[HHS+06] B. Herskind, G. Hagemann, G. Sletten, T. Dossing, C. Hansen, N. Schunck, S. O. degård, H. Hübel, P. Bringel, A. Bürger, A. Neußer, A. Singh, A. Al-Khatib, S. Patel, A. Bracco, S. Leoni, F. Camera, G. Benzoni, P. Mason, A. Paleni, B. Million, O. Wieland, P. Bednarczyk, F. Azaiez, T. Byrski, D. Curien, O. Dakov, G. Duchene, F. Khalfallah, B. Gall, I. Piqueras, J. Robin, J. Dudek, N. Rowley, B. Nyako, A. Algora, Z. Dombradi, J. Gal,

G. Kalinka, D. Sohler, J. Molnar, J. Timar, L. Zolnai, K. Juhasz, N. Redon, F. Hannachi, J. Scheurer, J. Wilson, A. Lopez-Martens, A. Korichi, K. Hauschild, J. Roccaz, S. Siem, P. Fallon, I. Lee, A. Gorgen, A. Maj, M. Kmiecik, M. Brekiesz, J. Styczen, K. Zuber, J. Lisle, B. Cederwall, K. Lagergren, A. Evans, G. Rainovski, G. D. Angelis, G. L. Rana, R. Moro, W. Gast, R. Lieder, E. Podsvirova, H. Jager, C. Petrache, and D. Petrache: «Charged particle feeding of hyperdeformed nuclei in the A=118-126 region». Phys. Scripta **T125**, 108 (2006). doi:10.1088/0031-8949/2006/T125/025. URL http://dx.doi.org/10.1088/0031-8949/2006/T125/025

[HJA+81] H.Helppi, J.Hattula, A.Luukko, M.Jaaskelainen, and F.Donau: «In-Beam Study of ^{127,129}Xe and Collective Description of the Level Structures in Odd-A Xe Nuclei». Nucl. Phys. A **357**, 333 (1981). URL http://dx.doi.org/10.1016/0375-9474(81)90225-6

[HRJ+99] D. J. Hartley, L. L. Riedinger, H. Q. Jin, W. Reviol, B. H. Smith, A. Galindo-Uribarri, D. G. Sarantites, D. R. LaFosse, J. N. Wilson, and S. M. Mullins: «Rotational structures in ^{125}La and alignments in $A \approx 130$ nuclei». Phys. Rev. C **60**, 014 308 (1999). doi:10.1103/PhysRevC.60.014308

[Hüb05a] H. Hübel: «Magnetic rotation in nuclei». Prog.Part.Nucl.Phys. **54**, 1 (2005). URL http://dx.doi.org/10.1016/j.ppnp.2004.06.002

[Hüb05b] H. Hübel: «Search for Hyperdeformation». Acta Phys. Pol. A **36**, 1015 (2005)

[Ing54] D. R. Inglis: «Particle Derivation of Nuclear Rotation Properties Associated with a Surface Wave». Phys. Rev. **96**, 1059 (1954). doi:10.1103/PhysRev.96.1059. URL http://link.aps.org/doi/10.1103/PhysRev.96.1059

[Ing55] D. R. Inglis: «Dynamics of Nuclear Deformation». Phys. Rev. **97**, 701 (1955). doi:10.1103/PhysRev.97.701. URL http://link.aps.org/doi/10.1103/PhysRev.97.701

[KFML+89] A. Krämer-Flecken, T. Morek, R. Lieder, W. Gast, G. Hebbinghaus, and W. U. H.M. Jäger: «Use of DCO ratios for spin determination in γ-γ coincidence measurements». Nucl. Instr. Meth. A **275**, 333 (1989). URL http://dx.doi.org/10.1016/0168-9002(89)90706-7

[KHS+89] T. Komatsubara, T. Hosoda, H. Sakamoto, T. Aoki, and K. Furuno: «Level structure of ^{124}Ba». Nucl. Phys. A **496**, 605 (1989). URL http://dx.doi.org/10.1016/0375-9474(89)90079-1

[KKS+83] H. Kusakari, K. Kitao, K. Sato, M. Sugawara, and H. Katsuragawa: «High-spin states in even-mass Xe nuclei and backbending phenomena». Nucl. Phys. A **401**, 445 (1983). URL http://dx.doi.org/10.1016/0375-9474(83)90359-7

[KN29] O. Klein and Y. Nishina: «Über die Streung von Strahlung durch freie Elektronen nach der neuen relativistischen Quantendynamik von Dirac». Z. Phys. A **52**, 853 (1929)

[Kra87] K. Krane: *Introductory nuclear physics* (John Wiley and Sons. Inc, USA, 1987)

[KSW73] K. S. Krane, R. M. Steffen, and R. M. Wheeler: «Directional correlations of gamma radiations emitted from nuclear states oriented by nuclear reactions or cryogenic methods». At. Data Nucl. Data Tables **11**, 351 (1973)

[KYK+75] H. Kusakari, N. Yoshikawa, H. Kawakami, M. Ishihara, Y. Shida, and M. Sakai: «Quasi-gamma bands in even-mass Xe AND Ba nuclei». Nucl. Phys. A **242**, 13 (1975). doi:10.1016/0375-9474(75)90030-5

[KYK+78] H. Kusakari, N. Yoshikawa, H. Kawakami, M. Ishihara, Y. Shida, and M. Sakai: «Study of the ^{124}Xe and ^{126}Xe structure». Z. Phys. A **284**, 297 (1978). URL http://dx.doi.org/10.1016/0375-9474(75)90030-5

[LDF+90] W. Lieberz, A. Dewald, W. Frank, A. Gelberg, W. Krips, D. Lieberz, R. Wirowski, and P. von Brentano: «Evidence for variable γ deformation in ^{126}Xe». Phys. Lett. B **240**, 38 (1990). doi:10.1016/0370-2693(90)90405-U. URL http://dx.doi.org/10.1016/0370-2693(90)90405-U

[LDV03] I. Y. Lee, M. A. Delepanque, and K. Vetter: «Developments in large gamma-ray detector arrays». Rep. Prog. Phys. **66**, 1095 (2003)

[Lee90] I. Y. Lee: «The Gammasphere». Nucl. Phys. A **520**, 641c (1990)

[Leo94] W. R. Leo: *Techniques for Nuclear and Particle Physics Experiments* (Springer-Verlag Berlin Heidelberg, 1987, 1994)

[LGG+91] D. Lieberz, A. Gelberg, A. Granderath, P. von Brentano, I. Ragnarsson, and P. B. Semmes: «Triaxial Rotor Plus Particle Description of Negative-Parity States in ^{125}Xe». Nucl. Phys. A **529**, 1 (1991). URL http://dx.doi.org/10.1016/0375-9474(91)90781-Z

[LNST63] S. Lindhard, V. Nielsen, M. Scharff, and P. V. Thomsen: Mat. Fys. Medd. Dan. Vid. Selsk. **33**, 10 (1963)

[LNST68] S. Lindhard, V. Nielsen, M. Scharff, and P. V. Thomsen: Mat. Fys. Medd. Dan. Vid. Selsk. **36**, 10 (1968)

[MBB+05] P. Mason, G. Benzoni, A. Bracco, F. Camera, B. Million, O. Wieland, S. Leoni, A. K. Singh, A. Al-Khatib, H. Hübel, P. Bringel, A. Bürger, A. Neußer, G. Schönwaßer, G. B. Hagemann, C. R. Hansen, B. Herskind, G. Sletten, A. Algora, Z. Dombrá, J. Gál, G. Kalinka, J. Molnár, B. M. Nyakó, D. Sohler, J. Timár, L. Zolnai, M. Kmiecik, A. Maj, J. Styczen, K. Zuber, F. Azaiez, K. Hauschild, A. Korichi, A. Lopez-Martens, J. Roccaz, S. Siem, F. Hannachi, J. N. Scheurer, P. Bednarczyk, T. Byrski, D. Curien, O. Dorvaux, G. Duchéne, B. Gall, F. Khalfallah, I. Piqueras, J. Robin, K. Juhász, S. B. Patel, A. O. Evans, G. Rainovski, C. M. Petrache, D. Petrache, G. L. Rana, R. Moro, G. D. Angelis, P. Fallon, I.-Y. Lee, J. C. Lisle, B. Cederwall, K. Lagergen, R. M. Lieder, E. Podsvirova, W. Gast, H. J. ger, N. Redon, and A. Görgen: «Evidence for octupole signature in ^{124,125}Ba». Phys. Rev. C **72**, 064 315 (2005). doi:10.1103/PhysRevC.72.064315. URL http://link.aps.org/doi/10.1103/PhysRevC.72.064315

[MBES+87] J. P. Martin, V. Barci, H. El-Samman, A. Gizon, J. Gizon, B. Nyakó, W. Klamra, F. A. Beck, T. Byrski, and J. C. Merdinger: «The band structure in ^{124}Ba». Z. Phys. A **326**, 337 (1987)

[MBES+88] J. P. Martin, V. Barci, H. El-Samman, A. Gizon, J. Gizon, W. Klamra, B. M. Nyakó, F. A. Beck, T. Byrski, and J. C. Merdinger: «Collective band structures and particle alignments in ^{124}Ba, ^{125}Ba and ^{125}Cs». Nucl. Phys. A **489**, 169 (1988). URL http://dx.doi.org/10.1016/0375-9474(88)90059-0

[MLK+07] C. B. Monn, C. S. Lee, T. Komatsubara, Y. Sasaki, and K. Furuno: «Structure of the negative parity bands in ^{125}Xe». Phys. Rev. C **76**, 067 301 (2007). doi:10.1103/PhysRevC.76.067301. URL http://link.aps.org/doi/10.1103/PhysRevC.76.067301

[Moo96] F. E. Moore: «Proceedings of the Workshop on Gammasphere Physics» (World Scientific Publishing Co., Singapore, 1996)

[NBF94] P. J. Nolan, F. A. Beck, and D. B. Fossan: «Large Arrays of Escape-Suppressed Gamma-ray Detectors». Ann. Rev. Nucl. Sci. **44**, 561 (1994). doi:0.1146/annurev.ns.44.120194.003021. URL http://arjournals.annualreviews.org/doi/pdf/10.1146/annurev.ns.44.120194.003021

[NDB+85] W. Nazarewicz, J. Dudek, R. Bengtsson, T. Bengtsson, and I. Ragnarsson: «Microscopic study of the high-spin behaviour in selected A $\approx$ 80 nuclei». Nucl. Phys. A **435**, 397 (1985). URL http://dx.doi.org/10.1016/0375-9474(85)90471-3

[NHAK+04] A. Neußer, H. Hübel, A. Al-Khatib, P. Bringel, A. Bürger, N. Nenoff, G. Schönwaßer, A. Singh, C. Petrache, G. Lo Bianco, I. Ragnarsson, G. Hagemann, B. Herskind, D. Jensen, G. Sletten, P. Fallon, A. Görgen, P. Bednarczyk, D. Curien, G. Gangopadhyay, A. Korichi, A. Lopez-Martens, B. Rao, T. Reddy, and N. Singh: «Superdeformed band at very high spin in ^{140}Nd». Phys. Rev. C **70**, 064 315 (2004). doi:10.1103/PhysRevC.70.064315. URL http://link.aps.org/abstract/PRC/v70/e064315

[Nil55] S. G. Nilsson: «Binding states of individual nucleon in strogly deformed nuclei». Mat. Fys. Medd. Dan. Vid. Selsk. **29** (1955)

[NKL+85] P. J. Nolan, A. Kirwan, D. J. G. Love, A. H. Nelson, D. J. Unwin, and P. J. Twin.: «A shape change along the yrast line in ^{132}Ce». J. Phys. G: Nucl. Part. Phys. A **11**, L17 (1985)

[NN05] A. Neußer-Neffgen: *Untersuchung der Formkoexistenz bei hohem Drehimpuls in den Isotopen ^{170}Hf, ^{140}Nd and ^{126}Xe*. Ph.D. thesis, Rheinischen Friedrich-Wilhelms-Universität Bonn (2005)

[NR95] S. G. Nilsson and I. Ragnarsson: *Shapes and Shells in Nuclear structure* (Cambridge University Press, UK, Cambridge, 1995)

[NR96] W. Nazarewicz and I. Ragnarsson: *Nuclear Deformation*. Oxford studies in nuclear physics, Handbook of Nuclear Properties (Clarendon Press Oxford, 1996)

[NSD+67] J. O. Newton, F. S. Stephens, R. M. Diamond, K. Kotajima, and E. Matthias: «Angular distributions of gamma rays produced in reactions with heavy ions». Nucl. Phys. A **95**, 357 (1967). URL http://dx.doi.org/10.1016/0375-9474(67)90507-6

[NSS79] P. J. Nolan and J. F. Sharpy-Schafer: «The measuremen of the lifetimes of excited nuclear states». Rep. Prog. Phys. **42**, 1 (1979). URL http://dx.doi.org/10.1088/0034-4885/42/1/001

[NTS+69] S. G. Nilsson, C. F. Tsang, A. Sobiczewski, Z. Szymański, S. Wycech, C. Gustafson, I. Lamm, P. Möller, and H. Nilsson: «On the Nuclear structure and stability of heavy and superheavy elements». Nucl. Phys. A **131**, 1 (1969). URL http://dx.doi.org/10.1016/0375-9474(69)90809-4

[OBE+06] J. N. Orce, A. M. Bruce, A. Emmanouilidis, A. P. Byrne, G. D. Dracoulis, T. Kibedi, M. Caamano, H. El-Masri, C. J. Pearson, Z. Podolyak, P. D. Stevenson, P. M. Walker, F. R. Xu, D. M. Cullen, and C. Wheldon: «Shape-driving effects in the triaxial nucleus, 128Xe». Phys. Rev. C **74**, 034 318 (2006). doi:10.1103/PhysRevC.74.034318. URL http://link.aps.org/abstract/PRC/v74/e034318

[PBB+01] C. M. Petrache, G. L. Bianco, D. Bazzacco, T. Kröll, S. Lunardi, R. Menegazzo, M. Nespolo, P. Pavan, C. R. Alvarez, G. de Angelis, E. Farnea, T. Martinez, N. Marginean, D. R. Napoli, and N. Blasi: «High-spin states in the deformed ^{122}Ba nucleus». Eur. Phys. J. **12**, 135 (2001)

[PBB+03] C. M. Petrache, G. L. Bianco, P. G. Bizzeti, A. M. Bizzeti-Sona, D. Bazzacco, S. Lunardi, M. Nespolo, G. de Angelis, D. R. Napoli, N. Blasi, S. Brant, and D. Vretenar: «Spectroscopy of the deformed ^{126}Ce nucleus». Eur. Phys. J. **16**, 337 (2003)

[PCA+05] E. S. Paul, P. T. W. Choy, C. Andreoiu, A. J. Boston, A. O. Evans, C. Fox, S. Gros, P. J. Nolan, G. Rainovski, J. A. Sampson, H. C. Scraggs, A. Walker, D. E. Appelbe, D. T. Joss, J. Simpson, J. Gizon, A. Astier, N. Buforn, A. Prévost, N. Redon, O. Stézowski, B. M. Nyakó, D. Sohler, J. Timár, L. Zolnai, D. Bazzacco, S. Lunardi, C. M. Petrachte, P. Bednarczyk, D. Curien, N. Kintz, and I. Ragnarsson.: «Highest spin discrete levels in ^{131,132}Ce: Spin generation near the mesoscopic limit». Phys. Rev. C **71**, 054 309 (2005)

[PFG+01] E. S. Paul, S. A. Forbes, J. Gizon, K. Hauschild, I. M. Hibbert, D. T. Joss, P. J. Nolan, B. M. Nyakó, J. A. Sampson, A. T. Semple, R. Wadsworth, L. Walker, J. N. Wilson, and L. Zolnai: «Measurement of transition quadrupole moments of high-spin states in the N=74 isotones ^{133}Pr, ^{132}Ce and ^{131}La». Nucl. Phys. A **690**, 341 (2001). doi:10.1016/S0375-9474(00)00695-3. URL http://dx.doi.org/10.1016/S0375-9474(00)00695-3

[PFM+90] S. Pilotte, S. Flibotte, S. Monaro, N. Nadon, N. Prevost, P. Taras, H. R. Andrews, D. Horn, V. P. Janzen, D. C. Radford, D. Ward, J. K. Johansson, J. C. Waddington, T. E. Drake, A. Galindo-Uribarri, and R. Wyss: «Rotaional bands and shape changes in ^{124}Ba». Nucl. Phys. A **514**, 545 (1990)

[PL91] R. Piepenbring and J. Leandri: «On the interpretation of low-lying negative-parity states in even-even transitional nuclei of the barium region». Phys. Lett. B **267**, 17 (1991)

[RAB+92] D. C. Radford, H. R. Andrews, G. C. Ball, D. Horn, D. Ward, F. Banville, S. Flibotte, S. Monaro, S. Pilotte, P. Taras, J. K. Johansson, D. Tucker, J. C. Waddington, M. A. Riley, G. B. Hagemann, and I. Hamamoto: «Multiple band structure and band termination in ^{157}Ho towards complete high-spin spectroscopy». Nucl. Phys. A **545**, 665 (1992). doi:10.1016/0375-9474(92)90298-X. URL http://dx.doi.org/10.1016/0375-9474(92)90298-X

[Rad95] D. C. Radford: «ESCL8R and LEVIT8R: Software for interactive graphical analysis of HPGe coincidence data sets». Nucl. Instr. Meth. A **361**, 297 (1995). doi:10.1016/0168-9002(95)00183-2

[RB85] I. Ragnarsson and T. Bengtsson: «Band crossiong and band terminations in rapidly rotating nuclei». Nucl. Phys. A **447**, 251c (1985)

[RBR+02] G. Rainovski, D. L. Balabanski, G. Roussev, G. Lo Bianco, G. Falconi, N. Blasi, D. Bazzacco, G. de Angelis, D. R. Napoli, F. Dönau, and V. I. Dimitrov: «Tilted dipole bands in ^{123}Xe». Phys. Rev. C **66**, 014 308 (2002). doi:10.1103/PhysRevC.66.014308. URL http://link.aps.org/abstract/PRC/v66/e014308

[RGH+01] D. Roßbach, A. Görgen, H. Hübel, E. Mergel, G. Schönwaßer, A. N. Wilson, F. Azaiez, A. Astier, D. Bazzacco, M. Bergström, C. Bourgeois, N. Buforn, F. Hannachi, K. Hauschild, A. Korichi, W. Korten, T. Kröll, A. Lopez-Martens, R. Lucas, H. J. Maier, N. Redon, P. Reiter, C. Rossi-Alvarez, O. Stezowski, and P. Thirolf: «Evidence for Octupole Vibration in Superdeformed ^{196}Pb». Phys. Lett. B **513**, 9 (2001)

[RHSH+07] C. Rønn Hansen, G. Sletten, G. B. Hagemann, B. Herskind, D. R. Jensen, P. Bringel, C. Engelhardt, H. Hübel, A. Neußer-Neffgen, A. K. Singh, M. P. Carpenter, R. Janssens, T. L. Khoo, T. Lauritsen, P. Bednarczyk, T. Byrski, D. Curien, G. Benzoni, A. Bracco, F. Camera, S. Leoni, R. M. Clark, P. Fallon, A. Korichi, J. Roccaz, A. Maj, J. N. Wilson, J. C. Lisle, T. Steinhardt, O. Thelen, and S. W. Ødegård: «Band structures extending to very high spin in ^{126}Xe». Phys. Rev. C **76**, 034 311 (2007)

[RS80] P. Ring and P. Schunk: *The nuclear many-body problem* (Springer- Verlag, New York, INc. US, 1980)

[RXBR86] I. Ragnarsson, Z. Xing, T. Bengtsson, and M. A. Riley: «Properties of Terminating Bands in Nuclei». Phys. Scripta **34**, 651 (1986)

[SA75] R. M. Steffen and K. Alder: *The Electromagnetic Interaction in Nuclear Spectroscopy* (North-Holad, Amsterdam, 1975)

[SAA+97] J. N. Scheurer, M. Aiche, M. M. Aleonard, G. Barreau, F. Bourgine, D. Boivin, D. Cabaussel, J. F. Chemin, T. P. Doan, J. P. Goudour, M. Harston, A. Brondi, G. L. Rana, R. Moro, E. Vardaci, and D. Curien: «Improvements in the in-beam γ-ray spectroscopy provided by an ancillary detector coupled to a Ge γ-spectrometer: the DIAMAND-EUROGAM II example». Nucl. Instr. Meth. A **385**, 501 (1997)

[SCF+00] J. F. Smith, C. J. Chiara, D. B. Fossan, G. J. Lane, J. M. Sears, I. Thorslund, I. M. Hibbert, R. Wadsworth, I. Y. Lee, and A. O. Macchiavelli: «Multiple shape-driving $\nu(h_{11/2})^2$ and $\pi(h_{11/2})^2$ alignments in ^{120}Ba». Phys. Lett. **483**, 7 (2000)

[SCW+99] I. Schneider, R. Chakrawarthy, I. Wiedenhöver, A. Schmidt, H. Meise, P. Petkov, A. Dewald, P. von Brentano, O. Stuch, K. Jessen, D. Weisshaar, C. Schumacher, O. Vogel, G. Sletten, B. Herskind, M. Bergström, and J. Wrzesinski: «Magnetic dipole band in ^{124}Xe». Phys. Rev. C **60**, 014 312 (1999)

[SDM+04] B. Saha, A. Dewald, O. Möller, R. Peusquens, K. Jessen, A. Fitzler, T. Klug, D. Tonev, P. von Brentano, J. Jolie, B. Gall, and P. Petkov: «Porbing nuclear structure of ^{124}Xe». Phys. Rev. C **70**, 034 313 (2004). doi:10.1103/PhysRevC.70.034313. URL http://link.aps.org/doi/10.1103/PhysRevC.70.034313

[SHD+04] A. K. Singh, H. Hübel, J. Domscheit, G. B. Hagemann, B. Herskind, D. R. Jensen, J. N. Wilson, R. Clark, M. Cromaz, P. Fallon, A. Görgen, I. Y. Lee, A. O. Macchiavelli, D. Ward, H. Amro, W. C. Ma, J. Timár, and I. Ragnarsson: «Evidence for noncollective oblate structures at high spin in ^{123}Cs». Phys. Rev. C **70**, 034 315 (2004)

[Sim97] J. Simpson: «The Euroball Spectrometer». Z. Phys. A **358**, 139 (1997)

[SLD+93] F. Seiffert, W. Lieberz, A. Dewald, S. Freund, A. Gelberg, A. Granderath, D. Lieberz, R. Wirowski, and P. von Brentano: «Band structures in ^{126}Xe». Nucl. Phys. A **554**, 287 (1993)

[SMA+98] G. J. Schmid, A. O. Macchiavelli, S. J. Asztalos, R. M. Clark, M. A. Deleplanque, R. M. Diamond, P. Fallon, R. Kruecken, I. Y. Lee, R. W. MacLeod, F. S. Stephens, and K. Vetter: «Gamma-ray polarization sensitivity of Gammasphere segmented germanium detectors». Nucl. Instr. Meth. A **417**, 95 (1998). URL http://dx.doi.org/10.1016/S0168-9002(98)00624-X

[SMCC+04] J. F. Smith, V. Medina-Chico, C. J. Chiara, M. P. Carpenter, C. N. Davids, M. Devlin, J. L. Durell, D. B. Fossan, S. J. Freeman, R. V. F. Janssens, D. R. LaFosse, M. J. Leddy, P. Reiter, D. G. Sarantites, D. Seweryniak, K. Starosta, R. Wadsworth, A. N. Wilson, and J. N. Wilson: «High-spin spectroscopy and quasiparticle alignments in ^{124,125}Ce». Phys. Rev. C **69**, 034 339 (2004)

[SPV+97] M. Serris, C. T. Papadopoulos, R. Vlastou, C. A. Kalfas, S. Kossionides, N. Fotiades, S. Harissopulos, C. W. Beausang, M. J. Joyce, E. S. Paul, M. A. Bentley, S. A. and. Simpson, and J. F. Sharpey-Schafer: «High spin structures of ^{122}Xe». Z. Phys. A **358**, 37 (1997)

[SRI] «The Stopping and Range of Ions in Matter». URL http://www.srim.org/

[SS72] F. S. Stephens and R. S. Simon: «Coriolis effects in the yrast states». Nucl. Phys. A **183**, 257 (1972)

[Ste75] F. Stephens, S.: «Coriolis effects and rotation alignment in nuclei». Rev. Mod. Phys. **47**, 43 (1975)

[Str67] V. M. Strutinsky: «Shell effects in nuclear masses and deformation energies». Nucl. Phys. A **95**, 420 (1967). URL http://dx.doi.org/10.1016/0375-9474(67)90510-6

[SW68] A. Z. Schwartzschild and E. K. Warburton: «The measurments of short nuclear lifetimes». Ann. Rev. Nucl. Sci. **18**, 265 (1968). URL http://arjournals.annualreviews.org/doi/pdf/10.1146/annurev.ns.18.120168.001405

[SZF02] B. Singh, R. Zywina, and R. Firestone: «Table of Superdeformed Nuclear Bands and Fission Isomers». Nucl. Data Sheets **97**, 241 (2002)

[Szy83] Z. Szymański: *Fast Nuclear Rotation* (Clarendon Press. Oxford, 1983)

[TAL+84] D. M. Todd, R. Aryaeinejad, D. J. G. Love, A. H. Nelson, P. J. Nolan, P. J. Smith, , and P. J. Twin: «Rotational band structures and lifetime measurements in ^{130}Ce». J. Phys. G: Nucl. Part. Phys. A **10**, 1407 (1984)

[TJJ+94] S. Törmänen, S. Juutinen, R. Julin, B. Cederwall, A. Johnson, R. Wyss, P. Ahonen, B. Fant, M. Matsuzaki, J. Nyberg, M. Piiparinen, S. Mitarai, J. Mukai, f, and A. Virtanena: «Competing proton and neutron alignments in neutron-deficient Xe-nuclei». Nucl. Phys. A **572**, 417 (1994). doi:doi:10.1016/0375-9474(94)90183-X. URL http://dx.doi.org/10.1016/0375-9474(94)90183-X

[TSP+95] J. Timár, J. Simpson, E. S. Paul, S. Araddad, C. W. Beausang, M. A. Bentley, M. J. Joyce, and J. F. Sharpey-Schafer: «High-spin structure of ^{121}Xe: triaxiality and band termination». J. Phys. G: Nucl. Part. Phys. A **21**, 783 (1995)

[TSR+94] H. Timmers, J. Simpson, M. A. Riley, T. Bengtsson, M. A. Bentley, F. Hanna, S. M. Mullins, J. F. Sharpey-Schafer, and R. Wyss: «High-spin γ-ray spectroscopy of ^{122}Xe». J. Phys. G: Nucl. Part. Phys. A **20**, 287 (1994)

[TW38] E. Teller and J. A. Wheeler: «On the Rotation of the Atomic Nucleus». Phys. Rev. **53**, 778 (1938). doi:10.1103/PhysRev.53.778. URL http://link.aps.org/doi/10.1103/PhysRev.53.778

[VCD+99] O. Vogel, R. S. Chakrawarthy, A. Dewald, P. Petkov, K. Jessen, J. Gableske, P. von Brentano, D. Bazzacco, A. Gizon, J. Gizon, S. Lunardi, D. R. Napoli, P. Pavan, C. R. Alvarez, and I. Wiedenhöver: «High spin states in ^{128}Ba». Eur. Phys. J. **4**, 323 (1999)

[VDS83] M. J. A. de Voigt, J. Dudek, and Z. Szymański: «High-spin phenomena in atomic nuclei». Rev. Mod. Phys. **55**, 949 (1983)

[WGB+89] R. Wyss, A. Granderath, R. Bengtsson, P. von Brentano, A. Dewald, A. Gelberg, A. Gizon, J. Gizon, S. Harissopulos, A. Johnson, W. Lieberz, W. Nazarewicz, J. Nyberg, and K. Schiffer: «Interplay between proton and neutron s-bands in the Xe-Ba-Ce-REGION». Nucl. Phys. A **505**, 337 (1989)

[WJA+91] D. Ward, V. P. Janzen, H. R. Andrews, D. C. Radford, G. C. Ball, D. Horn, J. C. Waddington, J. K. Johansson, F. Banville, J. Gascon, S. Monaro, N. Nadon, S. Pilotte, D. Prevost, P. Taras, and R. Wyss: «Gamma-Ray Spectroscopy of ^{126}Ba». Nucl. Phys. A **529**, 315 (1991)

[WJL+89] R. Wyss, A. Johnson, D. J. G. Love, M. J. Godfrey, and S. M. Mullins: «High spin spectroscopy of ^{124}Ba and $h_{11/2}$ neutron alignment». Z. Phys. A **332**, 241 (1989)

[WMW+01] V. Werner, H. Meise, I. Wiedenhöver, A. Gade, and P. von Brentano: «Collective bands in the triaxial nucleus ^{124}Xe». Nucl. Phys. A **692**, 451 (2001)

[WNJ+88] R. Wyss, J. Nyberg, A. Johnson, R. Bengtsson, and W. Nazarewicz: «Highly deformed intruder bands in the A $\approx$ 130 mass region». Phys. Lett. B **215**, 211 (1988). URL http://dx.doi.org/10.1016/0370-2693(88)91422-0

[WUC+93] I. .Wiedenhover, U.Neuneyer, C.Kerskens, J.Altmann, O.Stuch, J.Theuerkauf, G.Siems, R.Wirowski, M.Eschenauer, P. Brentano, R.Schubart, H.Kluge, and K.H.Maier: «High Spin Structure in ^{127}Xe and ^{125}Xe». Z. Phys. A **347**, 71 (1993)

[WYN+95] I. Wiedenhöver, J. Yan, U. Neuneyer, R. Wirowski, P. von Brentano, A. Gelberg, N. Yoshida, and T. Otsuka: «Non-yrast states in ^{125}Xe». Nucl. Phys. A **582**, 77 (1995)

[Yam67] T. Yamazaki: «Tables of Coefficients for Angular Disttribution of Gamma Rays from Aligned Nuclei». Nucl. Data **3**, 1 (1967)

[ZBL85] J. F. Ziegler, J. P. Biersack, and U. Littmark: *The Stopping and Range of Ions in Solids* (Pergamon, New York, 1985)

Acknowledgements

I am deeply indebted to my supervisor Prof. Dr. H. Hübel, for providing me the possibility to performed my Ph.D. study in his group. I am grateful to him for his enthusiasm, inspiration, patience, constant support and for providing an amiable working environment. Throughout my thesis-writing period, he provided encouragement, valuable discussions and lots of good ideas. Due to his engagement, I could participate in many experiments in different labs, gathered unforgettable experience and met many interesting people. Without your help I would have lost. For every thing you have done for me Dr. Hübel, I thank you.

Special thanks goes to Prof. Dr. K. T. Brinkmann for taking the role of the co-referee for my dissertation.

I would like to express my profound gratitude to Dr. A. K. Singh for his great help and guidance on data analysis and for the long discussions and suggestions, as well as for reviewing my thesis. I have enjoyed working with you. Thank you very much indeed Dr. Singh.

I am grateful to Prof. Dr. G. Hagemann for her great help and support. Particularly, working on the level schemes of ^{124,125}Xe. I am also thankful for the worthwhile discussions and suggestions. It was a great pleasure for me to work with you.

I have spent a week at Lund university. I have enjoyed it very much. I would like to take this opportunity to express my gratitude to Prof. Dr. R. Bengtsson for his great help and patience on teaching me the Ultimate Cranker code and for the valuable discussions of the CSM. Special thank also goes to Prof. Dr. I. Ragnarsson for his help and support with the CNS calculation.

My thanks go to all former members of Prof. Hübel research group for their friendly support and amiable working atmosphere. It was a great pleasure to work with Dr. Patrik Bringel, Dr. Alexander Bürger, Dr. Sebastian Chmel, Claudia Engelhardt, Dr. Edger Mergel, Dr. Nentscho Nenoff, Dr. Andrea Neußer-Neffgen, Dr. Gero Schönwaßer and Dr. Ajay Kummar Singh. Special gratitude goes to Dr. Alexander Bürger for providing help and support and for reviewing part of my dissertation.

I am deeply indebted and grateful to my parents and siblings. I do appreciate the unlimited support, love and encouragement that you have given to me during my study. Without you I would be nothing. Thank you very much.

Finally, I am very grateful to my lovely wife Yumen for her patience, endless love, help and support. I am amazingly lucky to have you. Ich danke dir Schätzchen.